Technische Universität München

Lehrstuhl für Luftfahrtsysteme

Methods for the Design and Evaluation of Future Aircraft Concepts Utilizing Electric Propulsion Systems

Stefan Stückl

Vollständiger Abdruck der von der Fakultät für Maschinenwesen der Technischen Universität München zur Erlangung des akademischen Grades eines
Doktor-Ingenieurs (Dr.-Ing.)
genehmigten Dissertation.

Vorsitzender:	Univ.-Prof. Dr.-Ing. Manfred Hajek
Prüfer der Dissertation:	1. Univ.-Prof. Dr.-Ing. Mirko Hornung
	2. Univ.-Prof. Dr.-Ing. Rudolf Voit-Nitschmann

Die Dissertation wurde am 24. Juni 2015 bei der Technischen Universität München eingereicht und durch die Fakultät für Maschinenwesen am 18. April 2016 angenommen.

Für Emma

Vorwort

Die vorliegende Arbeit entstand während meiner Tätigkeit bei Airbus Group Innovations in Zusammenarbeit mit dem Lehrstuhl für Luftfahrtsysteme der Technischen Universität München. Ich möchte mich herzlich bei Herrn Prof. Dr.-Ing. Mirko Hornung bedanken, der mir als Doktorvater sowohl die notwendigen Freiräume in der Gestaltung dieser Arbeit gegeben hat als auch stets mit wissenschaftlichem Rat zur Seite stand. Herrn Prof. Dr.-Ing. Rudolf Voit-Nitschmann möchte ich herzlich danken, dass er seine Expertise für das Zweitgutachten zur Verfügung gestellt hat sowie Herrn Prof. Dr.-Ing. Manfred Hajek für die freundliche Übernahme des Prüfungsvorsitzes.

Das internationale und interdisziplinäre Arbeitsumfeld der zentralen Forschungseinrichtung der Airbus Group haben wesentlich zum Erfolg dieser Arbeit beigetragen. Hier gilt mein besonderer Dank Herrn Jan van Toor und Herrn Dr. Jürgen Steinwandel, die mit ihrer langjährigen Unterstützung und fachlichen Begleitung vom ersten Tag an den Grundstein und das Fundament für diese Arbeit und meinen bisherigen Werdegang gelegt haben. Weiterhin möchte ich mich bei Herrn Dr. Hans Lobentanzer bedanken, der bei der Initiierung und Definition dieser Arbeit mitgewirkt hat. Für die immer zielführenden und konstruktiven Diskussionen und den fachlichen Rat möchte ich mich herzlich bei meinen Kollegen und Freunden Dr.-Ing. Corin Gologan, Dr.-Ing. Alexander Ohnesorge, Dr.-Ing. Michael Hofmann, Herrn Michael Pilawa und Herrn Ning Wang bedanken. Darüber hinaus gilt mein besonderer Dank Herrn Florian Stagliano für die Inspiration aus unzähligen Gesprächen, für das wertvolle Feedback und die kreativen Impulse die daraus entstanden sind.

Von ganzem Herzen möchte ich mich bei meinen Eltern bedanken, die mir für meinen Weg im Leben immer die notwendigen Freiräume und Unterstützung gegeben haben. Und zu guter Letzt gilt mein größter Dank meiner Lebensgefährtin Jasmin, die mir mit ihrem bedingungslosen Rückhalt über die vielen Jahre zur Seite stand und mir immer die notwendige Kraft und Sicherheit gegeben hat.

München, im Juli 2016 Stefan Stückl

Abstract

Contributing to the recent research activities regarding electric propulsion for aeronautical applications, the objective of this thesis is to develop methods for the design and evaluation of future electric propulsion aircraft, to identify critical technologies and main design drivers of the electric powertrain, and to identify the practical limits of electric propulsion aircraft based on the foreseeable technological progress.

In this context, the components of a battery-based electric powertrain are specified, and viable propulsion system architectures are assessed based on requirements equivalent to today's certification standards. Critical technologies and main design drivers for the propulsion system are identified by means of sensitivity studies and a baseline setup for an electric propulsion system is defined. Accounting for the different weight- and power characteristics of the electric powertrain, the implications on the aircraft structure and operational aspects are discussed and the sizing methodology is adapted accordingly.

The presented set of design methods is applied for the preliminary design of an electric baseline aircraft. The implications of battery integration and adapted operations on aircraft weight and performance are discussed and, taking these findings into account, the baseline is re-designed. Finally, the sizing limits of the considered aircraft class are evaluated for different battery technologies and typical payload-range requirements in a design space investigation.

Zusammenfassung

Elektrische Antriebssysteme für Luftfahrtanwendungen sind Gegenstand aktueller und zukünftig absehbarer Forschungsaktivitäten. Als Beitrag hierzu ist das Ziel dieser Arbeit die Entwicklung von Methoden für den Entwurf und die Bewertung von zukünftigen Flugzeugkonzepten mit elektrischem Antriebssystem. Darüber hinaus sollen kritische Technologien und Komponenten des Antriebssystems identifiziert und die praktischen Grenzen elektrisch angetriebener Regionalflugzeuge basierend auf aktuellen Prognosen zur Technologieentwicklung aufgezeigt werden.

Hierzu werden zunächst die Komponenten eines batteriegestützten Antriebsstranges spezifiziert und, unter Berücksichtigung heutiger Zertifizierungsvorgaben, mögliche Antriebssystem-Architekturen diskutiert. Kritische Technologien werden anhand von Sensitivitätsstudien ermittelt und eine Basis-Antriebsarchitektur wird definiert. Unter Berücksichtigung der spezifischen Gewichts- und Leistungscharakteristika der elektrischen Komponenten werden das Luftfahrzeug betreffende strukturelle und operationelle Besonderheiten diskutiert und entsprechende Anpassungen des Entwurfsprozesses vorgeschlagen.

Die erarbeiteten Methoden werden daraufhin im Entwurf eines batteriegestützten Regionalflugzeugkonzeptes angewandt. Im Vergleich mit einem konventionell angetriebenen Referenzflugzeug werden die Auswirkungen des elektrischen Antriebssystems bezüglich Gewichte und Betriebscharakteristik auf Gesamtflugzeugebene dargestellt und Optimierungspotentiale hinsichtlich Flugzeugkonfiguration und Betriebsstrategie aufgezeigt. Zum Abschluss wird der Entwurfsraum zukünftiger batteriegestützter Regionalflugzeuge evaluiert und gewichtsbedingte Limitationen in Abhängigkeit der verfügbaren Batteriegüte aufgezeigt.

Contents

List of Figures

List of Tables

Nomenclature

A	Area
C	Cell capacity/ Force coefficient
D	Diameter/ Drag area
E	Energy
I	Electric current
J	Advance ratio (propeller)
K	Gearbox technology factor/ Rate of reaction
L	Lift/ Inductivity
M	Torque / Mach number
N	Rotational speed
P	Power
Q	Heat
R	Gas constant/ electric resistance/ range
S	Area
T	Temperature
U	Voltage
V	Volume
c	Cord length
g	Gravity constant
n	Number
p	Part load factor
r	Radius
s	Separation
t	Thickness/ Thrust
v	Velocity
w	Weight
x	Length
α	Temperature coefficient
δ	Ambient temperature ratio
ε	Carnot efficiency
η	efficiency
θ	Ambient pressure ratio
ρ	Density
σ	Density ratio
ω	Angular velocity
C_p	Power coefficient (propeller)
K_w	Propeller weight correction factor
$U_{CE,sat}$	IGBT forward voltage drop
e_E	Component cooling efficiency
f_s	Propeller slipstream structure drag area
k_0	Arrheius equation constant
ζ_{cell}	Cell weight share of battery pack

Subscripts

a	Actuator
ac	Aircraft
ABO	All batteries operating
alu	Aluminum
BAT	Battery
b	Blades (propeller)
$block$	Blocking (voltage)
$cable$	Cable
$cell$	Cell level
cg	Center of gravity
$comp$	Component
$cond$	Conductor
$cool$	Cooling
$cut-off$	Cut-off
dis	Discharge(d)
eff	Effective
el	Electric
e	Electric lead
env	Environment
FOM	Figure of merit
$heat$	Heat
h	High(er)/ Hinge
ht	Horizontal tail
ind	Induced
iso	Isolation
l	Low(er)
mo	Max operating
$mech$	Mechanic
mot	Motor
np	Neutral point
OBI	One battery inoperative
OC	Open circuit
O	Outer
ov	Overall
par	Parallel
pc	Passenger cabin
PAX	Passengers
po	polarization
p	Propeller
r	Radiator
req	Required
SL	Sea level
SC	Semiconductor
ser	Serial
$shaft$	Shaft (motor/ engine)
$sheath$	Sheath
$spec$	Specific

sys	System
$term$	Thermal
tot	Total
u	Undercarriage
vac	Vacuum (relays)

Abbreviations

AC	Alternating current/ aircraft
AEO	All engines/motors operating
BCU	Battery control unit
BMS	Battery management system
CAS	Calibrated airspeed
CFRP	Carbon fiber reinforced plastic
CONT	Contactor
DC	Direct current
ECS	Environmental control system
EHA	Electro-hydrostatic actuator
ELOS	Equivalent level of safety
EMA	Electro-mechanical actuator
EMER	Emergency
EMC	Electromagnetic compatibility
EPR/ HEPR	Ethylene propylene rubber
ESAR	Energy specific air range
ESS	Essential
EVA	Ethylene-vinyl acetate
EWIS	Electrical wiring interconnection systems
HTS	High temperature superconducting
HV	High voltage
IFE	Inflight entertainment
IGBT	Insulated-gate bipolar transistors
LFL	Landing field length
LRC	Long range cruise
LTS	Low temperature superconducting
MAX	Mean aerodynamic chord
Mot	Motors
OC	Open circuit
OEI	One engine/motor inoperative
PAX	Passengers
PR	Power rating
SC	Superconducting
SEP	Specific excess power
SFC	Specific fuel consumption
SM	Static margin
SoC	State of charge
TOFL	Take-off field length
TRU	Transformer rectifier unit
TSPC	Thrust specific power consumption
XLPE	Cross-linked polyethylene

1. Introduction

The air transport industry will face fundamental challenges in the coming decades. As the concerns about human-induced global warming persist, most industrialized countries are looking for ways to limit and reduce the emission of greenhouse gases. The principal approaches therefore are an increased use of renewable energy sources and reducing energy consumption by adapted consumer behavior and more efficient technology. Though aviation currently accounts for around 2-3% of global greenhouse gases, the public and political pressure rises to achieve a reduction of aviation related emissions. The inclusion of the European air traffic in the European Union Emission Trading Scheme is a recent example [1]. As a consequence, the European aviation industry agreed on ambitious goals to reduce aircraft related emissions on the long term as reported in ACARE 2020 and "Flightpath 2050" [2], the latter asking for a 75% reduction of CO_2 emissions per passenger kilometer until the mid of this century. However, considering the continuous growth in global air traffic, this goal can hardly be achieved by evolutionary improvement of aircraft structures and combustion engines. Hence a more radical step change in technology is necessary to meet the reduction targets.

A second challenge the aviation industry is facing today and in the future is the price and availability of crude oil as source of conventional jet fuel. In the past decades, global economic growth especially in developing countries created a constantly increasing demand for crude oil as basis for fuels and other chemical products. Crude oil production has been increased accordingly, but in an environment of unabated high demand, natural disasters, and political instabilities in producing countries, average oil and fuel prices have fluctuated significantly during the past decade. Predicting oil prices for the mid- and long-term future is a difficult task since technological, geological, and socio-economic factors impact its development. On the long-term (~2030), optimistic studies estimate an average of around 130$ per barrel [3]. In a rather pessimistic scenario, the IMF [4] expects an oil price of around 300$, which would have a severe impact on today's airline business models.

In principle, the car industry faces similar challenges as the aviation industry since it shares its dependency on fossil fuels. Next to continuous efforts to reduce fuel consumption by better engine- and system efficiencies, the most serious approach today to address these challenges is the introduction of hybrid- and fully battery powered electric cars, featuring less or zero emission during operation. Political support for this technology was expressed exemplary in Germany by aiming for one million electric cars on the streets by 2020 [5]. The resulting need for compact and lightweight batteries and electric motors lead to significant investments in research and development. In this environment, the performance of the components building an electric powertrain has been improved significantly during the recent years.

In this context, a key question arises for the aviation industry: are electric, battery powered propulsion systems also a viable option for commercial transport aircraft? As of today, pure electric powertrains suffer from significant performance and weight deficits compared to systems with internal combustion engines. Therefore, electric powered aircraft are yet limited to small experimental and general aviation applications. However, assuming ongoing investments in

battery- and motor development, rising oil and fuel prices, and increasing public pressure to limit air traffic emissions, the introduction of electric propulsion in future commercial transport aircraft emerges as an option that has to be addressed and investigated in more detail.

1.1. Challenges in Design and Assessment of Battery Powered Electric Propulsion Aircraft

Aircraft design is characterized by a high degree of interdependencies between aerodynamics, structure, systems and propulsion. The best solution can only be achieved if each domain is optimized with respect to overall aircraft performance. A decent assessment of a new aircraft propulsion system with fundamentally different characteristics therefore cannot be done independently, but should be conducted in the frame of an integrated overall aircraft study. Consequently, preliminary aircraft design in conjunction with electric propulsion system modeling is a reasonable approach to evaluate the viability of electric propulsion aircraft in a first step.

However, the introduction of an electric propulsion system leads to new challenges concerning the preliminary aircraft design methodology. In case of a conventional aircraft, a large statistical base about component weight, geometry, and system characteristics is available from previously designed and build planes. The fact that these went into service implies that all certification requirements concerning the system architectures have been fulfilled. Hence, surrogate models e.g. for weight estimation can be derived on this basis and be applied for the preliminary design of a new aircraft. For the electric propulsion case however, there are no existing commercial air transport applications yet and hence methods for component modeling cannot be generated based on statistical data. Moreover, especially concerning the electric powertrain, there are not even regulations or certification requirements for an application in large aircraft (CS 25), given the novelty of the technology in aircraft propulsion. These however are necessary since they provide requirements and guidelines to design appropriate propulsion system architectures. The storage of electric energy has further major implications on the aircraft design. As will be detailed during this thesis, these storage devices differ significantly in their characteristics compared to conventional combustion fuels. The conventional approach of energy storage in wing-tanks may hence not be appropriate anymore and other solutions for energy storage system integration into the aircraft have to be considered. As a consequence, the weight allocation and hence stress distribution across the airframe may change fundamentally, leading to characteristic structural implications.

Next to the issues mentioned so far, an electric propulsion system also affects the operational characteristics of an aircraft. Conventional gas turbines burn fuel with oxygen out of the atmosphere, convert the resulting energy in a Joule-Brayton cycle and instantly eject the reaction products in form of exhaust gas. The propulsion system performance hence has a direct dependency on ambient conditions like air temperature and density, and it constantly loses weight due to fuel burn during flight. Electric propulsion systems, in contrast, feature fundamentally different operational characteristics, which in turn directly impact flight performance. Common mission profiles, weight accounting conventions, and design approaches as usually used in preliminary aircraft design may not be appropriate anymore.

1.2. Main Objectives

Considering the prospects and challenges of electric powered aircraft as mentioned above, the objective of this thesis is to address the methodical issues and evaluate the technological viability in the following steps:

Adaption of aircraft preliminary sizing methodology for electric aircraft
As outlined in the previous section, the standard preliminary aircraft design approach does not account for electric propulsion systems. The scope of this thesis is to identify these gaps and to develop a set of methods to build a consistent parametric aircraft model.

Identification of critical technologies and main design drivers for electric aircraft propulsion
The electric propulsion system consists of a number of different components responsible for storage, transmission, conversion and monitoring of electric energy. Within this thesis, the critical components in the powertrain that are substantially driving weight and impact safety or applicability shall be identified.

Identification of the practical limits of electric propulsion aircraft based on the foreseeable technological progress
Based on predictions of the technological progress concerning electric propulsion systems in the next decades, practical limits of electric propulsion aircraft will be evaluated. Furthermore, the potential of pushing these limits by adapting aircraft operations to the characteristics of the electric propulsion system shall be assessed.

1.3. Structure of Work

The goals as outlined are being achieved by the following steps, determining also the structure of this thesis:

Discussion of the current state and research needs in electric propulsion aircraft
After a short outline of the history of demonstrated electric aircraft, the current state of the literature concerning modeling methods for electric aircraft design and assessment is being discussed. By means of an evaluation of the available methods with respect to the objectives of this thesis, research needs are being derived.

Definition of modeling methods for the components of electric propulsion systems
In a first step, the components of the electric powertrain including storage, transmission, conversion, cooling, and switching will be detailed. Based on predictions of future technology development, parametric models determining component characteristics will be presented. Next to the powertrain itself, this includes also electrified aircraft systems.

Evaluation of propulsion system architectures in due consideration of certification aspects
The components defined in the first step will be assessed regarding their functionality and characteristics as sub-systems of a propulsion system architecture. Based on present certification standards for conventional propulsion systems, electric powertrain architectures will

be derived fulfilling an equivalent level of safety in terms of system redundancy and fail-save characteristics.

Identification of design drivers and critical components in sensitivity analyses

By means of sensitivity studies, the powertrain setup will be optimized and critical components with high impact on propulsion system weight will be identified for further analysis on overall aircraft level.

Adaption of the sizing methodology for electric propulsion aircraft

The implications of the electric powertrain will be discussed with respect to necessary adaptions in the preliminary aircraft design and sizing process, and respective solutions will be presented. Common methods for aerodynamic-, weight- and performance assessment will be adapted to the characteristic features of the new propulsion system and implemented into a parametric aircraft design model. This model will be validated and calibrated by a re-design of in-service reference aircraft.

Conceptual design and analysis of an electric propulsion aircraft

In a final step, the generated methods will be applied to analyze the characteristics and potential limitations of future electric propulsion aircraft. Results will be generated and discussed for an electric baseline design that matches the top-level requirements of an in-service reference aircraft. Applying sensitivity studies, adapted design aspects and operational strategies will be identified and applied in a re-design of the baseline design. Finally, the design space in terms of payload and range requirements will be evaluated, and practical limits for electric flight will be identified for different scenarios regarding technological development.

2. Current State of Electric Propulsion Aircraft and Research Needs

In this chapter, the history and the present state of electric propulsion aircraft is being presented. The current state of research on future electric transport aircraft is being examined and different basic sub-types of electric propulsion systems are being differentiated. Based on this evaluation, the gaps in electric propulsion aircraft design methodology are being identified and an associated research need is formulated.

2.1. Electric Flight in the Past

The first documented electrically powered manned flight was demonstrated in **1881**, when the Tissandier brothers Albert and Gaston attached an electric motor to a dirigible. Three years later, the airship “La France” (see figure 1), powered by a nine horsepower electric motor and a 435 kg battery, won the 10 km speed race around Villacoulbay and Medon in France against its steam engine powered competitors, reaching a top speed of around 19 km/h [6] [7]. The use of electric propulsion in the early time of manned flight came to a sudden end when another source of light-weight power became available: the internal combustion engine.

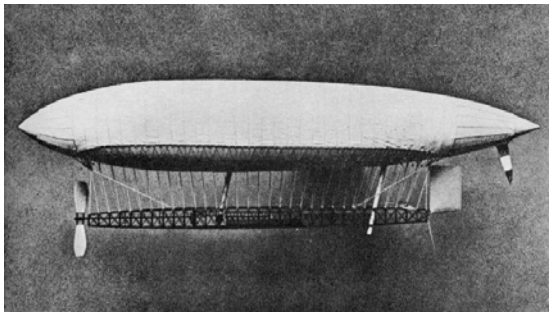

Figure 1: “La France”, 1884 [8]

Due to the high power density of liquid hydrocarbon fuels and advances in the manufacturing and design of light and efficient piston engines, electric propulsion was no longer considered for the time being. It took until **1973**, that the hobbyist model aircraft builder Fred Militky equipped a HB-3 motor-glider with an electric powertrain at the Austrian light-plane manufacturer HB-Flugtechnik. Using a 10 kW Bosch motor and Varta rechargeable nickel-cadmium batteries, the pilot Heino Brditschka took off for the world’s first manned heavier than air electric flight. [9]

Figure 2, HB-3: First electric airplane [9]

In the following years, several attempts towards solar powered aircraft have been made. In **1979**, Larry Mauro accomplished the first flight in his “Solar Riser” ultra-light plane, using solar cells attached on the wing to recharge the batteries on the ground. In the same year, Freddie To made his maiden flight on the “Solar One”, which was originally constructed for the Kramer competition for a muscle powered aircraft. Though, as in case of Mauro’s plane, the solar cells on Solar One’s wings did not supply sufficient power for continuous flight. The first purely solar powered flight was accomplished with the “Gossamer Penguin” in May **1980**, followed by Gunter Rochelt’s “Solair I” and the “Solar Challenger”, which made the first solar powered international flight crossing the English Channel in **1981**. [6]

While all pure battery- and solar hybrid-powered airplanes up to that point have been of experimental nature, advances especially in the field of battery performance lead to an improved performance of electric propulsion systems. As a result, the self-launching ultra-light sailplane “Alisport Silent Club”, which first flew in **1997**, was the first commercial electrically powered aircraft. In **2003**, the German manufacturer Lange Aviation offered the “Antares 20e” in the open sailplane class. Using a 42 kW brushless Motor and Li-ion batteries, the “Antares” is able for self-launch, climb to 3000 m, and subsequent thermal gliding flight [10].

After the first commercial launch of an electric sailplane, also the first commercial ultra-light airplane in a trike configuration was available in **2007**: the “Electraflyer”. Equipped with a 13 kW electric motor and a 35 kg Li-ion polymer battery, a single pilot can conduct flights of up to 1.5 hours [11].

With further advances in weight and efficiency of electric power components, the following years showed a large number of experimental and commercial electric aircraft projects, leading to several hours of demonstrated flight endurance time. Following this development, the CAFÉ foundation initiated the so called Green Flight Challenge, for which a 320 km course has to be flown in less than 2 hours while consuming less energy than the equivalent of 3.8 l kerosene. Out of the four participating electric aircraft, the Slovenian Pipistrel team around the four-seater “Taurus G4” won the competition with a milage of 171.8 km per liter and transported person and a total energy consumption of 65.4 kWh. The second place was achieved with the two-seater aircraft “e-Genius”, built by the IFB (Institut für Flugzeugbau, University of Stuttgart) in Germany. In terms of total energy consumption, the “e-Genius” has beaten all competition with only 34.7 kWh. With respect to the mileage-metric however, it achieved 159.9 km per liter and person and was bested by the “Taurus” due to its lower seat count. Representing the state of the art in today’s electric aircraft capabilities by the metrics of the green flight challenge, both the “Taurus G4” and the “eGenuis” utilize the low weight- and low drag characteristics of a motor-glider airplane. Both aircraft are shown in figure 3 and technical data is given in table 1. [12] [13]

Figure 3, NASA green flight challenge winners: “Taurus” (1st) and “e-Genius” (2nd) [12] [13]

	Taurus	e-Genius	
Span	21.4	16.9	[m]
Length	7.4	8.1	[m]
Empty weight	632	384	[kg]
Battery weight	500	336	[kg]
MTOW	1500	900	[kg]
Power installed	150	65	[kW]
System voltage	325	450	[V]
Battery capacity	90	56	[kWh]
Max. cruise speed	201	235	[km/h]
Endurance	2:45+	4:00+	[h]
Range	400+	500	[km]

Table 1, “Taurus” and “e-Genius” main characteristics [12] [13]

In case of the “Taurus”, the electric propulsion system powers a central fixed-pitch propeller from three battery groups integrated in the two fuselages and the central engine pod. Each battery group contains 88 Li-Po cells, connected in series to reach a nominal system voltage level of 325 Volts DC. Battery control units monitor the state of each cell and disconnect individual groups from the electrical bus with 400 A fuses and 500 A vacuum relays in case of a cell failure. The DC power is converted by a controller/ inverter unit to the required AC power for the electric motor depending on the thrust setting. Cooling for the battery packs, the inverter, and the electric motor is provided by a 50/50 glycol/ water liquid cooling system [12]. A schematic of the propulsion system is given in figure 4.

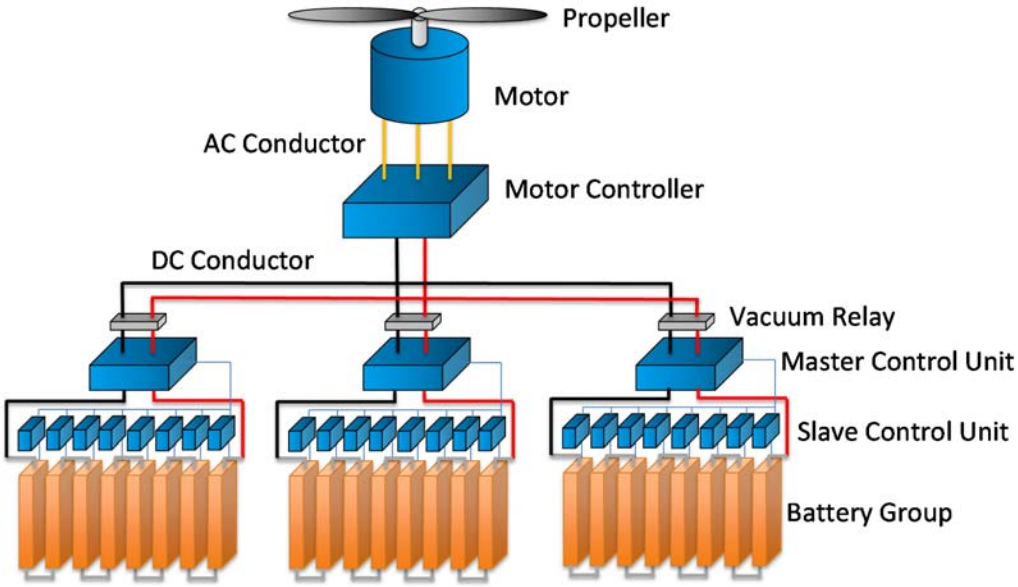

Figure 4, Pipistrel “Taurus” propulsion system schematic

2.2. Current State of Design Methods for Electric Propulsion Aircraft

Large advances in the field of power electronics, electric motors, and especially batteries could be observed within the past several years. This development was mainly pushed by the industrial demand of the mobile entertainment electronic and automobile market. And yet, there is still a considerable potential for improvement. As outlined in the following in detail, it is a permissible assumption that electric propulsion systems will improve in terms of weight, efficiency, and reliability in a mid- and long-term timeframe. With the worldwide discussion about greenhouse gas emissions, climate change and crude oil availability continuing, aircraft designers began to upscale their thoughts from small-scale experimental and general aviation electric aircraft to hybrid and purely electrically powered aircraft concepts for commercial air transportation. In the recent years, aircraft manufacturers and research institutes investigated electric powertrains for future transport aircraft to an increasing extent. In this regard, three basic approaches are being considered:

Electric distribution of fuel-based propulsion power

In this concept, an electric powertrain is used to distribute propulsion power from combustion engines across the aircraft to a certain number of electric motor-driven propulsors (fans/ propellers). The powertrain consists of generators that are driven by the combustion engines, delivering electric power to a power management and distribution (PMAD) system. The PMAD contains electric conductors, switches, and sensor equipment, and ensures safe and reliable transmission of power to the electric motors that are driving the propulsive devices. This setup is generally defined as a pure serial hybrid. If cryogenic hydrogen is used as fuel for the combustion engines, this can also be used as heat sink for superconducting electric motors and cables.

The main focus in this approach is to improve the overall system efficiency by an increased freedom in propulsion system integration like distributed propulsion. Since combustion fuels are used, no weight penalty occurs due to electric energy storage and there is hence no specific limit in the considered aircraft size or range. The potential for fuel burn reduction however is limited to the gains in airframe- and propulsion efficiency. Respective studies have been published in the literature, exemplary in [14] [15] [16].

Hybrid electric propulsion

In addition to the pure distribution concept, electric energy storage devices such as batteries or fuel cell systems can be integrated in the propulsion system, substituting a certain share of the total propulsion energy required for the flight mission. The arrangement of motors, generators, and combustion engines, the amount of electrical energy versus conventional fuel, as well as the composition of installed electric- versus combustion engine power allows for a wide range of different propulsion system architectures. A serial hybrid powertrain is used if the total propeller/ fan shaft is powered by an electric motor alone, in a parallel hybrid setup, the combustion engine and electric motor are both connected to a common propeller/fan shaft. Batteries, but also a fuel cell system, can be used for electric energy storage.

The main objective in hybrid electric propulsion system design for aircraft propulsion is to reduce the overall aircraft fuel burn and/ or overall energy consumption despite potential weight penalties due to electric energy storage. A detailed classification of hybrid powertrain architectures including aspects concerning the application on transport aircraft has been done in [17]. Sizing and performance assessment methodologies for hybrid electric aircraft propulsion systems have been developed e.g. in [18] and [19]. The main focus of these publications is to provide a generalized power-based sizing methodology, suitable to combine multiple energy sources in an integrated aircraft sizing environment. Special emphasis is given on the interaction of combustion engine- and electric motor characteristics. Furthermore, the two leading aircraft manufacturers published conceptual studies for future hybrid passenger aircraft: Boeing's Sugar Volt [20] and the Airbus eThrust concept [21].

Pure electric propulsion

If combustion engines are fully eliminated in the propulsion system, all energy required to supply the propulsion units and aircraft systems has to be provided by electric storage devices. Apart from fuel cells which require hydrocarbon or pure hydrogen fuels, batteries are the obvious candidates for electric energy storage. In view of the initial motivation of emission reduction and kerosene replacement, this option offers the most consequent and effective solution. However, as outlined in the following chapters, batteries do not reach the weight specific energy storage capacity of kerosene by far. As a consequence, pure battery powered aircraft are challenged in terms of energy storage capability and hence might be limited to short and medium cruise ranges. In the recent past, conceptual studies of purely electric aircraft have been published by aircraft manufacturers and research institutes. Airbus Group Innovations, the corporate research unit of the Airbus Group presented a concept for an electric regional aircraft called "VoltAir" in 2011 (see figure 5). Being in charge of the concept definition, the author of this thesis published a report about the technical background of the "VoltAir" concept, covering aspects of electric aircraft design and exemplary aircraft sizing results [22]. In 2012, a case study of a re-designed ATR 72-500 using battery powered propulsion was published by Vratny [23]. In this report,

methods for electric component- and propulsion system modeling are presented, and integration aspects are discussed. Using an aircraft sizing model, battery technology requirements are derived to match the characteristics of the reference aircraft. In the same year, Bauhaus Luftfahrt e.V. presented the universally-electric aircraft concept “Ce-Liner”, carrying up to 190 passengers over a 900 nautical miles distance at a speed of M 0.75 (see figure 6). In subsequent publications [24] [25], descriptions about the underlying methods for aircraft system modeling and the propulsion architecture design are given. In another 2012 publication, M. Hepperle discussed general electric aircraft propulsion system aspects and derived analytical sizing trends based on statistical aircraft empty weight fractions and potential battery weight fractions [26]. In a more generic approach, these sizing aspects and limitations have also been addressed by McDonald for constant- or increasing weight aircraft [27]. In 2013, Seitz et al. published methods for an in-detail comparison of open rotor- and fan propulsors for electric aircraft propulsion [28], including an exemplary application on the “Ce-Liner” concept. Also in 2013, Rakov presented a preliminary design of a battery powered regional aircraft and investigated the impact of external take-off support technologies such as winch launches [29].

Figure 5, “VoltAir” electric aircraft concept platform [22]

Figure 6, “Ce-Liner” universally-electric aircraft concept [25]

As summarized above, numerous publications dealing with different aspects of future electric propulsion aircraft are available in the literature. The challenges in electric aircraft design are thereby covered in each report to a different extent. In order to give a better overview about the state of the literature with respect to the scope of this thesis, the named publications are classified regarding their focus on the challenges in electric aircraft design as defined in section 1.1. In line with the main objectives as given in section 1.2, the evaluation also includes the aspects “Integrated Design”, “Adaptions in Aircraft Operation”, “Feasibility Analysis & Evaluation”, and “Design Space Exploration”. The results are summarized in table 2.

++ is a main focus + is a focus o is not the focus

	Component Modeling	Propulsion System Modeling	Certification Aspects	Battery Integration	Structural Implications	Adaptions in Weight Accounting	Integrated Design	Adapions in Aircraft Operation	Feasibility Analysis & Evaluation	Design Space Exploration
Felder et al. [14]	++	+	o	o	o	o	+	o	+	o
Gibson et al. [15]	++	+	o	o	o	o	+	o	+	o
Greitzer et al. [16]	o	o	o	o	o	o	+	+	+	o
Lorenz et al. [17]	o	+	o	o	o	o	o	o	o	o
Pornet et al. [18]	+	++	o	o	o	o	o	o	+	o
Seitz et al. [28]	+	++	o	o	o	o	+	o	+	o
Bradley et al. [20]	o	+	o	+	o	o	+	+	++	o
Kluge [21]	o	o	o	+	o	o	o	o	o	o
Hornung et al. [24]	o	+	o	+	+	o	+	o	++	o
Isikveren et al. [25]	+	+	+	+	o	o	++	+	++	o
Hepperle [26]	+	o	o	o	o	o	o	o	++	o
McDonald [27]	o	o	o	o	o	++	o	o	++	o
Rakov [29]	+	o	o	o	o	+	+	++	+	o
Vratny et al. [52]	++	o	o	o	o	o	+	o	o	o
Vratny [23]	+	+	+	+	+	+	+	+	+	o
Stückl et al. [22]	+	+	o	+	+	+	+	o	+	+

Table 2, Survey of relevant literature

As it turns out, some aspects of electric propulsion aircraft design are covered to a larger extent than others. Component modeling and feasibility analysis & evaluation is addressed in the majority of publications, while less emphasis was given on certification aspects, structural implications, and the design space regarding design payload and range sensitivities. The widest coverage of the relevant design aspects is found in the in the reports of Vratny [23] and Isikveren et al. [25], both containing case studies about electric aircraft designs.

However, no publication is known by the author that provides an in-depth coverage of all relevant modeling challenges as addressed above in a consistent and comprehensive manner. The analytical sizing considerations of electric propulsion aircraft as discussed in [26] and [27] are based on fundamental assumptions regarding aircraft empty weight share, system efficiencies, and aircraft lift-to-drag ratio. Yet, statistical data about aircraft empty weight share are only available for conventional aircraft whereas electric powered aircraft may differ significantly in this regard due to fundamentally different weight build-ups and system components. Furthermore, the efficiency of the powertrain as well as the aerodynamic properties cannot be generalized but require an assessment case-by-case. The available literature addressing more detailed electric propulsion aircraft design aspects provides a good basis especially in terms of methods for component modeling, but some relevant design considerations in the electric propulsion system design including certification aspects, failure scenarios, and operating characteristics have not yet been fully addressed or fully documented. Relating to electric propulsion aircraft sizing, critical constraints and the resulting potential for optimization have not been discussed thoroughly using adaptions in aircraft design and operational strategies. Furthermore, the electric propulsion aircraft sizing methodology yet has only been applied on specific case studies, while an extensive design space exploration with respect to top-level requirements and technological advance has not been addressed.

2.3. Research Needs and Specification of Work

Compared to hybrid solutions, pure battery powered aircraft offer the highest emission reduction potential, given that electric energy is being generated in an environmentally friendly and sustainable manner on the ground. The consequence, however, is that the aircraft design is fully driven and limited by the batteries' capabilities and weight. Nevertheless, battery powered aircraft could be feasible for certain applications, depending on the technologic advance of powertrain components. With all emphasis on this opportunity, the focus of this thesis lies on batteries as sole energy storage device for electric propulsion aircraft. Though, even if significant improvements for future batteries and high system efficiencies are anticipated, severe weight penalties have to be expected compared to conventional propulsion systems. For a qualitative assessment of the magnitude of this penalty, the relative fuel weight of the conventional reference aircraft can be considered. This relative fuel weight is generally expressed by the fuel fraction, defined by the weight of the propellant divided by the aircraft (maximal take-off) weight. Given the weight disadvantage of batteries, the absolute weight increase will be higher for aircraft with a large fuel fraction than for aircraft with a small fraction. Among commercially relevant aircraft, regional commuter aircraft have the lowest fuel fractions due to typically short cruise ranges and slow cruise speeds. Typical representatives of this class are exemplary the Dornier Do 328, ATR 42/72, and DHC-8 series aircraft. Evaluating the viability of battery powered propulsion, the commuter segment is therefore being chosen as the considered aircraft class in this thesis. The Majority of the questions concerning electric propulsion systems addressed herein are also relevant for hybrid variants, so a significant part of the findings and results can be used for potential follow-on studies.

In this regard, considering the gaps in the state of the current literature, the following research needs are defined:

- For the selected target category, a **consistent and comprehensive set of modeling methods for electric propulsion aircraft** has to be developed.

- This requires **methods to describe the components** of an electric powertrain, based on available predictions for future technological advance.

- Methods for propulsion system design have to be developed that are capable to define the operating characteristics under consideration of certification aspects and failure scenarios, as well as to **identify critical technologies and design drivers**.

- Furthermore, implications related to electric propulsion systems integration into the aircraft structure, sizing dependencies, as well as new operational characteristics have to be accounted for in an **adapted preliminary design process.**

- Since **practical limits** of electric propulsion have not been addressed thoroughly in the literature for the considered aircraft class, a better understanding of these limits depending on the available state of technology has to be generated.

- In order to improve the applicability and accuracy of analytical sizing methods for electric propulsion aircraft, **reference values** regarding the aircraft weight build-up, aerodynamic properties, and system efficiencies have to be generated by application of the presented methodology.

3. Methods for Electric Aircraft Propulsion System Design

In this chapter, the current state and predictions for the future development of the main components composing a battery powered electric powertrain are presented. The exemplary basic propulsion system architecture shown in figure 7 illustrates these main system components. Electric power is provided by a battery or an assembly of battery cells that are monitored by a battery management system (BMS). For power distribution, transmission cables connect power sources and consumers, and protection is provided by switches that are capable of full load switching (full rated electric current at nominal voltage). The power provided by the transmission system is then converted into a multi-phase power signal for the motor by the motor controller and finally converted to mechanic power by the electric motor. Depending on the respective speed characteristics, motor and propulsor can be coupled directly or via a reduction gearbox. If aircraft systems such as air conditioning and actuators are also powered by the propulsion system batteries, a voltage converter might be necessary if the systems grid voltage differs from the propulsion grid voltage.

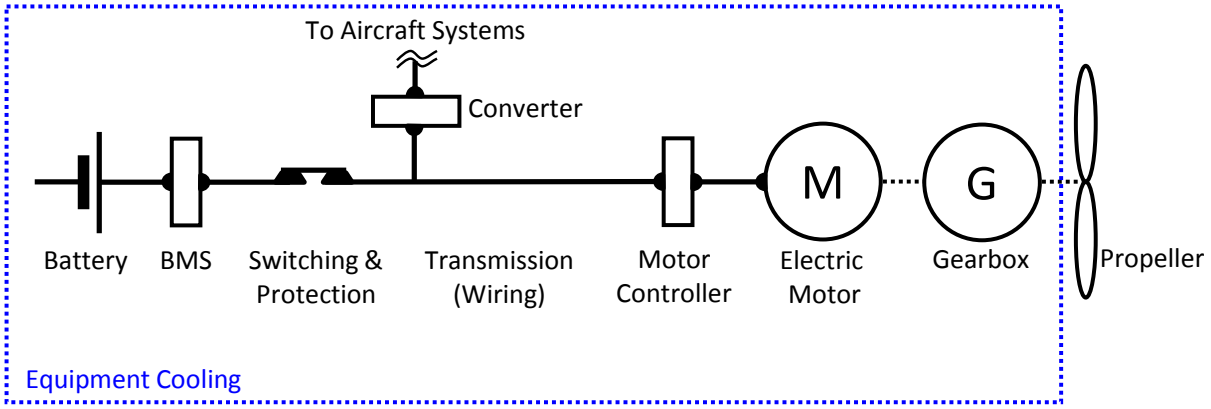

Figure 7, Basic propulsion system architecture

For these components, modeling methods concerning weight and operational characteristics are being presented. On this basis, electric propulsion system architecture variants are being defined with respect to aviation-related safety requirements. The chapter concludes with a sensitivity study, identifying high impact parameters and taking system architecture decisions.

3.1. Specification of Components

In the following, the components of a battery powered electric powertrain including propulsor are being described in detail. Based on current and predicted weights and characteristics, parametric models are being derived.

3.1.1. Storage of Electric Energy

For electric aircraft propulsion, large amounts of electric energy have to be stored safely and readily available on board. In principle, various technologic approaches for electric energy storage exist, the most common ones being batteries, fuel cells systems, and capacitors. As outlined in the previous chapter however, only batteries are being considered as the sole

storage technology for electric energy in the frame of this thesis. Capacitors outperform batteries in terms of power capability per weight unit, but are inferior in their weight-specific energy storage capability. Capacitors are hence used typically for very short term (seconds) and high-power applications (c.f. Ragone chart, figure 16). In contrast to that, fuel cells mark the other extreme. The fuel cell itself is only the energy converter and the energy is stored externally, mostly in hydrogen or also a light hydrocarbon-based fuel. In long term low-power applications, a fuel cell system is advantageous compared to batteries especially in terms of weight due to the fact that the fuel cell itself is sized on the system power only, not on the system energy. For higher power demands however, fuel cell systems do not reach the weight-specific power capability of batteries [30].
Regarding power- and energy characteristics, batteries are in between fuel cells and capacitors, providing a compromise between weight-specific energy and power. More technological details, an overview of the current state as well as predictions for future battery development are given in the following.

3.1.1.1. State of the Art Battery Cells

In principle, batteries convert the energy released in a chemical reaction into electric current. In rechargeable batteries, this process is reversible and can be repeated for a certain amount of cycles. Inside the battery, the positive (cathode) and the negative (anode) electrodes contain the species involved in reduction-oxidation (redox) processes. The electrodes are separated by an electrolyte, which is only penetrable for ions and non-penetrable for electrons. During discharge, the electro-active material separates into electrons and ions that are exchanged between the electrodes via the electrolyte. Depending on the kind of redox reaction, the respective electrons are conducted externally via an electric load, closing an electric circuit. A schematic drawing of a principle battery buildup is given in figure 8. A single electrochemical unit is generally defined as a cell, a combination of two or more cells as a battery, whereas the terminology is often not consistent in the literature and a single cell is also often named a battery. [31]

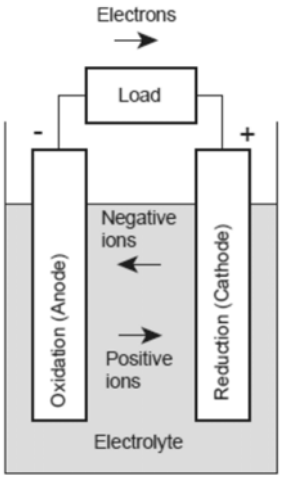

Figure 8, Basic battery cell schematic [31]

In a battery cell, the amount of energy stored per weight unit is depending on three main factors: the weight of the active (reactive electrode) and passive (electrolyte, housing etc.) materials, the number of electrons exchanged and the electrochemical potential in the redox reaction. As

negative electrode material, metallic elements are typically being used. Densities and the electrochemical potentials of suitable metallic electrode materials versus a standard hydrogen electrode are given in figure 9. Evidently, lithium features the highest reaction potential as well as the lowest density, making it the most favorable electrode material for high energy density battery cells. For that reason, lithium-based cell systems represent today's state of the art by the common metrics for characterization: specific energy [Wh/kg], specific power [W/kg], energy density [Wh/l] and power density [W/l].

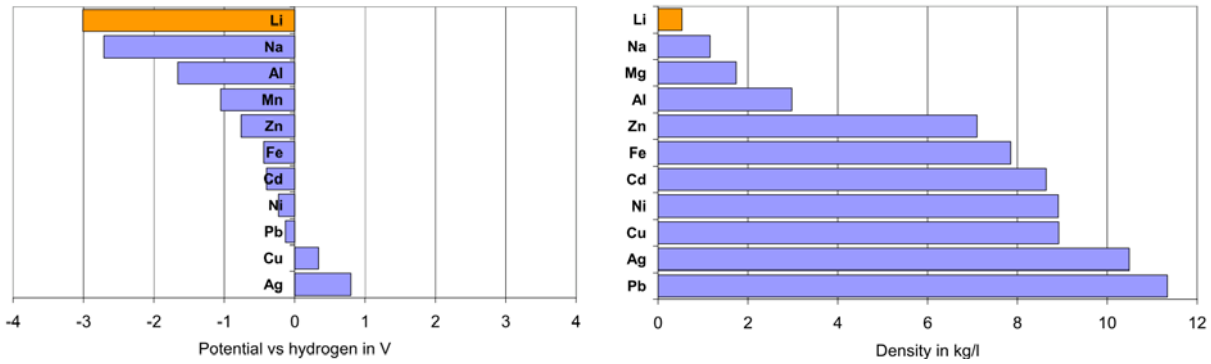

Figure 9, Standard potential and density of electrode materials [32]

Today's most widely used cell type, especially in all kinds of mobile electric applications, from personal communication and entertainment systems to electric vehicles where compact and lightweight energy storage is desired, is the Li-ion cell. Its anode consists of Li atoms bound in a carbon grid, its cathode counterpart of lithium metal oxides like Li, Ni, Co, and Mn compounds. Having a look at the redox potential of a specific electrode pairing, the characteristic cell voltage can be determined. Figure 10 shows the redox potentials for various electrode pairings, including the chemistry of Ni-MH and Li-ion cells. For the Li-ion combinations given, a cell voltage of around 3.9 V can be determined.

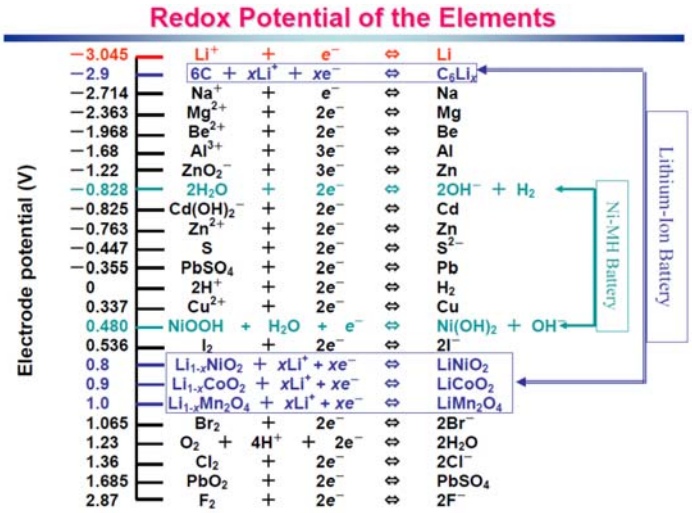

Figure 10, Redox potential of typical electrode pairings [33]

The performance of battery cells is highly dependent on the discharge profile and environmental conditions. Generally, the energy storage capability of the battery cell is defined by the discharge current and the cell voltage as given in eq. (1):

$$E = \int V(t) \cdot I(t) \cdot dt \tag{1}$$

The voltage provided by the battery cell is thereby not constant but reaches the electrode's redox potential only if the electric circuit is not closed and the current load is zero. It is therefore called the "open circuit voltage" (OC voltage). Connecting the cell to an electric load, a cell voltage drop appears depending on the parameters as described hereafter.

Rate of discharge (C-rate)

A battery cell is getting discharged at a certain "rate of discharge" or in short "C-rate", which expresses the discharge current relative to the current required to discharge the cell in one hour. This one-hour current is typically defined as the rated capacity of the cell in [Ah]. As an example, if a battery cell has a rated capacity of 10 Ah, a discharging current of 10 A represents a C-rate of one. A 20 A current results in a C-rate of two, respectively.

The voltage drop caused by the rate of discharge is caused by losses due to the cell's inner resistance. A simplified surrogate model of a battery cell is given in figure 11. The inner resistance R_i is mainly caused by the ohmic resistance of the active material, electrolytes, and metallic collector materials. Further contributors are chemical activation losses as well as concentration losses. Activation losses arise from over-potentials necessary to start the chemical reaction, concentration losses occur due to local de-concentration of the active material close to the electrolyte. Discharging the cell with a certain C-rate and the related current I_{eff}, a voltage drop U_Ω occurs reducing the available cell voltage U_{eff} relative to the open circuit voltage. The resulting operating voltage range for Li-ion batteries typically lies between around 4.2 V in the charged state and 2.7-3.0 V at the end of discharge. [30]

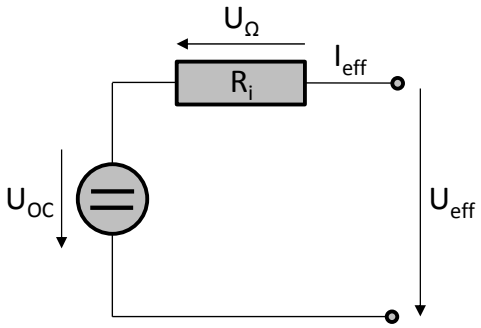

Figure 11, Simplified battery cell model

State of charge (SoC)

The charge status of a battery cell is characterized by the "state of charge" which reflects the percentage of the remaining charge relative to the cell's rated capacity. The cell voltage shows a moderate decline with proceeding discharge, caused by effects in the basic chemical cell reactions during the discharge process. The cell should not be discharged below a minimum cell voltage, called cut-off voltage, since the resulting corrosion effects cause irreversible damage to

the electrode materials. The actual cut-off voltage for a specific cell is defined by the manufacturer and has a direct effect on its cycle stability. A detailed explanation of the actual reaction processes can be found exemplary in [30]. Typical cell discharge curves are given in figure 12, in this case exemplary for a Li-ion cell but the general trends are characteristic for other cell types as well.

Temperature

The temperature affects the cell performance in three ways. At first, the chemical cell reaction itself depends on the temperature. Following the Arrhenius equation, the rate of reaction K increases with the temperature T. Further parameters are the gas constant R, the activation energy e, and a constant k_0 [30]:

$$K = k_0 e^{\frac{-e}{RT}} \tag{2}$$

Second, the main transport mechanism of ions and reaction species inside the battery cell is diffusion. The rate of diffusion rises with increasing temperature according to Fick's law. The battery cell performance benefits from improved diffusion because it counteracts local de-concentration effects at the electrodes due to high discharge rates. At last, higher temperatures increase the ohmic resistance of metallic components in the cell, but decrease the resistance of the electrolytes. Since the electrolytes are usually the dominating contributor to ohmic losses, the net effect is a decrease in the inner resistance. Although cell performance benefits from increased operating temperatures, a certain limit must not be exceeded since otherwise battery cell cycle stability is negatively affected. Exemplary for Li-ion cells, electrolyte degradation sets in above 50 °C and causes irreversible cell damage [30]. Exemplary discharge characteristics of a Li-ion cell for different cell temperatures are given in figure 13.

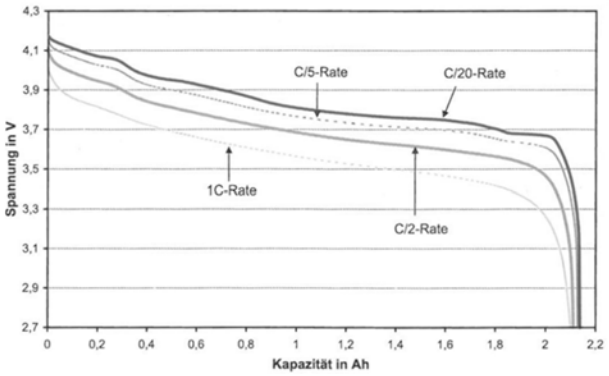

Figure 12, C-Rate effect on discharge characteristics [30]

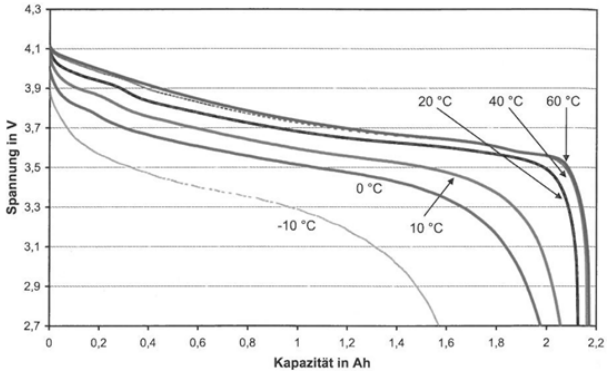

Figure 13, Temperature effect on discharge characteristics [30]

When using batteries under real-world conditions, some further effects and characteristics have to be taken into account that affect the operational performance and the energy storage capability. In this regard, the most significant aspects are discussed hereafter.

Self-discharge

During long time battery cell storage, a certain leakage current occurs, leading to a slow continuous self-discharge. The rate of self-discharge as well as over-potentials, concentration losses, and ohmic losses highly depend on the cell type and can differ significantly.

Cycle stability

As a matter of fact, the storage capability of a rechargeable battery cell is not constant but declines with the number of charging/ discharging cycles due to side reactions and corrosion effects. Thereby, the performance of a cell also depends on its operating history. Temperatures above 50 °C for Li-ion cells, charging/ discharging beyond allowed voltage limitations, as well as the applied depth of discharge are the main factors. Figure 14 shows the cycle performance of a Li-ion cell with a nominal capacity of 720 mAh at 1 C discharge rate and 100% depth of discharge. Commonly, the end-of-life of a battery cell is defined when its capacity drops down to 80% of the nominal capacity, resulting in a 700 cycle lifespan for the cell displayed. Yet, this number increases significantly if the cells are cycled with a lower depth of discharge, but this improvement differs depending on the specific cell chemistry used.

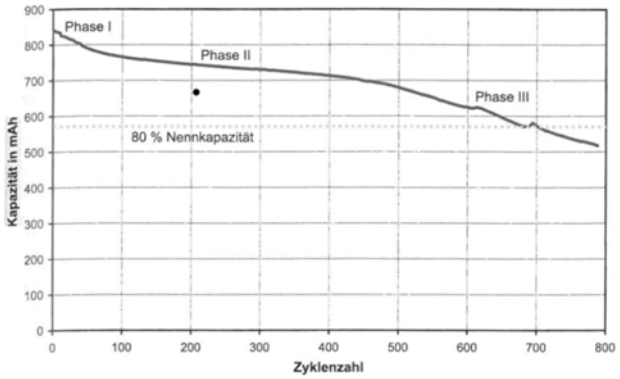

Figure 14, Cycle stability of a Li-ion cell [30]

Heat output

Capacity losses that occur during discharge of a battery cell are mainly dissipated into heat. In this regard, the two major loss mechanisms that generate heat are the ohmic resistance and polarization losses. A (simplified) equivalent circuit diagram of these heat sources is given in figure 15, a definition of the losses by ohmic resistance and polarization effects is given in equations (3) und (4). The generated heat either increases the cell temperature depending on the cell's heat capacity or has to be dissipated by external cooling.

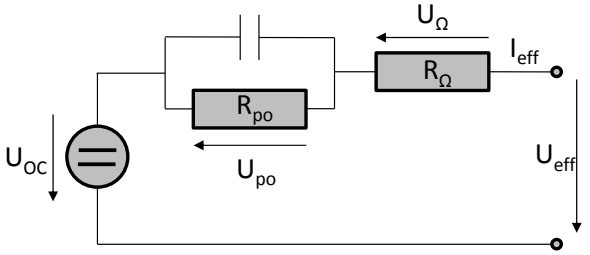

Figure 15, Main heat sources of a battery cell, based on [30]

$$P_{heat,\Omega} = R_{\Omega} \cdot {I_{eff}}^2 \quad (3)$$

$$P_{heat,p} = U_p \cdot I_{eff} \quad (4)$$

Classification in the Ragone chart

As outlined previously, the amount of energy extractable from a battery cell is affected by internal losses due to the discharge current. Increasing the discharge rate, and hence the power, the losses increase and less electric energy is extractable. As a consequence, the energy storage capability and the power output of a battery cell are interdependent. Commonly, the relation of power- and energy storage capability of any kind of storage device is visualized in a Ragone chart. In figure 16, the specific power of various state of the art cell types is plotted over the specific energy, using a double logarithmic scaling. Since for each point in the diagram the corresponding value of energy and power is defined, the quotient of both values gives information about the time of power extraction.

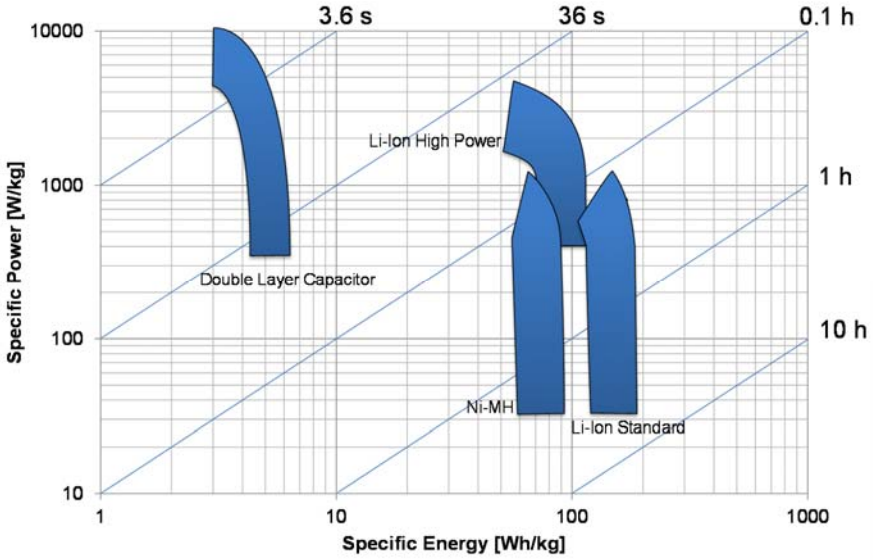

Figure 16, State of the art electric energy storage devices in a Ragone chart [30]

As can be seen for Li-ion cells, a trade-off in cell design exists between high power- and high energy cells. Since the extractable power is limited by the inner resistance, performance enhancements can be achieved by improving the conductivity inside the cell. This is mainly done by more metallic collector material, but also by thinner electrolyte layers. Though, adding more passive material leads to increased weight and hence reduced specific energy. A schematic build-up of a high power cell and a high energy cell is given in figure 17.

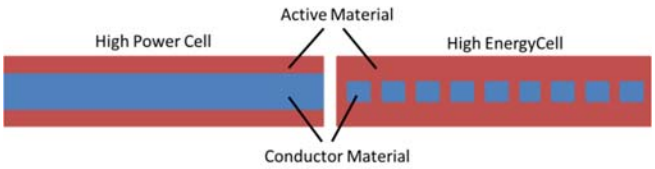

Figure 17, Battery cell design tradeoff, based on [30]

3.1.1.2. Expected Progress for Li-based Cells

Electric aircraft propulsion systems based on today's established lithium-ion batteries, providing more than 200 Wh/kg on cell level, have been successfully demonstrated in model aircraft, motor-gliders, and small experimental general aviation aircraft (cf. section 2.1). Although the Li-ion technology is currently still being developed further, a practical limit is expected between 300 Wh/kg [30] and 480 Wh/kg [34]. If an even higher specific energy is required, new electrode materials with a higher reaction potential have to be considered. In figure 18, the theoretical specific energy of a number of possible electrode pairings against their equivalent weight is shown. From that it becomes apparent, that Lithium-sulfur and lithium-air concepts are the most promising candidates today that are seriously being investigated.

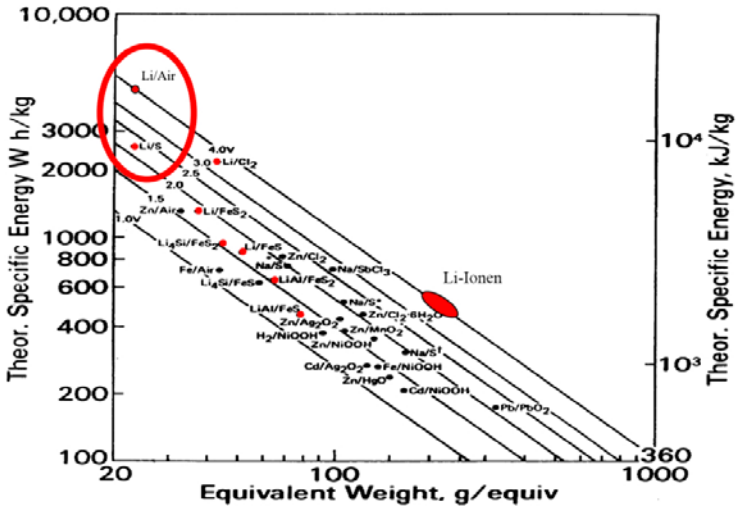

Figure 18, Theoretical specific energy of lithium-based cell systems [34]

Li-S cells

Lithium-sulfur, or in short Li-S cells, use sulfur in the positive electrode reacting with Lithium in the negative electrode in the following way:

$$2\,LI + S \rightarrow Li2S \quad \Delta G \sim -425\,kJ/mol \tag{5}$$

Considering only the weight of the active materials, this reaction delivers a theoretical specific energy of 2500 Wh/kg. In real-life cells, taking losses and the weight of passive materials into account, around 350 Wh/kg are reached in first commercially available cells at the time of writing [35]. The typical discharge characteristic of a Li-S cell, as given in figure 19, can be divided into

two parts. At a high SoC, a steep voltage drop occurs from around 2.4 V to 2.1 V in the first part, followed by a quite steady voltage plateau at around 2.1 V for the rest of the discharge process. This characteristic arises from the succession of different reaction phases in the cell chemistry and is described in detail in the literature [36]. C-rate and temperature (see figure 20) have a similar impact on the discharge capacity as for Li-ion cells.

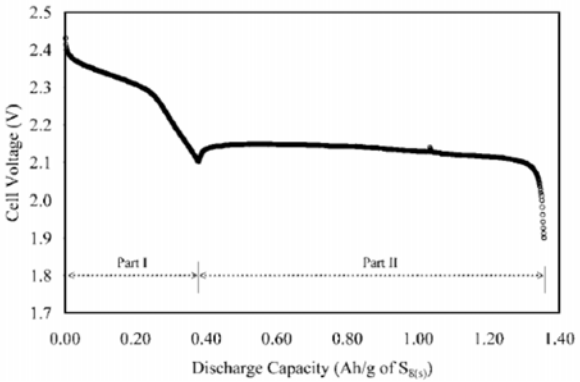

Figure 19, Li-S discharge characteristics [36]

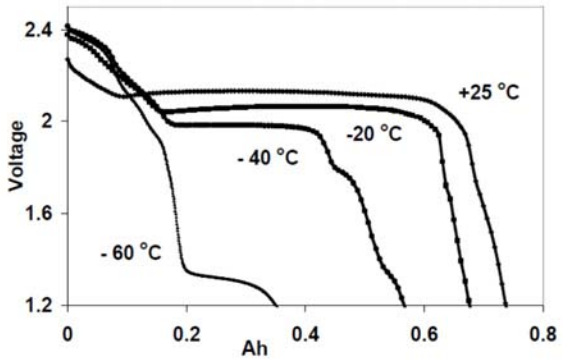

Figure 20, Li-S temperature characteristics [37]

Since the Li-S technology is in its early stage of market introduction, only few cell types are commercially available and the amount of specification data is limited. The US-based company SION Power offers a 2.5 Ah cell at nominal 2.1 V, 0.2 C-rate and 25 °C, providing 350 Wh/kg. Further performance data of several prototype systems is given in the following Ragone chart.

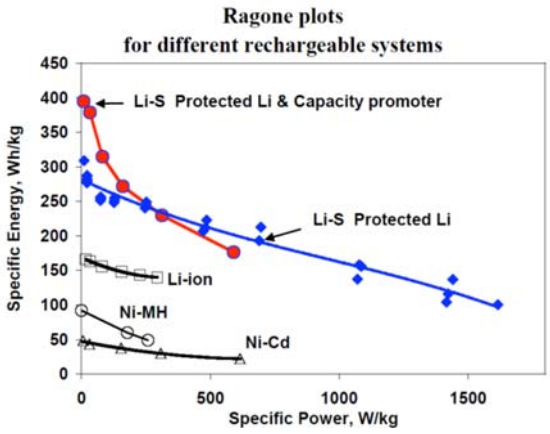

Figure 21, Li-S Ragone chart [37]

The main drawbacks of Li-S system's today that prevent a real market breakthrough are a bad cycle stability and operational safety issues. While in 2005, cells lost around 50% of their capacity after 100 discharging cycles, significant improvements by the usage of carbon nanotubes have been reported [38]. Safety concerns arise due to the fact that the sulfur and the lithium in the cell could directly react exothermically in case of cell damaging. For future commercial applications of Li-S cells, this issue has to be addressed and solved. Common approaches include thermal protective measures like melting separators and/ or chemical measures like reaction inhibiting additives [30].

For Li-S systems, SION Power demonstrated a continuous specific power of 2000 W/kg at 200 Wh/kg for a prototype cell that was also able to provide up to 3000 W/kg for 10 second pulses [39]. For future Li-S cells, a specific energy of up to 600 Wh/kg is expected [30]. The volumetric density is expected to be between 320 Wh/l [35] and 600 Wh/l [40]. The discharge efficiency is assumed to be comparable to today's Li-ion batteries, exceeding 90% [37].

Lithium-air cells

As can be seen in figure 18, the Li-air cell concept offers the highest theoretical specific energy among the relevant Li-based battery systems. The redox coupling in a Li-air ($Li\text{-}O_2$) reaction is:

$$2Li + O_2 \rightarrow Li_2O_2 \quad \Delta G \sim -607\ kJ/mol \tag{6}$$

The fundamental difference of this cell type relative to conventional battery systems is the fact that the oxygen is not stored in the cell's cathode but provided externally. Sources of oxygen can be a tank or oxygen available from the ambient air. Li-air systems hence offer two advantages: first, the redox reaction itself provides a high specific energy and second, the oxygen does not have to be stored inside the cell system from the beginning of discharge. Given that the oxygen is taken from the surrounding air, Li-air systems are constantly gaining weight by accumulating the reaction product lithium-peroxide during discharge. The rate of mass accumulation can be calculated based on the reaction potential as follows:

- Reaction Potential Li_2O_2: 3.1 V
- Faraday constant: 96485 C/mol
- Specific mass O_2: 0.016 kg/mol

For Li_2O_2 follows:

$$\frac{\partial}{\partial E}\, m_{cell}\left[\frac{kg}{Wh}\right] = \frac{0.016\left[\frac{kg}{mol}\right]\ 3600\left[\frac{C}{Ah}\right]}{3.1\ [V]\ 96485\ \left[\frac{C}{mol}\right]} = 1.92\ \cdot 10^{-4} \tag{7}$$

At the time of writing, Li-air cells are being investigated in an early development stage. First lab-scale prototypes have been demonstrated [41] [42]. The major challenge is to stabilize the charging/ discharging process since the cycle performance is yet unsatisfying. The cathode material, which consists commonly of porous carbon material to permit the oxygen to diffuse, is prone to become clogged by the reaction species and has to be effectively protected from humidity. The anode, which consists of metallic lithium, has to be protected likewise due to its high activity and tends to fast degradation after few cycles. Further challenges persist with other electrochemical effects. [43]

An exemplary discharge characteristic of a Li-air cell is given in figure 22. After a steep drop from the open circuit voltage slightly above 3.0 V, the operating voltage shows a plateau with a slight decline, reaching around 2.5 Volts at the end of discharge. As shown in the cycle characteristic of an experimental Li-air cell in figure 23, a significant over-potential is necessary to reduce the Li-peroxide in the recharging process. This leads to a poor cycle efficiency of around 57%. Additionally, voltage stability at high rates of discharge is an issue due to kinetic

charge transfer limitations. Promising improvements concerning discharge characteristics and general cell performance could be achieved by using catalysts [44]. Since the major process for oxygen transport in the cell is diffusion, battery performance improves at increased operating temperatures of up to 60-80 °C. Recently simulated discharge efficiencies are ca. 75-85%. [43]
Despite the mentioned challenges and the need for extensive further research to develop commercially available Li-air cells, this technology is considered to be a promising cell concept for future lightweight energy storage.

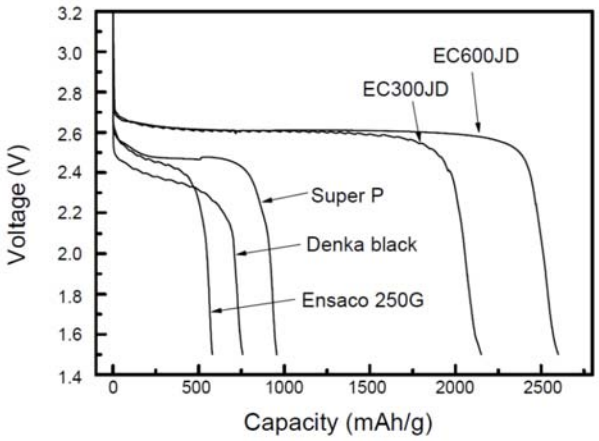

Figure 22, Li-air discharge characteristics [45]

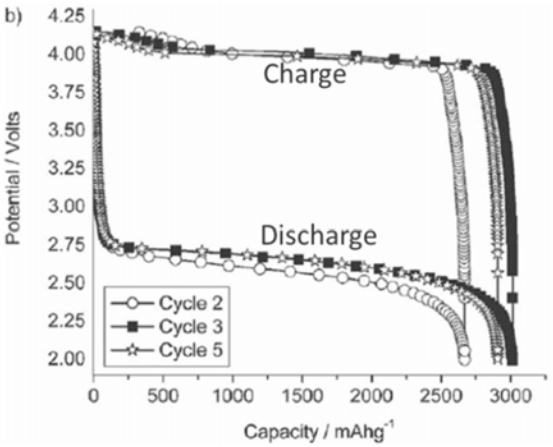

Figure 23, Li-air cycle performance [46]

Due to its high redox potential, the oxidation of lithium yields a theoretical specific energy exceeding 11000 Wh/kg. Yet, considering the weight of accumulating Li-peroxide, this value reduces to 3500 Wh/kg at the end of the discharge process. Zheng et al. [47] further investigated the weight impact of electrolyte and passive cathode materials, concluding that the best theoretical specific energy is 2790 Wh/kg. For real life cells, the weight of current collector material as well as battery housing has also to be considered. Respective predictions range from 800 to 2000 Wh/kg: Visco predicts 1000 Wh/kg [48], Girishkumar 1700 Wh/kg [41], Johnson up to 2000 Wh/kg [49]. Estimations for the specific power of future cells are between 140-1400 W/kg [43] [49] for a 700 Wh/kg cell. Predictions regarding energy density are given in [43] [47] [49], and range from 475 Wh/l to 2000 Wh/l.

Development roadmaps

The growing demand for high-performance battery systems in portable electronic devices and electric vehicles leads to increased research efforts across the industry. Carmakers and research institutes published roadmaps to set targets for technological development. Volkswagen for example has set development milestones that show good accordance with the future cell systems discussed above. As shown in figure 24, Volkswagen expects a limit in the Li-ion technology at above 200 Wh/kg [50]. Cells with up to 600 Wh/kg, considered as “technological change”, fit well with predictions for Li-S batteries, whereas cells with 1500 Wh/kg and 1000 W/kg represent potential future values for Li-air systems. Due to the long term research perspective necessary for the latter technology, these cells are considered a “technologic vision”. Accordingly, the Fraunhofer Institute estimates that Li-air cells will not be commercially available before 2030 [51].

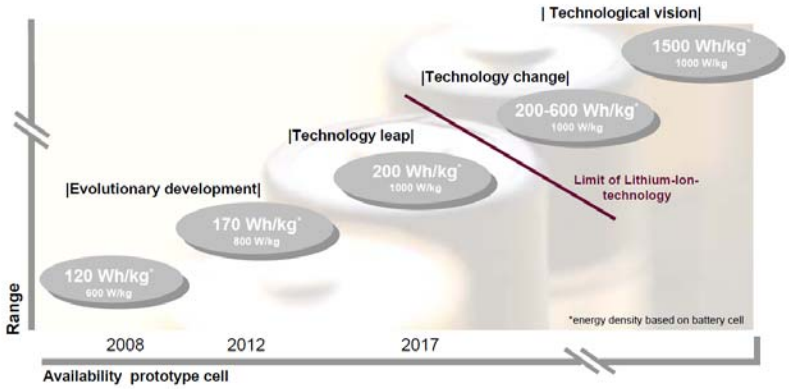

Figure 24, Battery development roadmap by Volkswagen [50]

Summary & comparison

The perspectives for future battery systems, more precisely the respective performance targets according to the presented publications and roadmaps, are summarized in the Ragone chart shown in figure 25. Compared to state of the art as represented by Ni-MH and Li-ion cell systems, significant improvements in specific energy and specific power are expected by the industry and research institutions. Due to the early state of some new battery concepts and current issues concerning safety and cycle stability, further extensive research is necessary during the coming decades to reach market readiness. Yet, if the lithium-air technology becomes available in around 2030, a large gap in specific energy to kerosene persists even for the most optimistic battery predictions. The resulting weight impact on potential electric propulsion aircraft then strongly depends on the efficiency of the propulsion system and will be evaluated later in this thesis.

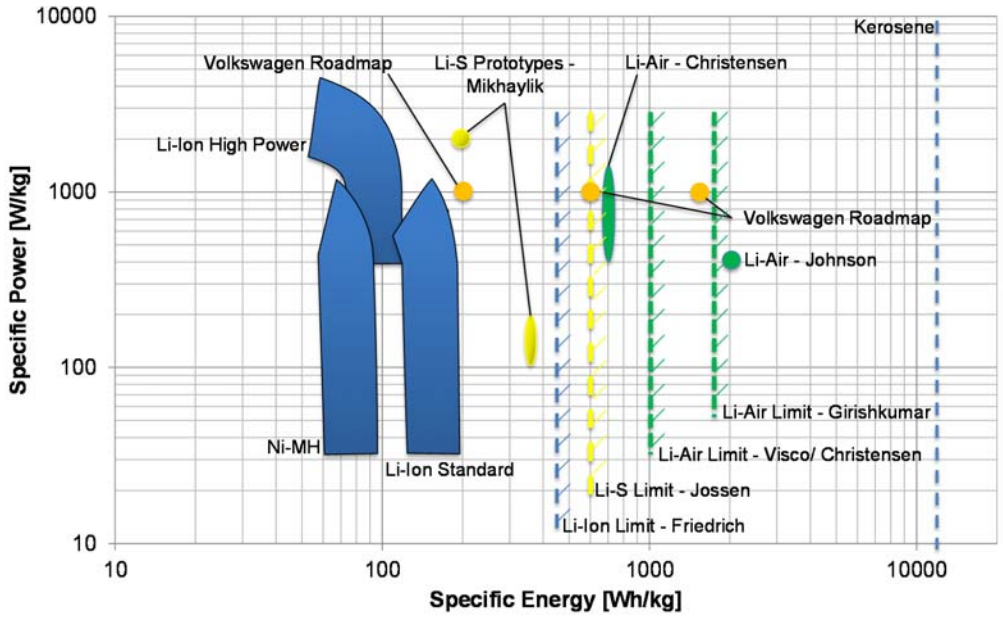

Figure 25, Summary of future battery performance predictions

3.1.1.3. Battery Cell Modeling

For the assessment of the electric powertrain, the battery cells have to be modeled by mapping the weight-, power-, and thermal characteristics. The available methods differ in the level of modeling depth and detail. A common approach is to use published or assumed values for specific energy e_{cell} and specific power p_{cell} to determine cell weight for a given application case. Knowing the required energy E_{req}, the cell weight is determined as follows:

$$w_{cell} = \frac{E_{req}}{e_{cell}} \tag{8}$$

For that given cell, the maximal available discharge power P_{cell} is hence:

$$P_{cell} = p_{cell}\, w_{cell} \tag{9}$$

The volume requirement and heat development can be determined likewise using the energy density v_{cell} and the discharge efficiency η_{dis}. Accordingly, the cell volume is:

$$V_{cell} = \frac{E_{req}}{v_{cell}} \tag{10}$$

And the loss heat developed by the cell:

$$P_{heat,cell} = P_{cell} * (1 - \eta_{dis}) \tag{11}$$

If the specific cell design that is considered is known in more detail, a more sophisticated cell model can be applied. As outlined previously, the inner resistance and hence the discharge characteristics depend mainly on the ohmic resistance, as well as activation- and concentration losses. These in turn are affected by specific cell properties including the cell build-up, available electrolyte materials, the use of catalysts, the operating temperature etc. If these characteristics are known, the resulting cell voltage can be determined as a function of state of charge and the discharge current, providing also information about the decline of the maximal power output during the discharge process. A corresponding approach was exemplary described by Vratny et al. in [52]. However, a comparison of this approach with a simplified method is also given in the same report. The findings indicate, that the error made by simply integrating the required propulsion energy without a detailed continuous calculation of the discharge characteristics remains below plus two and minus one percent for a 500 minute mission. Furthermore, considering the early state of the relevant battery technologies for large-scale aero-propulsion, only lab-scale prototype- and demonstrator cells are available today. Future, market ready cells that tap the full technological potential will rely on new materials and manufacturing techniques that are yet to be developed [44]. Due to this fact, predictions about the performance of future batteries systems are mostly given using high level metrics such as specific energy and specific power. Assumptions about internal losses and discharge efficiencies are thereby implicitly included since the extracted energy is affected by the provided power and the related discharge current. In the frame of this thesis, battery cell modeling will hence be limited to the methods given in equations (8) to (11). For a given battery prediction in terms of specific energy and

specific power, it is thereby assumed that the specific power is available at any time in the discharge cycle.
In addition, the total cell voltage drop experienced during the discharge process will be approximated. As outlined in the previous section, the maximum voltage is limited by the reaction potential of the basic cell reaction, determining the open circuit voltage U_{OC}. On the other side, a cut-off voltage $U_{cut-off}$ was reported for existing Li-S and Li-air prototype cells. Assuming that this lower limit is also valid for future production cells, a voltage ratio is defined to bring the maximum and minimum cell voltages into relation:

$$\zeta_{cell} = \frac{U_{cut-off}}{U_{OC}} \tag{12}$$

This ratio will be relevant in the frame of transmission system design considerations as presented in section 3.2.2.

3.1.2. Electric Power Transmission

Conductors are the central element of the transmission system, transferring electric energy from the storage system to the electric propulsion motors and to the aircraft systems like actuators, avionics, and the air conditioning system. While electric power distribution in “more-electric” aircraft systems is state of the art, the transmission of electric propulsion power in the megawatt range represents a new challenge without precedent in aviation. Corresponding methods for conductor modeling are not covered in the common aircraft design literature. Hence, a model for high power conductors is developed hereafter.

3.1.2.1. Conventional Materials for Power Transmission

In the electric powertrain of a battery powered (air-) vehicle, the batteries deliver a direct current (DC) voltage that has to be converted into alternating current for the electric motor by the motor controller/ inverter unit. As outlined in section 3.2.2, DC power transmission provides advantages in terms of conductor weight and electromagnetic compatibility (EMC) compared to AC transmission, hence only DC power distribution is considered for the electric powertrain.
Among conventional conductor materials, copper and aluminum are today’s most common design options. Both materials are currently being used in electric grids onboard aircraft, depending on the required cable characteristics. With 56 m/Ω/mm², copper offers the best conductivity of all technically relevant conductor materials, though at the high specific weight of 8.9 g/cm³. With 2.8 g/cm³, aluminum offers significant less specific weight but its 35 m/Ω/mm² mean also lower conductivity. Due to its better ductility, better corrosive characteristic and smaller conductor cross sections, copper cables are more widespread today [53]. However, in the frame of weight reduction efforts, aluminum cables are gaining importance in today’s “more electric” aircraft architectures.
The electric power transmitted in a DC conductor can be expressed by the product of the voltage and the current, as given by equation (13).

$$P = U \cdot I \tag{13}$$

The required conductor cross section area of a DC cable is mainly a function of the current load. According to equation (3), ohmic losses and the associated heat generated in the conductor material correlate with the ohmic resistance and the square of the current. A constant operating temperature is reached when the loss heat induction into the conductor equals the heat dissipation to the surrounding. For the conductor and isolation materials used, a maximum allowable temperature is given which limits the current load for a cable of a specific conductor cross section. Further increasing the current load is only possible by improving the heat dissipation or increasing the conductor cross section area in order to reduce the ohmic resistance and hence the heat induction. For conductors with circular cross section, the surface to volume ratio declines with growing diameter, leading to lower acceptable current densities (A/mm²) for larger conductor cross sections.
Since standards for aircraft power distribution cables are only available for low power/ low voltage applications, the buildup of high power cables according to DIN 0276 603 and DIN 50264 is considered for modeling of the DC cables. According to these standards, which are actually valid for ground-based power installations, a circular conductor from aluminum or copper is covered by an electric insulation layer and a protecting covering sheath. This buildup is shown in figure 26.

Figure 26, Aluminum power cable according to DIN 0276 603

For these cables, nominal current densities for aluminum and copper conductors can be found in DIN 0276 603. Due to the cross-linked polyethylene (XLPE) isolation material, the conductor temperature is limited to 90°. The resulting maximum current density depending on the conductor area is given in figure 27. For copper conductors, the allowable current density is higher due their lower ohmic losses. Based on these characteristics, the required conductor cross section can be shown as a function of the nominal current, as given in figure 28.

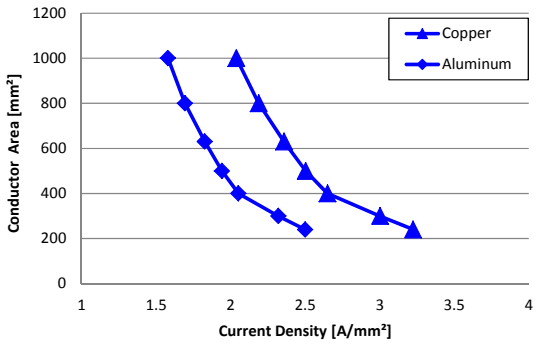

Figure 27, Maximum cable current density

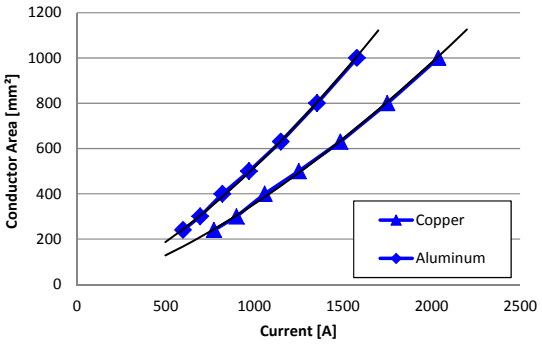

Figure 28, Required cable cross section area

Since the DIN standards only give information on specific cable cross sections, a regression formula is derived for further modeling:

$$A_{req,alu}[mm^2] = 0.02098 \cdot (I[A])^{1.46349} \quad (14)$$

$$A_{req,copper}[mm^2] = 0.0144 \cdot (I[A])^{1.4642} \quad (15)$$

Considering the densities of aluminum (2.8 g/cm³) and copper (8.9 g/cm³), the length-specific weight of the conductor material can be calculated:

$$\frac{\partial}{\partial x} w_{cond,alu} = \rho_{alu} \cdot A_{req,alu} \quad (16)$$

$$\frac{\partial}{\partial x} w_{cond,copper} = \rho_{copper} \cdot A_{req,copper} \quad (17)$$

Due to their electric potential (voltage), the conductors have to be covered by an isolation material which has a high dielectric strength to prevent an unintended short circuit to the cable's environment. The higher the electric potential relative to the surrounding is, the thicker the isolation material must be chosen. The required isolation thickness for the cables considered is given in DIN VDE 0276 603, DIN VDE 0276 620 and DIN 50264.

The standards used to define the cable properties are applicable to ground-based applications, like for example power distribution in industrial facilities. For transport applications like e.g. in trains, the PVC sheath material can be replaced by ethylene-vinyl acetate (EVA) material for improved fire characteristics as described in DIN EN 50264-1. For the same reason, also the isolation material can be replaced by ethylene propylene rubber (EPR/ HEPR). Using HEPR and EVA materials instead of XLPE and PVC and considering the densities given in table 3, only marginal differences in specific cable weight are found.

	Max operating temp. [°C]	Density [g/cm³]
XLPE	90	1.4
HEPR (EDPM)	90	1.6
PVC	90	1.3
EVA	90	0.93

Table 3, Densities of insulation materials

Except for a small impact of the conductor diameter due to mechanical properties, the required isolation thickness is mainly depending on the nominal voltage, as can be seen in figure 29 for XLPE as the isolation material. For further modeling, a linear regression for the required isolation thickness is derived, see equation (18).

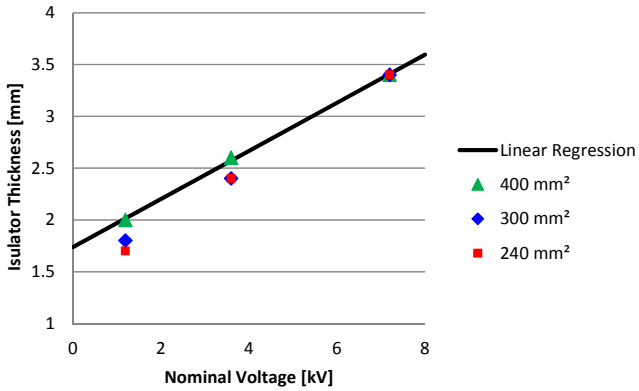

Figure 29, Required cable isolation thickness

$$t_{iso}[mm] = 0.2325 \cdot U[kV] + 1.7368 \tag{18}$$

The length-specific weight of the isolation can be calculated by multiplying the isolation thickness with the circumference of the conductor and the density of the isolation material.

$$\frac{\partial}{\partial x} w_{iso} = \rho_{iso} \cdot t_{iso} \cdot c_{cond} \tag{19}$$

For protection of the isolation material from damaging, an outer sheath is foreseen. The standard VDE 0276 620 gives a method to determine an appropriate sheath thickness as function of the cable diameter:

$$t_{sheath}[mm] = 0.035\, D_O[mm] + 1.0 \tag{20}$$

The length-specific weight of the sheath is determined by multiplying the sheath thickness with the circumference of the isolation material and the density of the sheath material.

$$\frac{\partial}{\partial x} w_{sheath} = \rho_{sheath} \cdot t_{sheath} \cdot c_{iso} \tag{21}$$

Adding the specific weight of conductor, isolation, and sheath as defined above, the total specific cable weight can be determined:

$$\frac{\partial}{\partial x} w_{cable} = \frac{\partial}{\partial x} w_{cond} + \frac{\partial}{\partial x} w_{iso} + \frac{\partial}{\partial x} w_{sheath} \tag{22}$$

In figure 30 and figure 31, the results are plotted against the conductor cross section area. For comparison, actual specific cable weights for NA2XY/ N2XY cables that are offered by a cable

manufacturer are also shown [54]. A good matching can be found between model and actual product data.

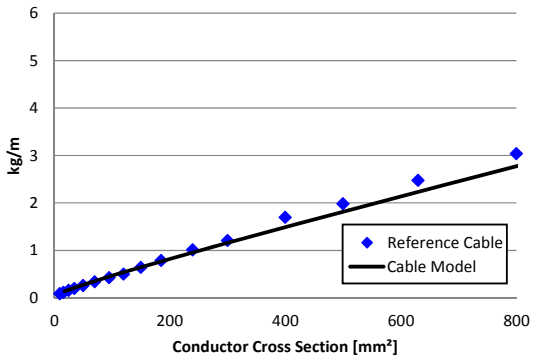

Figure 30, Aluminum cable specific weight validation

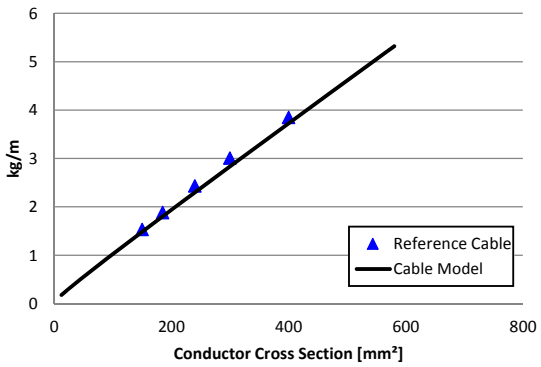

Figure 31, Copper cable specific weight validation

As outlined above, the maximal current loading of a cable is depending on the ability to dissipate its loss heat to the surrounding. The nominal current densities given in figure 27 are valid for a cable installation in free air or on perforated plates as given in figure 32.
Concerning cables for power transmission in aircraft, the decrease in air density with altitude and the resulting reduction in heat conduction has to be considered. For this effect, ref. [55] gives a method to determine an altitude-dependent correction factor for the allowable cable current, as shown in figure 33.

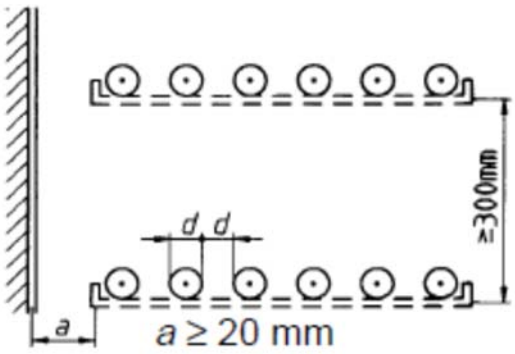

Figure 32, Required cable spacing (DIN 0276)

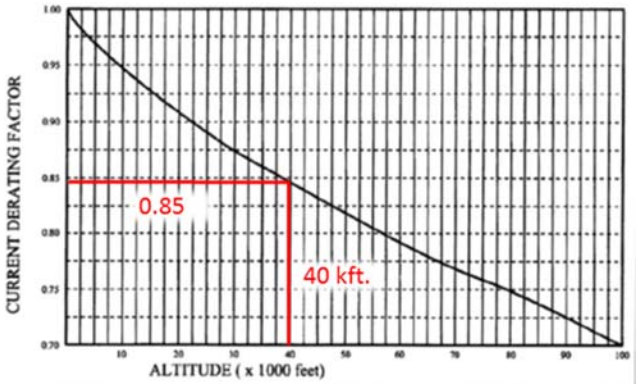

Figure 33, Current correction factor for altitude [55]

Assuming a maximal flight altitude of 40 000 ft., the allowable current rating decreases by 15%. This degradation factor will be considered for further cable modeling:

$$I_{eff} = I_{SL} \cdot 0.85 \tag{23}$$

Obviously, the actual thermal conditions and the heat dissipation characteristics of the cables integrated in the airframe structure might differ from these modeling assumptions. The dissipation could be negatively affected if a cable is integrated in an unventilated, closed plenum, or in proximity of other heat sources. On the other side, the heat dissipation of the cables could be further improved by an active forced-convection cooling system, exemplary

linked to the cabin air-conditioning system, though requiring an appropriate air ducting installation along the critical cable sections. However, these aspects can only be thoroughly addressed by discussing a more detailed structural integration concept, which is beyond the scope of this thesis. For further modeling, the methods and underlying assumptions as stated above are hence being used.
Based on that, the cable weight can finally be determined in dependence of the transmission power and the nominal transmission voltage level. Resulting specific cable weights for a voltage range of 1000-4000 V are given in figure 34 for aluminum and in figure 35 for copper conductors. The values refer to one single core cable, so for DC power transmission, the specific weights have to be multiplied by two to account for a “plus” and “minus” pole cable. It becomes apparent, that aluminum conductors offer significant weight advantages compared to copper conductors for the same transmission power.

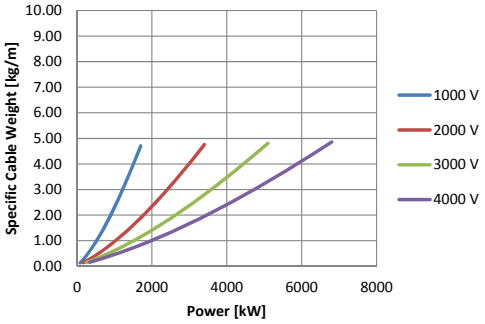

Figure 34, Specific aluminum cable weights

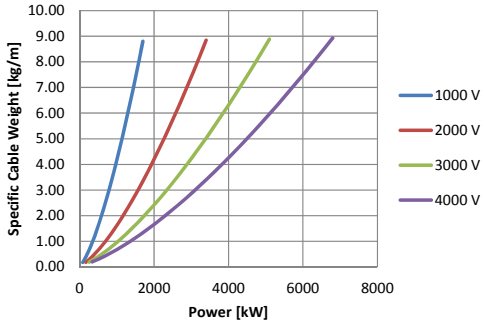

Figure 35, Specific copper cable weights

Exemplary for a cable rated at 3 kV and 1 kA, the weight breakdown according to the cable model is given in figure 36 for an aluminum- and a copper conductor. In case of the aluminum cable, the conductor accounts for about three quarters of the total cable weight. In case of the copper core, the conductor accounts for 87% of the cable weight due to its higher specific weight.

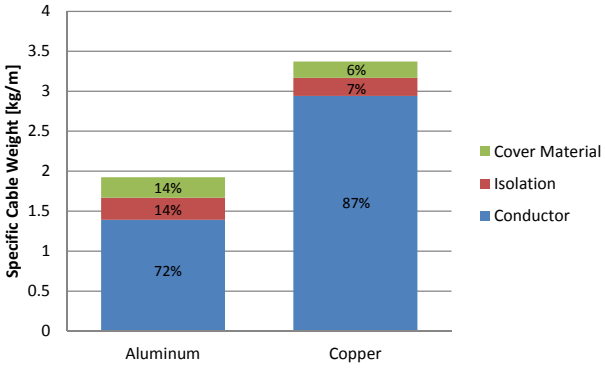

Figure 36, Cable weight breakdown

Due to the ohmic resistance of the conducting material, losses occur that are dissipated as heat to the surrounding. The resistivity of the conductor materials considered is temperature dependent and can be calculated with the temperature coefficient α respectively for aluminum and copper according to equation (24).

$$R = R_{20}(1 + \alpha \cdot \Delta T) \quad (24)$$

The resulting resistivity of aluminum and copper at different temperatures is given in table 4.

	Specific resistivity $\left[\frac{\Omega\, mm^2}{m}\right]$	
	Aluminum	Copper
20 °C	0.0286	0.0178
60 °C	0.0332	0.0205
90 °C	0.0366	0.0225

Table 4, Conductor temperature characteristics

At nominal conditions, the cables defined above reach a maximal operating temperature of 90 °C. Figure 37 and figure 38 show the related specific cable losses for a single cable with aluminum and copper conductor, respectively.

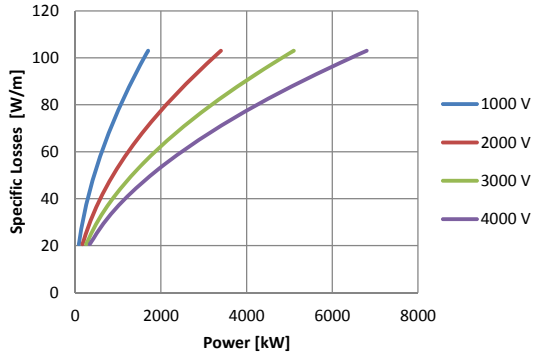

Figure 37, Aluminum cable losses

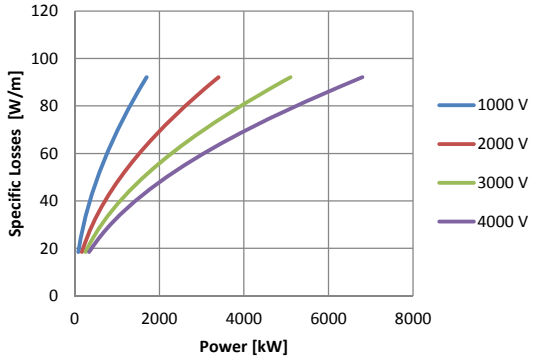

Figure 38, Copper cable losses

3.1.2.2. Superconducting Materials for Power Transmission

While conventional cables using metallic conductors offer reliable energy transmission at low level of complexity, superconducting cables are gaining increasing attention due to recent advances in high temperature superconducting (HTS) materials (cf. section 3.1.4). The obvious advantage of superconducting DC energy transmission is the absence of any ohmic resistance when cooled down below its critical temperature. In that condition, the HTS conductor is able to withstand enormous current densities compared to conventional conductor materials. The resulting small conductor geometries lead to potential cable weight savings and loss reductions. The drawback of this technology is the necessity of a cryogenic cooling system that in turn adds weight and power demand to the transmission system. Superconducting DC cables are a state of the art technology in medical screening applications (Magnetic Resonance Imaging, MRI) and are being considered for ground-based high power transmission systems [56].

Typical materials used in today's HTS applications like yttrium barium copper oxide (YBCO) and bismuth strontium calcium copper oxide (BSCCO) maintain their superconducting state up to more than 90 K, so liquid nitrogen can be used for cryogenic cooling. The typical buildup of a HTS power cable is given in figure 39. The superconducting material is usually stranded around a former core, covered by a dielectric isolation material and a second HTS layer that acts as

electromagnetic shield or as the returning current conductor. A cryogen around the conductors and inside the former core ensures to keep the HTS material at its required operating temperature. Vacuum steel tubes ensure thermal insulation, minimizing heat induction from the cable environment.

Figure 39, HTS cable buildup [57]

At both ends of an HTS cable, terminations are necessary to connect the HTS wires to conventional conductors. A termination for a bipolar HTS DC cable is shown in figure 40, displaying the upper temperature metal leads and the transition to the lower temperature HTS leads.

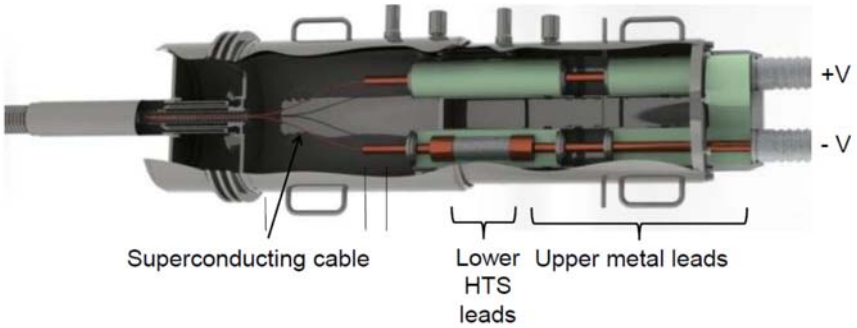

Figure 40, HTS cable termination [57]

While practically zero ohmic losses occur in the HTS wire at DC transmission, imperfections in the thermal isolation create a heat flow into the cryogenic system that has to be removed by the cooling system to maintain the HTS operating temperature. The main sources of heat induction are:

- Vacuum tube isolation imperfections (spacers, imperfect vacuum, heat radiation)
- Terminations: heat conduction and ohmic losses in the resistive current leads connecting the HTS wires to the conventional grid.

Typical cable cryostat losses for 77 K HTS cables are in the range of 0.5 W/m [58]. The magnitude of losses occurring in the termination is determined using a method from [59] and shown in eq. (25). According to that, each current lead causes 45 W/kA heat input into the cryogenic fluid. Exemplary for a coaxial cable like shown in figure 39, two leads are necessary on each cable end. Additionally, isolation losses occur which account for 200 W heat input per termination.

$$Q_{term}[W] = 45 \cdot n_e.I_e[kA] + 200 \quad (25)$$

In contrast to conventional cables with resistive conductors, the weight of a HTS cable is predominantly determined by the thermal isolation and the cryogen cooling medium while the conductor itself only accounts for a very small weight share. As a consequence, the impact of voltage and current rating on cable weight is low.
Today's demonstrated HTS cables for ground-based applications have a specific weight of around 10 kg/m for AC transmission systems (13 kg/m in [60]; 9.8 kg/m in [61]). Since these cables are ground-based and not weight optimized, weight savings are possible using lighter materials for the vacuum isolation sheath materials. Brown [62] states a weight goal of 5 kg/m [58] and presents a conceptual design of a 270 VDC HTS cable for power transmission onboard aircraft, also featuring 5 kg/m. Hence, a specific HTS cable weight of 5 kg/m is assumed for further considerations. The HTS cable definitions are summarized in table 5.

Cable losses	0.5	[W/m]
Termination losses	$Q_{term} = 45 \cdot n_e.I_e[kA] + 200$	[W]
Specific weight	5	[kg/m]

Table 5, HTS cable definitions (77 K)

3.1.3. Power Switches and Circuit Breakers

While switching and protection of low-power loads can be done with simple mechanical relays and fuses, connecting and disconnecting high voltage/ high power transmission lines is more challenging. Mechanically separating two conductor ends under high power load causes a conducting plasma arc under certain conditions which prohibits the electric disconnection and threatens to damage the conductor ends due to the occurring high temperatures. DC current is more prone to electric arcing than AC since there is no voltage zero-crossing that could extinguish the plasma arc. Electric arcing becomes more critical as air density drops with rising altitude (cf. section 3.2.2).

Solid state relays

Next to mechanical solutions, switching of high power DC loads can be done using solid state devices that are build up from high power semiconductors. Since the semiconductor material can be triggered into a conductive or isolating state (e.g. using a transistor layout), current interruption can be realized without moving parts and without the issue of electric arcing.
Solid state switches are used today in a wide range from low power products up to high voltage, high current applications in power grid systems. In figure 41, the most common switch types and their typical operating ranges are shown. While MOSFET's are typically limited to a blocking voltage of 1 kV, so called IGBT's (insulated-gate bipolar transistors) offer a higher blocking voltage up to several kV. At the upper power end, thyristors are mostly used in power grid systems due to their high blocking capability. For switching loads in the range necessary for electric aircraft propulsion (cf. section 3.3), IGBT's are best suited and hence considered for further investigations.

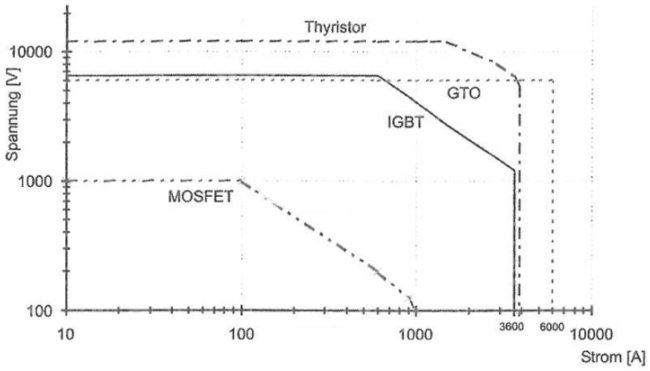

Figure 41, Solid state switch types [63]

The electronic symbol of an IGBT is given in figure 42, a picture of an of the shelf IGBT module in figure 43. For turn-on, a positive voltage is applied to the gate (G) relative to the collector (C) and the IGBT becomes forward conductive for a current between collector and emitter (E). To interrupt the current, turn-off is achieved by applying a zero or minus bias between gate and emitter. Switching times of IGBTs are in the range of 50-200 ns [64], outperforming every electro mechanical switching device by orders of magnitude. Operating IGBTs onboard aircraft, radiation protection provisions and sufficient blocking voltage margins have to be foreseen because high-altitude radiation can cause degradation of the semiconductor materials and hence negatively affect the switching performance over time. In this process, high-energy particles or quanta either displace atoms in the semiconducting layer from their lattice sites (displacement damage) or cause electronic ionization in insulating layers, leading to unintended parasitic fields (ionization damage) [65]. Though, the low weight and good operational characteristics make solid state switches a suitable technology for aerospace applications, as the widespread use in modern aircraft power distribution systems (e.g. A380, B787) confirms [66].

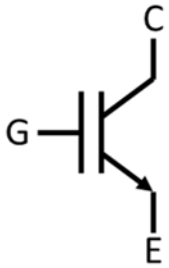

Figure 42, Electronic symbol of an IGBT

Figure 43, IGBT module [67]

Solid state switches have no moving parts, are compact and lightweight compared to mechanical switching systems. Typical state of the art weights of IGBT's are shown in figure 44. Based on this data, a weight trend is derived as given in eq. (26). This linearized weight trend is also displayed in figure 44, including the effect of a 20% deviation.

$$w_{IGBT}[kg] = 1.6 \cdot 10^{-4} \cdot P_{IGBT}[kW] + 0.6 \quad (26)$$

In the forward conducting state, a voltage drop occurs due to internal semiconductor characteristics. This voltage drop is not current dependent like in case of an ohmic resistance, but on the blocking voltage capability of the IGBT. Accordingly, transmission losses occur that can be calculated multiplying the voltage drop $U_{CE,sat}$ with the current load I as given in equation (27) [64].The resulting loss power is dissipated into heat and has to be removed from the switching device by appropriate cooling.

$$P_{loss,IGBT} = U_{CE,sat} \cdot I \tag{27}$$

Typical values for the voltage drop of state of the art IGBT's are shown in figure 45. As mentioned above, the voltage drop is depending on the blocking voltage capability of the device. Based on these figures, a linear regression formula is defined as given in equation (28), mapping the lower boundary of the voltage losses observed. By this, potential improvements in semiconductor materials shall be accounted for.

$$U_{CE,sat}[V] = 4.3 \cdot 10^{-4} \cdot U_{block}[V] + 1.4 \tag{28}$$

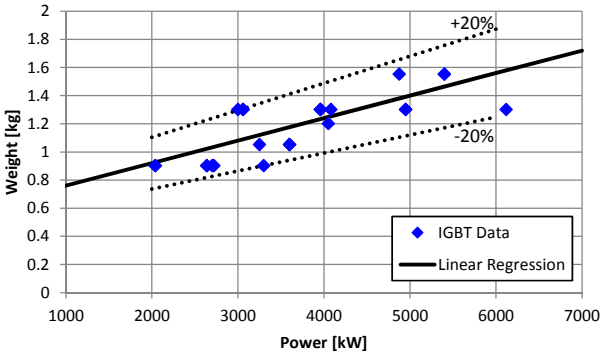

Figure 44, IGBT weight vs. power [67]

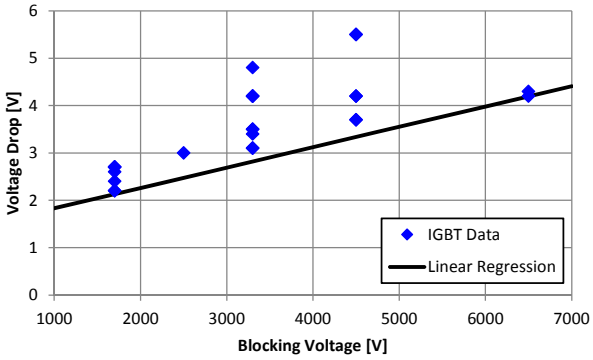

Figure 45, IGBT voltage drop vs. blocking voltage [67]

Vacuum conductors

A drawback of semiconductor switches is that there is no galvanic separation in the switched-off state. If galvanic separation is required, a serial mechanic switch upstream or downstream of the solid state switch should be considered. This mechanic relay is only used for zero-load switching, so the issues regarding high power DC switching do not occur. However, taking into account the reduced dielectric strength of air in high altitudes, vacuum contactors should be used. In these, the mechanical switching takes place in a vacuum vessel, effectively hampering electric arcing (cf. section 3.2.2). Weights and continuous current ratings for commercial off-the-shelve vacuum connectors are shown in figure 46. Based on these values, a linear regression is derived for further vacuum switch modeling:

$$w_{vac}[\mathrm{kg}] = 1.015 \cdot 10^{-3}\, I_{vac}[A] + 0.228 \tag{29}$$

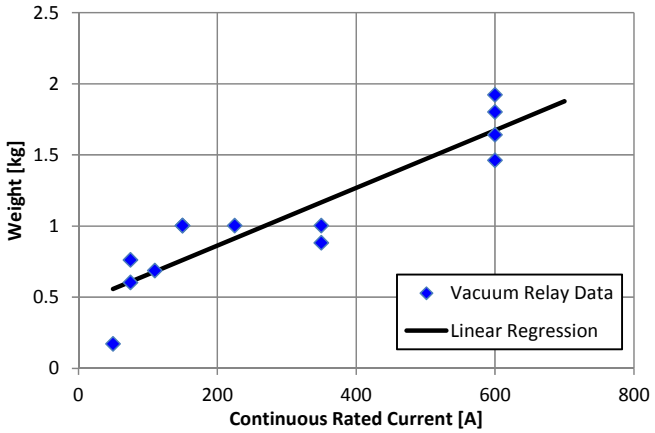

Figure 46, Vacuum relay weights [68]

3.1.4. Electric Motors

In electric powertrains, electric machines convert the electric power into mechanical power on the propeller shaft in case of aircraft propulsion. This mechanical power is defined by the shaft speed N_{shaft} and the applied torque M_{shaft}:

$$P_{shaft} = N_{shaft} \cdot M_{shaft} \cdot 2\pi \tag{30}$$

The conversion process from electric power into shaft power is affected by losses like e.g. due to ohmic resistance, eddy currents and mechanical friction. Hence, a motor efficiency can be defined as follows:

$$\eta_{mot} = \frac{P_{shaft}}{P_{el,in}} \tag{31}$$

Typical operational characteristics of electric motors are given in figure 47. At low shaft speeds, the maximal motor torque is available up to the point when the maximum rated motor power is reached. The motor shaft speed can be increased further at constant power according to equation (30) until the maximum allowed shaft speed is reached.

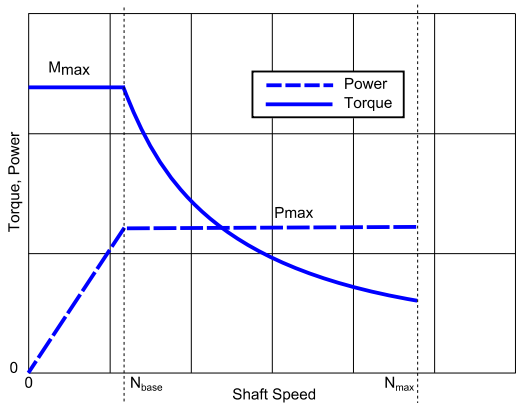

Figure 47, Typical electric motor characteristics, based on [63]

Electric motors are used today in a wide range of power classes. Depending on the application case, various motor types with different architectures and conductor types have been developed.

Conventional motors

While electric machines have been state of the art in trains, increased research efforts have been spent on compact and light-weight motors for electric bicycles, motorbikes, cars and busses. For these applications, the most common motor designs are the asynchronous motor, the synchronous motor, and the switched reluctance motor. Detailed descriptions and working principles of these motor architectures are available in the literature, exemplary in [63].

Current-generation machines for electric ground vehicles and aircraft up to a few hundred kW provide a maximum specific continuous power in the range of 2-6 kW/kg excluding weight associated with a cooling system. Motor efficiencies in this class depend on the operating point but mostly exceed 90% over a wide range of power and shaft speed. [69] [70] [71] [13]

Though state of the art electric traction motors provide a specific power comparable to turbo-shaft engines, these cannot be simply scaled up to the power range required for aircraft propulsion [72]. The critical constraint limiting the maximal motor power is mostly the thermal management. At its maximum continuous rating, equilibrium is reached between heat losses and heat dissipation by the cooling system. Scaling up electric motor dimensions, the ratio of available cooling surface to inner motor volume declines and hence effective motor cooling is hampered. In ground based applications like power plant generators, this issue is addressed by reducing the current density in the windings at the cost of increased motor mass. As outlined below, other motor technologies are expected to provide a significantly higher specific power than today's state of the art concepts, even in the MW range. For that reason, conventional electric motors are not further considered as power converters in the frame of this thesis.

Superconducting (SC) motors

Due to the limitations in specific power of large conventional electric motors, their applicability for electric aircraft propulsion is doubtful. Further increasing the specific power beyond the limits of conventional electric machines requires a step change in the technology used. A promising approach to achieve this technological leap could be the use of superconducting materials. Superconducting wires are able to sustain current densities magnitudes above what is possible with conventional conductors, leading to reduced wire cross sections and reduced weight. The higher current capability can further be used to increase magnetic field strength and hence motor torque. Thus, replacing a part or all current leading elements in an electric machine with superconductors offers the potential of a significant increase in specific power.

Superconductivity is a state of practically zero electric resistance that certain materials reach when they are cooled down below a critical temperature. This effect was discovered in 1911 by Heike Kamerlingh Onnes by cooling mercury below 4.2 K. The underlying physics where explained later with the BSC theory by Bardeen, Cooper and Schrieffer [73]. Until the 1980's only metal-alloy superconductor materials have been known. Their typical critical temperature (T_c) ranges from below 11 K for niobium-titanium up to 39 K for magnesium-diboride. Complex, heavy and expensive cooling systems limited the technical usability of these so called low-temperature superconductors (LTS). In 1986, superconductivity was discovered to occur also in certain ceramic compounds at a temperature above 30 K. Based on these findings, compounds with even higher critical temperatures could be developed in the following years, classified as

the high-temperature superconductors (HTS). The most technically relevant HTS materials today are yttrium barium copper oxide (YBCO) with a T_c of 93 K and bismuth strontium calcium copper oxide (BSCCO) with a T_c of 108 K. [74]
As a matter of fact, the superconducting state is not only limited by the temperature, but also by the current density and the magnetic field, as illustrated in figure 48. For that reason, superconducting wires have to be operated somewhat below their critical temperature, depending on the current and the magnetic field the wire is exposed to.

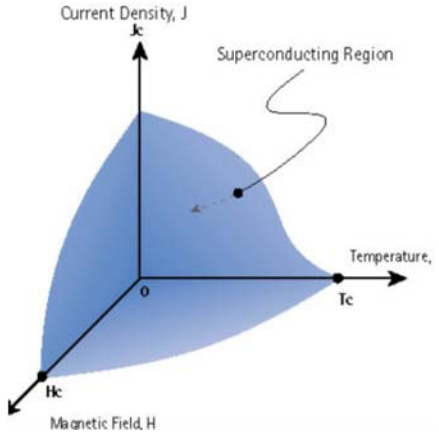

Figure 48, Limits of the superconducting state [75]

Another operational limitation for superconducting materials is alternating current. While actually zero losses occur in direct current transmission, alternating magnetic fields that occur in AC transmission lines and AC coils cause hysteretic-, ferromagnetic-, eddy current- and coupling current losses. Ferromagnetic losses are inherent to the superconducting material itself, but hysteretic-, eddy current-, and coupling-losses depend on the conductor geometry and layer buildup. These losses increase with rising alternating frequency and are dissipated into joule heat which would increase the conductor temperature if no appropriate cooling measures are taken. [74]
At the time of writing, mainly four different motor designs incorporating superconducting materials have been demonstrated or proposed for ground based as well as for airborne applications. The most common SC motor/generator design is a **synchronous machine with superconducting excitation coils**. Two sub-types of this machine are possible: either the excitation coils are stationary and the armature is rotating, or vice versa. In both cases, the coils are fed by a DC current generating a static magnetic field in the coil fixed reference frame. The coils are encapsulated in a vacuum vessel that contains also an eddy current shield to protect the superconducting material from heat radiation and eddy current heat induction from the armature electric field. Since the insulation capability of the vacuum vessel is not entirely perfect and heat leak-in occurs, a cryogenic cooling system provides continuous heat removal. In order to keep the cryogenic cooing loads low, the stator (AC voltage) is build up from resistive copper or aluminum operating at room temperature. Figure 49 shows a schematic drawing of a machine in rotating coil design. Both machine designs where first successfully demonstrated using LTS materials in the late 1960's and early 1970's, and using HTS materials starting from the mid 1990's. Prototypes where build for stationary ground basted power applications, ship propulsion,

and airborne generators. Furthermore, conceptual motor- and generator designs for electric aircraft propulsion have been published [76] [77] [78] [15].

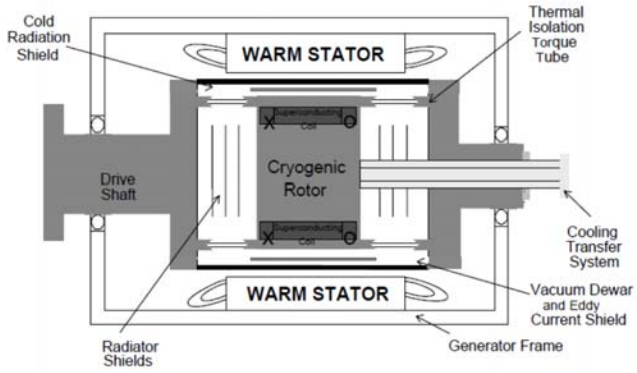

Figure 49, Synchronous machine with SC rotor [74]

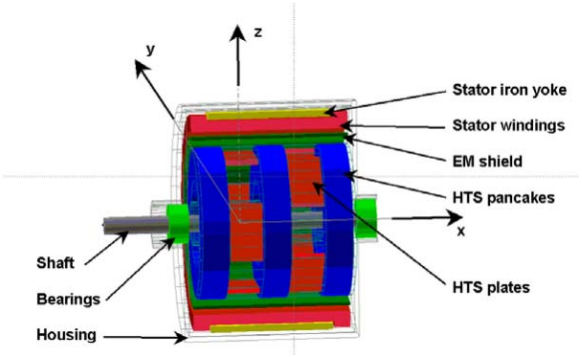

Figure 50, Trapped flux machine [79]

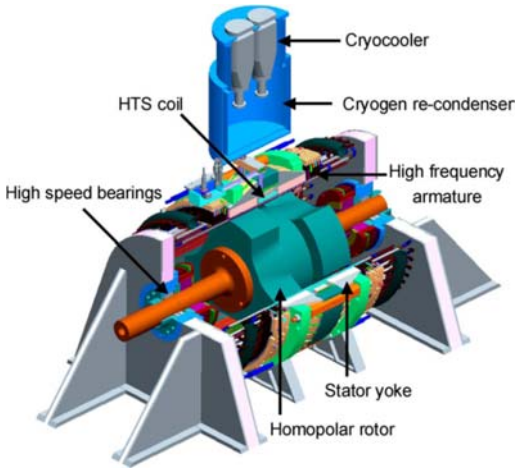

Figure 51, Homopolar HTS generator [80]

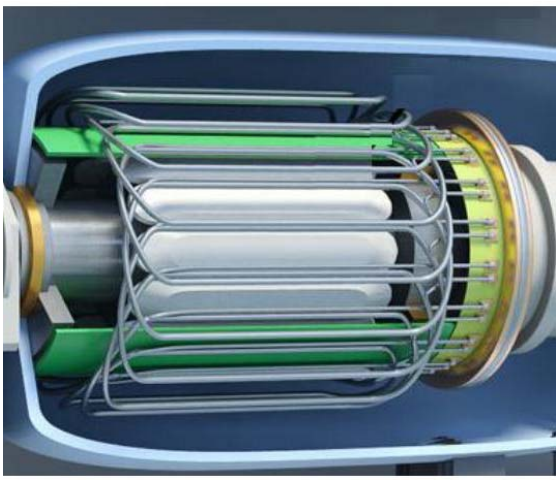

Figure 52, Fully HTS machine [81]

Another possible design is the **trapped flux machine**. This concept is similar to the machine described above, incorporating stationary and resistive room temperature armature windings and superconducting material on the rotor, generating a rotor-frame-fixed magnetic excitation field. The difference is that the magnetic field is not generated by superconducting coils carrying a DC current but by HTS bulk material that has been turned into a permanent magnet using flux trapping. A magnetic field is not able to penetrate a bulk material in a superconducting state, which is known as the Meissner-effect. Placing the superconducting bulk material in a magnetic field in its resistive state and cooling it down below its critical temperature, the magnetic field gets “trapped” in the material turning it into a permanent magnet until the superconductivity is lost again. The advantage of this approach is that no continuous current needs to be applied on the rotor coil during operation, reducing weight, heat leak-in and complexity. This motor concept for electric aircraft propulsion has been proposed e.g. by [79] [82] [83] [84]. A schematic view of a trapped flux machine is given in figure 50.

Since HTS materials today are made from ceramic materials, they tend to be brittle and more sensitive to vibrations compared to metallic conductors. This is an issue for motors and

generators that are designed for high rotational speed, since the high g-loads on the rotor require sufficient mechanical strength of the rotating components. The **superconducting homopolar machine** avoids this problem by placing both the armature winding as well as the superconducting excitation coil in the stationary outer part of the machine. The stationary SC coil magnetizes a homopolar steel rotor with two salient poles, giving this type of machine the characteristics of a synchronous generator. A 5 MW homopolar HTS generator for airborne applications has been build and tested by [80], a schematic view of this generator is given in figure 51.
Superconducting materials in the machines described so far have been limited to DC components because of their limited tolerance of alternating currents due to the associated loss mechanisms. This limits the weight saving potential since conventional copper or aluminum has to be used for the AC armature windings. In theory, also the armature could be made from superconductors, resulting in a **fully superconducting machine**, if the cryogenic cooling system is capable to remove the AC losses continuously. Though, considering state of the art cooler technology and the AC tolerance of available HTS materials, the associated cooler weight would more than offset any weight advantage coming from superconducting materials. However, future advances in minimizing HTS AC losses as well as weight optimized cryogen cooling systems could be enabling technologies to exploit the full potential of all-superconducting machines for airborne applications. Preliminary designs of fully HTS motors and generators including closed cooling system for aero-propulsion have been published by [14] [81] [84]. Figure 52 shows the schematic of a fully HTS motor.

During the last decades, several superconducting machines have been built and demonstrated for ground based and airborne applications. The technical scope of the ground based prototypes, which have been mainly designed for power plant or ship propulsion use, has been primarily to increase the efficiency and to reduce the motor size. While weight has been a minor concern in the conception of these machines, it is a key characteristic for all airborne applications. Thus, only weight optimized superconducting motor designs for aircraft power generation or aircraft propulsion are being considered for performance evaluation. Results from preliminary trapped flux motor designs indicate that 5.8 – 6.6 kW/kg at 3000 RPM can be reached in a power range of 170 kW to 1.5 MW [83], or 6.6 - 7.5 kw/kg at 3000 RPM in the power range of 450 kW and 1.5 MW, respectively [82]. According to recent studies [84] [15] [79], long term development goals for all superconducting machines are up to 40 kW/kg for electric motors and 80 kW/kg for high rotation speed generators. Though, in these trapped flux and all superconducting motor designs, liquid hydrogen is assumed to be available onboard the aircraft as primary fuel. The hydrogen is supposed to be used as a 20 K heat sink for cryogenic cooling before fueling a gas turbine or a fuel cell. Since this provides a free source of cooling and no extra cryogenic cooler has to be foreseen, these motors allow for relatively high losses and low operating temperatures below 30 K, which in turn allows increasing the electric loading in the motor. Though, in electric aircraft powered by batteries, no liquid hydrogen will be available for cooling. Instead, cryogenic cooling has to be assured by a closed cycle system.

Closed-loop cryogenic cooling systems

Superconducting materials must be operated below their critical temperatures which are in the range of 20 K to 80 K. Though isolated thermally, heat is induced into these materials due to

conduction and AC losses. Rejecting this heat requires cryogenic cooling systems. The most common cooling designs include Stirling-, Gifford-McMahon-, and Brayton cycles, as well as pulse tubes. Typical working fluids are gases with a low boiling point such as hydrogen, helium, argon, neon, or nitrogen, depending on the required temperature level. Today available off-the-shelf systems tend to be heavy and bulky, especially due to the weight of the compressors and their drive motors. The lightest systems provide a specific weight of about 14 kg/kW of input power [85]. Since these coolers are designed for ground based applications, significant weight savings can be achieved if they are optimized for aircraft use. In this regard, Brayton cycle coolers are considered to offer a high weight reduction potential by use of a turbo-compressor layout as shown in figure 53. The working fluid is compressed and the compression heat is rejected at a high temperature level T_h to the environment, e.g. via the aircraft equipment cooling system. Afterwards, the fluid is pre-cooled by a recuperator and subsequently decompressed in a turbine that is connected by a shaft to the compressor. After decompression, the working fluid has reached its lower temperature T_l and is ready to absorb the cryogenic heat load. Finally, the fluid absorbs the recuperator heat load and enters the compressor again for a new cooling cycle.

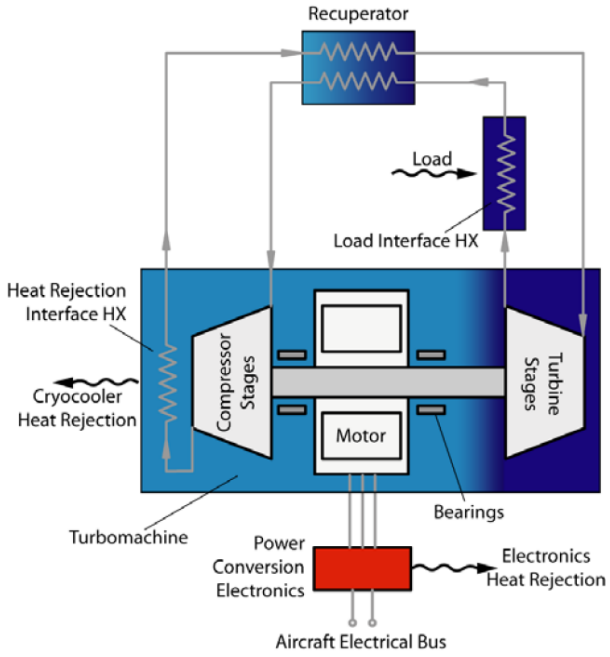

Figure 53, Concept for a lightweight Brayton cryo-cooler [86]

The maximal theoretic efficiency of a cryo-cooler transferring heat from a low temperature medium to a higher temperature medium is the Carnot-efficiency:

$$\varepsilon = \frac{T_l}{T_h - T_l} \tag{32}$$

Since this efficiency is never reached in real machines due to non-optimal thermodynamic cycles and mechanic losses, the additional component efficiency η_{comp} is defined. The mechanical

power P_{cool} required to cool a heat load Q_{cool} at cryogenic temperature is hence defined as follows [87]:

$$P_{cool} = \frac{Q_{cool}}{\varepsilon \, \eta_{comp}} \tag{33}$$

Cryo-coolers today reach a component efficiency of about 30% and, as stated above, around 14 kg per kW of input power. Lightweight design concepts of Brayton coolers for aerospace applications have been addressed e.g. in a NASA SBIR study [86], aiming for a specific weight goal of 3 kg/kW at 30% Carnot efficiency. These designs have yet to be validated by prototype testing to demonstrate the targeted weight and efficiency goals. Furthermore, airworthiness requirements regarding safety and reliability have to be proven.
In the frame of this study, a 3 kg/kW, 30% Carnot efficiency cryo-cooler is being assumed for the considered electric propulsion aircraft. HTS motor losses, thermal isolation losses, and cryogenic motor controller losses are accounted for as thermal load at the respective operating temperatures.

Combined motor/ cooler systems

The size and power consumption of the cryogenic refrigerator increases as the temperature of the cold system is decreased. In a decent design process, motor and cooling system are hence optimized for best combined weight and performance. Such a combined optimization process has been published by Masson et al. in 2005 [77] for a 150 kW aircraft propulsion motor with a HTS DC rotor rotating at 3000 RPM. The weight trends of the motor and the cooling system are given in figure 54, based on currently available cryo-cooler technology. At lower temperatures, the current density and hence the electric loading of the motor can be increased, and as a consequence the motor weight decreases. In contrast, the cryogenic cooling system weight increases as the operating temperature is reduced, resulting in a combined weight minimum between 50 and 60 K. For this class of motors, Masson gives also sizing trends for motor weight and volume up to 5000 kW without cooling system (see figure 55). These trends are approximated using a linear regression according to equations (34) and (35). Cryogen cooling losses are given constant as 20 W.

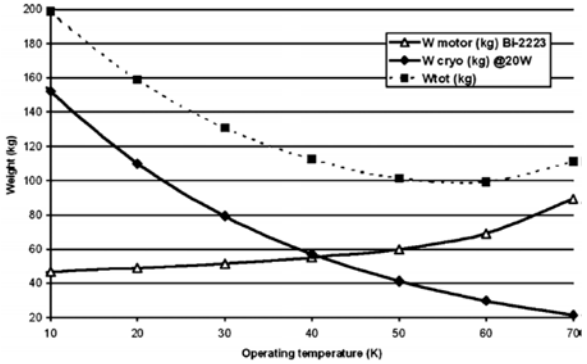

Figure 54, Combined HTS motor & cooler weight [77]

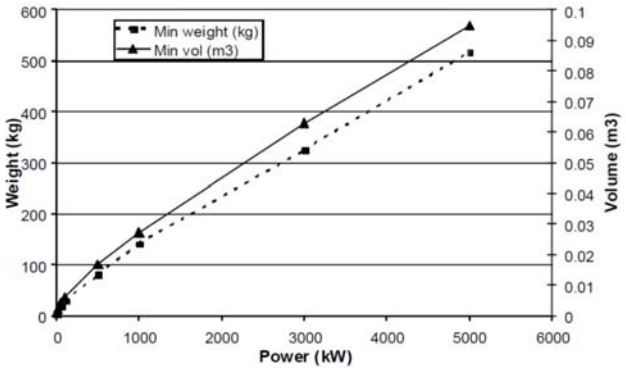

Figure 55, HTS motor weight and volume [77]

$$w_{HTS,DC}[kg] = 0.095 \cdot P_{HTS,DC}[kw] + 38 \quad (34)$$

$$V_{HTS,DC}[m^3] = 1.7^{-5} \cdot P_{HTS,DC}[kw] + 0.01 \quad (35)$$

In 2009, test results of a homopolar HTS generator prototype have been published by [80] (see figure 51). Rated for 5 MVA at 35000 RPM, the generator is excited by a stationary superconducting coil made from BSCCO, operating at about 30 K. A total of 40 W insulation heat leak-in is cooled by a single stage neon cryo-cooler, the combined efficiency of motor and cooler is reported as 98%. The motor weight accounts for 500 kg, added by 45.5 kg for the cooling system.

Preliminary designs of future fully superconducting machines with closed loop cooling system for aircraft propulsion have been published in [14]. Based on advanced cryogenic cooling system designs capable of 30% Carnot-efficiency at 3 kg/kW input power and more AC tolerant BSCCO materials, motor and cooler have been optimized for best combined characteristics. Sizing results for specific motor weight without cooling depending on power are given in figure 56. The values are approximated using the power regression as given in equation (36). However, a follow-up paper was published in 2011, presenting refined methods regarding weight and AC loss modeling. In this publication, a fully SC BSCCO motor is designed rated for 5742 kW at 4800 RPM. The motor operates at 50 K and reaches an efficiency of 99.95% at nominal rating excluding cooling power [81]. Based on the refined weight model, this motor provides a specific power of 29.2 kW/kg which means a 38% reduction relative to the trend published in 2009. This relative reduction in specific power is applied on the 2009 trend for a power range of 500-20000 kW as shown in figure 57. The resulting adapted weight trend as given in equation (37) is used for fully superconducting motor modeling in further considerations. Furthermore, the nominal motor speed is assumed to be at 4800 RPM, the motor efficiency is regarded independent of nominal power rating and part load operation.

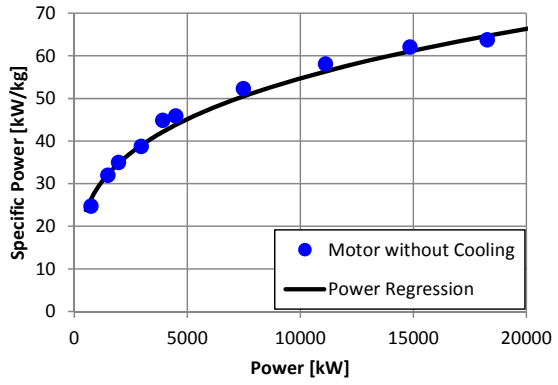

Figure 56, Fully superconducting motor designs, based on [14]

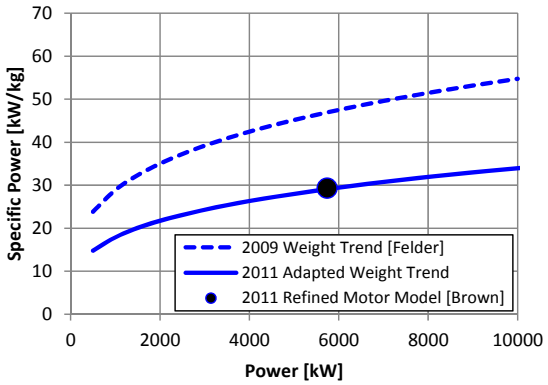

Figure 57, Adapted superconducting motor trend, based on [80]

$$\frac{\partial}{\partial w} P_{HTS,fully,old}[\mathrm{kW/kg}] = 4.2388 \cdot \left(P_{HTS,fully,old}[kw]\right)^{0.277} \quad (36)$$

$$\frac{\partial}{\partial w} P_{HTS,fully,adapted}[\mathrm{kW/kg}] = 0.62 \cdot 4.2388 \cdot \left(P_{HTS,fully,adapted}[kw]\right)^{0.277} \quad (37)$$

Figures about motor geometry for fully superconducting motor designs with liquid H2 cooling is provided e.g. by [78]. The motor considered has a diameter to length ratio of 0.76 and a volumetric density of 1105 kg/m³. These values are used for fully superconducting motor modeling in further considerations.
Since the superconducting motors used for modeling rotate at speeds above typical values for turboprop propellers, a gearbox is necessary to match the desired propeller speed. A weight correlation for propeller gearboxes is given in eq. (38), depending on the transmission power and the rotational speeds at the input- and output shaft [88]. Furthermore, advances in design and materials are taken into account using a technology factor which is given as 72 for future applications. This value is used for further modeling.

$$w_{Gearbox}[\mathrm{kg}] = K \cdot \frac{(P_{Gearbox}[kW])^{0.76} \cdot (N_{mot}[RPM])^{0.13}}{\left(N_p[RPM]\right)^{0.89}} \tag{38}$$

$$K = 43\ (Year\ 1980)$$
$$K = 34\ (Year\ 2000)$$
$$K = 26\ (Future)$$

Gearbox losses that occur due to mechanical friction are modeled using test data of an Allison T56/501 turboprop gearbox as given in figure 58. For a fixed propeller speed, the efficiency shows a dependency on the applied input power. Normalizing the input power by the take-off rating, a generalized efficiency trend is derived and approximated by a power regression, as given in equation (39). The resulting efficiency trend curve for a power rating (PR) between 0.3 and 1 is given if figure 59.

$$\eta_{gearbox} = 98.9 \cdot (PR)^{0.0135} \tag{39}$$

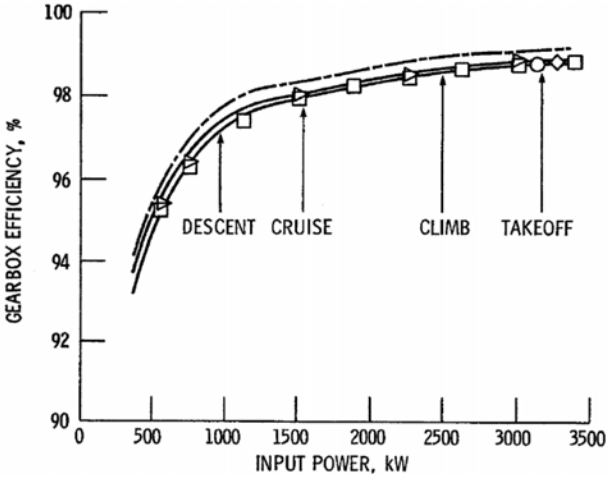

Figure 58, T56/501 gearbox efficiency [89]

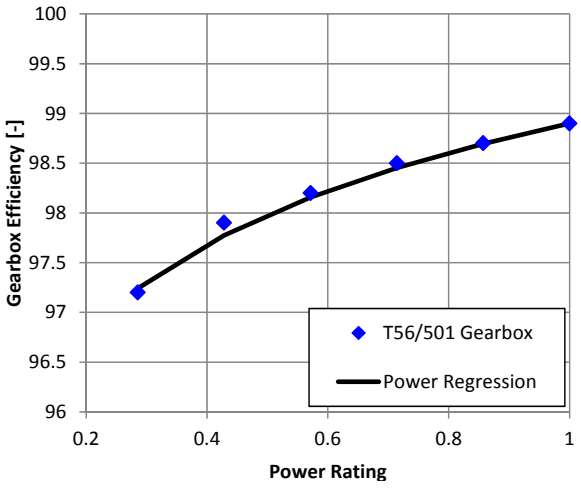

Figure 59, Gearbox efficiency model

3.1.5. Equipment Cooling

Virtually all system components of an aircraft, powered hydraulically or electrically, generate loss heat as a result of friction due to viscosity or electric resistance. This heat has to be rejected to the environment to keep the component below its maximum allowable operating temperature. For applications in aircraft, different cooling system designs have been developed. Apart from cooling systems that involve aircraft fuel or engine bleed-air, these are mainly ram air cooling, expendable cooling, and vapor cycle refrigeration designs. Ram air cooling systems use ambient air to cool the aircraft components directly or indirectly via an intermediate cooling fluid, while expendable systems use the heat absorption capability of fluids during phase change. In an expendable system, a sufficient amount of cooling fluid has to be stored onboard the aircraft that is evaporated and afterwards rejected to the environment. In contrast, vapor cycle refrigeration designs re-condense the cooling medium using a mechanical compressor and reject the absorbed heat via a ram air cooling system to the environment. The applicability of each cooling system depends on the atmospheric- and flight conditions, as well as the temperature level of the components to be cooled. Detailed weight comparisons of different cooling approaches have been performed in [90]. In this publication it was concluded that direct ram air cooling is superior for subsonic flight regimes, while expendable or vapor cycle systems are necessary for supersonic flight due to the rise of total air temperature.

According to the methods available from source [90], the specific weight of a direct ram air cooling system is a function of the component cooling efficiency e_E as defined in equation (40):

$$e_E = \frac{\left(T_{E_e} - T_{E_i}\right)}{\left(T_{E_s} - T_{E_i}\right)} \tag{40}$$

This component efficiency is the quotient of the temperature increase of the cooling medium and the maximal temperature difference between the component surface and the cooling medium. A value of $e_E = 1$ would mean that the cooling fluid is being heated up from its initial to the component temperature. The magnitude of e_E is a function of the heat exchanger surface, hence a detailed design would be necessary to determine actual values. Reference [90] states that typical values for e_E are in the range between 0.2 - 0.9. However, in the frame of this study, a value of 0.8 is assumed for the large battery arrays due to their high surface, and 0.5 for all other system components.

$$e_{E,Batt} = 0.8$$

$$e_{E,sys} = 0.5$$

The specific cooling weight is given in terms of $\Delta w_g\left(1 - X_{ref}\right)$. Thereby, Δw_g resembles the weight of the cooling system itself, and $\left(1 - X_{ref}\right)$ is a term taking the aircraft's fuel weight share into account. In the referenced methodology, an aircraft weight increase due to additional fuel is being considered since the cooling system weight and drag cause a fuel burn increase on overall aircraft level. Since an integrated sizing methodology is being used for aircraft modeling in the frame of this thesis, this fuel impact is being neglected by setting the term $\left(1 - X_{ref}\right)$ to 1.

Sizing results of direct ram air cooling systems depending on the system temperature potential (ΔT_t between component- and cooling air) are given in figure 60. Since the results are based on

1950's technology, only the lower boundary curve is considered to account for advances in technology.
In the frame of this study, a maximal ambient air temperature of 37°C at sea level is assumed as reference condition (cf. section 3.2.3). Resulting weight trends depending on the component surface temperature can be derived. These trends for an e_E of 0.8 and 0.5 respectively are approximated with a power regression as given in equations (41) and (42). The trends are also visualized in figure 61.

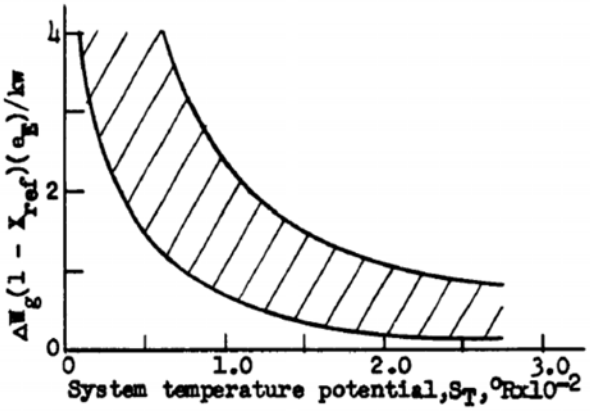

Figure 60, Direct ram air cooling weight trend [90]

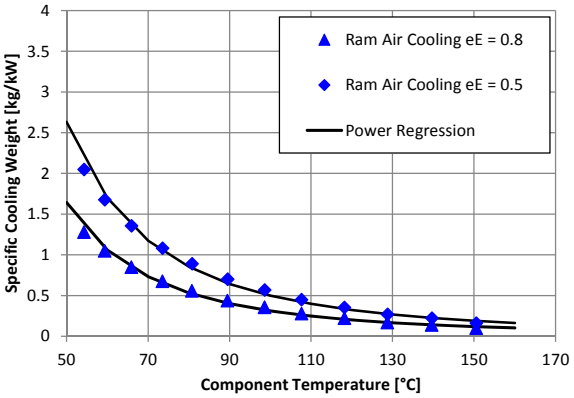

Figure 61, Cooling weight model

$$w_{cool,0.8}\,[kg] = 19316\left(T_{comp}\,[°C]\right)^{-2.396} \quad (41)$$

$$w_{cool,0.5}\,[kg] = 31097\left(T_{comp}\,[°C]\right)^{-2.397} \quad (42)$$

Altitude effects on cooling

For the cooling systems as defined above, sea level has been assumed as reference altitude. Though, flying at cruise altitude means lower ambient air temperature, which is beneficial for cooling, but also lower air density which reduces the heat transfer in the heat exchangers of the cooling system. Considering the general characteristics of heat exchangers, it can be shown that the heat transfer is proportional to the temperature difference and to the square root of air density, flight velocity and air viscosity:

$$\dot{Q} \sim (T_r - T_{env})(\rho_{env} v_{env} \mu_{env})^{0.5} \quad (43)$$

Based on that, the required air flow velocity through a heat exchanger v to cool a constant heat load has been calculated in reference [91] for the standard ISA atmosphere. It is found, that the effect of falling temperature with altitude outweighs the reduction in air density, and hence a required airflow velocity minimum v_{min} is found at the tropopause at an altitude of around 11 km. In figure 62, the required airflow velocity v is plotted relative to its minimum value v_{min} for three different radiator temperatures T_r. Given that flight altitudes above 15 km are excluded in this study, the cooling requirements at sea level are considered as the critical design condition for the cooling system.

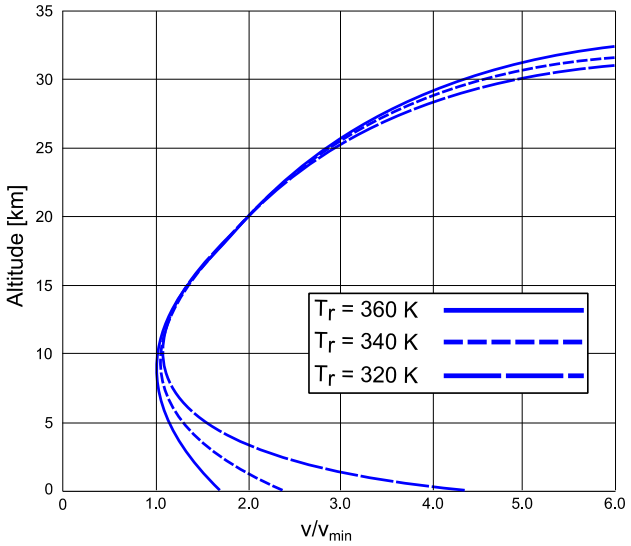

Figure 62, Altitude effects on cooling characteristics, based on [91]

3.1.6. Motor Inverters & Controllers

The motor controller is connected to the DC power distribution system and provides alternating current to the motor in the required frequency and voltage level to match the desired operating point in terms of shaft speed and torque. In the MW range, they are typically build up using solid-state MOSFET, IGBT or thyristor switches (cf. section 3.1.3), and filters to eliminate disturbance in the power signal. A basic layout of the switch arrangement in the controller of a 3-phase motor is given in figure 63. Depending on the rotor position in the motor, the switches S_1 - S_3 are being closed and opened in order to provide electric current to the respective part of armature winding in the motor.

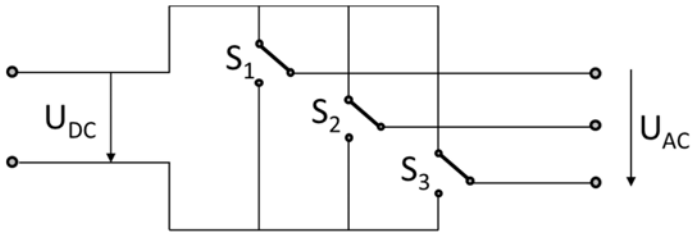

Figure 63, Basic motor inverter build-up, based on [92]

During operation, losses occur due to voltage drops in the semiconducting materials and due to switching losses. Typical efficiencies of motor controllers are in the range of 95%, recent designs for traction motors reach a specific power around 3-11 kW/kg [82].

Future prospects for motor controllers include new materials like Si-C semiconductors and operation under cryogenic cooling. The advantage of Si-C is its higher operating temperature compared to conventional Si semiconductors and the related better cooling characteristics. In a next step, forward resistance, switching losses, and filtering requirements can be reduced significantly when semiconductors are cooled down and operated at 77 K [93]. For these cryogenic controllers, a goal of 33 kW/kg at an efficiency of 99.8% excluding cooling system has been set in [81].

DC/DC converters

In the power system architecture, the propulsion system and the aircraft systems are supplied by power busses operating at different DC voltage levels (cf. section 3.2.4). Feeding power from one bus to another, DC/DC converters are necessary to compensate this voltage mismatch. Compact and lightweight converters are currently being developed for electric vehicle applications, providing a specific power of about 8 kW/kg [94] [95]. Conversion efficiencies are in the range of 97%. These characteristics are being used for further DC/DC converter modeling.

3.1.7. Propeller

For the speed range of the aircraft class considered, propellers are the most efficient device for thrust generation. Converting mechanical shaft power into thrust, the efficiency of the propeller can be defined as the propulsive power (thrust times flight velocity), divided by the mechanical shaft power delivered to the propeller:

$$\eta_p = \frac{t\ v}{P_{shaft}} \tag{44}$$

Basically acting like a rotating wing, each propeller blade segment generates lift (thrust) depending on the local flow velocity and its angle of attack relative to the blade cord line. Since the movement of a propeller blade through the air is a combination of the forward speed of the aircraft and the rotational speed of the propeller, this angle of attack varies for different operating points. In common propeller theory, the operational parameters propeller speed, diameter, and forward velocity are translated into the advance ratio J as a non-dimensional characteristic figure:

$$J = \frac{v}{N_p\ D_p} \tag{45}$$

In a similar approach, also the power absorbed by the propeller is expressed in relation to the propeller speed, diameter, and air density, defined as the power coefficient C_p:

$$C_p = \frac{P_{shaft}}{\rho\ N_p^3\ D_p^5} \tag{46}$$

Given that the speed of the propeller tip remains below the speed of sound and no flow separation occurs, the operational performance of a propeller can be characterized in a non-dimensional diagram based on the advance ratio and the power coefficient only. Such a diagram for a 4-bladed propeller with variable pitch control is shown in figure 64.

Blade pitch angle control is used in modern propeller driven transport aircraft in order to maintain high efficiency over a large range of speed, from take-off to high speed cruise. By this, the angle of attack at the propeller blade can be adapted to changing flow conditions due to propeller speed and flight velocity. Using turbo-shaft engines to drive the propeller, the shaft speed range for optimal engine efficiency is quite narrow in flight, so the propeller speed is kept constant at this optimal speed. Power absorption by the propeller is controlled via blade pitch control. The effects of this constant speed operation on the propeller efficiency are shown in figure 64,

exemplary for a 4 m diameter propeller. Assuming that the propeller is designed for optimal cruise efficiency, this nominal operating point would be reached for the following reference conditions:

- Propeller speed: 1040 [RPM]
- Power rating: 1200 [shp]
- Flight Velocity: 460 [km/h]
- Flight Altitude: 6000 [m]

With these figures, the coefficients C_p and J result in 0.25 and 1.84 for the optimal propeller efficiency of 88.5%. Though, flying at a lower power setting e. g. due to low payload or at a higher air density in a lower cruise altitude leads to a vertical shift of the operating point in the propeller diagram, resulting in a slight loss in efficiency.
Compared to turbo-shaft engines, electric motors maintain their efficiency over a wider range of motor speeds. Furthermore considering superconducting motors, the overall motor efficiency is mainly depending on the power required for cooling and the amount of AC losses (cf. section 3.1.4) which actually decrease with declining motor speed. Hence, electric motors do not necessarily require a constant operating speed giving another degree of freedom for optimal propeller operation. This optimization potential is exemplary shown in figure 65 for the propeller described above. Assuming a low-payload, short-range and hence low fuel weight mission, the required power to maintain the design cruise speed could be exemplary 30% below the power setting in the design case. With all other parameters unchanged, the constant speed propeller's C_p would be reduced to 0.18 at constant advance ratio, losing more than 3% in propeller efficiency (point 2 in figure 65). If the propeller speed can be varied however, the operating point can be shifted along the dashed line and a new optimal operating point is found for a propeller speed of 825 RPM at about 88% (point 3).

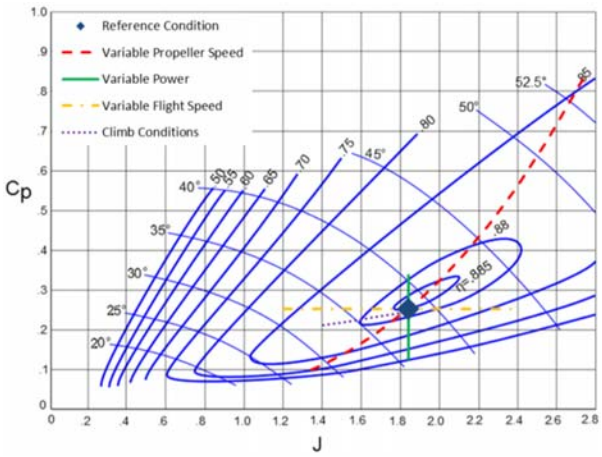

Figure 64, 4-blade propeller efficiency map, based on [96]

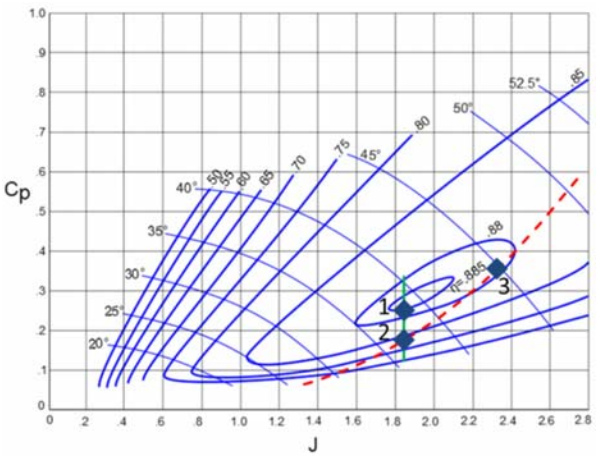

Figure 65, Variable propeller speed operation

A suited modeling method taking propeller speed effects into account would be a blade element theory approach as e.g. described in [97]. In this method, the aerodynamic properties at the propeller blade are evaluated at several blade sections using airfoil polar data to determine the overall aerodynamic blade force via radial and circumferential integration. Next to the proper

selection of suitable airfoils, this approach requires determination and optimization of typical propeller characteristics like diameter, number of blades, activity factor and blade twist, as well as the determination of the blade angle in case of a variable pitch propeller for every flight condition. Due to the complex and (numerical calculation-) time consuming nature of this approach, especially in the frame of aircraft design space considerations (cf. section 5.4), a different propeller modeling approach is used in the frame of this study.
In a first step, the propeller diameter and propeller design speed are selected based on empirical methods. Depending on the mechanical power absorbed per blade, the propeller diameter is determined using a method given in reference [98]:

$$D_p[m] = 0.232 \left(\frac{P_{TO}[kW]}{n_{blades}}\right)^{0.485} \tag{47}$$

Assuming a six blade propeller like used in modern transport turboprop aircraft (ATR 72/ 42, Dash-8, Saab 2000), the propeller diameter is determined based on the power as only input parameter. The propeller tip speed is typically limited by efficiency on the one hand, but more importantly by noise considerations on the other hand. In this regard, 250 m/s is considered as the upper limit in static conditions according to [96] and will be assumed as propeller tip speed in further considerations. Accordingly, the design propeller speed can be determined as follows:

$$N_p[\mathrm{RPM}] = \frac{250\,\frac{m}{s}}{60\,D_p[m]\,\pi} \tag{48}$$

The efficiency of the propeller is modeled using an actuator disc theory approach. As e.g. outlined in [99], this can be expressed by an ideal efficiency η_{ideal} accounting for momentum losses in the propeller slipstream, and a figure of merit η_{FOM} accounting for losses due to propeller effects such as friction and vortex drag. For this figure of merit, a typical value of 0.88 is stated in [99]. The propeller efficiency is then:

$$\eta_p = \eta_{ideal}\ \eta_{FOM} \tag{49}$$

Momentum losses occur since the propeller generates thrust by (air-) mass acceleration. This thrust can be defined as the mass flow of the propeller stream-tube times its velocity increment, which is constant in some distance after the propeller plane as shown in figure 66. Hence, the thrust is:

$$t = \rho\, V_2 A_2 (V_2 - V_0) \tag{50}$$

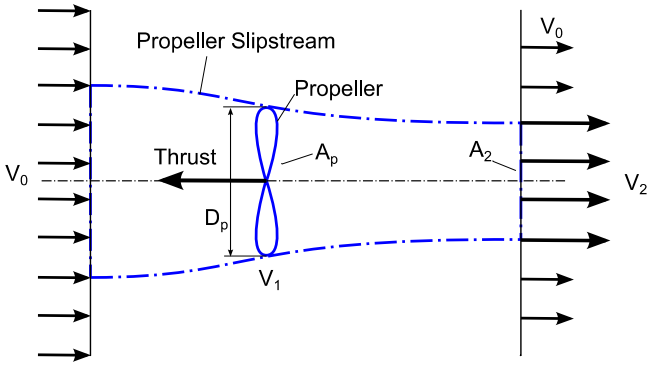

Figure 66, Propeller stream-tube

The kinetic energy in the slipstream which results from the momentum transfer by the propeller is lost and is being dissipated into turbulence and finally heat downstream of the propulsor. Further considering Bernoulli's equations, it can be shown that:

$$A_p = 2\,A_2 \tag{51}$$

$$v_2 = 2\,v_1 \tag{52}$$

As given in [99], these equations can be transferred into equation (53) for the ideal propeller efficiency which accounts for momentum losses. This polynomial equation is solved numerically in the aircraft sizing code (cf. section 4.2).

$$\eta_{ideal}^3 + \left(\frac{2\rho\, v_0^3}{P/A_p}\right)\eta_{ideal} - \left(\frac{2\rho\, v_0^3}{P/A_p}\right) = 0 \tag{53}$$

Next to the losses related to the isolated propeller, further installation losses occur due to increased friction drag of aircraft structures that are immersed in the propeller slipstream. This slipstream velocity dependent drag increment is accounted for by a slipstream factor F as given by [96]. The required parameters are the air density ratio σ, the drag area of the aircraft parts in the slipstream f_s, and the propeller diameter D_p:

$$F = \frac{effective\ propeller\ thrust}{isolated\ \ propeller\ thrust} = \frac{T_{eff}}{T_{is}} \tag{54}$$

$$F = 1 - 1.558\,\frac{\sigma f_s[m^2]}{\left(D_p[m^2]\right)^2} \tag{55}$$

The weight of the propeller assembly is modeled using a method from ref [100], which is based on the propeller diameter, the number of blades, the activity factor, the propeller shaft speed, the absorbed power, and the cruise Mach number:

$$w_p[\mathrm{kg}] = K_w \left(\frac{D_p[m]}{10}\right)^2 \left(\frac{n_b}{4}\right)^{0.7} \left(\frac{AF}{100}\right)^{0.75} \left(\frac{N_p[rpm]D_p[m]}{20000}\right)^{0.5} (M+1)^{0.5} \left(\frac{P_p[kW]}{10\,D^2[m]}\right)^{0.12} \tag{56}$$

The impact of the materials used is accounted for by the correction factor K_w which is 2445 for solid aluminum blades and 1240 for a composite structure. Composite propeller blades are assumed for further modeling.

3.1.8. Aircraft Systems

In classical aircraft system layouts, three different power distribution systems are used for aircraft control and sub-systems power supply: an electric, hydraulic, and pneumatic system. If not controlled mechanically by the pilot's physical control column forces, a hydraulic system is used to actuate the flight control surfaces and the retractable landing gear. Given that an auxiliary power unit or an external power source is available, main engine start is typically done with a high pressure pneumatic system. In modern aircraft system design, there is a trend towards the "more electric" aircraft which means a partial replacement of hydraulic and pneumatic system functionalities by the electric system with the aim of reduced weight and enhanced overall system efficiency. In fact, also "all electric" aircraft systems are being considered, meaning that the hydraulic and pneumatic systems are replaced completely and all system functions like e.g. actuation, engine start, air conditioning etc. are done using electrically powered equipment. This approach is also being considered for the electric propulsion aircraft in the frame of this study.

3.1.8.1. Electric Actuators

Electrically powered actuators for control surface and landing gear actuation are a state of the art technology in today's "more electric" aircraft system design. There are two different types of electric actuators: the electro-hydrostatic actuator (EHA) and the electro-mechanical actuator (EMA). The electro-hydrostatic actuator is basically a hydraulic actuator with a local hydraulic circuit powered by an electric motor driven pump. A schematic view of an EHA build-up is shown in figure 67. Due to its design characteristics, EHAs are not prone to mechanical jamming and provide a high level of reliability. Furthermore, the actuator can bear static loads without electric power consumption by closing the valves of the hydraulic circuit. Following a fail-save design philosophy, the hydraulic rams can be moved without severe residual force in case of an actuator failure, so redundancy is being achieved using two separate actuators per control surface. [101]

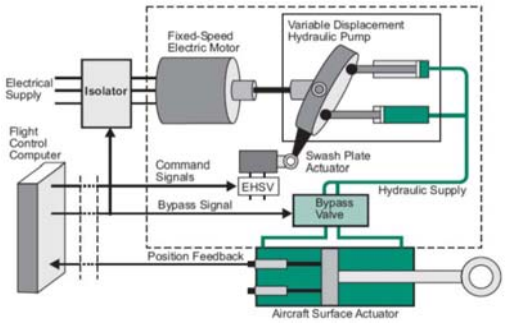

Figure 67, Schematics of an electro-hydrostatic actuator [102]

The final step towards pure electric actuation is the electro-mechanical actuator, which eliminates the need for any hydraulic components [103]. Instead of powering a hydraulic pump, the electric motor directly moves the actuator by a gearbox and ball screw system. A schematic

of an EMA is given in figure 68. Compared to the EHA, a pure mechanical design is supposed to have advantages in terms of less weight and a higher efficiency. Though, the ball screw system implies the risk of mechanical jamming in case of a component failure, but this issue can be solved by fault-tolerant design measures [104].

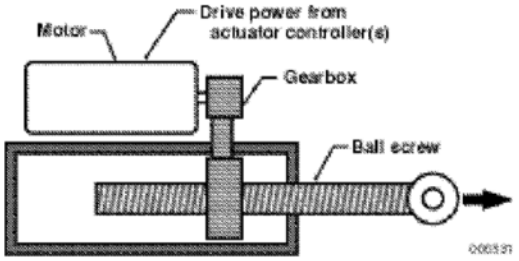

Figure 68, Schematics of an electro-mechanical actuator [105]

Power requirements of electric actuators can be determined by evaluating the required hinge moment and angular velocity of the respective control surface or other actuation function. This approach is e.g. applied in reference [101]. Accordingly, the hinge moment can be determined as given in equation (57), depending on the dynamic pressure, a hinge coefficient, and the reference area and mean chord of the control surface:

$$M_h = \frac{\rho}{2}\, v^2\, C_h\, S\, \bar{c} \tag{57}$$

The required power can then be written as the product of the hinge moment and the angular flap velocity:

$$P_a = M_h\, \omega_a \tag{58}$$

$$\omega_a = const. \;\rightarrow\; P_a \sim M_h \tag{59}$$

Exemplary actuator peak power ratings for an Airbus A320 aircraft are given in table 6 [106]. Assuming that the angular velocity of a specific control surface is independent of aircraft size, the actuator peak power is proportional to the hinge moment. Accordingly, the actuator power rating is calculated by scaling the A320 reference value for actuator power as given in equation (60). As reference speed $V_{mo,ref}$, the A320 maximum operating speed (V_{mo}, CAS) is used:

$$P_a = P_{a,ref}\, \frac{M_h}{M_{h,ref}} = P_{a,ref} \left(\frac{V_{mo}}{V_{mo,ref}}\right)^2 \frac{S}{S_{ref}}\, \frac{\bar{c}}{\bar{c}_{ref}} \tag{60}$$

$$V_{mo,ref} = 350\ [kts]$$

Reference values of the A320 for the different flight control surface actuation functions are given in the following table:

	No. of actuators [-]	Power per actuator [kW]	Surface ref. area [m²]	Surface mean cord [m]
Aileron	4	3.02	2.74	0.5
Elevator	4	1.16	3.7	0.75
Rudder	3	3.41	6.7	1.14
Spoiler	8	3.14	8.64	0.65

Table 6, Reference data of flight control surfaces [106]

For actuation of the trailing edge flaps of the high-lift system, the flap area related power requirement is significantly lower than for primary flight control functions due to the lower required deployment speed. Hence it is assumed, that the flap actuators have the same power characteristics as the aileron actuators, but at only 20% of the angular velocity.
Assuming that the power required for landing gear actuation is mainly a function of the landing gear weight, the actuator power estimation is done by using a weight specific power coefficient:

$$P_{u,spec} = \frac{P_{a,ref}}{w_{u,ref}} \tag{61}$$

$$P_u = P_{u,spec}\, w_u \tag{62}$$

Reference values for landing gears as found in [107] are shown in table 7. For the main gear actuators, the specific power appears to be 5.5 W/kg, for the nose gear 9.5 W/kg. These values include the power required for the wheel brakes. Additionally, a further actuator is required for nose gear steering; the specific power for this component is 2.9 W/kg.

	Weight [kg]	Actuator power [kW]	Specific actuator power [W/kg]	Steering power [kW]	Specific steering power [W/kg]
Main landing gear	982	5.4	5.5	-	-
Nose landing gear	147	1.4	9.5	0.43	2.9

Table 7, Landing gear actuation reference data

Since the major part of a transport aircraft mission is flown in a quite steady flight condition, full actuation power is only exceptionally applied on flight control surfaces. As proposed in [106], the average power consumption can be approximated using the 80/20 rule. According to that, primary flight controls are working at full power during 20% at the time, and operating at 20% power in the remaining 80%. This results in an average power consumption of 36% of nominal peak power.
Weight trends regarding electro-mechanic actuators are derived based on weight data from references [107] and [105] as shown in figure 69. Weight modeling is done based on actuator input power using the logarithmic regression as given in equation (63).

$$\frac{\partial}{\partial w} P_{ema}\left[\frac{kW}{kg}\right] = 0.212\ \ln(P_{ema}\ [kW]) + 0.22 \tag{63}$$

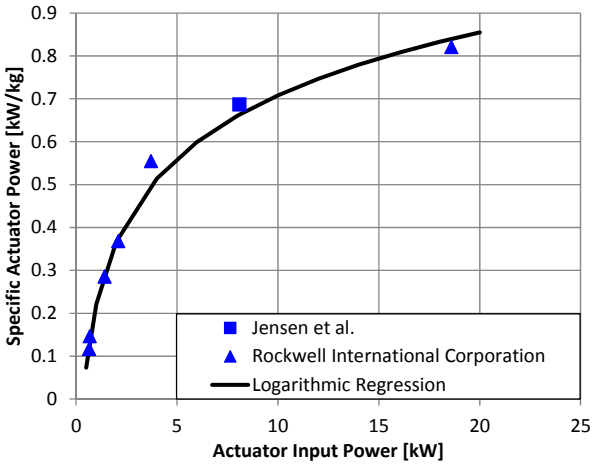

Figure 69, Electro-mechanical actuator weight trend

3.1.8.2. Air Conditioning

The environmental control system (ECS) of an aircraft ensures comfortable air conditions for passengers and the crew. Therefore, the cabin air has to be ventilated and replaced with ambient air. This implies cooling or heating on the ground and in flight, as well as pressurizing ambient air in high altitude. Cabin air pressurization and conditioning in today's commercial air transport aircraft is conventionally done using bleed air from the engine compressors. Depending on the ambient air conditions and the desired cabin pressure, the high temperature bleed air is expanded and cooled by ambient ram air in a simple Joule or Bootstrap cycle. In the absence of combustion engines, cabin pressurization has to be done using electric environmental control systems. In this case, an electrically powered compressor supplies the pressurized air. A schematic of an electric ECS system is given in figure 70.

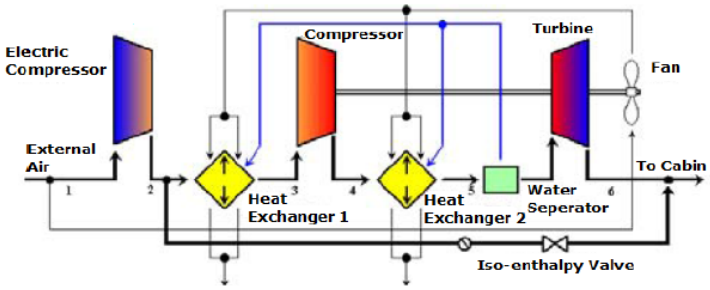

Figure 70, Electric ECS based on a Bootstrap cycle [108]

Weight and power requirements of electric ECS have been investigated in several preliminary studies. The nominal power requirement is found to be directly dependent on the required air mass flow and hence of the number of persons onboard the aircraft. Based on the results of references [108] and [109], this correlation is modeled using the linear sizing trend given in equation (64) and figure 71.

$$P_{ECS}[\mathrm{kW}] = 0.9 \cdot n_{PAX} + 67 \tag{64}$$

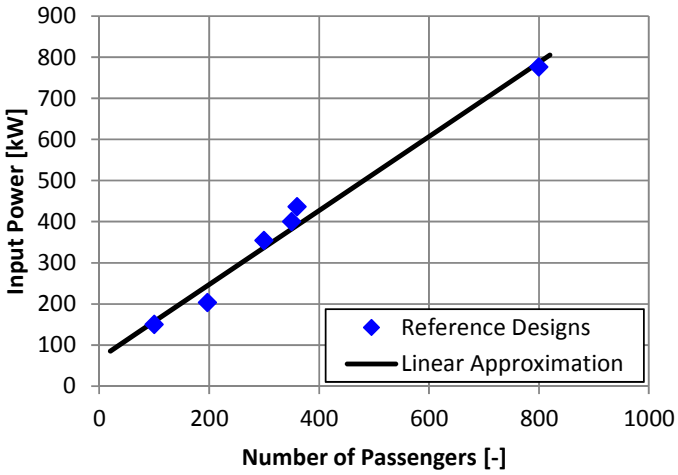

Figure 71, Electric ECS power consumption

The actual power consumption of the electric ECS is depending on the flight phase and the related operating conditions. While study [108] concludes that heating the aircraft at a cold day on the ground is the most power demanding task, studies [110] [[109] show that high altitude cruise operation is the critical design case. By mean of simplification, it is assumed in the frame of this study that the environmental control system operates at its nominal power during the entire mission. The weight of the electric ECS including electric motor, compressors, fans, heat exchangers, and piping has been reported to be in the range of 2.6 kg/kW [108].This value is being used for ECS weight modeling.

3.1.8.3. Ice Protection

Wing- and tail ice protection of transport aircraft can be achieved either thermally by bleed air or electric heating, or mechanically by pneumatic boots and electro-mechanical systems. In case of an electrically propelled aircraft powered by batteries, thermal solutions are unfavorable since hot engine bleed air is not available and electric heating is rather inefficient. Generally considering the low specific energy of batteries compared to kerosene, energy demanding de-icing systems would imply significant weight penalties due to additional required battery capacity. Thus, mechanic or electro-mechanic systems are being favored in this case.

One common variant of a mechanic de-icing system is a pneumatic boot. This boot is installed at the leading edge of the wing and the horizontal stabilizer, and is periodically inflated with pressurized air in an interval of several seconds. In this way, ice that accumulates at the leading edge is being shed into the slipstream [111]. While normally engine bleed air is used for this purpose, the required pressurized air could also be taken from the environmental control system compressors.

Another method of mechanical de-icing is based on an electrically generated pulse. Here, a short-time, high-current electric charge is discharged into a coil that is integrated the wing structure beneath the outer surface. Depending on its specific design, this pulse induces a shock wave or high frequency vibration into the wing structure, resulting in an acceleration-based cracking and detachment of ice from the wing surface. The advantages of this approach compared to thermal de-icing methods are low maintenance requirements, long lifetime, and the lack of unfavorable aerodynamic implications. An exemplary electric power demand is 60 W per

meter of wingspan [112]. The weight is reported to be similar to conventional pneumatic boots. In the frame of this study, an electric de-ice system is assumed for further modeling, its weight is considered to be included in the wing weight group.

3.1.8.4. Various Items Power Consumption

Next to the aircraft systems described above, there are various other items onboard the aircraft that are powered electrically. This includes avionics, galleys, lighting, inflight entertainment systems, etc. The maximum power requirement for these systems is modeled using a method provided by [96], depending on the volume of the passenger cabin:

$$P_{max,items}[kW] = 0.565\, V_{pc}[m^3] \tag{65}$$

Like already applied in case of the actuator power consumption (cf. section 3.1.8.1), the 80/20 rule is used to estimate the average power consumption of the electric items.

3.2. Electric Propulsion System Architecture

The propulsion system architecture of the electric transport aircraft has to satisfy all safety requirements at the highest possible efficiency and lowest achievable weight. The basic system architecture, as already outlined in the introduction section, includes a storage system that delivers electrical power to a distribution system. This distribution system provides the power across the aircraft to the consumers, mainly the electric motors via their controllers. This principal chain is illustrated in figure 72.

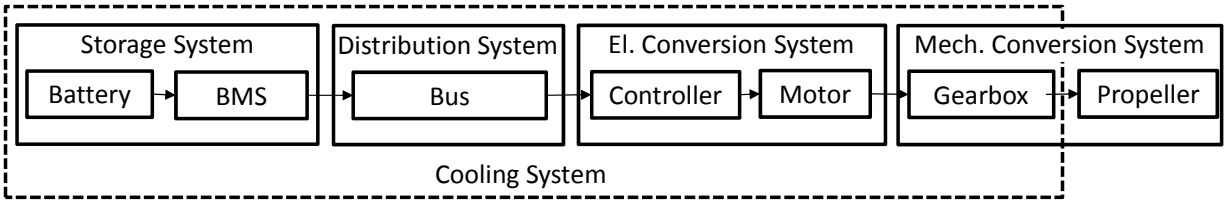

Figure 72, Basic propulsion system components and sub-systems

Certification aspects and system requirements

For civil propeller driven transport aircraft heavier than 8618 kg certification specifications are defined in the FAR 25 or CS 25 [113]. In case of the propulsion system or other critical aircraft equipment, this includes system redundancy and fail-save requirements. Since up to now electric propulsion has only been demonstrated for aircraft far below eight tons, the CS 25 does not cover electric propulsion systems yet. This problem does also occur in today's aircraft development programs if manufacturers introduce new technologies like large CFRP structures or "more electric" system architectures to their products and no certification procedures exist therefor either. In this case, the manufacturer has the option to propose a certification under conditions of equivalent level of safety (ELOS) (14 CFR 21.21) or certification under special conditions (14 CFR 21.16). As far as applicable, this approach is being used in order to derive design guidelines for the electric propulsion system. For major safety aspects regarding the

propulsion system, CS 25 requirements are consulted and, where appropriate, transferred to the actual case so that the basic intention is maintained.
In general, certification requirements for critical systems ask for two basic design principles: redundancy and fail-safe characteristics. Redundancy means that in case of a failure of a single system component or subsystem, the functionality of this system can be fulfilled by at least one other independent system. The fail-save requirement, in addition, assures that the initial failure is contained and has no adverse effect on other systems. In this chapter, these principles are being applied in the definition of the systems shown in figure 72, in each case with reference to present CS 25 standards. Due to their high interdependency in terms of power supply, also the aircraft systems will be included.

3.2.1. Battery System

While in section 3.1.1 battery characteristics were described on cell level, a system of battery cells including control equipment is necessary to provide the required power to the propulsion system.
The operating voltage range of a single battery cell depends on the cell type and is typically in the order of a few Volts. If the voltage required for the consumer is higher than the single cell voltage, commonly a number of n cells are connected in series. The voltage of the battery pack then is the sum of the single cell voltages and the total capacity in terms of Ah equals the capacity of one single cell:

$$U_{pack,ser} = \sum_n U_{cell,n} \tag{66}$$

$$C_{pack,ser} = C_{cell} \tag{67}$$

In case the cells voltage is sufficient but the battery capacity has to be increased, single cells are being connected in a parallel circuit. In this setup, the pack voltage equals the cell voltage and the capacity of the battery pack equals the sum of the single cell capacities:

$$C_{pack,par} = \sum_m C_{cell,m} \tag{68}$$

$$U_{pack,par} = U_{cell} \tag{69}$$

Combining serial and parallel circuiting, a system of batteries, or in short a battery pack, can be designed that has the desired voltage and capacity required for the relevant application. Figure 73 shows a principle layout of a battery pack.

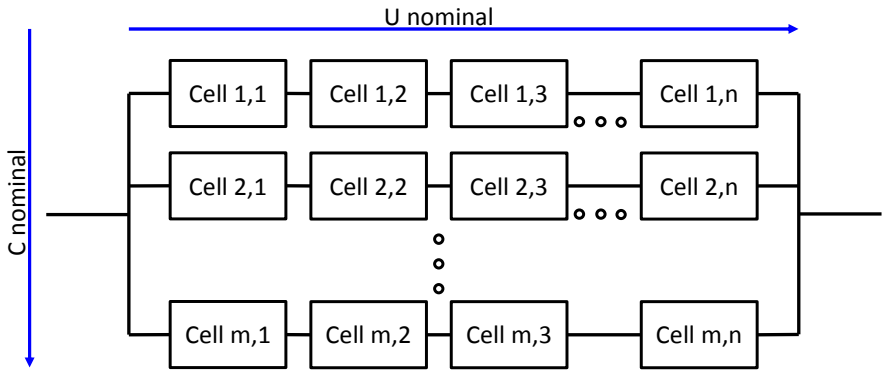

Figure 73, Generic battery pack layout

For battery applications in aircraft, CS 25 certification regulations ask for provisions to maintain the batteries within its operation envelope at any operational condition:

CS 25.1353 (c):
"Storage batteries must be designed and installed as follows: (1) Safe cell temperatures and pressures must be maintained during any probable charging or discharging condition. No uncontrolled increase in cell temperature may result when the battery is recharged (after previous complete discharge) – (i) At maximum regulated voltage or power; (ii) During a flight of maximum duration; and (iii) Under the most adverse cooling condition likely to occur in service."

In order to meet these requirements, the battery has to be monitored and controlled by a battery management system (BMS). This system assures that the cells are operated within their specifications during charging and discharging. Otherwise, operation beyond the cell's specification could result in damage to the cell ranging from reduced service lifetime to excessive heat production and fire hazard. Depending on the cell type and the required level of safety, the voltage, current, temperature, state of charge, and the state of health of each cell in the pack is monitored by a battery control unit (BCU). Furthermore, the BCUs ensure that the current load of all cells is balanced equally, in order to protect single cells from overload conditions and the associated damage. If any cell approaches and exceeds its operational limitations, the BCU is capable of disconnecting the respective cell or the whole pack from the electric grid to avoid further damage to the cell and its environment. Commonly, the architecture of large battery systems used in electric vehicles includes several independent battery groups, each controlled by a master BCU [12] [13]. Within this group, several slave BCUs monitor and control the cells in battery packs that are interconnected in serial and parallel circuiting, depending on the operating voltage and total capacity required. The measured cell values are collected and processed by the master BCUs which connect the groups to the electric power grid of the application. As a part of a whole propulsion system, a sophisticated BMS possesses a data link to communicate information concerning the state of the battery system externally. An exemplary schematic of a battery master/ slave BCU architecture is given in figure 74.

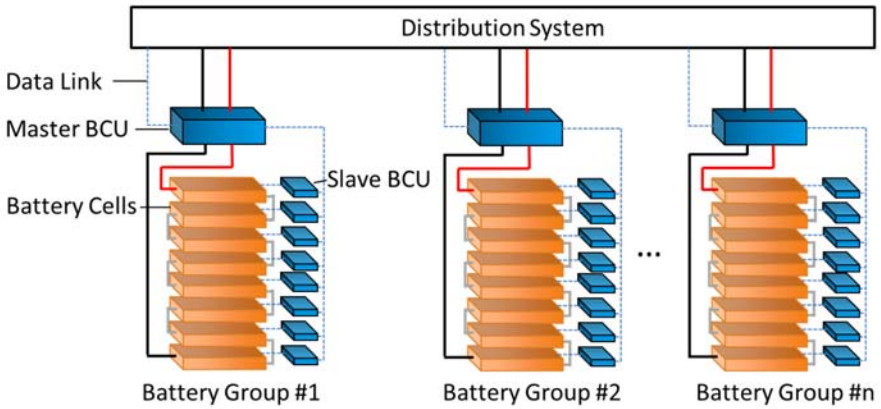

Figure 74, Schematics of a master/ slave BCU architecture

Due to its redundancy and the related safety advantages, this master-slave approach and the split-up into several battery groups is regarded as applicable to the battery system of the considered future electric transport aircraft. Each group accommodates at least a number of cells connected in serial circuiting to supply the required voltage level to the distribution system according to equation (66). Next to a pure serial circuiting also a set-up of serial and parallel connected cells is possible. However, each cell has to be monitored and eventually disconnected if it exceeds its permissible operating range. For safety reasons or if a pure serial set-up is used, also a disconnection of the complete affected battery group form the distribution system is indicated [13]. With one battery group inoperative, the decrease in available energy depends on the number of battery groups installed in the battery system:

$$E_{OBI} = \frac{n_{batt} - 1}{n_{batt}} E_{ABO} \tag{70}$$

And the available power accordingly:

$$P_{OBI} = \frac{n_{batt} - 1}{n_{batt}} P_{ABO} \tag{71}$$

As outlined in section 3.1.1, heat losses occur in a battery discharging process, which requires sufficient cooling capability to maintain the cell temperature within the specified limits. On the other side, temperatures below the batteries optimum temperature affect battery performance significantly, so the amount of cooling has to be controlled depending on the operating point and the corresponding heat losses.

If open battery concepts like Li-O2 systems are considered for energy storage, a high diffusion rate of ambient oxygen into the cell is necessary to sustain the cells redox reaction. Effective diffusion generally requires large diffusion areas, which in turn requires a decent distribution system for the oxygen throughout the entire battery. Since these characteristics also match the requirements of an effective cooling system, oxygen supply and cooling could be done using a single modified air cooling system. Modifications would include means to ensure that the air supplied for the reaction satisfies battery specific requirements e.g. in terms of humidity and air density.

Considering the total weight of the battery system, the additional weight due to control equipment (BMS) and structural components like bearings, separation walls, housing, etc. has to be accounted next to the cell weight itself. In battery pack designs for (hybrid-) electric cars, these components which are not cell-related make up for 40-60% of the total system weight [114] [115] [34]. Accordingly, the specific energy and specific power of the total battery system is reduced compared to the values of the single cell, as exemplary shown in figure 75.

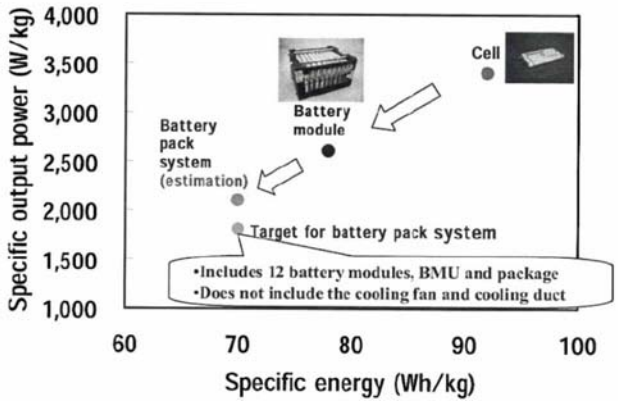

Figure 75, Exemplary cell weight vs. pack weight [34]

Though, since weight is a more critical design driver in aerospace than in automotive applications, a more lightweight battery pack design can be expected for aircraft use. As an example, the electric demonstrator aircraft e-Genius of the University of Stuttgart accommodates 5616 cylindrical Li-ion cells which account for a total of ca. 255 kg. The total integrated battery system weight including BMS results in 280 kg, which means a cell weight share of 91% [13]. This share could further be increased by using fewer cells. In case of the e-Genius, 18650-sized standard cells where used due to their relatively low cost and high availability. Using fewer but higher capacity cells instead, the monitoring effort, number of cell connectors, and required separation and insolation materials between the cells could be reduced, potentially leading to advantageous economy-of-scale effects in terms of system weight. However, in the frame of this study, a reference cell weight share of 88% excluding cooling weight is assumed, which is slightly below the demonstrated values for the e-Genius to account for potentially more demanding structural integration provisions and more complex monitoring requirements.

Fire protection

As outlined in section 3.1.1, the most promising battery technologies that potentially will meet the requirements for future electric air transport are lithium-based. The reason for this is the low specific weight of lithium metal on the one side, and its high electronegativity on the other side. However, lithium is an alkali metal and is highly reactive which makes it hazardous for fire. For that reason, a highly sophisticated battery management is mandatory to prevent an overcharging or thermal runaway by disconnecting the defective cell and applying maximum available cooling. Nevertheless, a potential battery fire has to be taken into account and the battery system has to be designed in order to sustain such an event without catastrophic consequences. Although the definition normally relates to gas turbine engine sections and fuel-burning heaters (see CS 25.1181), compartments inside the aircraft that contain lithium-based batteries are accordingly

rated as “fire zone”, which require special fire protection in order to meet certification specifications:

CS 25.1193 (e)
“Each aeroplane must – (1) Be designed and constructed so that no fire originating in any fire zone can enter, either through openings or by burning through external skin, any other zone or region where it would create additional hazards;”

Continuing:

CS 25.1195
“Except for combustor, turbine, and tail pipe sections of turbine engine installations that contain lines or components carrying flammable fluids or gases for which it is shown that a fire originating in these sections can be controlled, there must be a fire extinguisher system serving each designated fire zone.”

Handling each battery group as a separate fire zone brings significant safety advantages to the battery system: if a malfunction in one battery group causes a fire, this is being contained and prevented from spreading to other battery groups, ensuring that the loss of energy and overall power remains limited to the group affected. In order to achieve this containment, the battery groups have to be separated from each other and the aircraft structure by appropriate firewalls that sustain the effects of a battery fire including high temperatures. The firewall material should be highly heat-resistant and un-inflammable, typical candidates are oxide ceramics such as zirconium dioxide or aluminum oxide. These are very stable chemical compounds with melting points well beyond 2000°C and high thermal resistance [116]. Oxide ceramics can be manufactured as bulk material, foam or fiber mesh, further improving the heat resistance and the mechanical properties. An appropriate flue gas venting system should be foreseen to avoid an uncontrolled pressure increase.
Compared to fires onboard conventional aircraft that typically involve hydro-carbons (fuel, textiles, cargo, etc.), burning Lithium is relatively hard to extinguish due to its high reactivity. Even classic extinguishing agents like water, CO_2, or N_2 react exothermic and intensify the fire. According to [117], also Halon 1301 is not able to stop the fire but at least is “*effective in controlling the open flame and the spread of the fire to adjacent materials*”. Accordingly, each battery group should be equipped with a Halon extinguishing system.
Firewalls and provisions for fire extinguishing systems cause a certain weight penalty on the battery system. The exact amount of additional weight thereby depends on the specific firewall design, sustained temperatures in case of fire, battery form factor, etc. At this stage, no specific weight allocation is therefore being made, the fire protection weight is considered to be included in the battery pack weight and the cell share factor instead.

3.2.2. Distribution System

The amount of electric power to be distributed across the aircraft has been increased continuously in recent aircraft development programs as actuator functions and ECS systems are being electrified. As outlined in section 3.1.2, losses in electric power transmission are

proportional to the electric current, thus the classic architecture comprising a 28 V DC and a 115 V AC system has been complemented by higher voltage level busses carrying up to 235 V AC and 270 V DC [118] in order to achieve high system efficiency. Apparently, transmitting electrical power at the level of aircraft propulsion requires even higher voltage systems to keep losses and cable weights acceptable. On the other side, voltage levels exceeding today's established 270 V DC lead to handling safety issues and the risk of electric arcing. Furthermore, being an essential part of the propulsion system, the distribution system has to fulfill strict requirements regarding redundancy and fail-safe characteristics.
Transmission of electrical power in the propulsion order of magnitude is a challenging task, given the special operating conditions onboard aircraft and the demanding requirements concerning efficiency, weight and safety. Currently there is no CS-25 regulation that covers an electric distribution system for aircraft propulsion, though the fuel system in a conventional aircraft can be seen as an equivalent. For that, the CS 25 states:

CS 25.953 Fuel system independence
"Each fuel system must meet the requirements of CS 25.903(b) by (a) Allowing the supply of fuel to each engine through a system independent of each part of the system supplying fuel to any other engine; or (b) Any other acceptable method."

An independency requirement is also stated for electric systems:

CS 25.1351
"(b) Generating system. The generating system includes electrical power sources, main power busses, transmission cables, and associated control, regulation, and protective devices. It must be designed so that – (1) Power sources function properly when independent and when connected in combination; (2) No failure or malfunction of any power source can create a hazard or impair the ability of remaining sources to supply essential loads;"

These rules applied on an electric distribution system means the necessity of at least two independent power transmission lines (busses) for a standard configuration-, twin-motor aircraft. Switchable interconnections between these busses can further increase operational safety in case of a failure of one distribution bus by avoiding asymmetric thrust conditions.

Voltage type
In any battery powered powertrain architecture, both direct- and alternating current transmission appears: the battery delivers direct current, which is transformed into an alternating current by the motor controller/ inverter feeding the electric machine. In principle, the motor controller can be located close to the battery, distributing the multi-phase alternating current via the busses, or the controller can be installed close or within the motor, being supplied by a direct current bus connected to the battery system. Due to its inherent advantages, the common approach used in today's ground and air-based electric vehicles is a DC distribution system: In AC distribution, the conductors have to be designed to transmit reactive power on top of effective power, leading to larger cable cross sections and higher conductor weight [119]. Furthermore, DC lines are less critical with respect to EMC issues. However, switching of high power DC loads is more complex compared to AC due to the fact that no zero-voltage switching is possible in DC. In conclusion,

the advantages linked to DC distribution mentioned above are considered to outweigh the associated drawbacks, hence only a DC architecture is considered in the following.

Current characteristics

As outlined in section 3.1.1, battery cells are being considered as electric energy storage devices, providing a rated power in a certain voltage spectrum ranging from open circuit voltage to cut-off voltage. The resulting voltage ratio has been defined as ζ_{cell} in equation (12). Since a constant voltage requirement for the distribution system would cause the need for additional DC/DC converters, the voltage of the distribution system is directly determined by the battery voltage. The distribution system has to be capable of sustaining the maximum occurring (open circuit) voltage, as well as the maximum current appearing in case of transmission of the maximum rated power at cut-off voltage. If the maximum rated transmission voltage and power are known for a conductor line, the maximum current can be defined as a function of ζ_{cell}:

$$I_{max,cond} = \frac{P_{max,cond}}{\zeta_{cell}\, U_{max,cond}} \tag{72}$$

Fail-safe architecture

The distribution system of the electric powertrain is essential for the aircraft's airworthiness. Failing to transmit electric power from the storage system to the electric motors would cause an "all engines out" situation with potential catastrophic consequences. Hence, the distribution system has to be designed fail-safe to remain operational in case of a failure in any system component. This leads to the requirement of at least two redundant and independent power lines whereby each line must be capable of transmitting enough electric power for continued flight and a safe landing. Using the aircraft structure as a common return as done in past aircraft designs is ruled out since structural damages and discontinuities in the structure could lead to electric arcing and certification standards ask for a separation of power returns for critical electrical wiring interconnection systems (EWIS):

CS 25.1707 System Separation; EWIS

"(d) Each EWIS associated with independent aeroplane power sources or power sources connected in combination must be designed and installed to ensure adequate physical separation and electrical isolation so that a fault in any one aeroplane power source EWIS will not adversely affect any other independent power sources. In addition:
(1) Aeroplane independent electrical power sources must not share a common ground terminating location, and (2) Aeroplane system's static grounds must not share a common ground terminating location with any of the aeroplane independent electrical power sources"

Next to the independency of the power supply, certification regulations further require to limit the consequences of wiring faults by the use of circuit protective devices:

CS 25.1357 Circuit protective devices

"(a) Automatic protective devices must be used to minimise distress to the electrical system and hazard to the aeroplane in the event of wiring faults or serious malfunction of the system or connected equipment.(…)

(b) The protective and control devices in the generating system must be designed to deenergise and disconnect faulty power sources and power transmission equipment from their associated busses with sufficient rapidity to provide protection from hazardous overvoltage and other malfunctioning."

In figure 76, the application of the stated certification rules is shown exemplary for the Airbus A320 family aircraft electrical distribution system. All power sources (main engine generators GEN 1&2, APU GEN, emergency GEN, batteries and external power supply) are connected to the distribution system by contactors, so they can be safely disconnected in case of a failure or malfunction. The system is protected from wiring- or equipment faults by contactors und bus tie breakers. (C.f. section 3.2.4 for aircraft system architecture and supply)

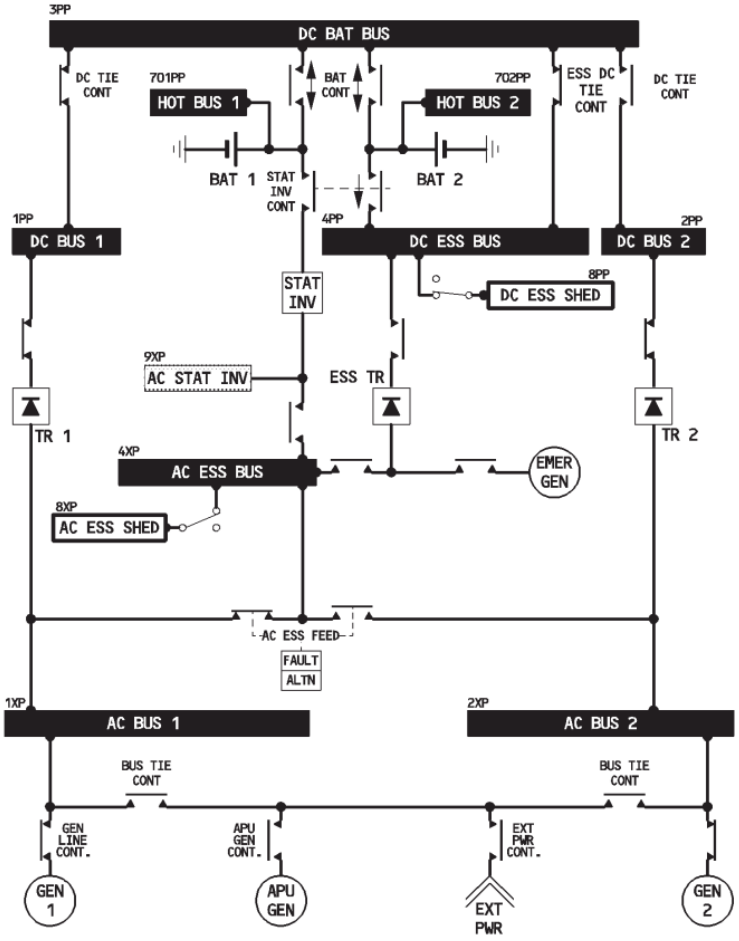

Figure 76, A320 electrical system layout [120]

A proposal of a distribution system architecture satisfying the requirements stated above is given in the figures below, exemplary incorporating four battery groups and two electric propulsion motors. In normal operation as given in figure 77, each half of the battery groups is connected to a high voltage (HV) DC bus dedicated to one motor/controller assembly. All switches between the two powertrains are disconnected, resulting in an independent operation of each powertrain.

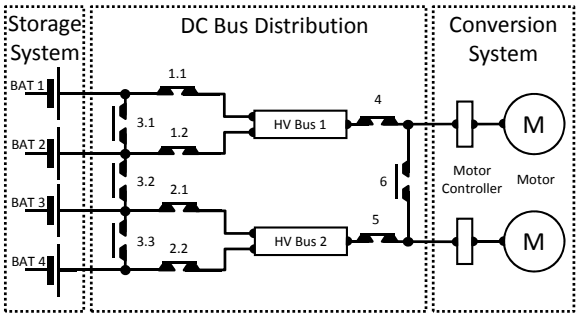

Figure 77, Distribution architecture, normal operation

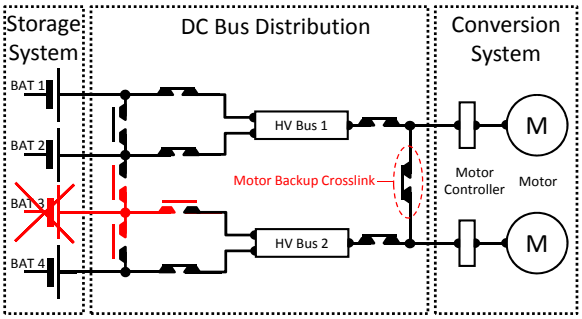

Figure 78, Distribution architecture, battery group failure

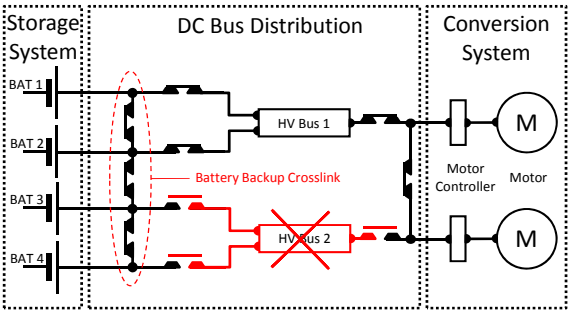

Figure 79, Distribution architecture, DC bus failure

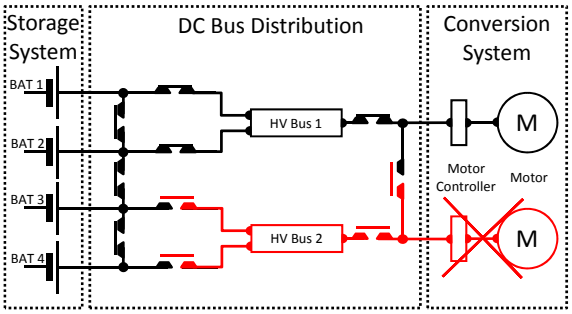

Figure 80, Distribution architecture, motor failure

In case of a battery group failure, the respective group is disconnected from its DC bus. Following that, a motor backup crosslink connection between the two motor/controller assemblies is closed to generate a parallel circuiting of the remaining battery groups. In this way it is ensured that the groups are being discharged equally and the same power level is supplied to all motors avoiding asymmetric thrust conditions. The “one battery out” distribution system layout is shown in figure 78.

The same approach is taken in case of a failing DC bus. Especially if the failure is caused by a short circuit, it is important to disconnect the affected bus entirely from the powered system to avoid further damage and overstressing of the batteries. The remaining charge in the battery groups associated to the failed bus is redirected via a battery backup crosslink and the motor backup crosslink, equally supplying power to the two electric motors. The “bus failure” switching status is shown in figure 79.

A failure in the controller/ motor assembly is isolated the same way as in case of a failed bus by a complete disconnection from the powered system. The remaining charge in the associated battery groups is redirected via the battery backup crosslink to the remaining operative electric motor. The associated switching layout is shown in figure 80.

While the fail-safe characteristics outlined above relate to a two-motor, four battery group design, the basic architecture can equally be applied to other powertrain configurations. For the battery/ bus interface, figure 81 shows the switching states for two and six battery groups, respectively.

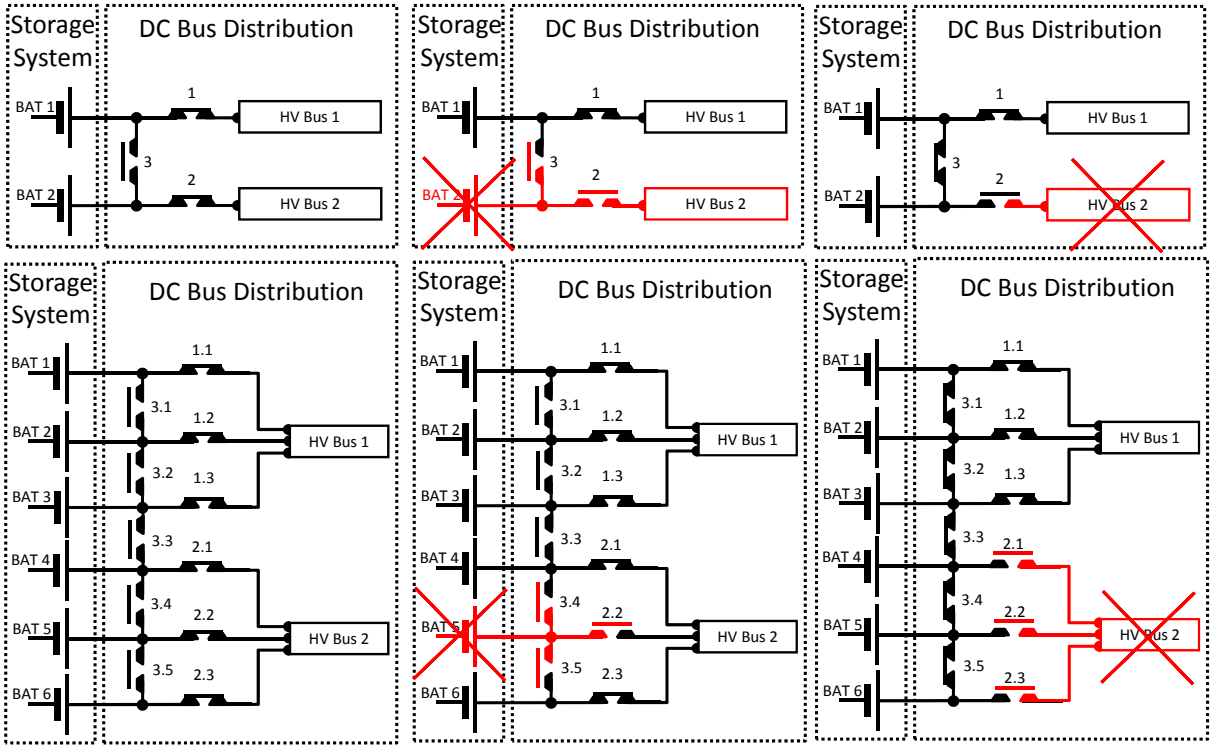

Figure 81, Battery/ distribution interfaces

In normal operation, each HV bus carries up to one half of the installed maximal motor power. If this is taken as the decisive load case and the HV bus is sized accordingly, the maximal available motor power is limited in case of a single bus failure: the remaining bus is then capable of delivering only one have of the nominal power, yet equally distributed to all propulsors with symmetrical thrust generation. The other option is to oversize the HV bus and the corresponding switching equipment for the double power rating so that the remaining bus can fully compensate the loss of the second bus and deliver the full battery power to the electric motors. In comparison to the previous solution, this setup improves system robustness, yet at the cost of increased conductor- and equipment weight.

For propulsion systems with two motors, a loss of one motor means a loss of half the normal available thrust and a drag increment due to an asymmetric thrust condition (cf. figure 80). This case is more critical compared to a HV bus failure. In the latter case, a uniform 50% power loss on both motors occurs, no extra trim drag appears due to thrust symmetry, and the propeller efficiency is increased by less disc loading. For two-motor systems, each HV bus is therefore sized to carry up to 50% of the total installed motor power only.

The same approach is followed for four-motor propulsion systems. The related HV busses are sized to carry up to 75% of the total installed motor power each. As in the two-motor setup, a HV bus failure is again less critical than a single motor failure (25% thrust loss) since the same symmetric thrust- and disc loading effects apply.

Current loadings of switches

Based on the presented distribution layouts and the considerations above, the nominal currents of each switch and each conductor can be determined relative to the current of a single HV bus.

The current of each battery line switch 1.x and 2.x connected to a bus is:

$$I_{1.x\&2.x} = \frac{I_{BUS}}{0.5\, n_{BAT}} \tag{73}$$

The crosslink between the two busses, controlled by switch 3 and 3.3 in figure 81, redirects power in case of a bus failure to the remaining available bus. Discharging all battery groups equally, the crosslink has to conduct half of the maximal HV bus current:

$$I_{cross,BAT} = 0.5\, I_{BUS} \tag{74}$$

In the case of six battery groups, the maximal currents on switches 3.1 to 3.5 are:

$$I_{3.2\&3.4} = \frac{2}{6}\, I_{BUS} \tag{75}$$

$$I_{3.1\&3.5} = \frac{1}{6}\, I_{BUS} \tag{76}$$

In the case of four battery groups, the maximal currents on switches 3.1 and 3.3 are:

$$I_{3.1\&3.3} = \frac{1}{4}\, I_{BUS} \tag{77}$$

Next to two propulsion motors, also a four-motor arrangement is considered in the distribution layout. The respective schematic is shown in figure 82. In this configuration, lines 4 and 5 carry the full current load of their associated HV busses:

$$I_{4\&5} = I_{BUS} \tag{78}$$

Analogue to the battery crosslink, the motor crosslink line (nr. 6) is sized to provide one half of the current delivered by the remaining bus in case of a bus failure, regardless of the number of motors used:

$$I_{cross,MOT} = 0.5\, I_{BUS} \tag{79}$$

Finally, in case of a four-motor configuration, lines 7.1 to 7.4 supply each motor up to its nominal current:

$$I_{7.1-7.4} = \frac{I_{BUS}}{0.5\, n_{MOT}} \tag{80}$$

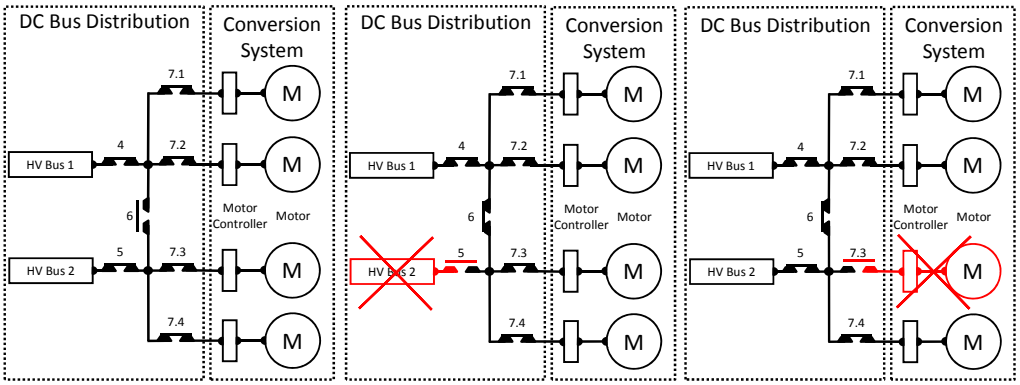

Figure 82, Four-motor interface to the HV busses

Voltage level

As discussed previously, there is an increasing demand for electric power onboard aircraft due to the replacement of hydraulic and pneumatic functions by electric systems. While trying to keep the electric current and hence the conductor cross sections low, the voltage level has been increased up to 230 V AC in recent development programs [118]. Further increasing the system voltage beyond this value, electric arcing becomes an issue and corresponding measures have to be taken.

The dielectric strength of gases can be determined using the Paschen's law. It describes the breakdown voltage in a homogeneous electric field depending on the gas pressure and the electrode spacing. Figure 83 shows the application of Paschen's law for dry air. Temperature and humidity variations as well as the electrode shape have a considerable effect on the breakdown voltage, but the general characteristics remain the same. It becomes apparent that, in laboratory conditions, no electric arcing occurs below an electrode voltage of 327 V regardless of distance or air pressure. In a sinusoidal AC voltage, this represents a RMS voltage of 231 V AC, which means that no arcing has to be expected in today's 230 V AC aircraft systems, as long as Paschen's standard conditions are considered [121]. Passing this voltage threshold in order to enable high power transmission for aircraft propulsion means that electric arcing trough air can occur in case of an isolation fault. Since a DC distribution system is considered, an arc discharge is not being interrupted by a zero voltage crossing. Consequently, a plasma arc would persist continuously, potentially causing damage to the conductor as well as the surrounding structure and equipment until the power supply is actively interrupted. Hence, next to decent and redundant cable isolation design, the distribution system has to be equipped with effective and reliable fault protection capabilities.

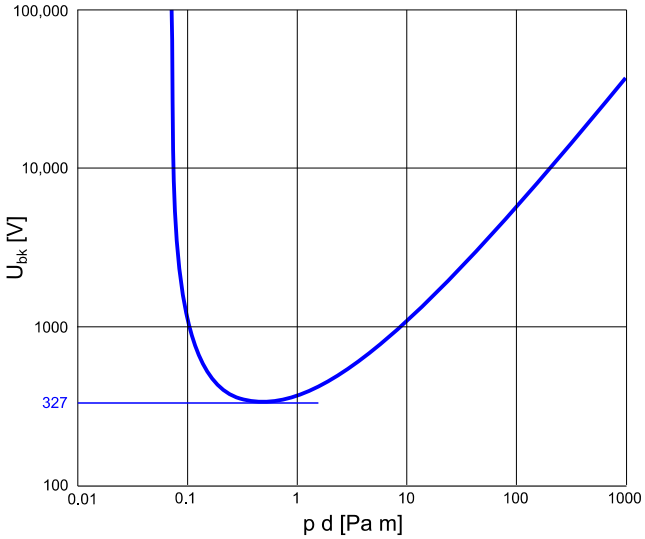

Figure 83, Paschen's law for dry air, based on [121]

Fault detection

The initial requirement for active fault protection is fault detection. Following that, the faulty lines can be disconnected from the power source by an automatized monitoring system, preventing further damage. Principally, there are three potential major conductor malfunctions:

Damage to the conductor material, exemplary caused by vibration, heat or production issues, can lead to a loss of cable conductivity. Without further knowledge regarding the cause of the conductor malfunction, the respective line has to be shut down. In this case the power can be redirected as outlined above.

The second and more severe failure would be short circuiting between the positive and negative conductor, potentially including electric arcing. In this situation, instant action is mandatory since the occurring currents as well as the thermal energy induced by the plasma arc can cause significant damage to the aircraft. Reliable detection also of small fault currents can effectively be done by measuring the current close to the source (battery) and the load (e.g. motor controller) on each single conductor. If a fault current occurs on the power line between the ampere meters, a current differential is measured triggering the disconnection of the respective lines from the distribution system. A schematic of the inter-conductor fault detecting layout is shown in figure 84.

Another potential failure scenario is a short circuit between a conductor and the aircraft structure, exemplary caused by cable abrasion. A common method to detect this is shown in figure 85. For this, the electric potential of the aircraft structure is aligned to the middle potential of the battery group by a high-ohmic connection. This way, the potential difference (voltage) between the structure and the conductors is reduced to half the system voltage which is already a safety advantage taken by itself. For fault detection, the voltage of the positive- and the negative conductor to the aircraft structure is being monitored. In normal operation, the absolute values of both voltages are equal. In case of a shortcut between a conductor and the structure, the voltage differential measured between the intact and the short-circuiting conductor to the structure identifies the failure. Since the fault current is limited by the high-ohmic connection between the structure and the battery, no immediate safety threat is given. Nevertheless, the

affected power line is being disconnected from the distribution system since the power can be redirected as outline above.
Electric current measurement can be done using hall probes; voltage measurement is done by appropriate measurement equipment (voltage dividers). The weight of the measuring equipment including probes (around 500g for a 2 kA hall probe [122]), signal cables and signal processing equipment is being considered to be included within the electric system weight group (c.f. section 4.3.2).

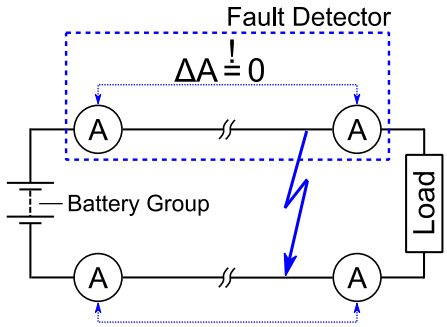

Figure 84, Inter-conductor fault detection

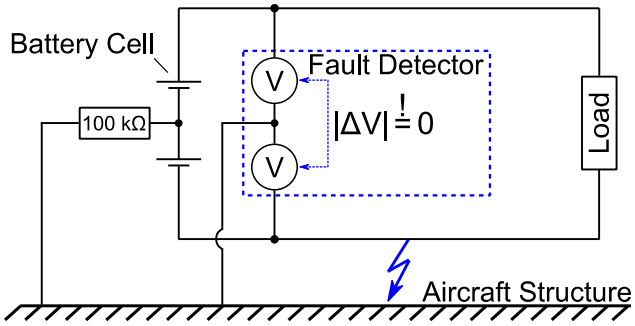

Figure 85, Conductor/ structure fault detection

High power DC switching

When a fault is detected in in the electric powertrain, the affected component has to be isolated from any power source. Therefore necessary switches have to be designed to disconnect high voltage/ high current DC loads in an unfavorable environment regarding electric arcing. High power AC loads are conventionally being switched using vacuum switching technology (see section 3.1.3). However, this switching method is inapplicable to DC currents, since there is no voltage zero-crossing that would extinguish the arc. DC-operated vacuum switches hence are limited so significantly lower voltage ratings compared to switching AC loads. A solution to this is the semiconductor switching technology. Yet, while solving the arcing problem, semiconductor switches suffer from losses due to a characteristic forward voltage drop. Next to efficiency penalties and additional required battery capacity, the loss energy is transformed into heat that has to be dissipated by an appropriate cooling system. Furthermore, semiconductors do not provide galvanic separation even in the “open” switching state, so an additional mechanic disconnector upstream or downstream of the semiconductor switch is necessary to achieve complete separation. The switching procedure considered here is to interrupt the current with the semiconductor first, and then to open the disconnector in the zero-load state. Hence, issues related to high power DC switching as described above are being avoided. This switching assembly is shown in figure 86. Due to their compactness and air-density independence, vacuum switches as covered in section 3.1.3 are being used as disconnectors.
A possibility to avoid losses related to semiconductors is to use mechanic and semiconductor switches in parallel. The related circuit layout is given in figure 87. In the closed state, both the semiconductor and the mechanic switch are conductive, yet the mechanic connection has considerably lower resistance. As a result, the total switch resistance is reduced according to eq. (81), even below the value of the mechanic switch.

$$R_{tot} = \frac{1}{\frac{1}{R_{SC}} + \frac{1}{R_{mech}}} \tag{81}$$

Interrupting the connection is done by first opening the mechanic switch. In this moment, the total DC current is lead via the solid state switch, so the voltage drop at the mechanic switch equals the voltage drop of the semiconductor. Since this is typically in the order of only a few Volts, no electric arcing occurs. After mechanic separation is completed, the solid state switch disconnects, the zero-load disconnector opens and the switching sequence is completed. Semiconductor switches such as MOSFETs or IGBTs are commonly combined with microcontroller units to form a solid state power controller (SSPC), which are able to detect short circuits and communicate with a data bus for external control.

As shown in the figures below, switches are used on both the plus- and the minus cable while already one switch would be sufficient for current interruption. The reason for this is an approach to be fail-safe by redundancy. Semiconductors have unpredictable conductivity characteristics after thermal damage, e.g. due to overloading. They can either become isolating, high-ohmic, or low-ohmic while the low-ohmic state is considered as the most critical. If this occurs to one semiconductor switch, the second one is still available for safe power interruption and subsequent disconnection by the mechanic disconnectors.

A further issue especially regarding today's common IGBT switches is their limited reverse blocking capability. In some distribution system setups, for example if a bus suffers a shortcut and is being disconnected according to figure 79, the switches have to sustain reverse currents fed by the motor crosslink downstream of the HV busses. Using reverse blocking diodes serially connected to the IGBTs would accomplish this task, though at the cost further forward voltage losses. These losses could be avoided using recently developed IGBTs with internal reverse blocking capability but without a significant increase in forward voltage [123].

If controlled reverse flow is required, e.g. for propeller wind-milling energy recovery, a switching setup like in the crosslink connector switches can be applied. Since they have to allow current in both directions, depending on which HV bus fails, two reverse blocking IGBTs switches are being used per line as shown in figure 88. Galvanic separation is again secured by mechanic disconnectors.

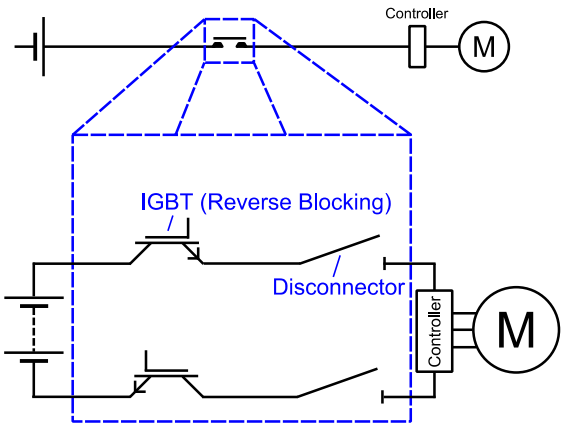

Figure 86, Solid state relay switching assembly

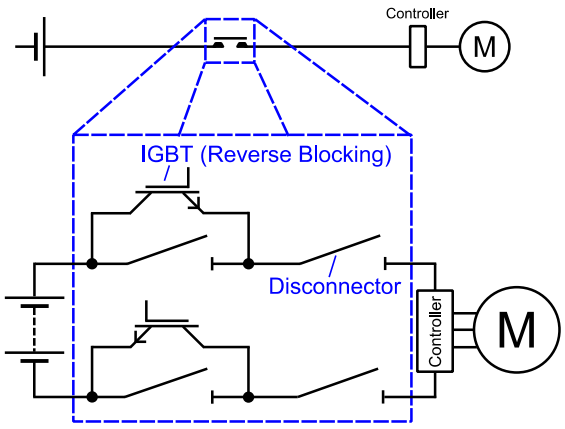

Figure 87, Parallel switching assembly

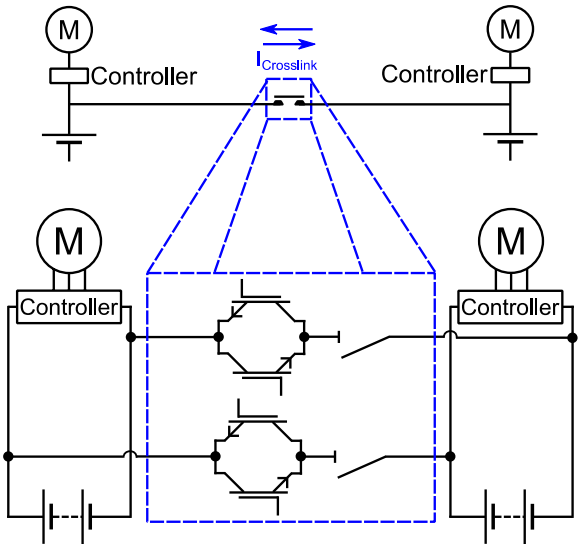

Figure 88, Bi-directional current switching assembly

Conductor inductivity

The forward- and the return lead of the distribution busses generate a magnetic field which stores energy proportional to their electric current. In case of a sudden change in current, e.g. due to emergency shut-down of a failed HV bus, the magnetic field induces a voltage in the conductors potentially leading to damage due to overvoltage. The voltage induced is described by:

$$U_{ind} = L \frac{\partial I}{\partial t} \tag{82}$$

The inductance L is depending on the conductor setup, an approximation for parallel conductors is given in equation (83), with s as the distance between the conductor center lines and r_{cond} the conductor radius [119].

$$\frac{\partial}{\partial x} L_{||}[\mathrm{mH/km}] = 0.4\ (ln \frac{s[mm]}{r_{cond}[mm]} + 0.25) \tag{83}$$

Depending on the conductor geometry, the occurring currents and reasonable shut-down times, induced inductive voltages must not lead to overvoltage threats, otherwise protective provisions have to be considered.

3.2.3. Cooling System

System components that generate loss heat during operation like switches, batteries, power electronics, etc. have to be cooled continuously to prevent the equipment from overheating. A failure of the cooling system hence would lead to the necessity to shut down the affected component in short time. As a consequence, the cooling system has to meet the same fail-safe and redundancy requirements as the electric powertrain itself.

Since batteries generate loss heat due to their internal resistance, continuous cooling has to be provided during discharge. Satisfying fail-safe requirements, each battery group, being

separated from the other groups by firewalls and thermal isolation, should be equipped with its own cooling provisions.
Using conventional conducting materials in the distribution system, the conductor cross sections are sized to generate loss heat at an amount that is dissipated to the environment with passive conduction (cf. section 3.1.2). Hence no extra cooling system is being provided for the power distribution. Superconducting transmission lines on the other hand require a cryogenic cooling system to keep the conductor material below its critical temperature. Consequently, each superconducting line should have its own cryo-cooling system, since in this case redundancy is already given by the use of two independent transmission lines. The same applies to the motors and their controllers, no matter if operated cryogenic or conventional: each motor has to be equipped with its own and independent cooling system. The resulting cooling system layout is given in figure 89.

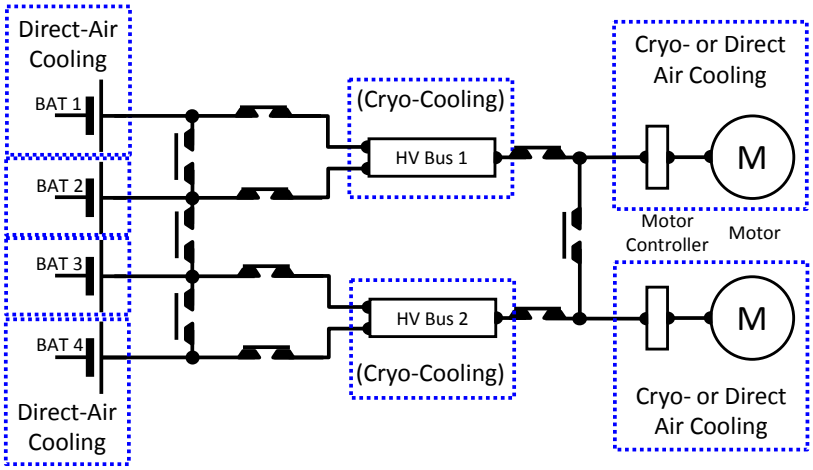

Figure 89, The cooling system

The cooling efficiency depends on the temperature delta between the hot component and the heat sink, which is the ambient air in case of aircraft cooling systems. CS 25 regulations ask for sufficient cooling capabilities up to a maximum ambient temperature, which will be taken as the design case:

CS 25.1043 Cooling tests
"(b) Maximum ambient atmospheric temperature. A maximum ambient atmospheric temperature corresponding to sea level conditions of at least 37.8ºC (100ºF) must be established."

3.2.4. Aircraft System Architecture

In conventional aircraft system architectures, power generation is done by engine-driven electric generators and hydraulic pumps connected to the accessory gearbox. For the electric propulsion aircraft, an "all electric" system layout is considered. In recent aircraft programs like the B787, "more electric" architectures are already being used, eliminating the pneumatic system and powering the hydraulic pumps partially electric. The associated electric system layout is shown in figure 90. Engine- and APU mounted generators power a 230 V AC distribution bus which supplies high power loads like wing ice protection. Further +/- 270/ 115 and 28 V DC busses are

connected via transformer rectifier units (TRU's) to this bus, supplying other lower power consumers.

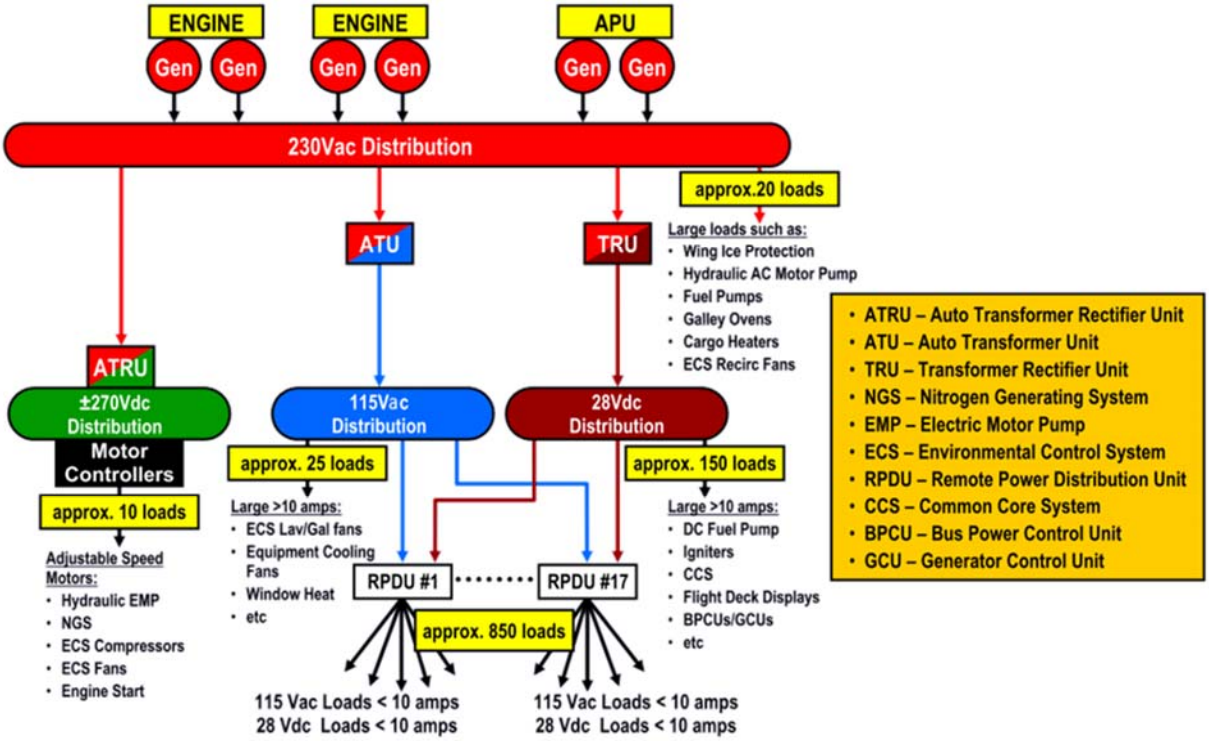

Figure 90, B787 electric system [118]

Especially "all electric" aircraft systems include electric components that are essential for controllability and safe operation of the aircraft like for example control surface actuators. Thus special requirements are being defined by CS 25 regulations regarding the power supply to these "essential loads". First, operability must be ensured after a single component failure:

CS 25.1310 Power source capacity and distribution
"(a) Each installation whose functioning is required for type certification or by operating rules and that requires a power supply is an "essential load" on the power supply. The power sources and the system must be able to supply the following power loads in probable operating combinations and for probable durations (…):
(2) Essential loads, after failure of any one prime mover, power converter, or energy storage device.
(4) Essential loads for which an alternate source of power is required, after any failure or malfunction in any onepower supply system, distribution system, or other utilisation system."

Next to the fail-safe nature of the normal power supply, there has to be an independent and separated backup system:
AMC 25.1351(d) Operation without Normal Electrical Power
"1 Provision should be made to ensure adequate electrical supplies to those services, which are necessary to complete the flight and make a safe landing in the event of a failure of all normal

generated electrical power. All components and wiring of the alternate supplies should be physically and electrically segregated from the normal system and be such that no single failure, including the effects of fire, the cutting of a cable bundle, the loss of a junction box or control panel, will affect both normal and alternate supplies.“ (see also CS 25.1351 (d))

These two major requirements, fail-safe normal power distribution and a backup system, are being considered in the proposed system architecture of the electric propulsion aircraft. As illustrated in figure 91, the normal power supply to the essential loads is ensured by the two redundant “green” and “yellow” DC essential (ESS) busses which are fed by the HV propulsion busses via DC/DC converters. The voltage level of the essential busses is set to +-270 V DC as common in modern electric distribution systems. Fulfilling the requirements of CS 25.1310 (a) (2) und (4), a single failure of any converter, connector or distribution bus can be tolerated since all essential loads including control surface actuation are being supplied by both ESS busses.
In case of a total loss of normal power supply, exemplary due to complete inflight discharge of the propulsion batteries, an emergency battery powered emergency bus provides power to essential loads required for a controlled descend and forced landing to comply with AMC 25.1351(d).
Commercial transport aircraft today commonly are equipped with a ram air turbine that is deployed if the normal power supply by the engines fails. In an electric propulsion aircraft using propellers for thrust generation, the propeller-motor assembly could be used equally, working as a ram air turbine feeding emergency power to the electric systems. While possible in principle, this requires closer examination of the propeller aerodynamics and blade angle control as well as motor controller functionality on component level and is hence not considered further in the frame of this study.
Loads that are non-essential for flight worthiness like galley and inflight entertainment are fed by a non-ESS bus that can be shut down in case of abnormal and emergency situations if necessary.

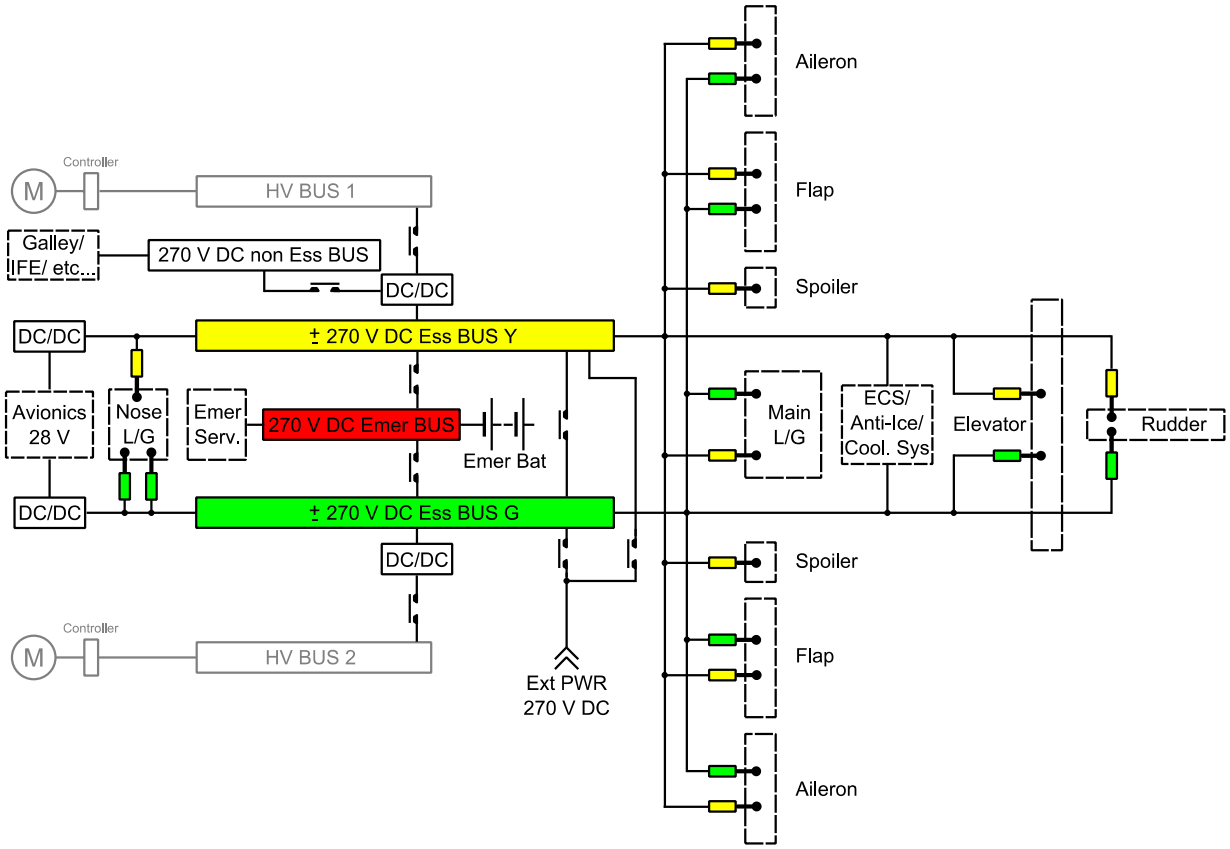

Figure 91, Aircraft systems layout

If the emergency power delivered to the system is time-limited as in case of an emergency battery, AMC 25.1351(d) 6.1 states that this power source *“should have an endurance of at least 60 (…) minutes.”* Thereby, it is stated that 72% of the nominal rated capacity at 20°C may therefore be assumed.

Emergency services

Following CS 25.1362, *"A suitable supply must be provided to those services, which are required, in order that emergency procedures may be carried out, after an emergency landing or ditching."* This relates mainly to the emergency lighting, which has to be supplied independently to the main lighting systems (CS 25.812 (a)), providing illumination for at least 10 minutes (CS 25.812 (h)(i)) and which has to maintain sufficient illumination even in case of “*any single transverse vertical separation of the fuselage during crash landing*”. A suitable solution to this are small distributed batteries integrated in the emergency lighting system which uses energy efficient LED’s.

3.3. Weight Trends and Sensitivities of the Electric Powertrain

In the previous chapters, different technologies and architecture variants have been proposed for the electric propulsion system. Using parameter studies and sensitivity analyses, these design options are being evaluated and discussed in the following. In this regard, a reference propulsion system arrangement is being defined as shown in figure 92. If not stated otherwise,

this this arrangement is used as the basis for the technology comparisons and sensitivity considerations. This reference propulsion system comprises four disconnectable battery groups, two main HV busses, two disconnectable electric motors including motor controllers, and crosslink connections at the battery side as well as the motor side.

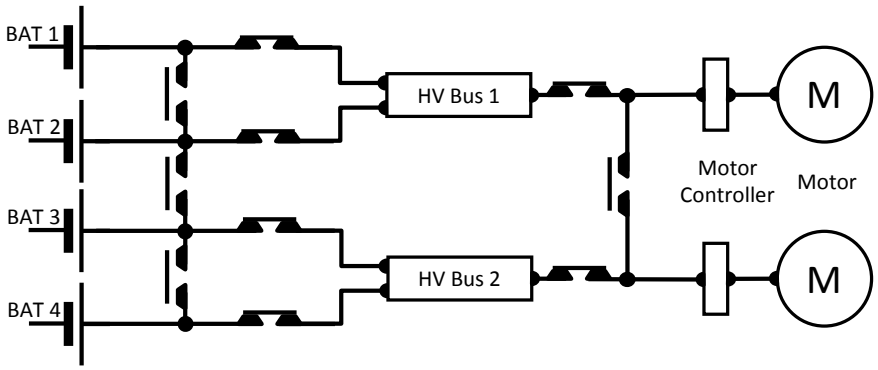

Figure 92, Reference propulsion system arrangement

3.3.1. Conventional vs. Superconducting Power Transmission

In section 3.1.2, superconducting cables have been described for energy distribution across the propulsion system. As mentioned, these cables require cryogenic cooling and sophisticated thermal isolation to keep thermal losses below an acceptable level. The cable weight is mainly driven by the isolation and the conductor material itself makes up only for a small fraction of materials used, so the specific cable weight is considered to be independent from applied voltage and current at 5 kg/m. In figure 93, this value is compared with the specific weight of a single conventional cable for a range of voltage and current ratings, calculated using the models defined in section 3.1.2. Apparently, superconducting cables outperform conventional ones only in low voltage and high current applications, although additional weight for cryogenic cooling equipment is still neglected in this comparison. As shown in sections 3.2.2 and 3.2.4, there are several connections to and between the distribution busses, and to mainly non-superconducting consumers. Every connection has to be terminated at the superconducting side, resulting in additional weight and thermal losses into the cryostat. Additionally, low voltage distribution at high current negatively affects the performance of the semiconductor-based motor controllers and solid state switches. As outlined in section 3.1.3, a specific forward voltage drop of a few Volts occurs in the semiconductor technology considered. At high voltage and small current, the related losses (product of voltage drop and current) remain within an acceptable range (cf. sequent section) but grow accordingly when applying high currents. These high losses in turn lead to extensive cooling requirements and hence to heavy and bulky switching equipment. For the stated reasons, superconducting power distribution is ruled out in the frame of this study.

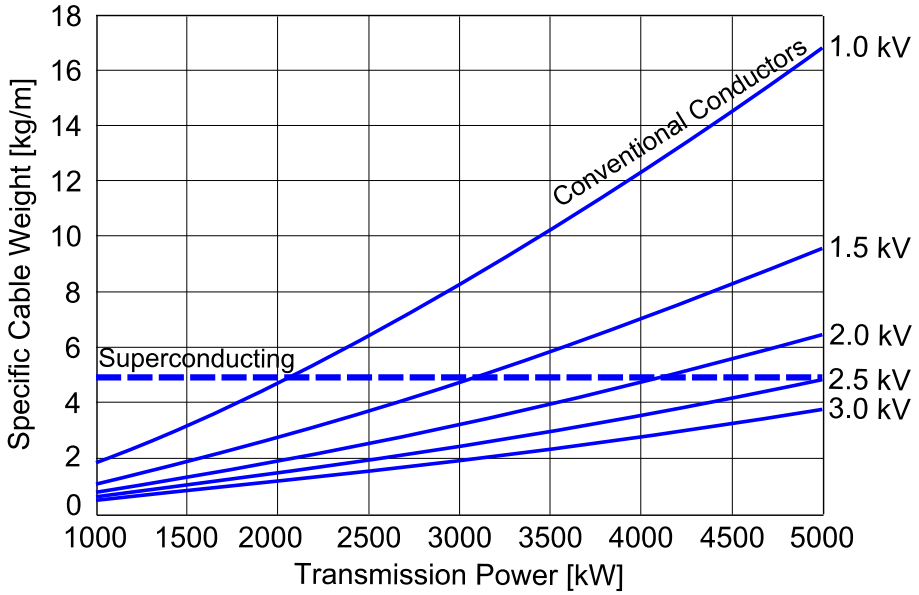

Figure 93, Comparison of superconducting & conventional specific cable weights

3.3.2. Direct vs. Bypass Switching

In section 3.2.2, two different switching assemblies have been proposed: one comprising a semiconductor switch and a zero-power disconnector for galvanic separation, the other using the same components but with an additional mechanic switch bypassing the semiconductor for increased efficiency. While the latter solution is more efficient and hence safes battery weight, these weight savings have to be compared with the weight of the additional switches to evaluate their overall benefit.

The additional battery weight due to semiconductor switching losses depends mainly on the timespan of operation and the electric current in the transmission system. The average current is thereby a function of transmitted power and average bus voltage. For a given range of power and average bus voltage, this additional battery weight is compared to the additional hardware weight related to the bypass switching approach in figure 94.

Based on a distribution layout of four battery packs and two propulsion motors (see figure 77), the distribution weight difference using bypass switching versus semiconductor switching is displayed on the x-axis. With these additional switches, the losses are reduced which corresponds to a certain battery weight saving per operation time. Based on an assumed 1000 Wh/kg battery, these weight savings are displayed on the y-axis per hour of operation. As an example, a distribution system delivering 2000 kW per motor at 4000V bus voltage is gaining around 5 kg additional weight due to bypass switching, on the other hand saves 10 kg of battery weight per hour. This means that a weight break-even is reached after half an hour of operation. In figure 94, lines of constant break even times are shown in dashed lines.

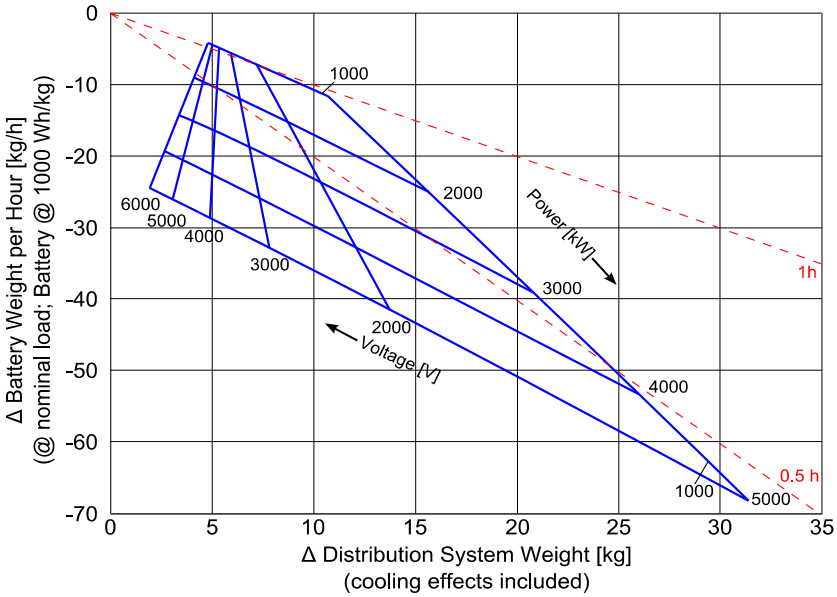

Figure 94, Comparison of switching layouts

For the mentioned conditions, it can be seen in figure 94 that for almost all considered power and voltage design ratings, break-even is reached within one hour of operation. Using batteries with higher specific energy would lead to a longer break-even time, batteries with lower specific energy vice versa. Given that the typical mission time of the considered aircraft class is generally at or above one hour and the weight impact is relatively small, only bypass switching is used for further modeling.

With the conductor and switching technology defined, the weight and the efficiency of the whole distribution system can be calculated. The result is shown in figure 95, again representing a four-battery group/ two-motor arrangement. Power levels refer to the design power on one HV bus, the voltage represents the average bus voltage.

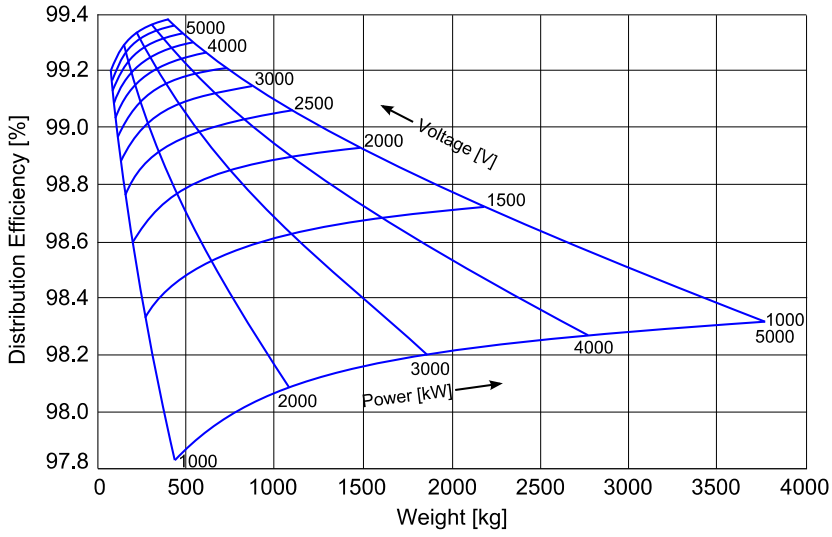

Figure 95, Distribution system weight and efficiency

3.3.3. Sensitivity vs. Component Performance

On the basis of the findings up to this point, the whole electric powertrain from the battery cell to the propeller can be modeled. Since the scope of this thesis lies on future electric powered aircraft, the weight and performance assumptions of most system components are based on predictions published in the literature. As each prediction implies a certain level of uncertainty, the weight and performance of the electric powertrain is assessed regarding the impact of variations of component characteristics. For this sensitivity analysis a reference design point is defined, and the impact of a variation of a single parameter is evaluated while all other parameters remain constant. The reference point is chosen to match typical power and energy characteristics of a conventional regional aircraft propulsion system. For this purpose, a Pratt&Whitney PW127 engine as installed in an ATR 72 regional turboprop aircraft is considered. The PW127f is rated at 2750 equivalent shaft horsepower (2050 kW). In [124], a total fuel consumption of 605 kg is stated for a typical one hour, 380 km mission, which translates into around 1650 kWh on the propeller shafts using average SFC values which are also given in cited reference. For these power and energy definitions, the weight of an electric powertrain including battery, distribution system, inverter, motor, and cooling is being determined using the methods and architectures as discussed above. In figure 96, a breakdown of the resulting 3170 kg total weight shows the dominating share of the battery system among the other system components. Another noteworthy result is the fact that the cryogenic cooling systems outweigh the systems they are cooling.

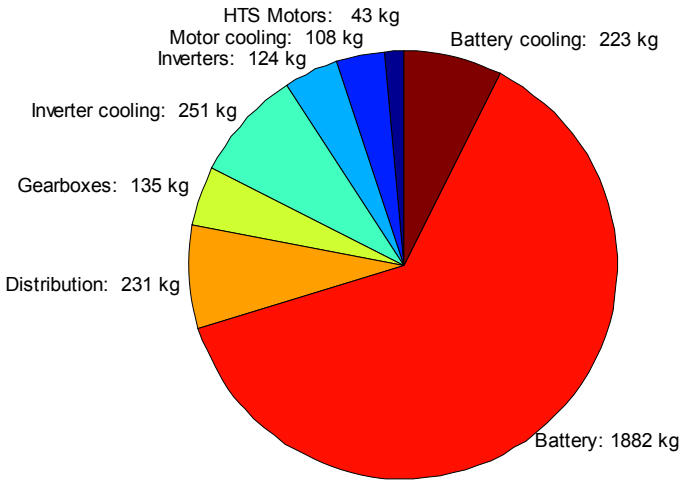

Figure 96, Propulsion system weight breakdown

In the following sensitivity study, a characteristic figure of a system component is varied while all other components are kept at their reference value. The impact of the variation is evaluated regarding the total system weight. The parameters used and their range of variation is given in table 8:

	Reference value	Min. variation value	Max. variation value
Battery specific energy [Wh/kg]	1000	500	2000
Cell share	0.88	0.6	0.95
No. of battery groups	4	2	8
No. of propulsion motors	2	2	4
Gearbox factor	1	0.8	1.2
Equipment cooling factor	1	0.8	1.2
IGBT weight factor	1	0.8	1.2
Switch weight factor	1	0.8	1.2
Cable weight factor	1	0.8	1.2
Inverter weight factor	1	0.8	1.2
Cryo-cooler weight factor	1	0.8	1.2
Cryo-cooler efficiency	0.3	0.24	0.36
Motor weight factor	1	0.8	1.2
Motor efficiency	0.9995	0.9994	0.9996
HV bus Voltage [V]	4000	3000	5000

Table 8, Parameter variations for sensitivity analysis

For better visualization, the results of the sensitivity study are divided into two groups: results for components with high impact are shown in figure 97, results for components with low impact in figure 98. Unsurprisingly, the battery system storing the propulsion energy shows by far the highest impact on total propulsion system weight. The specific energy considered ranges from 500 to 2000 Wh/kg. Compared to the reference case using 1000 Wh/kg cells, the impact on the propulsion system weight results in a 60% increase for the lower technology assumption and a 30% decrease for the high end assumption. In the same way, also the cell share (of total battery system weight, see section 3.2.1) shows strong weight sensitivity. The weight increase with four propulsion motors relative to two motors results from a more complex distribution system and the economy-of-scale characteristics of HTS motors.

The other considered parameters have only limited impact on the total propulsion weight. Within the typical range of variation (+/- 20%) the maximum weight variation in the entire propulsion system remains below +/- 4%.

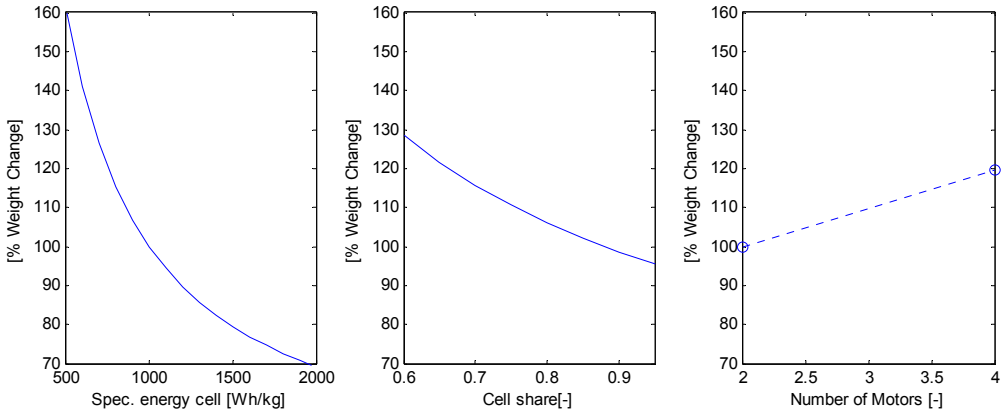

Figure 97, High impact parameters

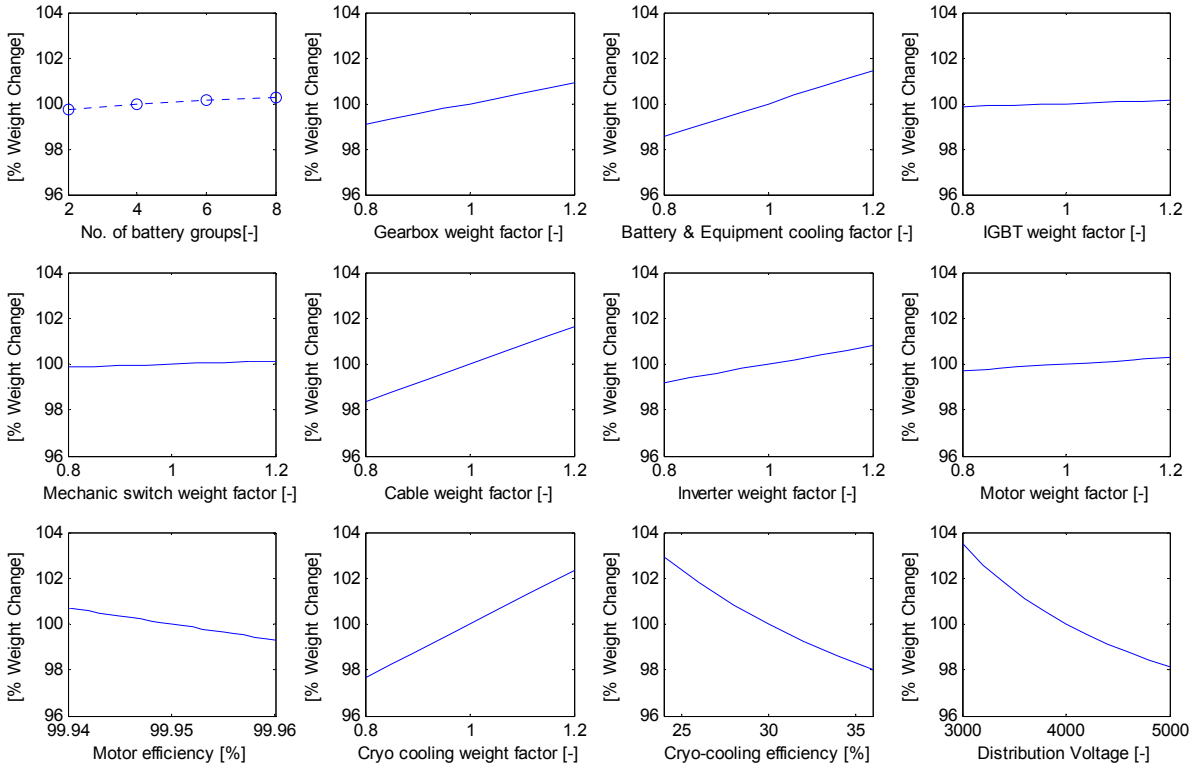

Figure 98, Low impact parameters

Although the propulsion system weight increases when using four propulsion motors instead of two, the result might be different on aircraft level. Failure characteristics, propeller disc loadings, and aerodynamic effects are affected by the number of propulsion units, so the best suited number of motors has to be determined within the aircraft preliminary design process. The battery weight, being the other parameter with high impact on the overall propulsion system weight, will be an open parameter in the aircraft sizing considerations in the following. All other parameters which have relatively low impact on the propulsion system weight will be modeled using the methods and reference values defined in the previous sections.

4. Design Methodology for Electric Propulsion Aircraft

The following chapter covers the methods and the modeling approach used for preliminary aircraft sizing. Implications of electric propulsion systems in aircraft design are outlined, and the aircraft sizing and optimization approach is being presented. Existing methods as published in the standard literature for weight estimation, aerodynamic assessment, as well as flight mechanics- and performance modeling are being adapted to the specific characteristics of an electric propulsion system if necessary. Finally, a sizing model validation and calibration is done based on a re-design exercise of in-service reference aircraft.

4.1. Implications of Electric Propulsion Systems in Aircraft Design

Compared to the preliminary design of conventional aircraft, the introduction of an electric propulsion system leads to necessary adaptions in weight accounting conventions, requires new aircraft system components, and necessitates an investigation of possible battery integration approaches.

Adaptions in aircraft systems

Conventional aircraft in the considered aircraft class are typically powered by turbo-prop engines. Since mechanic and pneumatic power can be extracted from these engines using accessory gearboxes and compressor bleed air, various aircraft system functions are being powered based on these two forms of power. In electric propulsion aircraft however, these components have to be replaced by electrically powered devices. The removed and the added systems and components are:

Removed systems:

- Combustion engines
- Accessory gearboxes and drives
- Oil & fuel system
- Conventional air conditioning system
- Surface controls
- Hydraulic system
- Pneumatic system

Added systems:

- Electric motors and controllers
- Electric transmission system
- Electric air conditioning
- Electric actuators
- El. Wing anti-ice
- Component cooling system

Adaptions in weight accounting

The battery weight gain during discharge as defined in section 3.1.1.2 leads to necessary adaptions in the aircraft sizing process because the maximum aircraft weight occurs at the very end of the design mission. The **maximum landing weight** thus becomes the critical parameter for most aircraft weight-related modeling methods regarding performance and weight estimation instead of the maximum take-off weight. Though, this does not apply for the performance evaluation of the take-off field length and the initial climb-out segment since the battery is charged in this segment and no or only little oxygen has accumulated in the battery yet. For that reason, a minimum state of charge for the batteries is defined for the **maximum take-off weight**. In the frame of this study, this is set to 80% SOC and hence 20% accumulated reaction oxygen. The mentioned take-off related performance conditions are being evaluated for this

battery condition. In the design mission however, the batteries are assumed to be fully charged for take-off and thus in their lowest weight status. This fully charged weight is defined as **nominal take-off weight**. Figure 99 gives an overview regarding the different weight classifications as described.
Obviously, this kind of weight accounting scheme and the circumstance that the maximum landing weight exceeds the maximum take-off weight is not being covered by today's regulations and certification standards. Respective adaptions and extensions of these standards have to be made in case an actual certification process is being initiated.

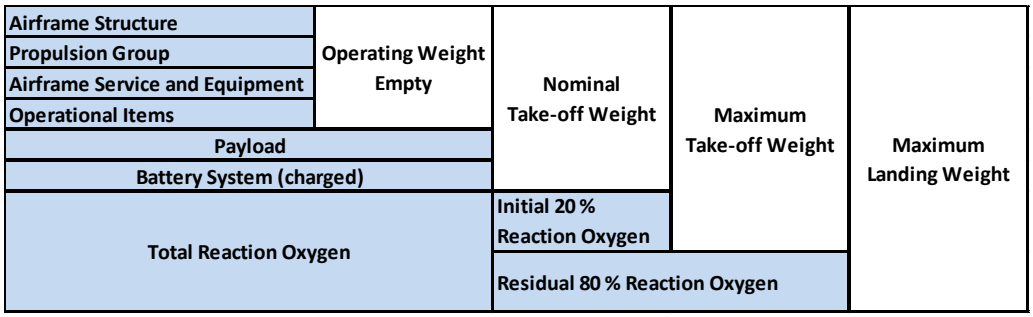

Figure 99, Weight accounting scheme

Battery system integration

Compared to the volumetric energy density of kerosene (roughly 9160 Wh/l), the considered battery technology as defined in section 3.1.1 provides significantly lower values that are in the range of 475 to 2000 Wh/l. Even assuming a system efficiency of 100% for electric propulsion and 30% for the kerosene based system, a volumetric disadvantage of batteries remains. As a consequence, more volume has to be allocated for battery integration than for fuel tanks of comparable conventional aircraft. Furthermore, the integration should allow for a quick and easy battery exchange on the ground between flights, since turn-around times have a strong impact on operating costs and aircraft utilization. Given that the batteries are capable of a fast recharging process that can be done within standard turn-around times, the batteries might also be fully integrated into the aircraft structure without a mechanism for quick exchange. However, the maximum charging power should not exceed the maximum installed motor power since otherwise the charging current would be design-critical for the distribution system and the battery switches, leading to potential oversizing and associated weight penalties.
Battery integration within the wing like the standard approach in case of conventional fuels implies the same structural benefits: battery weight distributed across the wing span reliefs the wing root bending moment and hence enables a weight-efficient wing structure. At the same time, electrical power transmission lines can be designed short and hence light-weight due to the close proximity to the electric motors. If batteries with fast recharging capabilities are available, integration in the wing should be considered. If it is necessary to exchange the discharged batteries during turn-around, the integrity of the wing box should not be impacted since the main mechanic loads are carried by this structure.
One approach to minimize the need for access doors and structure cut-outs could be loading and de-loading of battery units from the wing tips, as schematically shown in figure 100. After removing the tip cover, a battery pack could be inserted into a well between the main wing spars

and could be connected to the aircraft's high voltage busses. Next to the general technical challenges of such a concept, only a certain fraction of the wing's internal volume can be used since the size of the access opening is constrained by the tip wing section cord length and its relative cord thickness.

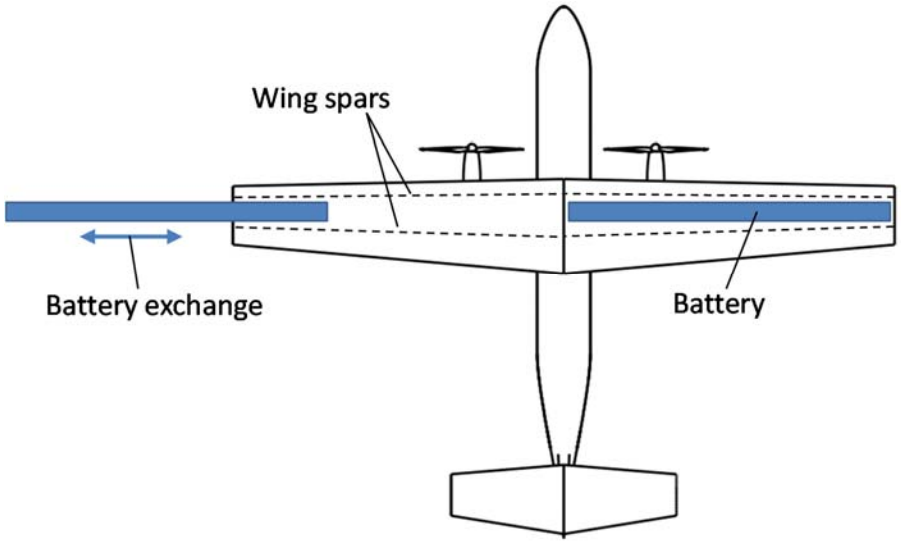

Figure 100, Battery exchange concept from the wing tip

Another, more radical approach would be the exchange of the whole wing including a fully integrated battery system as shown in figure 101. In this way, the whole available wing-internal volume could be used and no cut-outs and openings whatsoever would weaken the wing structure. With the high power consumers installed at the wing, only the relatively low systems power and control signals have to be transmitted across the interface to the fuselage. On the other hand, this approach of course would result in additional structural weight in the wing and fuselage and would require extensive ground provisions and storage of spare-wings at the airport site, as well as a very decent detailed design to ensure safety and reliability.

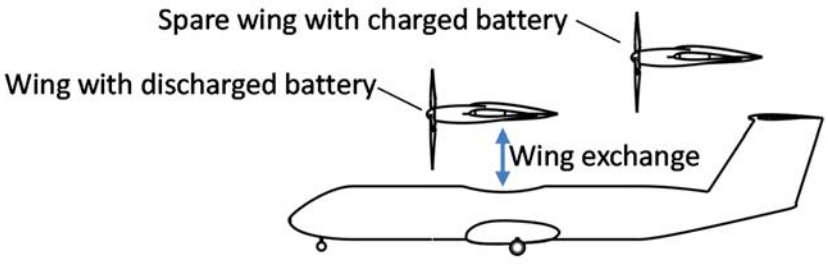

Figure 101, Wing exchange concept

Under-wing mounted external battery containers like external tanks for conventional aircraft would be a further option for the integration issue. This approach offers the wing relief advantage and good accessibility for exchanging, but on the other side causes additional wetted area and interference drag with the wing. Furthermore, the available volume is relatively small compared to other integration options.

The last approach presented here are fuselage-internal and fuselage-conformal compartments. The main inherent advantages are a potentially large volume and none or only small additional wetted area. Loading and de-loading can be done like with standard cargo equipment through fuselage access hatches. In a typical regional commuter aircraft cabin layout, available volume could be provided in an under-floor compartment. If this space is not sufficient, these compartments could be extended by enlarging already existing wheel bay fairings as shown in figure 102. On the downside, missing wing relief and additional mechanic stress in the fuselage will cause structural weight penalties. Furthermore, integration of batteries within the fuselage involves safety issues for passengers in the cabin in case of a crash scenario.

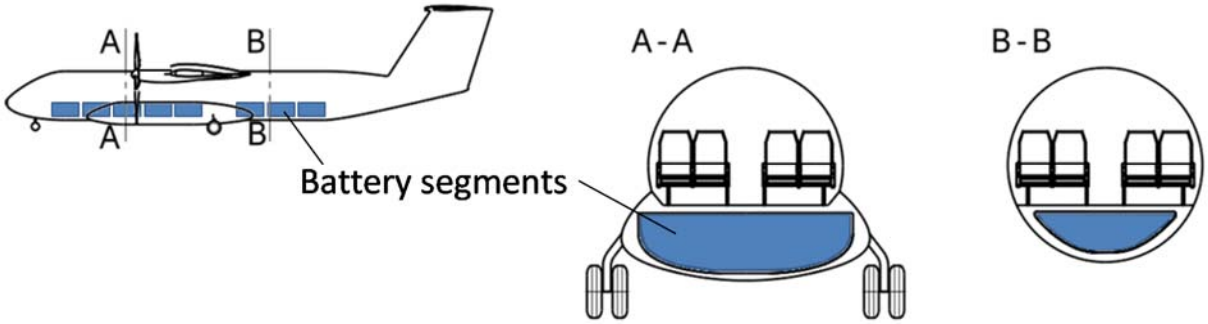

Figure 102, Fuselage battery Integration

Although some aspects and issues concerning battery integration have been discussed here, the consequences and implications are quite complex and cannot be fully covered in the perimeter of this thesis. Further investigations on detailed structural design, safety and cost issues are necessary to give a final answer on the considered integration options. However, first order effects on structural weight are covered within the weight prediction methodology of wing and fuselage, and impacts of enlarged wheel bay fairings are accounted in the aerodynamic methods. These effects will be evaluated using sensitivity studies for the two different integration locations as summarized in table 9.

Battery location	Effects considered
Battery integrated in fuselage	• Fuselage structural weight increase • Wing weight increase due to missing load relief • Increased drag in case of extended wheel bay fairings
Battery integrated in wing	• Wing bending moment relief (cf. kerosene storage)

Table 9, Considered effects of battery integration

4.2. Aircraft Sizing and Optimization

In the aircraft sizing process, multiple interdependencies between structure, weight, and aerodynamics have to be taken into account. Commonly, the preliminary aircraft designer uses physical, semi-empirical, or empirical methods to generate mathematical models of the aircraft components. These models are then implemented in a numerical code allowing an iterative solving of the design cycle, optimizing for one specific or a set of target figures, and conducting trade-studies. The modeling methods for weight, aerodynamic characteristics and flight

performance that are used in the frame of this study are defined in section 4.3. For solving, optimization and analysis, these methods are implemented and compiled in the numerical computing environment MATLAB© [125].
The implemented sizing process is outlined in figure 103. Starting with the mission requirements, a set of initial starting values is generated which describe the basic aircraft dimensions and parameters. Then, assuming a certain wing loading and installed power-to-weight ratio, the aircraft geometry, masses and aerodynamic values are being determined. Trim and stability characteristics are set up modifying wing position and tail size. Based on the generated data, the fuel/ energy required to fly the reference mission is being calculated. The total takeoff-weight is then calculated adding structural-, payload- and fuel/ battery weight. This calculated weight is given back replacing the initial value and the iteration is repeated until the initial and the calculated takeoff weights match. Finally, flight performance calculations are conducted to check if the found design matches all performance requirements defined by the mission requirements and certification regulations. If one or several performance requirements are missed, the whole sizing process is repeated with another set of wing-loading and power-to-weight ratio specifications.

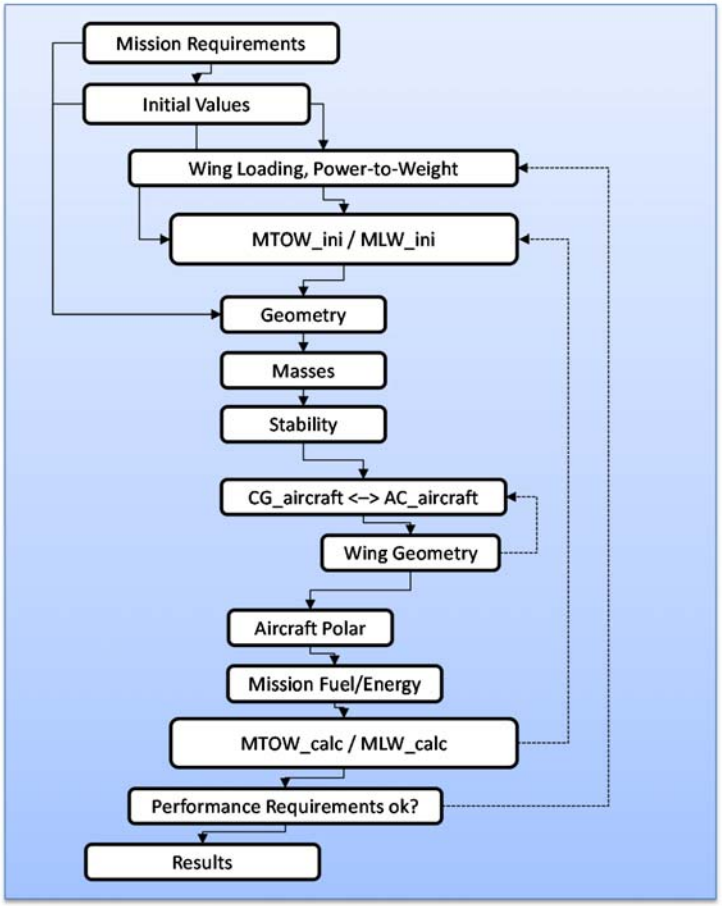

Figure 103, The aircraft sizing process

In the aircraft sizing process, it is the aim to define the key design parameters wing loading and power-to-weight ratio in a way that the aircraft weight and design mission energy consumption

are minimized. At the same time, the propulsion system and the wing size have to be chosen in a way that sufficient lift and thrust is available that the aircraft is able to fulfill the flight performance minima, as defined by the certification requirements (CS 25.101 - 25.125). The mission requirements that are considered in this study include:

- Payload & number of passengers
- Range @ design payload
- Cruise speed @ design altitude (including residual climb capability)
- Take-off and landing field length
- All required reserves including holding and diversion

Next to definitions and regulations for the take-off and the landing field length, the following minimum flight performance characteristics as required by CS 25 are being considered in the frame of this study:

- Second segment climb gradient with one engine inoperative
- Missed approach climb gradient with one engine inoperative

The amount of fuel or electric energy required is calculated based on a mission profile as given in figure 104. In the frame of this study, block fuel/ energy is always considered for a full mission including all loiter and diversion segments, as well as 5% contingency fuel/ energy.

1 Taxi
2 Take-off and initial climb
3 Climb
4 Cruise
5 Descend
6a Loiter
6b Diversion climb
6c Diversion cruise
6d Diversion descend
7 Approach and landing
8 Taxi

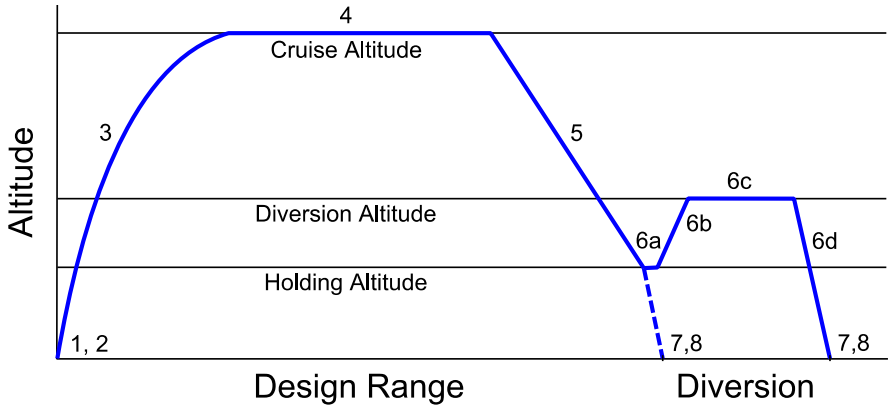

Figure 104, Mission profile

The strategy to find optimal key design parameters is a parametric study of wing loading and power-to-weight ratio. After defining the considered range of values, the numeric sizing code is executed for different combinations of the key parameters. For each resulting aircraft, flight performance calculations are conducted to figure out if all requirements are met. After the

parametric study is completed, all results including aircraft weight and energy consumption are evaluated in a matching chart and the set of optimal key parameters is identified. An exemplary matching chart evaluation for a conventional turbo-prop aircraft is shown in figure 105. In this example, the design is evaluated for wing-loadings in a range of 300 to 400 kg/m², and for a power-to-weight ratio range of 0.15 to 0.25 kW/kg. The best design point for minimal aircraft weight and fuel consumption is found at 344 kg/m² and 0.176 kW/kg. The approach in case of electric propulsion aircraft is identical, except that the required mission energy is displayed instead of the fuel burn.

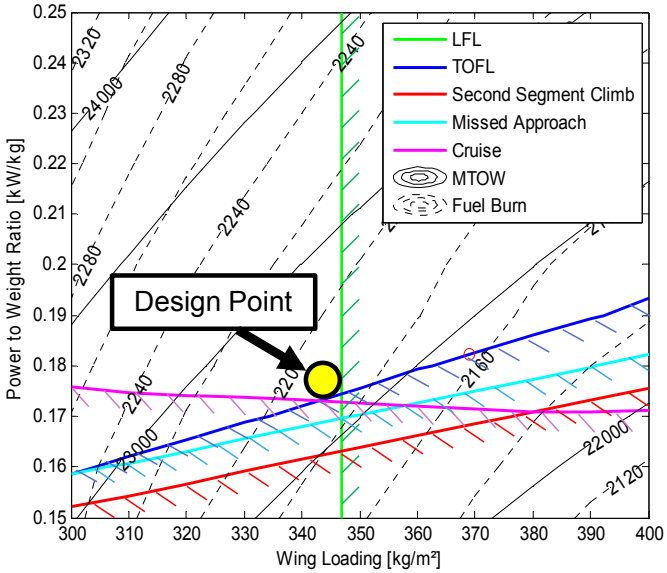

Figure 105, Exemplary matching chart to define key design parameters

4.3. Specification and Adaption of Implemented Methods

In this section, the methods used for modeling weight, aerodynamic-, and geometrical characteristics of standard aircraft components and sub-systems are being defined. Furthermore, flight mechanics and flight performance modeling is being addressed. While most of the standard methods are only named and referenced here, a more detailed presentation of these methods is given in the annex.

4.3.1. Fuselage Layout

The fuselage cross section and cabin length is sized according to the number of passengers to be transported. While there are various possible solutions in terms of seat configuration and cabin length, the cabin layout in the modeling process is adopted from three in-service regional aircraft. For any passenger number ranging from 22 to 38, a three-abreast layout is used as applied in the 30-seater Dornier Do 328. In the range from 40 to 80 passengers, a four-abreast is chosen like in an ATR 42 /72 that usually accommodates 50 to 74 passengers. For even larger numbers of passengers, a five-abreast solution is used as applied in an Avro Regional Jet. In all cabin configurations, a 34 inch seat pitch is assumed. Additional space for lavatories,

cargo compartments, and galleys is also provided according to the respective reference cabin. In figure 106, an overview of the seat arrangements of the reference cabins is given. As it turns out, cargo provisions in the underfloor-compartment that can be used for containerized battery accommodation is only available in the Avro RJ cross section. The four-abreast configuration as used in the ATR 72 series aircraft has no accessible underfloor compartment since a larger curvature radius was used for the fuselage bottom section. In order to generate volume to integrate batteries in this layout, the fuselage contour as to be adapted with a constant circular cross section (see figure 131, section 5.1). For the smallest considered cabin layout, only conformal fuselage compartments or an integration of the batteries in the wing is possible.

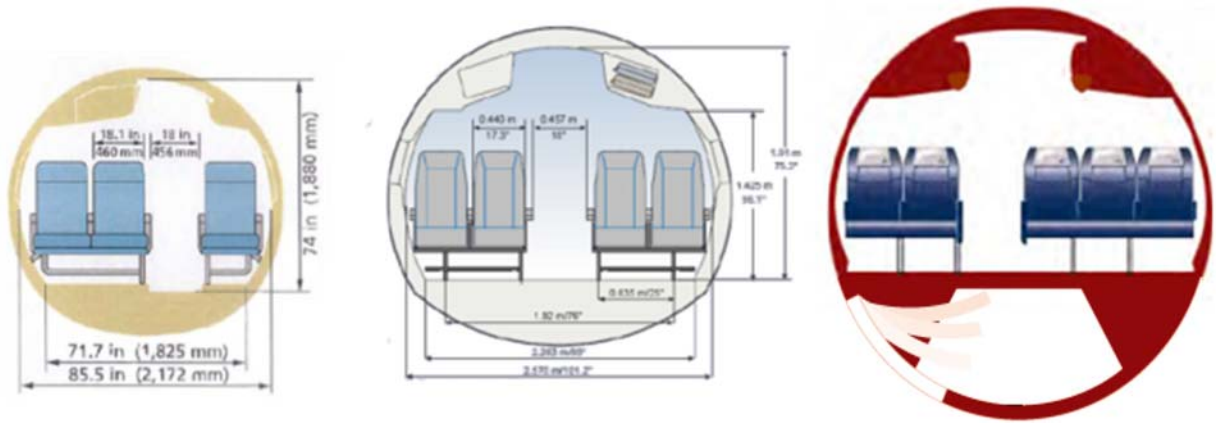

Figure 106, Seat configurations (Do 328, ATR 72, Avro RJ) [126] [127] [128]

4.3.2. Weight Modeling

The weight of the main aircraft groups is modeled using semi-empirical methods as published in the standard literature. For the major structural components, the following methods are being applied:

Component	Method	Comment
Wing	[96] eq. 8-12	As outlined in section 4.1, weight that is allocated in the wing leads to a relief of the maximal wing bending moment and hence to a reduction of the structural wing weight. In a standard method for wing weight determination as given by Torenbeek [96], this is accounted for by considering the maximum zero fuel weight as weight parameter instead of the maximum aircraft weight in case the fuel is stored in the wing. This approach is also applied for the wing weight modeling of electric propulsion aircraft. If the battery system is integrated in the wing, the total aircraft weight minus battery weight is being used as weight parameter. If the batteries are located in the fuselage, the maximum aircraft weight including batteries is used instead. Depending on the application, the maximum aircraft weight is either the maximum take-off weight or maximum landing weight, whichever is higher. Next to the aircraft weight, also the ultimate load factor and wing geometric parameters are further relevant parameters for this method.

Fuselage	[129] MA 508 12-02	A similar approach as in case of the wing is used for fuselage structural weight estimation. One sizing case for the fuselage structure is the mechanical stress induced during a hard landing, so the allocation of large weight shares within the fuselage has a significant impact [130]. Instead of the standard Torenbeek-method where the payload weight is not a parameter, a regression published in the “LTH” is used instead, accounting for geometric fuselage parameters, the design dive speed, the maximum aircraft weight, and the payload weight. Depending on the application, the maximum aircraft weight is either the maximum take-off weight or maximum landing weight, whichever is higher. If the battery system is integrated in the wing, the method is used as published. If a battery integration within the fuselage or in conformal compartments is considered, the battery system weight is added to the payload weight to account for the additional structural stress.

Table 10, Wing and fuselage weight methods

Since the other main structural elements are largely independent of the propulsion system, the standard methods are used as given in the cited sources:

Component	**Method**	**Comment**
Horizontal tail	[96] Eq.8-14	The horizontal tail weight is determined based on its geometry and the design dive speed.
Vertical tail	[96] Eq.8-15	Analog horizontal tail.
Nose landing gear	[96] Eq.8-17	The weight of the nose landing gear is determined based on the gear type and the aircraft weight.
Main landing gear	[96] Eq.8-17	Analog to nose landing gear.

Table 11, Aircraft structure weight methods

The propulsion system weight is modeled using the following relations:

Component	**Method**	**Comment**
Electric powertrain		See chapter 3.
Turbo-shaft engines	[131]	Turbo-shaft engine weight is determined based on a statistical correlation with the rated power as main parameter.
Nacelles	[96] Eq.8-24	-

Table 12, Propulsion system weight methods

The weight of the aircraft service and equipment group is determined as follows:

Component	**Method**	**Comment**
Surface controls	[96] Eq.8-18	Applicable to conventional aircraft
Electric surface controls		See section 3.1.8.
Instruments	[96] Eq.8-32	-
Electric system	[96] Eq.8-42	Applicable to conventional aircraft
Electric system		Applicable to electric propulsion aircraft, see section 3.1.8,

Furnishing	[96] Tab. 8-12	-
Operational items	[96] Tab. 8-13	-
Electric air-conditioning		See section 3.1.8

Table 13, Aircraft service and equipment weight methods

4.3.3. Aerodynamic Modeling

The determination of the aerodynamic characteristics is mainly done using methods compiled by Torenbeek [96]. Taking trim losses into account, the local lift coefficients of the wing and vertical tail-plane are calculated based on a momentum balance according to the schematic given in figure 107.

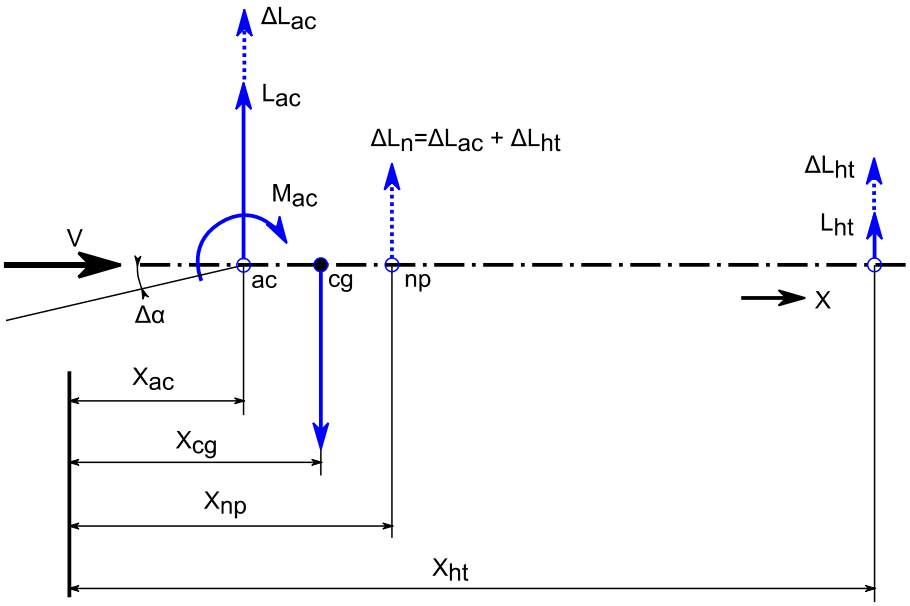

Figure 107, Geometrical definition of forces and moments, based on [96]

Accordingly, the wing lift- and the tail lift coefficients result in:

Component	**Method**
Wing lift coefficient	$Cl_{wing} = \frac{(x_{ht} - x_{cg})\, Cl_{A/C} - Cm_0 MAC}{x_{ht} - x_{ac}}$
Horizontal tail lift coefficient	$Cl_{ht} = \frac{Cl_{A/C} - Cl_{wing}}{rel\_S_{ht}}$ $rel\_S_{ht} = \frac{S_{ref,ht}}{S_{ref,wing}}$

Table 14, Determination of wing and tail lift coefficients

For drag accounting of conformal battery compartments, the method determining drag due to a wheel well fairing is adapted:

Wheel well fairing	[96], Section F-5.3	If a high wing configuration is considered, a wheel well fairing houses the main landing gear. The friction drag of the wheel well fairing is modeled using a standard literature method. If additional volume for fuselage battery integration is required, this fairing is extended to provide conformal fuselage compartments and the wetted area is increased accordingly.

Table 15, Wheel well fairing and conformal battery compartment drag

Table 16 summarizes the methods used for the determination of the other profile drag contributions of the respective aircraft components that are not directly affected by the kind of propulsion system:

Component	**Method**	**Comment**
Fuselage	[96], Section F-3.4	The fuselage drag area is calculated depending on the fuselage geometry, the free-stream angle of attack, and the Reynolds number.
Wing	[96], Section F-3.3	The friction drag of the wing is composed of a zero-lift drag component and a lift-dependent drag increment.
Vertical tail	[96], Section F-3.3	Analog to wing.
Horizontal tail	[96], Section F-3.3	Analog to wing.
Nacelle	[96], Eq. F-54	The nacelle profile drag is calculated based on its geometry and wetted area.
Wing fairing	[96], Section F-4.2 b	-
Nacelle interference	[96], Section F-4.3 a	Drag due to interference is taken into account by neglecting the wetted area correction (keeping the wetted areas of nacelle and actually covered wing uncorrected).
Cockpit windows	[96], Section F-5.2 b	Drag due to planar window panels well fitted into the fuselage nose.
Other	[96], Section F-5.7	Drag due to surface imperfections, door- and rudder slots, excrescences, etc.
High-lift system	[132], Eq. 12.37	$\Delta C_{D0,flap} = 0.0023 \frac{flap\ span}{wing\ span} \delta_{flap}$ Reference values taken from ATR 72: $\frac{flap\ span}{wing\ span} = 0.7 \quad \delta_{flap,\ take-off} = 15° \quad \delta_{flap,\ land} = 30°$

Landing gear	[96], Eq.G-65	Drag increment due to an extended undercarriage based on the wheel frontal area.

Table 16, Profile drag modeling

The total vortex drag is calculated based on the following component build-up:

Component	Method	Comment
Wing	[96], Section F-2.1&2.2	-
Fuselage	[96], Section F-2.4	-
Horizontal tail	[96], Section F-3.1	Calculated analog to wing, without the effect of twist.

Table 17, Vortex drag modeling

4.3.4. Trim and Stability Modeling

For each flight phase, the trim condition is established by applying the methods given in Table 14, defining the lift coefficients of the horizontal tail and the wing in order to eliminate the resulting moment around the center of gravity.

Static longitudinal and lateral stability is ensured by using typical tail volumes as appearing in the relevant aircraft class:

Component	Method	Comment
Horizontal tail	[132] Eq.6.29	Raymer proposes 0.9 for turboprop aircraft.
Vertical tail	[96] Eq.6.28	Raymer proposes 0.08 for turboprop aircraft.

Table 18, Tail volume estimation

The location of the aerodynamic center and the aircraft's neutral point are determined using the following methods:

Component	Method	Comment
Wing aerodynamic center	[96], Section E-7.1	The aerodynamic center of the wing is assumed to be at 25% of MAC.
Wing-body aerodynamic center	[96], Section E-7.1	The effect of fuselage and nacelles on the aerodynamic center is modeled based on their geometric characteristics.
Aircraft neutral point	[96], Section E-7.1	The neutral point of the total aircraft is calculated considering the stabilizing effect of the horizontal tail.

Table 19, Neutral point estimation

When the location of the neutral point is known, the static margin can be calculated:

$$SM = \frac{X_n - X_{cg}}{MAC} \tag{84}$$

4.3.5. Mission Modeling

While a weight variation during flight appears for conventional aircraft due to fuel burn, also future battery systems eventually will change their weight during discharge as outlined in section 3.1.1.2. The energy consumption and the related weight variation during the mission are calculated by discretizing the climb-, cruise-, and descend phases into short time segments. For each segment, all relevant flight parameters are evaluated. The total weight variation and energy consumption then are summed up by adding the results of each discrete segment.

The calculation procedure for an electric aircraft mission segment is given in figure 108. Based on the actual aircraft weight, the thrust requirement is calculated considering the aerodynamic characteristics and the available specific excess power (SEP) in case the aircraft is in climb. Depending on the propeller efficiency, this thrust requirement is translated into a motor shaft power setting. Within the discretization time of the considered segment, the amount of electric energy to be provided by the battery system is then determined including motor and distribution losses. On this basis, the related battery weight change Δw_i and the resulting new aircraft weight is calculated.

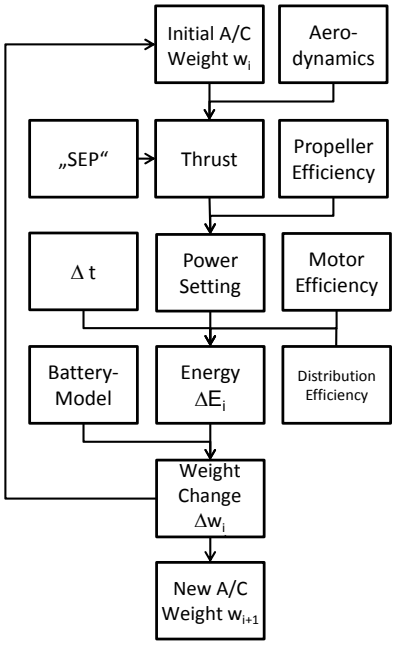

Figure 108, Mission modeling for weight-gaining battery systems

The total weight variation and total mission energy consumption can then be determined by summing up the results of all n time segments:

$$\Delta w = \sum_{i=1}^{n} \Delta w_i \quad (85)$$

$$\Delta E = \sum_{i=1}^{n} \Delta E_i \quad (86)$$

A direct comparison of the energy consumption of conventional propulsion aircraft and electric powered aircraft is difficult since the system efficiencies and the energy carrier characteristics differ. An adapted specific air range (SAR) figure has therefore been proposed in the literature as a suitable metric for comparison [133]. The SAR is adapted to an energy specific air range ESAR, relating the range increment on an energy consumption increment instead of a fuel mass increment:

$$ESAR = \frac{\partial R}{\partial E} = \frac{V_0 \frac{L}{D}}{TSPC\ w_{ac}\ g} = \frac{\eta_{ov} \frac{L}{D}}{w_{ac}\ g} \quad (87)$$

For both propulsion systems, conventional and electric, η_{ov} represents the overall propulsion system efficiency from the energy source to thrust generation. Technically, ESAR has to be evaluated for a specific flight condition with a given weight, L/D ratio, speed and propulsion system performance including thrust specific power consumption (TSPC). For simplicity reasons, facilitating the comparison of aircraft with difference propulsion systems, a block ESAR is being considered in the frame of this study, referencing the mission design range on the total 'block' energy including all reserves. In case of electric propulsion, this refers to the total electric energy stored in the battery including discharge losses; in case of conventional propulsion systems, this refers to the combustion enthalpy of the required quantity of kerosene.

4.3.6. Flight- and Field Performance Modeling

The methodology to investigate flight performance characteristics is outlined in the following table:

Segment	**Method**
Take-off field length	Take-off with one engine inoperative (OEI): Ground roll (from V_0 to V_r): $Acceleration = \frac{Thrust - Drag}{Weight}$ Thrust: • Calculation according to propulsion system characteristics Drag: • Wheel friction ([96], section K-4.1), • Aerodynamic drag as defined above Assumption: $V_1 = V_r$ [96]

	Airborne phase (from 0 ft to 35 ft) Climb-out to 35 ft and accelerate from V_r to V_2 with OEI ([96], section K-4.2) Take-off with all engines operating (AEO): • Take-off field length calculation like above, but with AEO • Addition of a 15% safety margin ([96] K-1e) **→The most critical case is used**
Second segment climb gradient (OEI)	The minimum climb gradients are: • 2.4% for twin-engine aircraft • 3% for four-engine aircraft Undercarriage is retracted, flaps are in take-off position (cf. CS 25.121(b)) The climb capability is evaluated based on the available specific excess power (SEP) ([96], section 5.4.3): $SEP = \frac{Thrust - Drag}{Weight} \cdot Flight\ Speed$ $climb\ gradient = \frac{SEP}{Flight\ Speed}$
Cruise	A residual climb capability requirement of 100 ft/min in cruise condition is assumed.
Landing field length	Un-factored dry landing field length from 15 m above the runway threshold to full stop: methodology following ([96], section 5.4.6). Factorization for turbo-propeller powered airplanes: 1.43 (cf. EU OPS 1.515(a)) [134]
Missed approach climb gradient (OEI)	The minimum required climb gradient is: • 2.1% for twin-engine aircraft • 2.7% for four-engine aircraft Undercarriage is retracted, flaps are in landing position (cf. CS 25.121(d)).

Table 20, Flight and field performance modeling

4.3.7. Turbo-Shaft Engine Performance & Fuel Tank Volume Modeling

In order to validate the aircraft sizing model presented above, in-service regional turboprop aircraft are being modeled and the results are compared with original product specifications. In this context, a parametric model of turbo-shaft engine fuel consumption is needed in addition to the methods presented so far. Due to the wide range of engine power levels to be considered in the sizing process, a generalized modeling approach is used instead of a detailed engine analysis.

During flight, the maximal power output of a turbo-shaft engine generally declines relative to its reference take-off value depending on the flight altitude, velocity, and ambient temperature. Additionally, engines are usually being limited in flight to maximum continuous/ climb/ cruise ratings to increase the service lifetime. Anderson [135] published a method to estimate the power lapse due to altitude effects based on the air density ratio σ:

$$\sigma = \frac{\rho}{\rho_0} \tag{88}$$

$$\frac{P}{P_0} = \sigma^{0.7} \tag{89}$$

Due to pressure recovery in the engine air intake, the available power increases with flight velocity. Based on “Pratt & Whitney PT6” engine data, [136] the following method is used to model the power increase due to velocity (Mach number):

$$\frac{P}{P_0} = 1 + M^2 \tag{90}$$

The main parameters influencing the specific fuel consumption of turbo-shaft engines are engine size (take-off power), actual power-setting relative to maximal available power (part-load characteristics), as well as environmental conditions (flight altitude, temperature, velocity). Generally, large and more powerful engines offer better specific fuel consumption due to a reduced blade tip clearance impact, higher Reynolds numbers, and enhanced blade cooling capabilities. This trend can be observed comparing reference take-off SFC values against rated take-off power of typical civil aircraft turbo-shaft engines, as exemplary done in [137]. From this publication, the regression as given in equation (91) has been derived:

$$SFC_{maxRated}[\mathrm{lb/hr/shp}] = 2.2381 \cdot (P_{maxRated}[shp])^{-0.21} \tag{91}$$

Using the full-load consumption as reference value, a relative increase in specific consumption is modeled based on a typical part-load characteristic description as presented in [137] and [138]. For this method, a part-load factor p is defined and corrected with the ambient pressure ratio and temperature ratio (θ and δ) as given in eq. (92) and (93):

$$p = \frac{P}{P_{maxRated}} \tag{92}$$

$$p_{corrected} = \frac{p\sqrt{\theta}}{\delta} \tag{93}$$

The total increase in SFC is then calculated using the regression given in eq. (94):

$$SFC = SFC_{maxRated} \frac{1}{(0.258 \log(p_{corrected}) + 1)} \quad (94)$$

The available tank volume in the wing for fuel storage is calculated as follows:

Component	Method	Comment
Wing tank volume	[96] eq. B-12	The wing tank volume is estimated based on wing geometry parameters that are referenced on a statistical database of existing aircraft.

Table 21, Wing tank volume modeling

4.4. Validation and Calibration of the Design Model

For validation of the sizing methodology and the modeling methods related to the conventional airframe components, three in-service regional turboprop aircraft are being re-designed and the results are compared with original specifications: the 30-seater regional turboprop Do 328, the 68-seater ATR 72-500 and the 80-seater DHC (Dash) 8 Q400. Top-level mission requirements, weights, and geometrical data of these reference aircraft are given in sources [126] [127] [139]. Maximum lift coefficients are extracted from [140] [111] [141]. Table 22 gives a summary of the input variables used for each aircraft.

	Do 328	ATR 72-500	Dash 8 Q400	
Passengers	32	68	80	[-]
Maximum payload	3492	7350	8490	[kg]
Range @ max payload	380	500	660	[NM]
Deviation range	100	87	100	[NM]
Holding time	-	-	45	[min]
Continued cruise[1]	45	45	-	[min]
Cruise altitude	6096	5181	6096[2]	[m]
Cruise speed	596	510	667	[km/h]
TOFL	1088	1360	1431	[m]
LFL	1075	1067	1290	[m]
Engine OEI rating	1.1	1.15	1.1	[-]
MLW/MTOW	0.95	0.994	0.95	[-]
Wing aspect Ratio	10.2	12	13.4	[-]
Wing taper Ratio	0.6	0.62	0.62	[-]
Landing $C_{L,max}$	2.66	2.73	2.76	[-]
Take-off $C_{L,max}$	2.03	2.25	2.514	[-]

Table 22, Input parameters of the reference aircraft

[1] Instead of a holding time, a continued cruise time is given in this case

[2] Assumed value

The comparison between the sizing results and actual aircraft data is done in three steps. First, the methodology determining the design point in terms of wing loading and power-to-weight ratio based on performance requirements is evaluated. Second, the weight estimation results are assessed for a design point that matches the real aircraft, and third, the fuel burn results for the respective design missions are compared.
For the given input parameters as stated above, the matching charts resulting from the sizing model are shown in figure 109. For comparison, also the data points of the respective real reference aircraft are added. It can be seen that the predicted design points match the real designs within a certain error margin. The largest deviation in wing loading can be observed in case of the ATR 72 with an underestimation of around 6%, the largest deviation concerning power-to-weight ratio occurs in case of the Do 328 with around 13%.

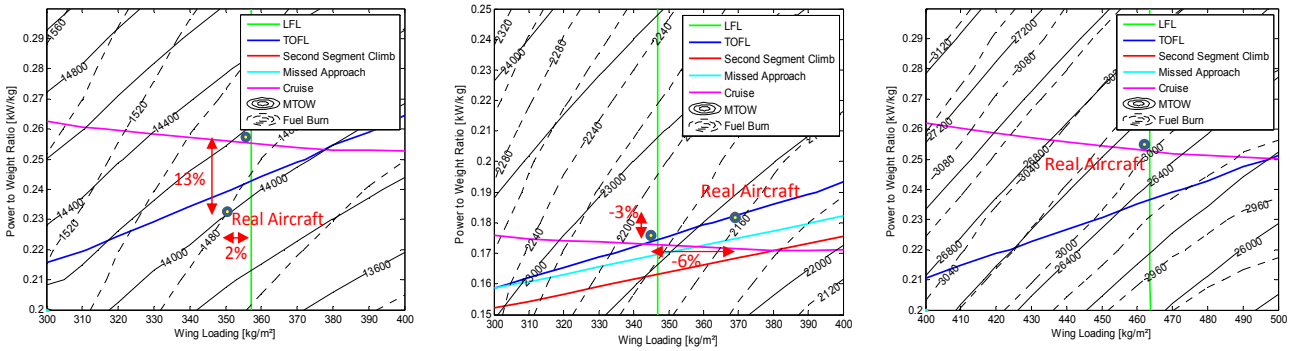

Do 328 ATR 72 Dash 8

Figure 109, Matching charts of the three reference aircraft

In the next step, the wing loading and the relative power are corrected to match the real reference aircraft. For these design points, build-ups of the resulting empty weights are given in figure 110.

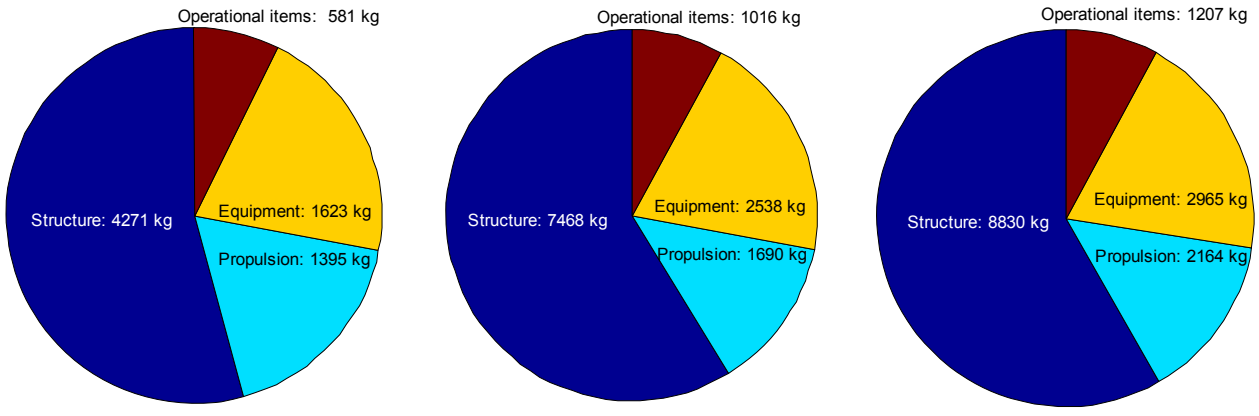

Do 328 ATR 72 Dash 8

Figure 110, Empty weight breakdwon of the modeled reference aircraft

The total OEWs are compared with the reference empty weights in table 23. It turns out, that the weight deviates around 1% in case of the ATR 72, and around 16% in case of the Do 328 and the Dash 8 Q400, presumably due to the empirical nature of the weight prediction methods. From these results, an empty weight calibration factor is defined for each aircraft, which is smaller than the original delta due to aircraft sizing ("snowball") effects:

OEW	Do 328	ATR 72	Dash 8	
Real	9100	12950	17689	[kg]
Model	7870	12712	15166	[kg]
Deviation	-15.6	-1.9	-16.6	[%]
Calibration Factor	1.09	1.01	1.10	[-]

Table 23, Comparison of empty weight results

With these calibration factors, the empty weights of the modeled aircraft are being adjusted to correspond with the original data. This is necessary to ensure that a reasonable comparison of aircraft fuel consumption can be done in the next step. For the calibrated aircraft, the calculated drag polars are shown in figure 111. Based on these results and the modeling methods describing the efficiencies of engine, gearbox, and propeller (cf. sections 3.1 and 4.3), the aircraft fuel consumption is calculated for the reference missions as given in table 22.

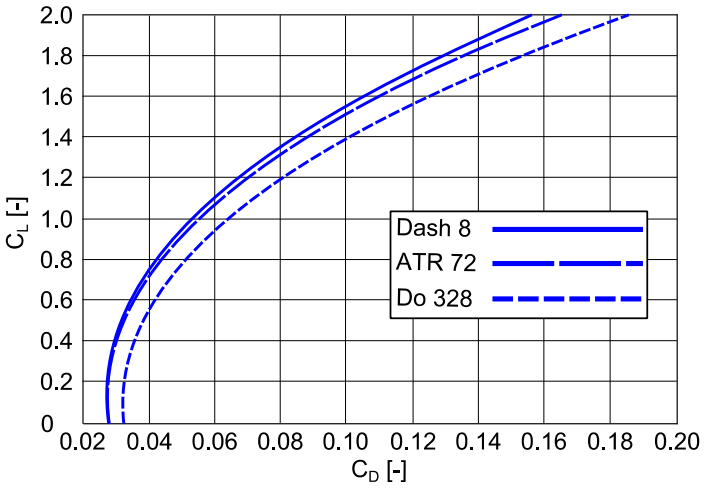

Figure 111, Reference aircraft drag polar results

In table 24, these results are compared to the actual fuel consumption data for the respective design missions [126] [127] [139]. The maximum deviation occurs in case of the Dash 8 with about 8%.

Fuel	Do 328	ATR 72	Dash 8	
Real	1398	2200	3401	[kg]
Model	1481	2165	3145	[kg]
Deviation	5.6	-1.6	-8.1	[%]

Table 24, Comparison of fuel burn results

The prediction of aerodynamic characteristics as well as component weight and efficiency in preliminary aircraft design is mainly done using empirical or semi-empirical methods that are based on statistical data. As a consequence, a certain margin of error is inherent to these methods. With this in mind, the deviations observed in the comparison between modeling results and real aircraft data are considered to be in an acceptable range. Hence no calibration factors are being applied to the weight- and aerodynamic performance prediction methods.

5. Conceptual Design and Assessment of Electric Propulsion Aircraft

Electric propulsion systems differ in many aspects from conventional systems based on a combustion engine, mainly in terms of weight, volume, and operational characteristics. Since the propulsion system is one of the main design drivers in the aircraft design process, changes to the propulsion system characteristics will cause changes in the design and operational aspects of the whole aircraft. In the following, the methods defined in chapters 3 and 4 are applied to assess these aspects in the design and sizing of regional electric propulsion aircraft and to show limits in the design space. An electric baseline aircraft is being sized based on similar operational requirements as common for today's regional turbo-prop aircraft. By means of sensitivity analyses, the optimization potential of the baseline design is being assessed and adapted solutions are being presented. Finally, the chapter concludes with a design space evaluation.

5.1. Sizing of a Baseline Configuration

In a first step, an electric baseline aircraft is sized to match the mission characteristics of a standard turboprop aircraft which was already used for sizing model validation: the ATR 72. The related mission requirements and further sizing assumptions are summarized in table 25. The propulsion arrangement with two propellers is chosen following the reference configuration, and the wing is selected for battery storage in this baseline design.

Payload	68	[PAX] (@ 95 kg/PAX)
Range	890	[NM]
Take-off field length (TOFL)	1360	[m]
Landing field length (LFL)	1067	[m]
Cruise speed	511	[km/h]
Cruise altitude	5181	[m]
Take-off $C_{L,max}$	2.26	[-]
Landing $C_{L,max}$	2.73	[-]
Battery spec. energy	1000	[Wh/kg]
Configuration	2	Motors
Span limitation	36	[m] (ICAO code C)
Max. aspect ratio	12	[-]
Battery integration	Wing	

Table 25, Top-level requirements of the electric baseline aircraft

With these values, the sizing process is done using the sizing model as defined in the previous chapter. At first, the wing loading and the power-to-weight ratio are identified which fulfill all performance requirements at minimum weight. As shown in figure 112, this is the case at a wing loading of 344 kg/m² and a power-to-weight ratio of 0.162 kW/kg.

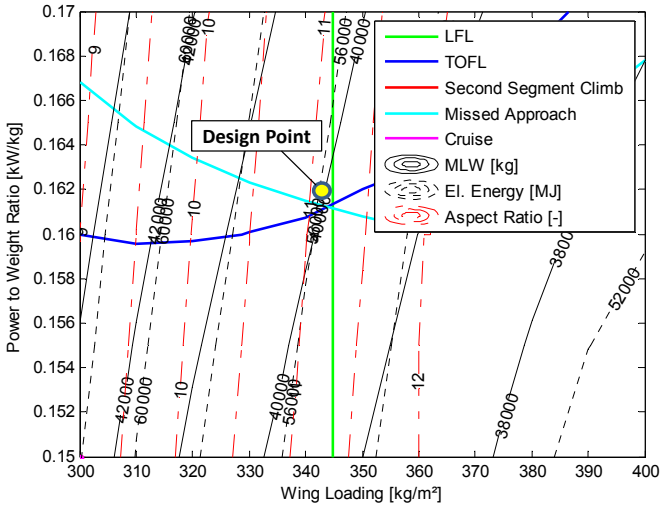

Figure 112, Matching chart of the electric propulsion baseline aircraft

The take-off field length, landing field length and the missed approach climb gradient turn out to be the critical requirements for the design point. The unusual dominance of the missed approach requirement, can be explained by the fact that the aircraft is gaining weight during the mission according to the battery model. The resulting increased landing weight relative to the take-off weight then leads to increased thrust and power requirements in case of an OEI missed approach maneuver.

Another effect which can be observed is that the power requirement for missed approach grows with increasing wing area. This is caused by the span limiation implemented in the sizing code. In order to maintain compatibility with existing airport provisions at regional airports, a 36 m span limiation (ICAO code C) should not be exceeded. When the 36 m span limit is reached and the wing area is further increased, the wing aspect ratio has to be reduced accordingly. Especially at low flight speeds, as e.g. during the take-off and landing phase, this leads to increased vortex drag and hence increased power requirements.

For the defined design point, a three-side view of the resulting baseline aircraft and the main aircraft characteristics are given in figure 113. The MLW of roughly 39.9 t exceeds the MTOW of the reference aircraft ATR 72-500 by 88%. The battery weight for the design mission accounts for 17.6 t, which is a vast increase compared to the fuel weight of the reference. The oxygen gain of the battery results in 3 t additional weight in the landing configuration. In total, an installed power of 6460 kW is necessary to meet the critical TOFL and missed approach requirements. Lift is provided by a wing with 116 m² reference area and an aspect ratio of 11.2 to stay within the 36 m span limit.

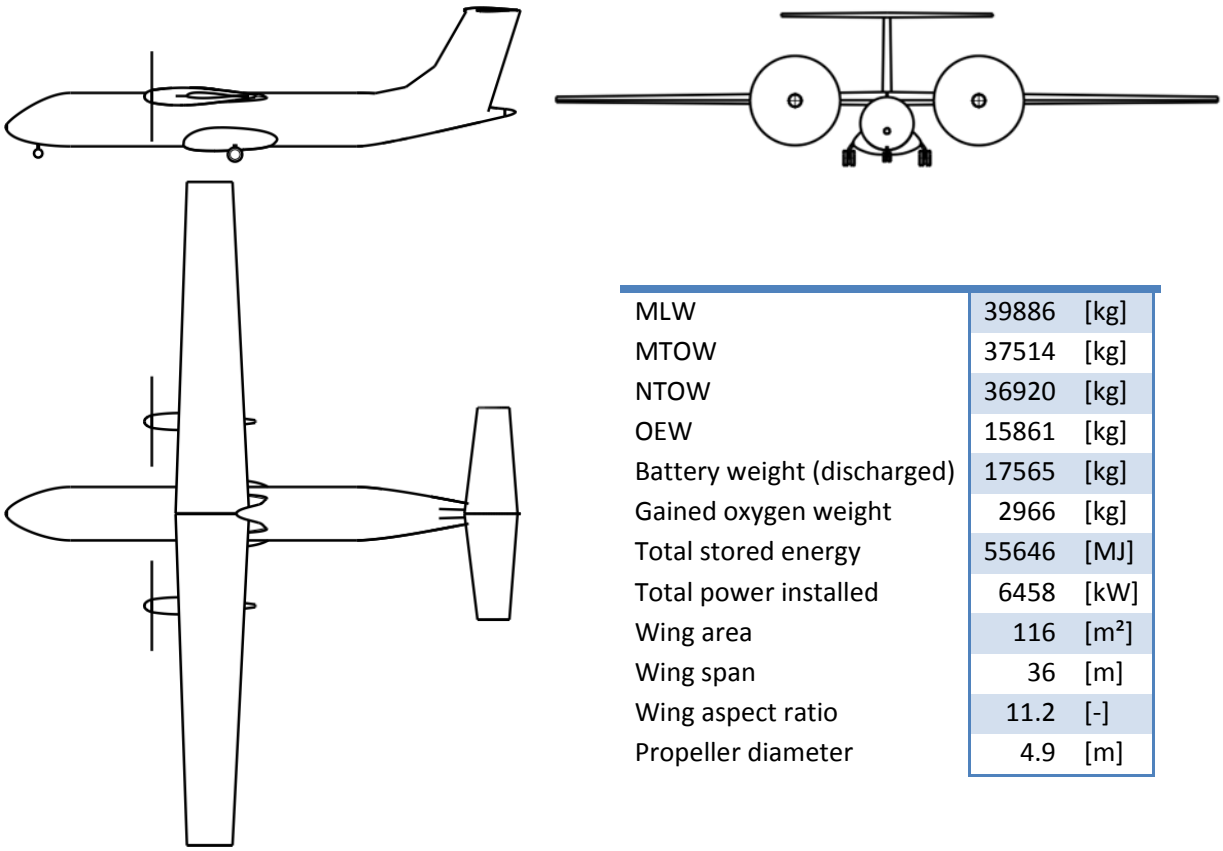

MLW	39886	[kg]
MTOW	37514	[kg]
NTOW	36920	[kg]
OEW	15861	[kg]
Battery weight (discharged)	17565	[kg]
Gained oxygen weight	2966	[kg]
Total stored energy	55646	[MJ]
Total power installed	6458	[kW]
Wing area	116	[m²]
Wing span	36	[m]
Wing aspect ratio	11.2	[-]
Propeller diameter	4.9	[m]

Figure 113, Three-side view of the baseline aircraft

Weight breakdwon

A detailed weight breakdwon of the baseline aircraft is given in table 26. Following the definitions in the previous chapter, the NTOW, MTOW, and MLW represent different amounts of accumulated oxygen in the battery cells.

Airframe Structure			OWE	NTOW	MTOW	MLW
Fuselage	3473	10573 (27 %)	15861 (40%)	36920 (93 %)	37514 (94 %)	39886 (100 %)
Wing	3893					
Horizontal Tail	445					
Vertical Tail	527					
Nose Gear	260					
Main Gear	1237					
Surface Controls	188					
Nacelles	550					
Propulsion Group						
Motors	49	2227 (6 %)				
Motor Cooling	170					
Inverters	196					
Inverter Cooling	396					
Propellers	629					
Gearboxes	233					
Cables	273					
Semicond. Switches	21					
Mech. Switches	27					
DC DC Converters	8					
Battery Cooling	224					
Airframe Service and Equipment						
ECS	333	2045 (5 %)				
Instruments	459					
Electrical Systems	173					
Furnishing	1079					
Operational Items						
Misc. Items	1016 (3 %)					
Payload						
PAX & Cargo	6460 (16 %)					
Battery System						
Cells (charged)	12492	14599 (37%)				
Housing and BMS	2108					
20 % Reaction Oxygen	593 (1 %)					
80 % Reaction Oxygen	2372 (6 %)					

(All values in kg, percentage of MLW in brackets)

Table 26, Electric baseline aircraft weight breakdown

Evaluating the impact of the electric propulsion system on the weight relations within the main weight groups, the respective distributions for the baseline- and the reference aircraft are shown in the figures below for comparison.

At first, looking at the weight relations in the maximum aircraft weight (MLW in case of the electric aircraft versus MTOW for the reference) the obvious difference is the weight share of the battery system versus conventional fuel. As shown in figure 114, the charged battery makes up for almost half of the MLW compared to only 14% fuel weight. The empty weight fraction reduces from 0.58 to 0.4 in case of the electric baseline aircraft.

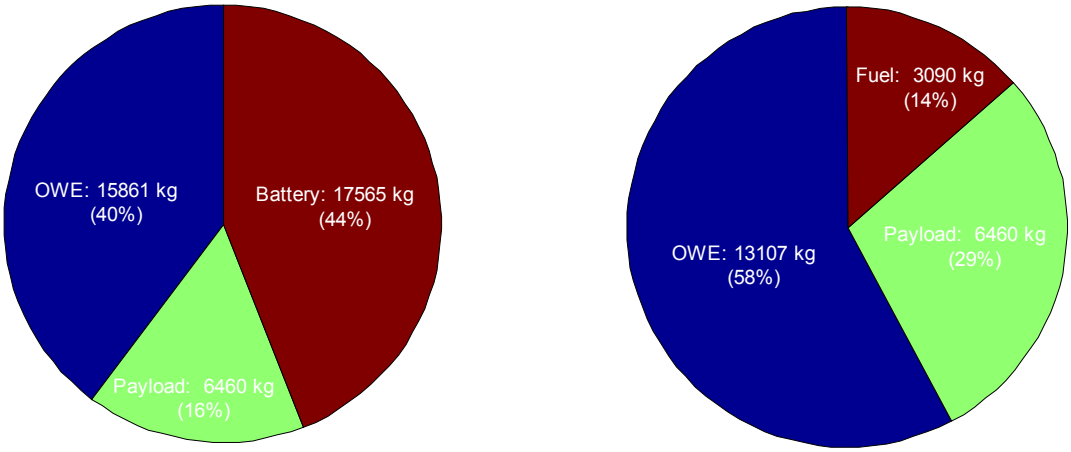

Figure 114, Maximum take-off/ landing weight breakdown

Looking at the empty weight components (figure 115), it turns out that the structure of the electric aircraft accounts for a greater share due to the increased overall aircraft weight compared to the reference. The absolute weights of operational items and equipment are similar in both cases since these are mainly a function of the number of passengers and not of aircraft weight, so their relative share is smaller in case of the baseline design.

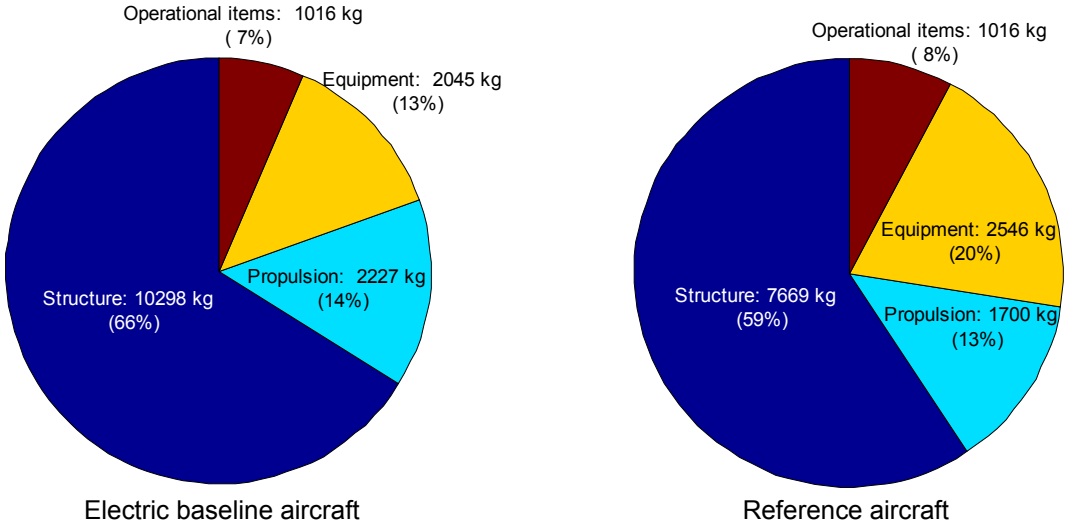

Figure 115, OEW breakdwon

Within the structural weight group (figure 116), the shares of the wing and the vertical/ horizontal tails are increased compared to the other components. This is mainly caused by the increased overall aircraft weight and the consequently larger wing. The tail surfaces are increased accordingly to maintain the required tail volumes.

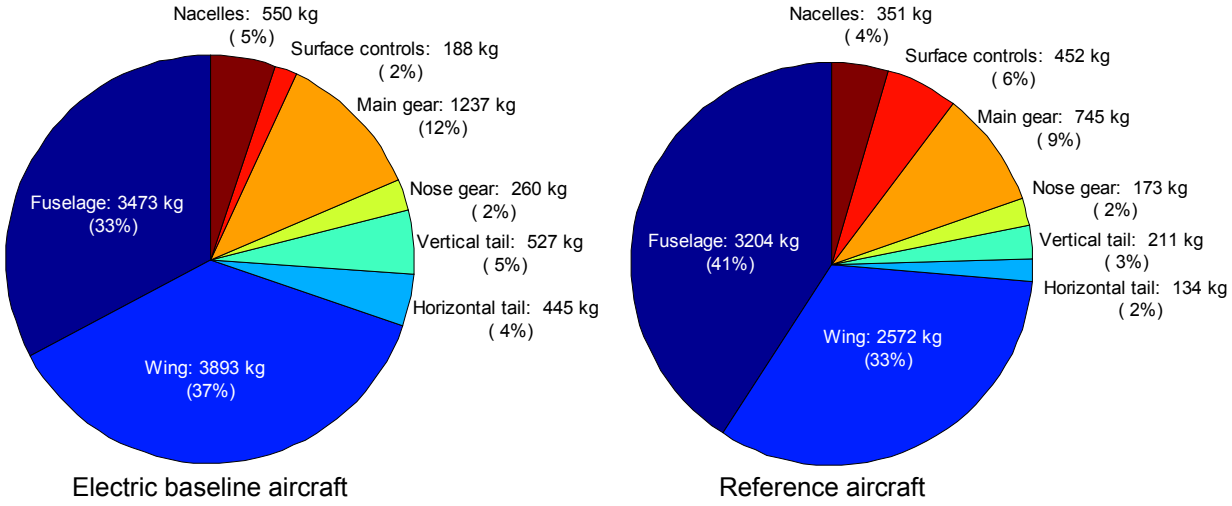

Figure 116, Structural weight breakdwon

Comparing the propulsion system components in figure 117, it turns out that the weight shares of the energy converters (inverters and electric motors vs. turbo-shaft engines), propellers, gearboxes, and supporting systems (distribution system vs. fuel and oil system) remain mainly unchanged.

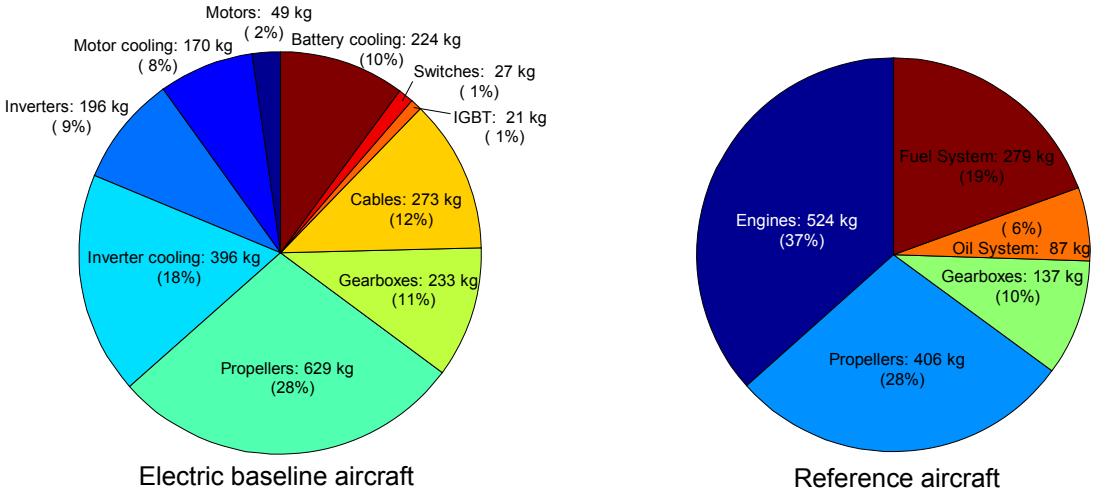

Figure 117, Propulsion system weight breakdwon

Aerodynamic characteristics

The increased aircraft weight due to the electric propulsion system affects the aerodynamic characteristics mainly in two ways: at first, as a result of the span limitation of 36 m (ICAO code C), sufficient wing area can only be obtained by increasing the wing cord and hence reducing the wing aspect ratio. Increased vortex drag especially at high lift coefficients is the consequence. The second effect refers to the friction drag or in more general terms the “zero-lift drag”. Since the fuselage geometry is unchanged, its absolute drag area is the same as for the reference aircraft. Its drag coefficient however is referenced on the wing reference area which is significantly larger in the electric propulsion case. The result is a decreased zero-lift drag coefficient compared to the reference. On total aircraft level, both effects can be seen in the

aircraft polar comparison in figure 118. Despite its higher effective zero-lift drag area D_0, the lower zero-lift friction drag coefficient $C_{D,0}$ allows the electric configuration to outperform the reference with an maximal L/D of roughly 22. At higher lift coefficients however, this gap is decreasing by an increased vortex drag component due to the slightly reduced wing aspect ratio (11.2 vs. 12).

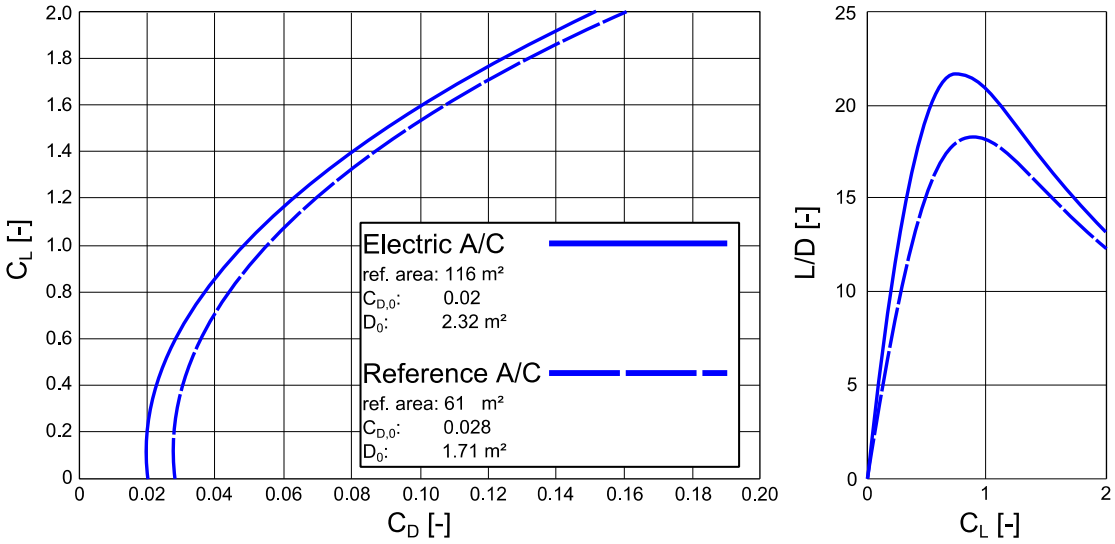

Figure 118, Drag polar comparison

Speed characteristics

In the design mission, the reference range of 890 nautical miles is flown at the design cruise speed of 511 km/h at an altitude of 5181 m. Deviating from this design speed, the impact on the effective mission range (excluding reserves) is given in figure 119. Flying slower than reference speed, the cruise lift-to-drag ratio improves and an optimum long range cruise (LRC) speed is reached at 400 km/h, providing a range of 1015 NM. Since the electric motors have no power lapse with flight altitude, all speeds up to the maximum operating (MO) speed at 603 km/h can be sustained in horizontal flight. In this case, the effective range is reduced to 738 NM.

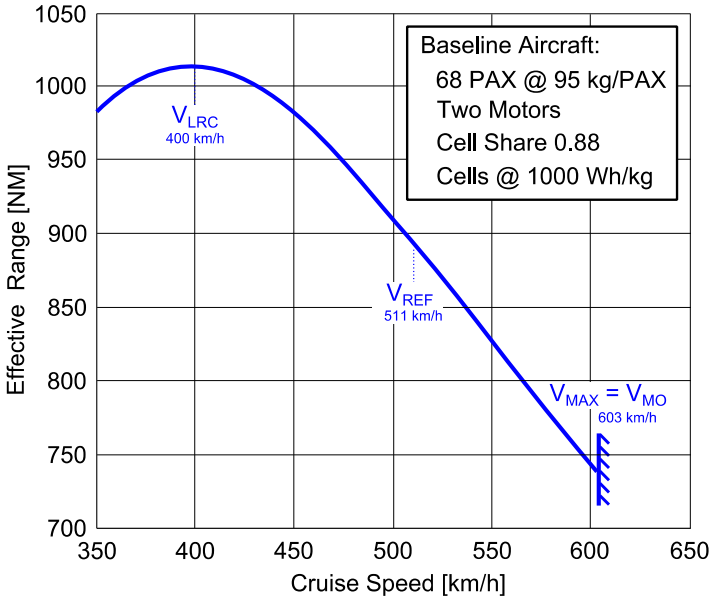

Figure 119, Cruise speed impact on range

Energy specific air range (ESAR)

As outlined in section 4.3.5, the ESAR offers a convenient metric to compare the energy consumption of aircraft with different energy carriers and propulsion systems. Since the number of passengers and the range requirements of the electric baseline aircraft are the same as for the ATR 72 reference, a block ESAR comparison can be done. The results are summarized in table 27. Despite its increased overall weight, the high efficiency of the electric propulsion system causes the ESAR of the electric baseline aircraft to exceed the ESAR of the reference by more than a factor of two.

	Kerosene weight [kg]	Energy [MJ]	Range [NM]	Range [m]	ESAR [m/MJ]	ESAR [%]
Reference aircraft (ATR 72)	3090	132870	890	1648280	12.4	100
Electric baseline aircraft	-	59834	890	1648280	27.5	222

Table 27, ESAR comparison of the baseline aircraft and the reference

Payload-range

The operational characteristics of conventional aircraft allow for an exchange of payload for additional fuel to increase the effective mission range. However, this concept is not considered for the electric aircraft in the frame of this study. The reason for this is the current loading of the batteries. Swapping batteries for more payload at unchanged take-off weight would mean that the fewer remaining batteries have to deliver the same power as in the nominal case, leading to increased discharge rates and hence lower battery efficiency. Modeling these effects requires detailed information about the battery discharge characteristics which are not available for the future cell-systems considered. However, long range operation with reduced payload is extremely seldom in today's real-world regional aircraft traffic. Figure 120 shows the payload-

range capabilities of the ATR 72-500 and actual operational RITA data of North American ATR 72 operators (year 2012) [142]. Additionally, the characteristics of the electric baseline aircraft are added to the chart. It can be seen that all flown missions in that timespan are within the capabilities of the baseline design, yet the majority of the missions flown is even below 500 nautical miles. The payload-range capabilities of the electric aircraft are hence considered to be satisfactory from a potential operator's perspective.

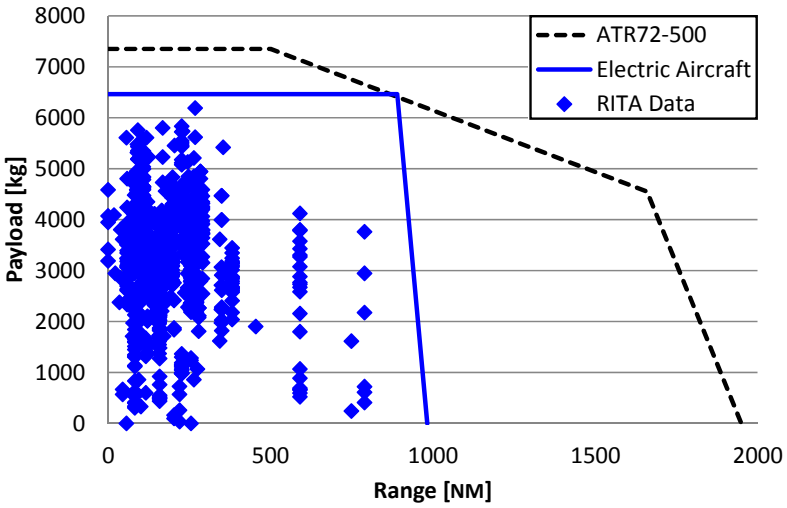

Figure 120, Payload-range performance comparison

Propulsion system layout

Following the considerations and results of section 3.2, the chosen propulsion system layout for the electric baseline aircraft incorporates four battery groups, powering two electric motors via two HV busses. Interconnections between the batteries as well as between the motors ensure redundancies in case of transmission line faults or single component failures. A schematic of the overall system architecture including aircraft systems is given in figure 121, the detailed propulsion system architecture including the selected switch concept is shown in figure 122.

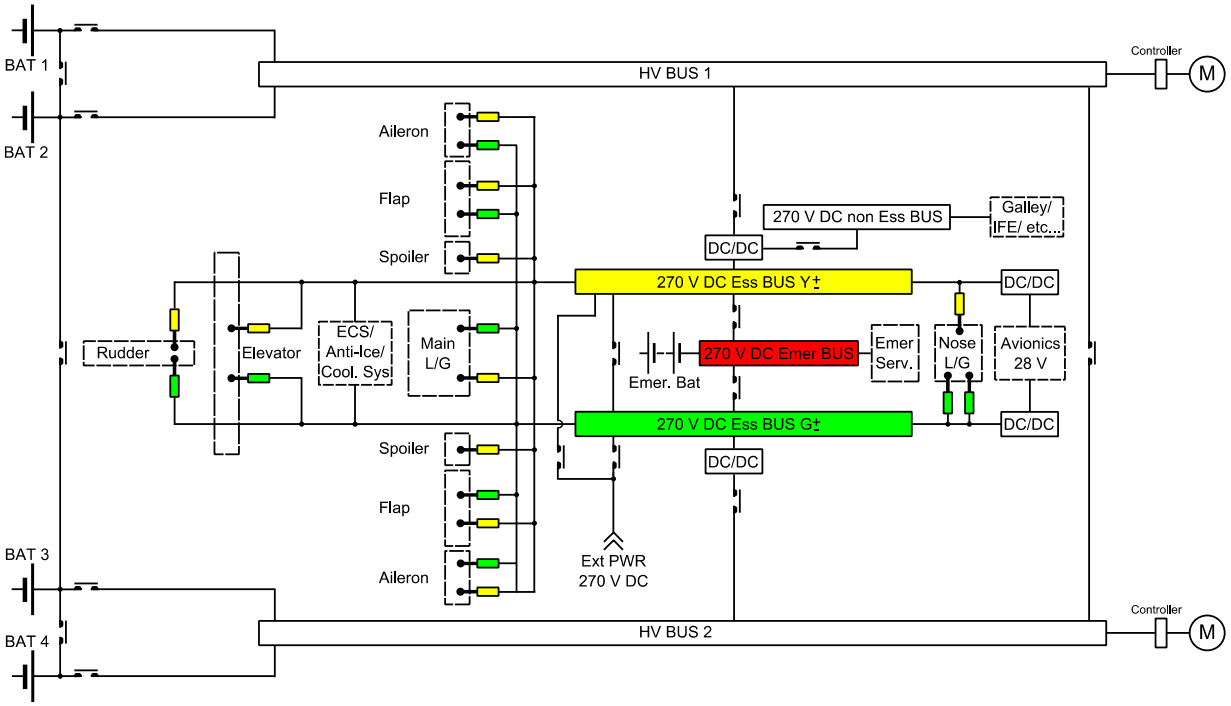

Figure 121, Overall system layout

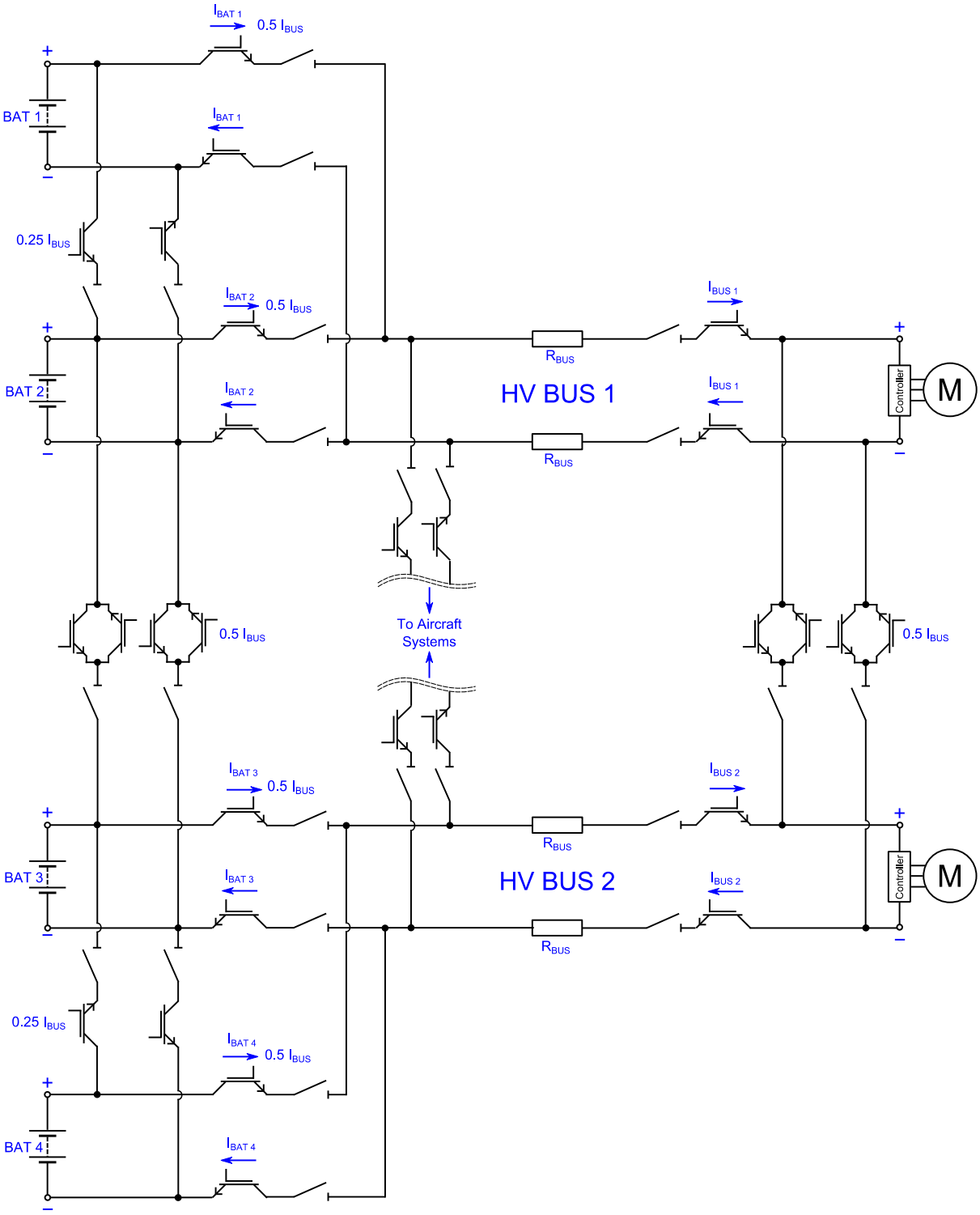

Figure 122, Propulsion system architecture

Mission power profile

The power consumption profiles of the propulsion system, the cryogenic cooling system, as well as the aircraft systems are given in figure 123. The propulsion power represents the sum of both electric motors driving the propellers according to the thrust requirements in the respective mission segments. The power requirement of the cryogenic cooling system is proportional to the associated heat losses and represents the power for driving the cryo-cooler compressors. Even with the electric motors idling, meaning propeller standstill or zero-power wind milling, a minimum of 25 kW power consumption per electric motor is assumed to account for cooling heat in-leaks through the thermal isolation. The aircraft systems power is modeled using average power consumption assumptions, the related power rating is hence constant during the whole mission.

The maximal power demand for propulsion, cooling and aircraft systems amounts roughly 6860 kW, which is at the same time the maximum power demand for the battery system. For the cells used, this peak power setting results in a specific power requirement of 444 W/kg. If the average power demand during the whole mission is taken for reference, the specific power requirement results in 226 Wh/kg. Considering the expected upper long-term limits of future battery cells (1000-1400 W/kg, cf. section 3.1.1), both cases appear to be well within the predicted performance range.

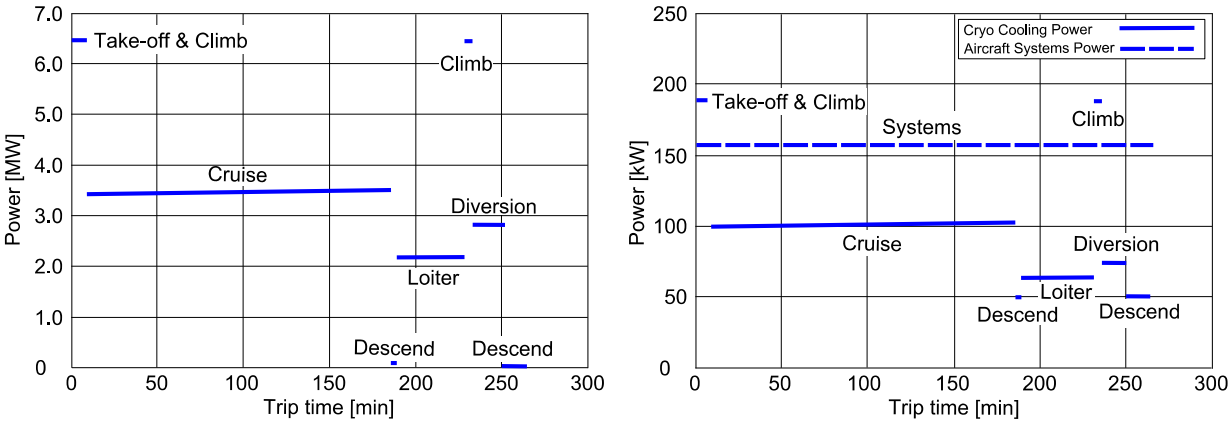

Propulsion system

Aircraft systems and propulsion system cooling

Figure 123, Mission power profile

Battery integration and recharging

For the selected battery integration option within the wing (cf. section 4.1), the maximal available volume is considered to be comparable to the wing tank volume of a conventional wing (cf. section 4.3.7). In case of the baseline aircraft, the 116 m² wing provides a total of 20.5 m³ for battery integration. Considering the required battery capacity of 55600 MJ, a battery energy density of 762 Wh/l is necessary, which is well below the maximum cited value in the literature (2000 Wh/l, cf. section 3.1.1). Even though additional installation space for cooling and BMS is required, the available volume is considered to be sufficient.

As stated above, the maximum power demand for the battery system amounts roughly 6860 kW. Given that the permitted charging power is similar to the maximum discharging power [30], roughly 2 hours and 15 minutes are necessary to recharge the full capacity of 55600 MJ into the

battery. Since this exceeds usual airport turn-around times, a reduction of aircraft utilization has to be accepted or battery exchange concepts have to be considered (cf. section 4.1).

5.2. Sensitivities and Operational Adaptions

The initial baseline design presented in the previous section was sized for the reference mission and based on specific technological assumptions. In the following, the sensitivity of the electric aircraft weight and performance on variations in component performance is evaluated. Furthermore, the impact of different battery integration options as discussed in the previous chapter is evaluated. And finally, the optimization potential of an adapted mission profile is investigated, taking into account the specific operational characteristics of the electric propulsion system.

Sensitivity w.r.t. component performance

In section 3.3, the sensitivity of the propulsion system weight on component performance was evaluated. It turned out that the specific energy of the battery cells, the cell share, and the number of motors are the most critical parameters. In the following sensitivity analysis, all parameters are kept constant at their reference value except for the parameter to be investigated. Mission requirements are unchanged compared to the baseline design. In the figures below, the impact of the parameter variations on the aircraft characteristics is shown.

At first, the sensitivity of aircraft weight on battery cell specific energy and cell share is being evaluated. Figure 124 and figure 125 show the resulting maximum landing weights for the respective cases. As defined in section 3.1.1, the considered specific energy ranges up to 2000 Wh/kg. As could be expected, the aircraft shows a strong sensitivity on the battery weight due to the high weight share of the battery system. Including cascade effects, a doubling in specific energy relative to the reference case (1000 Wh/kg to 2000 Wh/kg) results in a 63% decrease in maximum aircraft landing weight. In the other direction, converging aircraft sizing could only be done down to 810 Wh/kg. For cells with lower specific energy, a weight runaway occurs during the iterative sizing cycles and no valid solution is found for the given set of parameters.

Variations of the cell weight share of the battery system effectively affect its weight in the same way as variations in in the cell specific energy. The impact was investigated in a range from 0.7 to 1. The lower bound of 0.71 is again limited by aircraft sizing convergence, and the maximum value of 1 represents the theoretical case when the battery system weight equals the bare cell weight.

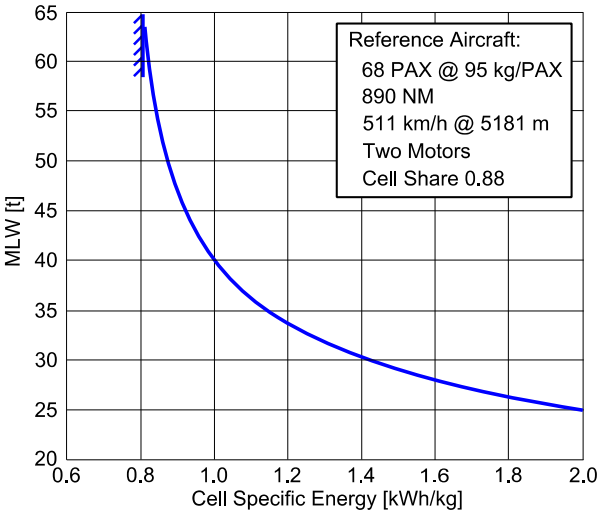

Figure 124, Sensitivity on cell specific energy

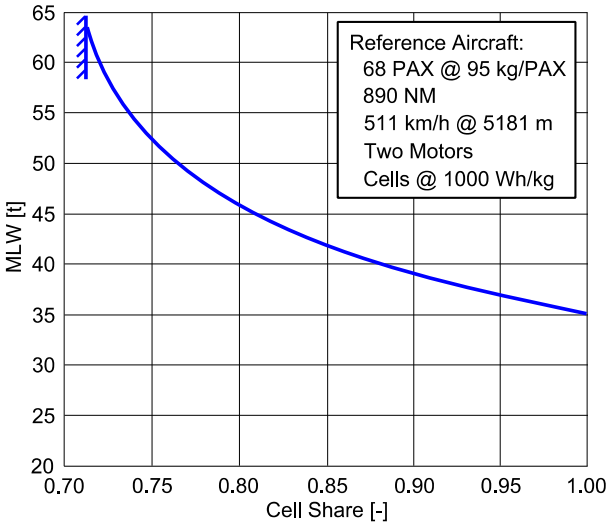

Figure 125, Sensitivity on cell share

Using a hypothetical 2000 Wh/kg cell, the battery weight is significantly lower compared to the baseline, so this case represents the most challenging scenario for the cell's required specific power. Accordingly, 811 W/kg are necessary if the peak power is taken for reference, or 453 W/kg are necessary if the average power is taken. At the same time, the reduced aircraft weight leads to a smaller wing reference area, and hence less available volume for battery integration. As a result, this is also the most demanding case for the required cell energy density: 1140 Wh/l. At the lower specific energy limit (810 Wh/kg), the total amount of stored energy is higher compared to the reference case since the aircraft weight is increased. At the same time, a larger wing is necessary to maintain the same field performance requirements. The resulting larger volume for battery integration leads to a less strict requirement regarding energy density compared to the baseline: 495 Wh/l. The higher battery weight also slightly reduces the specific power demand: 418 W/kg are necessary for the peak power, 183 W/kg if the average power is taken as reference.

Sensitivity w.r.t. number of motors

The second parameter to be evaluated is the motor configuration. Instead of the two-motor layout in case of the baseline, a design with four wing-mounted motors is being considered. Figure 126 shows the corresponding matching chart result. As can be seen, the main difference compared to the baseline are the much relaxed TOFL and missed approach related requirements due to better OEI characteristics, leading to a design power-to-weight ratio of 0.125 kW/kg instead of 0.162 kW/kg. This translates into 24% less total installed power and a reduced aircraft empty weight as shown in table 28. However, the additional propeller slipstream drag of the four-motor configuration as well as the additional wetted area from the two additional nacelles degrade the propulsive efficiency and increase the zero-lift drag. Together with the impact of a smaller wing reference area, as discussed in the previous section, these effects sum up to an 8% increase in the zero-lift drag coefficient. In total, the four-wing configuration shows a MLW benefit of around 1% but suffers a penalty of 5% in terms of energy consumption compared to the baseline.

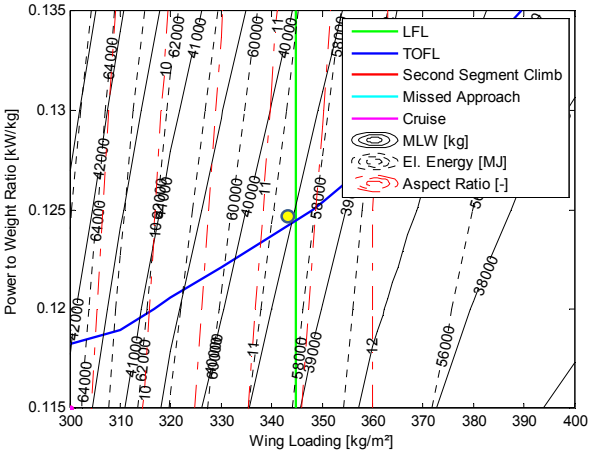

Figure 126, 4 motors - matching chart

	2 mot.	4 mot.		Δ
Power installed	6458	4930	[kW]	-23.7%
Total prop. area	37.7	29.6	[m²]	-21.5%
C_{D0} coefficient	0.0205	0.0222	[-]	+8.3%
Energy stored	55646	58402	[MJ]	+5.0%
Battery weight	17565	18435	[kg]	+5.0%
MLW	39886	39457	[kg]	-1.1%

Table 28, 4-motor layout - sizing results

Sensitivity w.r.t span limitation

As outlined previously, a 36 m span limitation was applied to the baseline aircraft to remain within the ICAO airport category “C”, as required for most regional aircraft. As a result, the wing aspect ratio had to be reduced in order to provide the wing area necessary to meet performance requirements. In figure 127, a matching chart result is shown for the baseline aircraft without this span limitation. The sizing results are shown in table 29. The driving effect here is the higher aspect ratio, leading to lower vortex drag and less required thrust at low flight speed. Yet, under consideration of the assumed maximum aspect ratio of 12, the removal of the span limit only provides a 3% span increase, leading to around 2% reduction in power- and energy consumption, respectively.

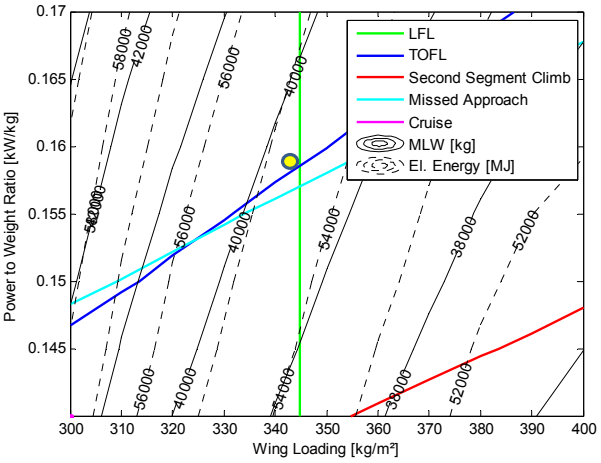

Figure 127, No span limitation - matching chart

	36 m	No lim.		Δ
Wing span	36	37.1	[m]	+3.1%
Power installed	6458	6290	[kW]	-2.6%
Energy stored	55646	54501	[MJ]	-2.1%
Battery weight	17565	17204	[kg]	-2.1%
MLW	39886	39588	[kg]	-0.7%

Table 29, No span limitation - sizing results

Sensitivity w.r.t flight altitude

For conventional regional turbo-prop aircraft, “top of climb” and the cruise speed are often the decisive requirements driving installed engine power. Thereby, the cruise altitude is usually

limited by engine characteristics since the available power is declining due to decreasing air density. In contrast, a battery powered electric propulsion system is largely independent of ambient air conditions, so the full take-off power is generally available in cruise. This characteristic can be used for an operational optimization. Given that a permission of air traffic control is granted, the cruise altitude can be increased to operate the aircraft with its optimal lift coefficient without losing speed performance. The impact of an optimized cruise altitude strongly depends on the respective aerodynamic characteristics, in case of the baseline aircraft the best condition has been found when the cruise altitude is altered from 5181m to 9000 at constant true air speed. By flying at or close to L/D_{max}, the average L/D could be increased from around 18.2 to slightly below 21, as shown in figure 128. Adopting this altitude for the design mission, significant improvements in weight, energy consumption, and installed power could be achieved as listed in table 30.

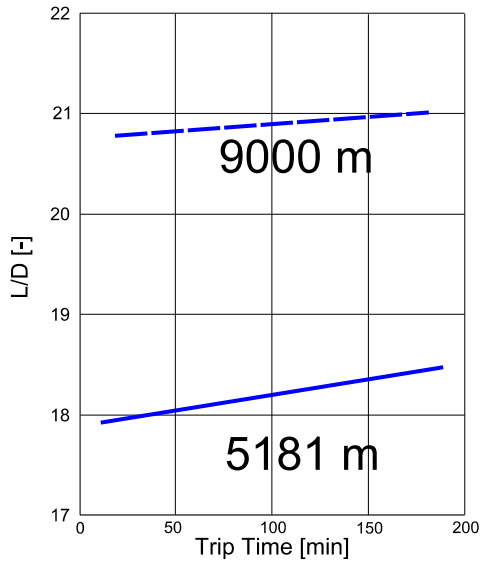

Figure 128, Cruise L/D for different cruise altitudes

	5181 m	9000 m		Δ
Power inst.	6458	5822	[kW]	-9.8%
Energy stored	55646	46504	[MJ]	-16.4%
Battery weight	17565	14679	[kg]	-16.4%
MLW	39886	36184	[kg]	-9.3%

Table 30, Optimized design cruise altitude - sizing results

Sensitivity w.r.t. battery integration

As discussed in section 4.1, two locations for battery integration are being considered in the frame of this study: in the fuselage under-floor compartment and in the wing. While the wing option was chosen for the baseline, the fuselage integration mainly impacts the structural weight of the wing and the fuselage. The missing bending moment relief due to span loading necessitates a structural reinforcement of the wing structure, while the additional battery weight in the fuselage causes likewise the need for structural fuselage reinforcements (cf. section 4.3.2).

The matching chart for the adapted baseline aircraft with the battery integrated in the fuselage is given in figure 129, main results are shown in table 31, and a structural weight breakdown is given in figure 130. The structural weigh penalties of fuselage and wing including the related “snowball” sizing effects cause a significant increase of the empty weight, power requirements and hence total energy consumption. In order to stay within the 36 m span limitation at the required wing area of 154 m², the aspect ratio has to be reduced to 8.4. This has a negative

effect on the low speed aerodynamics (increased vortex drag), with the consequence of higher power requirements for take-off and missed approach scenarios compared to the baseline.

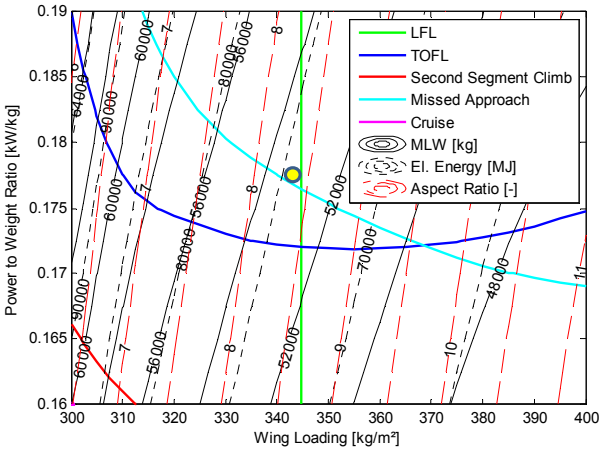

Figure 129, Fuselage battery - matching chart

	Wing batt.	Fusel. batt.		Δ
OEW	15861	23103	[kg]	+46%
Wing ref. area	116	154	[m²]	+32%
Wing AR	11.2	8.4	[-]	-25%
Power inst.	6458	9349	[kW]	+45%
Energy stored	55646	73765	[MJ]	+33%
Battery weight	17565	23284	[kg]	+33%
MLW	39886	52847	[kg]	+32%

Table 31, Fuselage battery - sizing results

In case of the baseline fuselage cross section, housing a four-abreast cabin as defined in section 4.3.1, the available volume in the under-floor compartment amounts roughly 12.5 m³. Considering the required battery capacity of 73770 MJ, a battery energy density of 1640 Wh/l is necessary which is still below the maximum cited value in the literature (2000 Wh/l, cf. section 3.1.1). If this space is sufficient, no further volume in extended wheel fairings is necessary. Figure 131 displays the fuselage cross section showing the cabin configuration and the battery compartment in the fuselage underfloor.

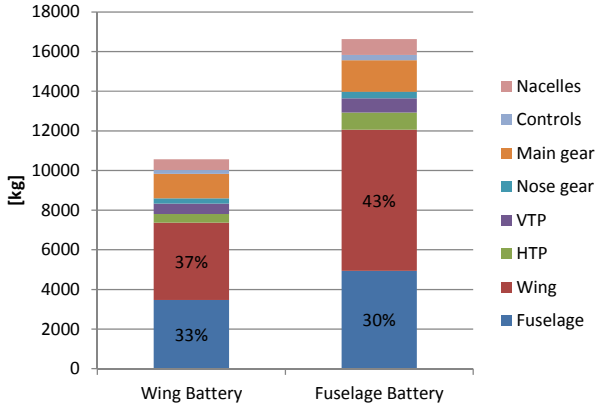

Figure 130, Structural aircraft weight comparison

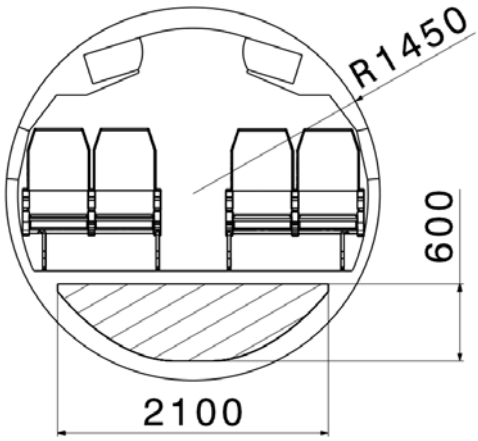

Figure 131, Cabin cross section and battery integration

Despite its structural weight drawbacks, the accessibility of the batteries in the fuselage appears to be much better than in the wing. In case the batteries have to be exchanged during turnaround on the ground, loading and unloading could be done similar to cargo container operation. In contrast, battery exchange provisions for the wing could be associated with additional weight penalties which have not been accounted in the frame of this thesis (cf. section 4.1). The wing integration results are hence to be taken as an ideal case that can be achieved if the wing battery integration can be done without weight penalty.

5.3. Re-Design of the Baseline Configuration

In the previous section, design options and operational adaptions have been identified that reduce the weight penalty related to the electric propulsion system. While up to now each of these adaptions has been evaluated individually, the initial electric baseline configuration is now being re-designed with a combined application of selected design options as summarized in table 32:

Cruise altitude	Adapted to optimized L/D
Span limitation	None
Battery spec. energy	1000 [Wh/kg]
Mission requirements	As baseline, except cruise altitude

Table 32, Parameters for the adapted baseline

Adapted baseline, wing battery

The re-designed baseline is again evaluated with a two- and with a four-motor layout. The matching chart for the two-motor option is given in figure 132, revealing an optimal design point at 344 kg/m² and 0.161 kW/kg. The associated sizing results are given in table 33. As it turns out, the results are identical to the results for optimized flight altitude alone (cf. table 30), since the resulting wing span stayed below the 36m limit and no further improvement could be achieved by removing this limit.

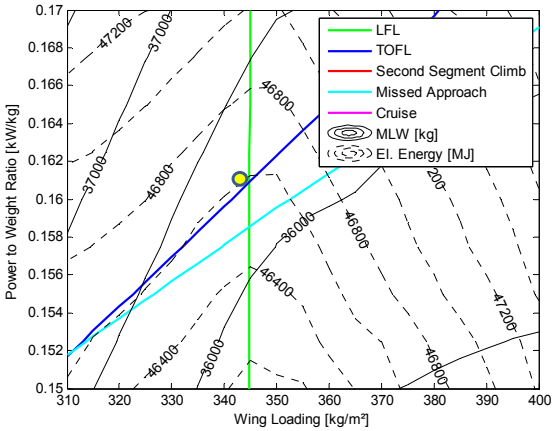

Figure 132, Optimized baseline, 2-motor configuration

	Baseline	Adapt.		Δ
Cruise altitude	5181	9000	[m]	+73.7%
OEW	15861	15044	[kg]	-5.1%
Power inst.	6458	5822	[kW]	-9.8%
Energy stored	55646	46504	[MJ]	-16.4%
Battery weight	17565	14679	[kg]	-16.4%
MLW	39886	36184	[kg]	-9.3%
Wing span	36	35.5	[m]	-1.3%

Table 33, Optimized baseline - 2 motors - sizing results

Similar results are obtained with the four-motor configuration as shown in figure 133 and table 34. Due to the more favorable OEI characteristics, take-off performance can be achieved with less install power, further decreasing the aircraft weight compared to the two-motor configuration. However, the two additional motor nacelles slightly decrease the aerodynamic efficiency, leading to slightly higher energy consumption despite the weight advantage.

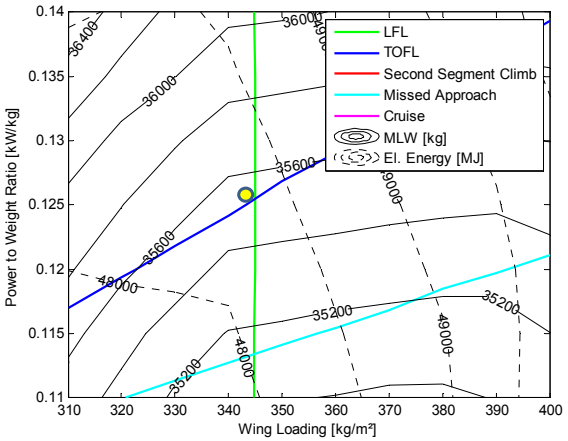

Figure 133, Optimized baseline, 4-motor configuration

	Baseline	Adapt.		Δ
Cruise alt.	5181	9200	[m]	+77.6%
OEW	15861	13826	[kg]	-12.8%
Power inst.	6458	4479	[kW]	-30.6%
Energy stored	55646	48270	[MJ]	-13.3%
Battery weight	17565	15237	[kg]	-13.3%
MLW	39886	35522	[kg]	-10.9%
Wing span	36	35.2	[m]	-2.2%

Table 34, Optimized baseline - 4 motors - sizing results

This optimum relates to an aircraft weight optimum, while the energy consumption optimum is at lower wing loadings in this case. This effect appears due to the high cruise altitude and the small wing area resulting from the design adaptations and the related lower aircraft weight. At cruise altitudes lower than this design case however (off-design), a lower wing loading would deteriorate the aerodynamic efficiency and cause increased energy consumption. The weight optimum is therefore selected as design point.

Adapted baseline, fuselage battery

In case the fuselage option has to be selected for battery integration, e.g. due to battery accessibility requirements, it was shown in the previous section that the wing aspect ratio had to be reduced to 8.4 in order to meet the 36m span limitation (see table 31). The related higher vortex drag at low flight speed had to be compensated by installing 45% more propulsion power. Hence, particularly this configuration benefits from removing the span limitation, optimizing the cruise altitude, and selecting a four-motor layout. The results of an adapted baseline aircraft with a fuselage battery are given in figure 134 and table 35. While there is still a 20% penalty in structural weight, the installed power is now reduced by 17% relative to the baseline. The energy consumption is mainly unchanged, and the resulting total aircraft weight is still around 8% above the baseline.

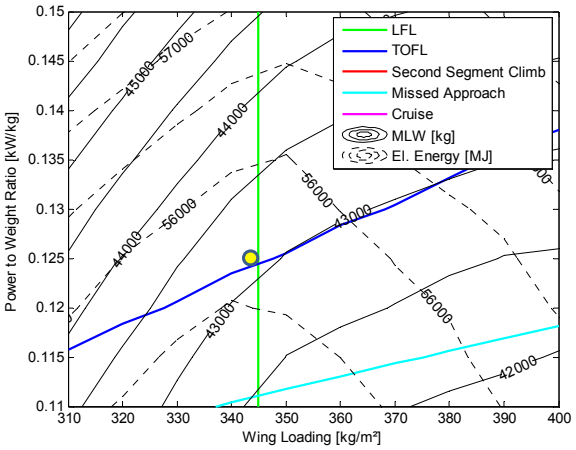

Figure 134, Optimized baseline, fuselage battery, 4-motor configuration

	Baseline	Adapt., fus. batt.		Δ
Cruise alt.	5181	9000	[m]	+73.7%
OEW	15861	19029	[kg]	+20.0%
Power inst.	6458	5372	[kW]	-16.8%
Energy stored	55646	55480	[MJ]	-0.3%
Battery weight	17565	17513	[kg]	-0.3%
MLW	39886	43001	[kg]	+7.8%
Wing span	36	38.7	[m]	+7.5%

Table 35, Optimized baseline, fuselage battery, - 4 motors - sizing results

Impact on ESAR

The design adaptions also improve the block ESAR of the considered aircraft significantly compared to the conventional reference and the baseline aircraft, as shown in table 36.

	Kerosene weight [kg]	Energy [MJ]	Range [NM]	ESAR [m/MJ]	ESAR [%]
Reference aircraft (ATR 72)	3090	132870	890	12.4	100
Electric baseline configuration	-	59834	890	27.5	222
Adapted baseline 2 mot	-	50004	890	33.0	266
Adapted baseline 4 mot	-	51903	890	31.8	256
Adapted baseline 4 mot (fus. battery)	-	59656	890	27.6	223

Table 36, ESAR comparison of the adapted baseline aircraft

The measures taken for the adapted designs enhance the applicability of the electric regional aircraft also with respect to the required battery technology. In figure 135, resulting aircraft landing weights are plotted versus battery cell specific energy for two and four motors and both battery integration options. The four-motor configurations show a weight benefit over the total considered cell range, and for both integration options. Especially at lower specific energy values and higher MLWs, the better OEI characteristics outweigh the aerodynamic degradation effects. In comparison to the baseline aircraft, the lower limit for specific energy is shifted towards lower values for the adapted variants. While design convergence could not be obtained for cells with less than 810 Wh/kg for the baseline design (cf. figure 124), this limit is lowered to 515 Wh/kg in case of the adapted design with four motors. For very advanced cells above 1750 Wh/kg, even the weight disadvantage compared to the conventional reference aircraft disappears.

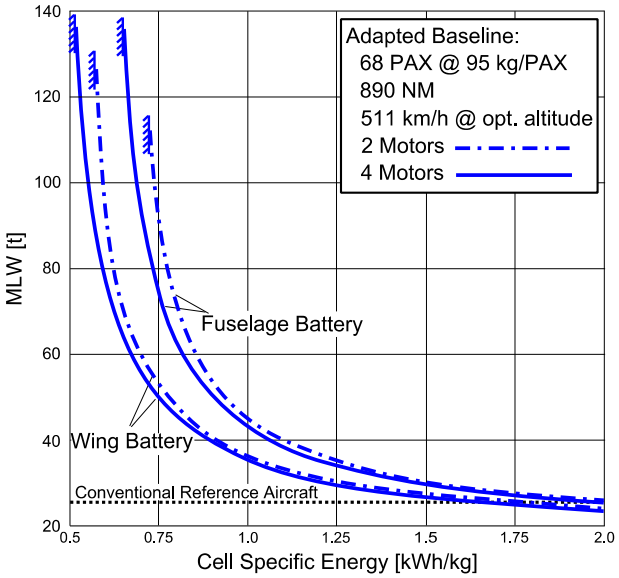

Figure 135, Sensitivity of the adapted baseline on cell specific energy

5.4. The Design Space of Electric Propulsion Aircraft

In the previous section, sizing aspects and sensitivities have been investigated for a regional transport aircraft with fixed mission requirements regarding range and payload. These results are complemented in this section by investigating the impact of different payload- (passengers) and range requirements on the aircraft characteristics. The design space considered therefore covers the 30-seater aircraft class like exemplary the Do 328 up to the 90-seater category as currently proposed by several aircraft manufactures [143]. In the range dimension, distances from 500 NM up to 1200 NM are being considered. The sizing methodology for each aircraft in the design space is the same as for the aircraft discussed so far. Within the study, a fixed set of main design parameters including field performance requirements and mission reserves is used (see table 37). In the sensitivity studies presented in the previous section, the battery technology was identified as the parameter with the highest impact on total aircraft weight. For that reason, the design space is evaluated for different levels of cell specific energy.

TOFL	1360	[m]
LFL	1067	[m]
Cruise speed	511	[km/h]
$C_{L,max}$ take-off/ landing	2.26/ 2.73	[-]
Payload	95	[kg/PAX]
Configuration	4	Motors
Flight altitude	Optimized for max L/D	
Span limitation	None	
Reserves	87 NM, 45 min loiter	
Battery integration	Within wing	

Table 37, Top-level requirements for the design space evaluation

For each considered aircraft in this evaluation, the resulting maximum landing weight and the associated ESAR value is calculated. For comparison, this ESAR value is presented relative to the ESAR of a conventional kerosene-powered aircraft in twin-engine configuration that is sized for the same mission requirements. Therefore, the sizing methodology as applied in case of the design model validation is used (cf. section 4.4). The quotient of both ESAR values provides an assessment of the overall energy efficiency of the electric aircraft compared to an equivalent conventional solution.

Design space granularity

Depending on the number of passengers, corresponding cabin layouts and fuselage geometries are selected as defined in section 4.3.1. The spacing in the passenger dimension (table 38) will be done in two seat-row steps for the three-abreast configuration, two rows for the four-abreast layout, and a single row for the five-abreast layout. In the range dimension, calculations are done using 100 NM increments. Given that a valid solution can be found for each combination of range and payload, this leads to a maximum of 104 aircraft sizing results per design space exploration. Taking also different levels of battery technology into account, this exploration is done for specific energy levels ranging from 400 to 2000 Wh/kg.

Payload dimension			
Passengers	23-38	40-48	83-98
Seat configuration	3 abreast	4 abreast	5 abreast
Spacing for investigation	6 (two rows)	8 (two rows)	5 (one row)

Range dimension	
Range	500-1200 [NM]
Spacing for investigation	100 [NM]

Battery technology	
Specific energy (cell level)	400-2000 [Wh/kg]
Spacing for investigation	100/ 200 [Wh/kg]

Table 38, Parameter resolution for the design space evaluation

Results

The figures below show the design space results for electric regional aircraft. Valid solutions could be generated for all combinations of payload and range for a specific cell energy between 800 Wh/kg and 2000 Wh/kg. Using cells at lower specific energy, some payload-range pairings lead to a battery-induced weight runaway during the iterative sizing process and hence no valid solution could be generated. In the case of the 400 Wh/kg battery, the payload capacities of 80 to 98 passengers could only be achieved for the shortest range of 500 NM.

For the majority of considered battery technologies, the electric aircraft outperform their conventional counterparts in terms of energy efficiency. Only if cells with a specific energy of 600 Wh/kg or less are used and the sizing limits are approached, the relative ESAR falls below unity

with the conventional reference. For the highest considered specific energy (2000 Wh/kg), the ESAR advantage becomes significant with a factor of three to four above the reference.

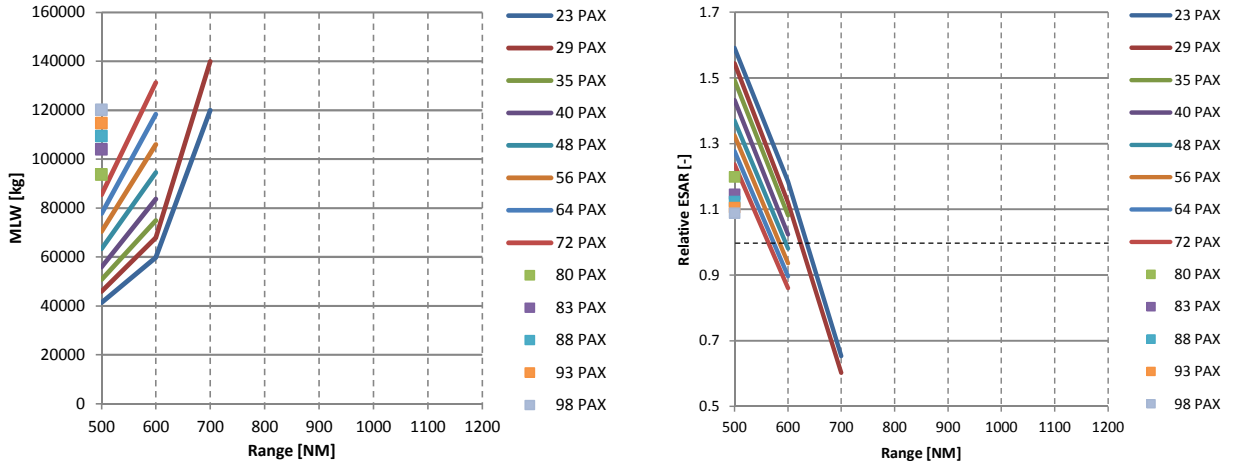

Figure 136, Design space results – 400 Wh/kg cells

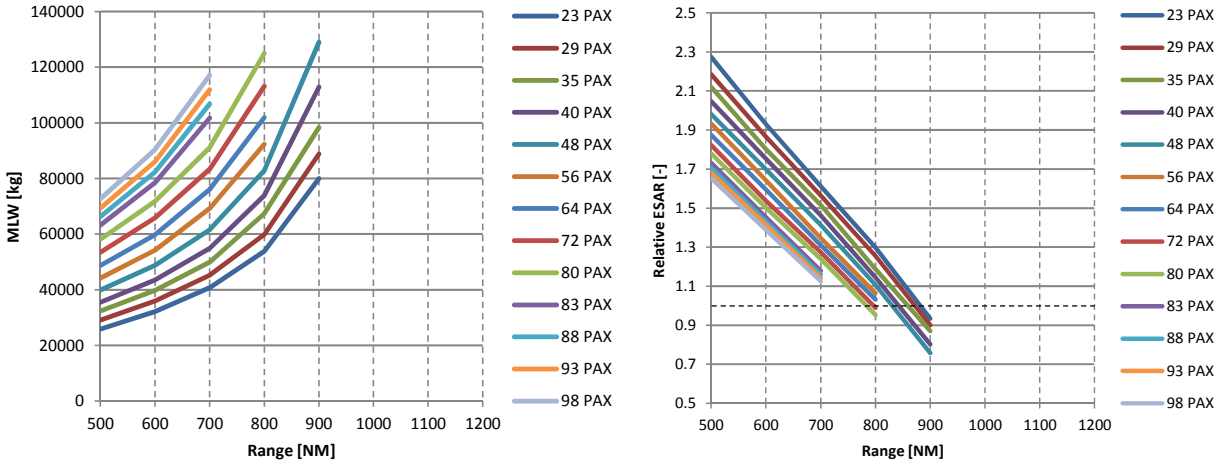

Figure 137, Design space results – 500 Wh/kg cells

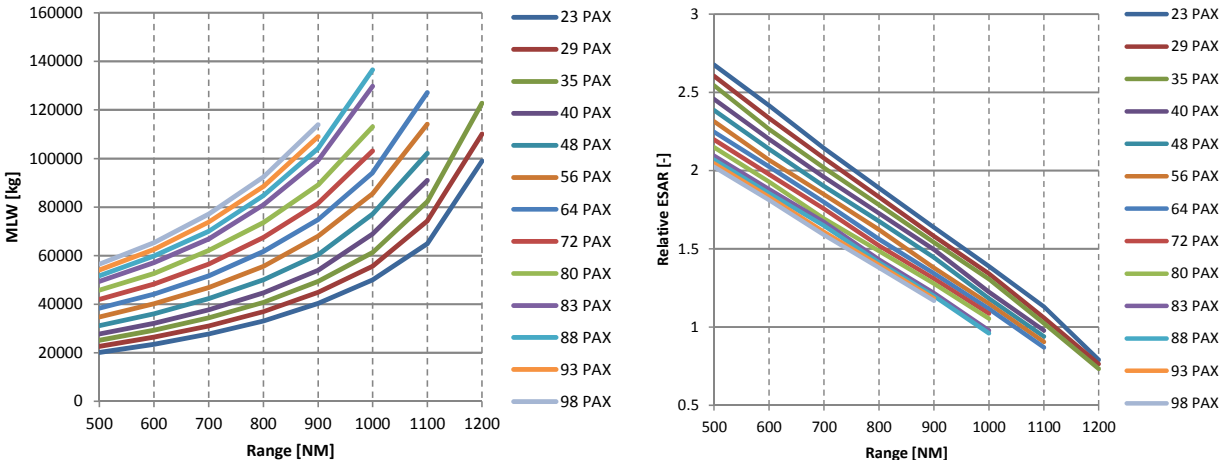

Figure 138, Design space results – 600 Wh/kg cells

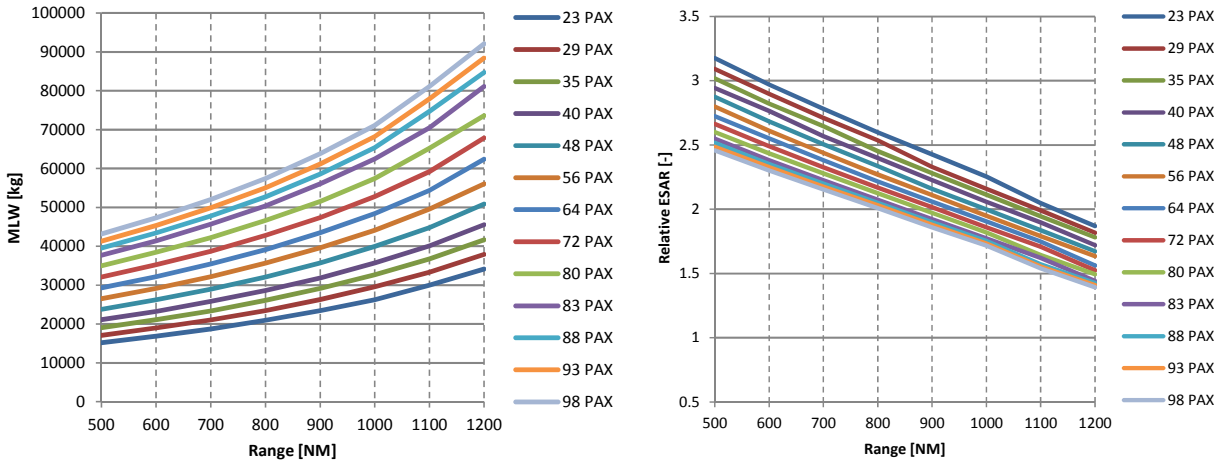

Figure 139, Design space results – 800 Wh/kg cells

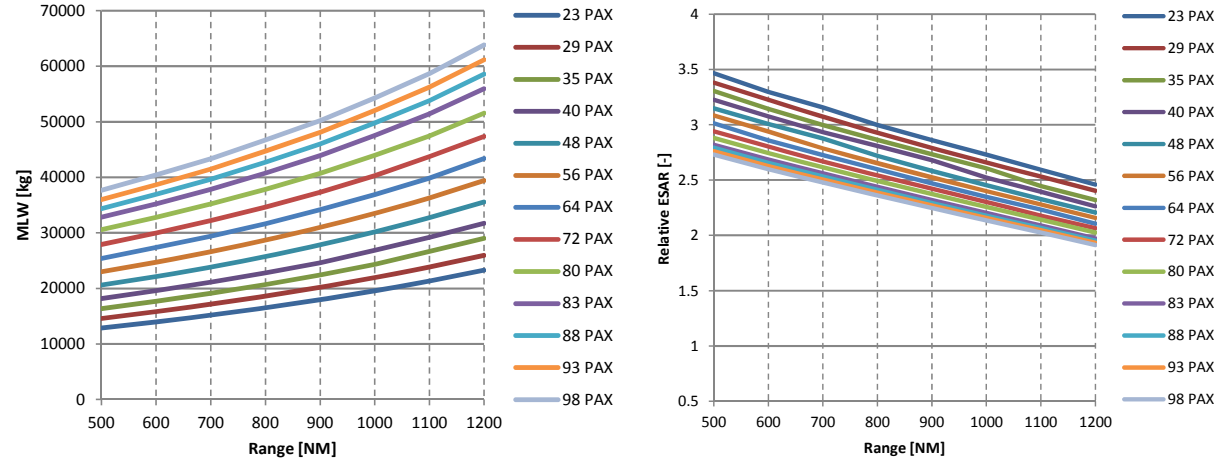

Figure 140, Design space results – 1000 Wh/kg cells

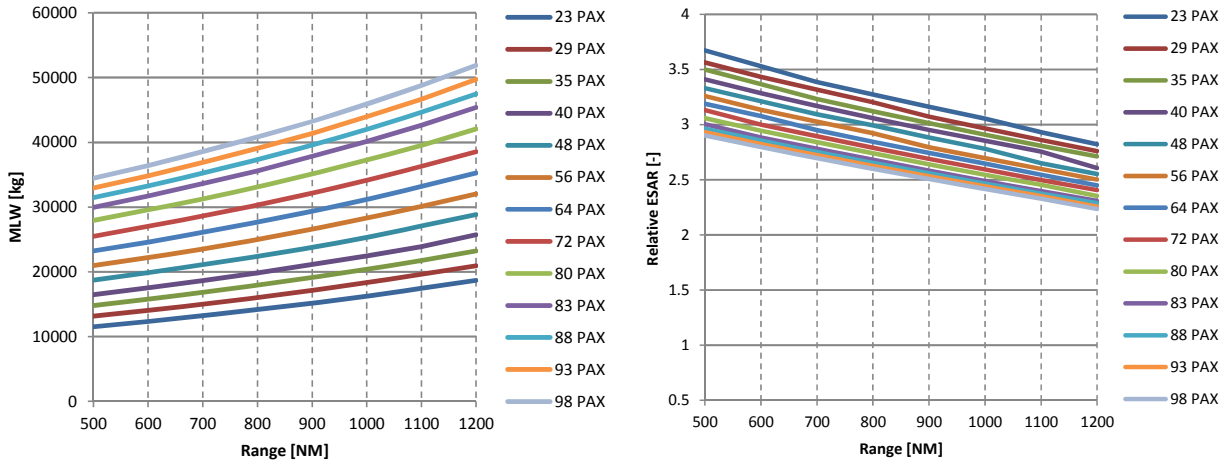

Figure 141, Design space results – 1200 Wh/kg cells

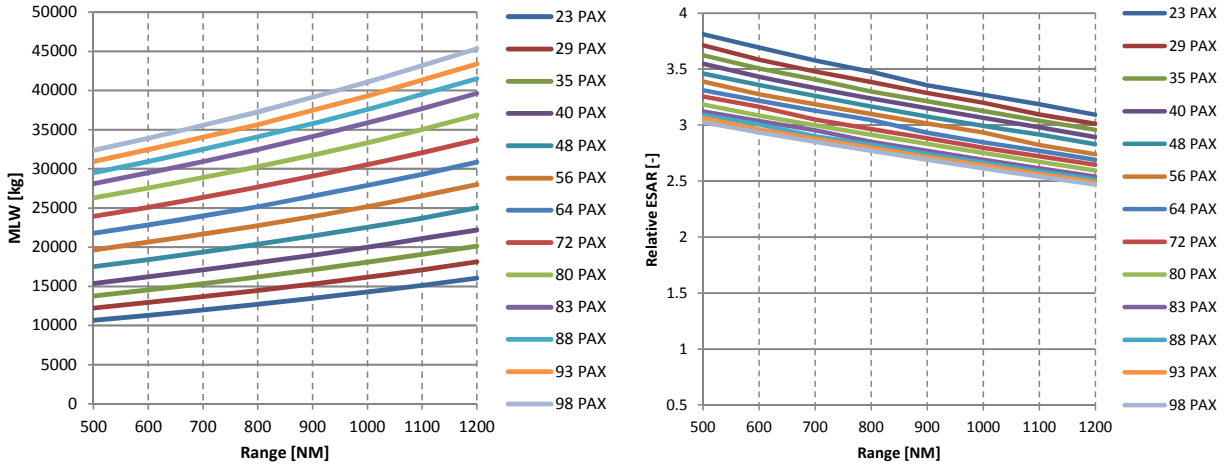

Figure 142, Design space results – 1400 Wh/kg cells

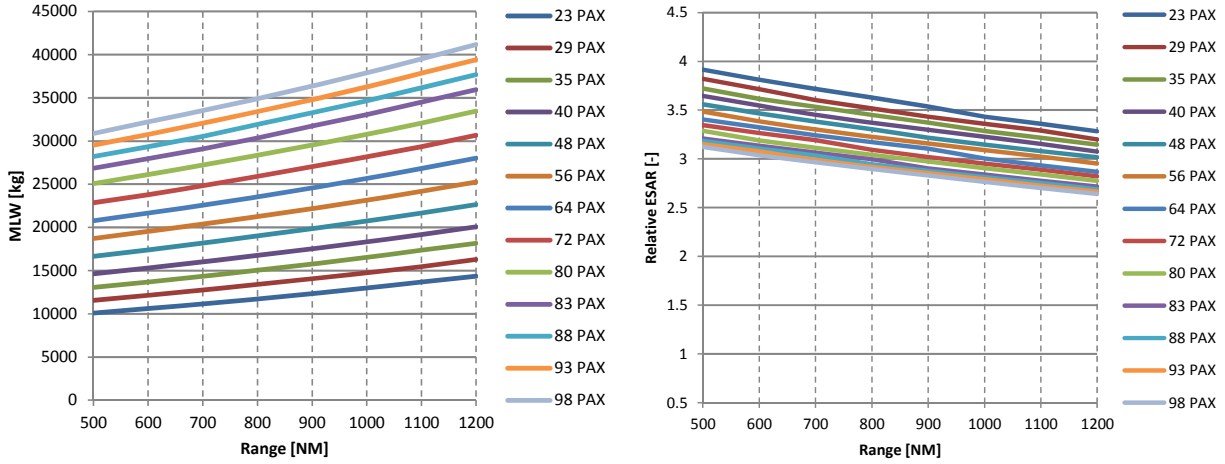

Figure 143, Design space results – 1600 Wh/kg cells

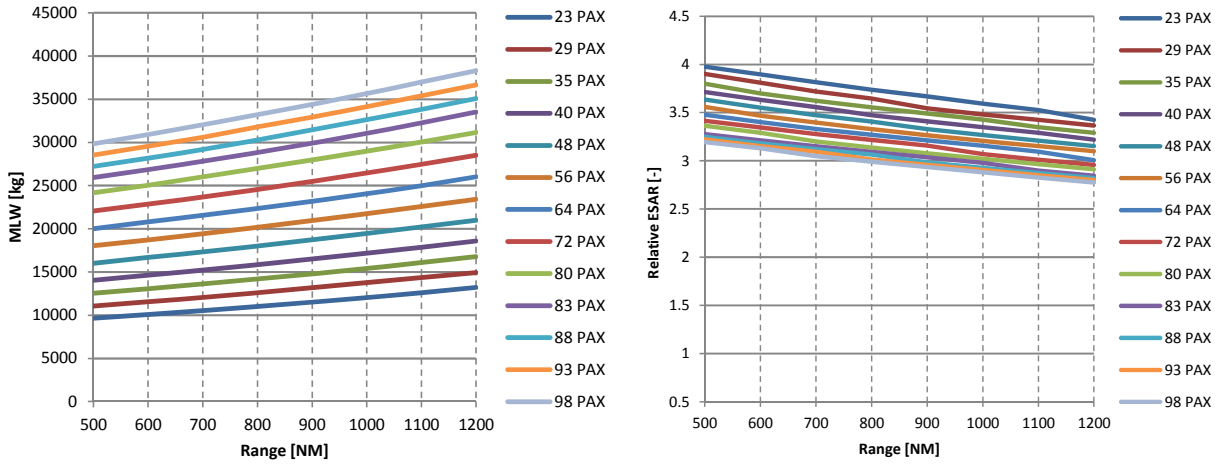

Figure 144, Design space results – 1800 Wh/kg cells

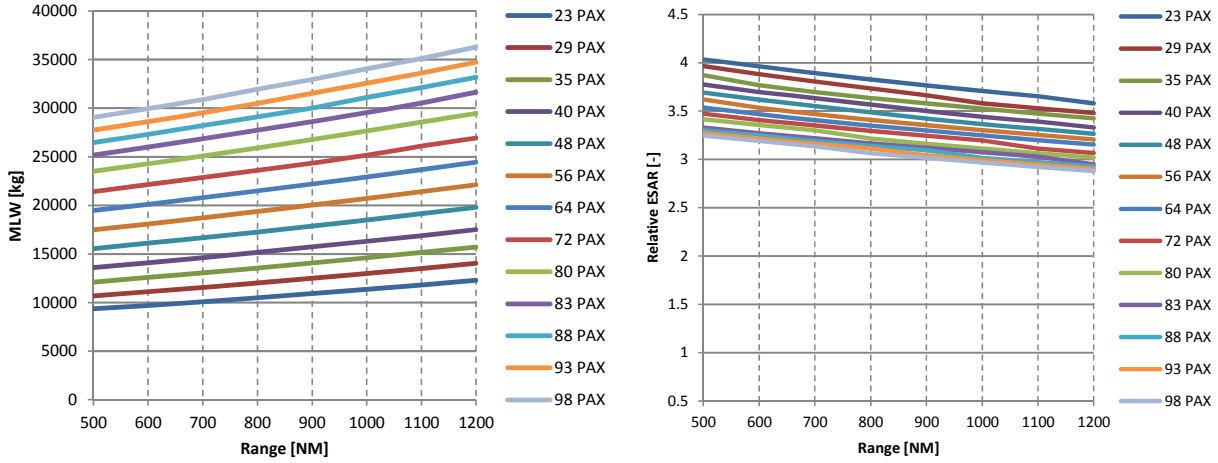

Figure 145, Design space results – 2000 Wh/kg cells

Limits of the design space for different battery technologies

The convergence limits observed in the design space calculations mainly depend on the battery specific energy. These limits are summarized in figure 146. For comparison, the design mission capabilities of in-service regional turboprop aircraft are added. Though there are differences in design speeds and field performance requirements across these reference aircraft, some conclusions about the generally feasible size of electric aircraft can be drawn. First, it turns out that range has a higher impact on the convergence limit than payload. Exemplary for the 500 Wh/kg limit, a 22% reduction in range allows for roughly a doubling of payload. And second, the majority of today's regional aircraft missions could be covered by electric aircraft using battery cells with 600 Wh/kg, given that all components of the electric powertrain are available at the predicted weight and performance levels as discussed (c.f. section 3.3.3). On this understanding, electric regional aircraft appear to be a feasible option, especially if the specific energy of suitable battery cells can be improved to 600 Wh/kg and beyond in the future.

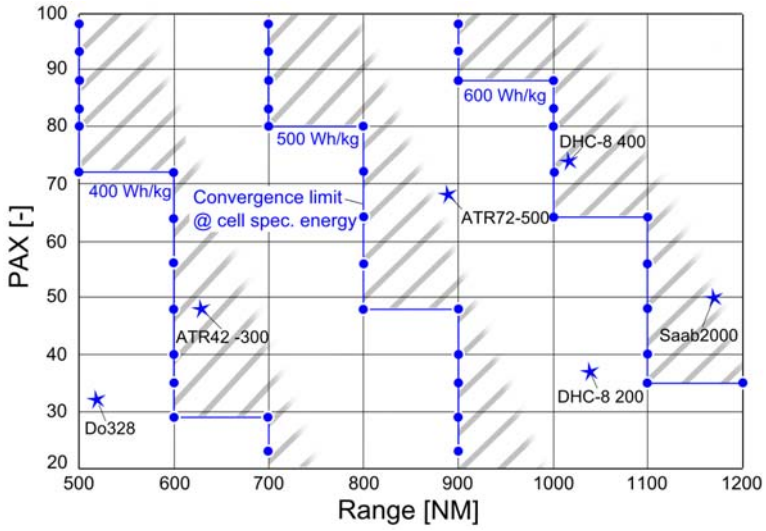

Figure 146, The design space – convergence limits

6. Summary and Outlook

The objective of this thesis was the development of methods for the design and evaluation of future aircraft concepts utilizing electric propulsion. Furthermore, this methodical framework was applied in the preliminary design of battery powered civil transport aircraft. The main design drivers and critical technologies have been identified, and operational and configurational adaptions have been proposed to account for the implications of the new propulsion system. In a design space assessment, weight-related limits of potential electric regional aircraft have been assessed for different levels of battery technology.

6.1. Summary of Results and Findings

For the components of the electric powertrain, state of the art performance data and predictions for future development have been cited. Regarding energy storage, new battery technologies like Li-S and Li-air offer the potential to improve the weight- and volume-specific energy characteristics of future cells significantly. Cited values range up to 2000 Wh/kg and 2000 Wh/l. Since Li-air cells accumulate oxygen compounds during the discharge process, their discharged weight is higher than in the charged state.

Due to potentially high power densities, high temperature superconducting (HTS) electric motors have been considered for power conversion. These machines are cooled by a closed loop cooling system operated by lightweight cryo-coolers. Conceptual designs of such HTS motors for future aerospace applications have been published, reporting around 30 kW/kg excluding cooling system. The related inverters are based on semiconductor materials and are cooled to cryogenic temperatures as well since this offers significant performance benefits. Out of copper, aluminum, and superconducting materials, aluminum has been selected as the best suited conductor material.

Since direct current (DC) has been selected for power transmission, solid state switches are applied for full-load switching. In order to avoid semiconductor losses, a switch arrangement consisting of a solid state switch and a parallel vacuum contactor is used.

The thermal management of the aircraft systems and the propulsion system excluding cryogenic components relies on direct ram air cooling.

As “more electric” aircraft system architectures are already state of the art today, “all electric” air conditioning, actuation, and anti-ice equipment has been selected.

The architectures of the battery system, the distribution system, and the aircraft systems have been designed in compliance with existing certification requirements, if applicable. Since electric propulsion is not covered in today’s certification standards for large aircraft (CS 25) yet, a system design approach following the “equivalent level of safety” principle was applied. In this way, the same redundancy and fail-save requirements of a system or component of a conventional aircraft have been applied on the equivalent system of the electric propulsion aircraft (e.g. fuel system vs. distribution system). As a result, the cells in a battery pack are being monitored by a management system, disconnecting single cells or cell arrays in case of a cell failure. A number of such battery packs are connected to two high voltage DC busses witch supply power to the electric motors. Each component is connected by switches that allow for a galvanic separation of that component in case of a failure. Redundancies ensure that any failure of a major component at any time of the flight does not compromise the continuation of the flight and a safe landing.

The electric propulsion system has several implications on the aircraft design. Since no engines and hence no bleed air is available, all pneumatic and thermal systems (anti-ice, air conditioning) are replaced by “all electric” systems including actuation functionalities.
Since the considered Li-air cells gain weight during discharge, the aircraft reaches its maximum weight at the end of the flight mission. The weight accounting scheme was adapted accordingly. For the considered aircraft, the decisive weight for structural sizing is the maximum landing weight instead of the maximum take-off weight. The field performance was assessed for the respective actual weight condition, while 80% state of charge has been defined as the weight maximum to achieve the take-off field length and initial climb requirements.
Battery accessibility, volumetric requirements, crashworthiness and structural implications are aspects that either favor a battery integration in the wing or in the fuselage. Integration in the wing implies structural- and safety benefits, but at the cost of poor accessibility. Integrating the batteries in the under-floor compartment, battery exchange could be done equivalent to cargo container handling procedures. Yet, increased structural stress in the fuselage, as well as the missing wing bending moment relief implies structural weight penalties.

The presented methods and design principles have been applied for the preliminary design of an electric baseline aircraft, sized for the mission and performance requirements of an ATR 72 reference: 68 passengers over 890 NM at 511 km/h. By this example it could be shown, that the differences in weight progression and propulsion system characteristics lead to different critical requirements for engine or motor sizing. For the ATR 72, the cruise speed and the take-off field length requirements are the decisive conditions. In contrast, the electric powertrain suffers no power lapse with flight altitude, but in relation requires more power at the end of the mission for a missed approach maneuver with OEI. As a consequence, the TOFL, the LFL, and the missed approach requirements are the critical case for the electric aircraft. This initial baseline, with the battery integrated in the wing, two motors, and a 1000 Wh/kg battery, was sized to a MLW of 39.9 t, which means an 88% increase compared to the conventional reference. Despite this weight penalty, the total energy of 55650 MJ, stored in the 17.5 t battery, results in a 120% improvement in energy specific air range due to a better power conversion efficiency.

In a following step, implications of operational and configurational adaptations on the performance and characteristics of the baseline aircraft have been investigated. It was shown, that by selecting a four-motor layout instead of two motors, the total installed power can be reduced by about 24%, leading to a structural weight benefit. On the downside, the additional slipstream drag and the increased wetted area of the additional nacelles increase the energy consumption and partly offset the structural weight advantages by an increased battery weight.
While the baseline aircraft’s span was limited to 36 m to comply with the ICAO airport category C specifications, it was shown that a slight aerodynamic advantage can be achieved by removing this limitation and allowing for a higher wing aspect ratio.
Since electric motors are not affected by air density effects like turboprop engines, electric aircraft can fly at higher cruise altitudes than their conventional counterparts. This ability can be used to select the right altitude for cruise at optimal lift coefficient with the best lift-to-drag ratio. By this, the energy consumption can be reduced by 16% and the aircraft weight by 9%.
While the wing was selected as battery integration option for the baseline aircraft, the impact on structural weight in case of an integration in the fuselage was investigated. Including cascade

effects, the empty weight increase amounts 46%, the power requirements grow by 45%, and the total aircraft weight is 32% higher than in case of the baseline.
By applying the operational and configurational adaptations in combination, synergies and additional cascade effects have been investigated in re-designs of the electric baseline aircraft. The best improvement in aircraft weight could be achieved with a 4-motor, wing-battery configuration and a cruise altitude of 9000m (cf. 5181m for the baseline). The maximum landing weight is reduced from 39.9 t to 35.5 t (-11%). For this re-designed baseline, the installed power requirement is reduced from 6460 kW to 4480 kW (-13%). In case a fuselage battery integration has to be selected for the re-design, e.g. due to accessibility reasons, the penalty in overall aircraft weight compared to the baseline is reduced from 32% to 8%.
It could be shown in sensitivity studies, that the most critical parameter for the electric aircraft is the specific energy of the battery cells used. The respective maximum aircraft weights have been evaluated for cells between 500 Wh/kg and 2000 Wh/kg. For each considered configuration, a minimal specific energy has been identified. Using cells below this limit, a weight runaway occurs during the iterative aircraft sizing process and no valid design solution could be found. This lower cell limit appears at 765 Wh/kg for the baseline design, and at 515 Wh/kg for the adapted baseline (four motors, wing battery). For very advanced cells above 1750 Wh/kg, the propulsion system weight was found to be comparable to a kerosene based conventional system, with the consequence that there is no weight penalty anymore for the corresponding electric aircraft compared a conventional turboprop.
At last, aircraft weight sensitivities, ESAR characteristics, and sizing limits have been evaluated for battery technologies up to 2000 Wh/kg and typical payload-range requirements in a design space investigation. It was shown, that the design range has a higher impact on overall aircraft weight than the number of transported passengers. For the lowest considered specific energy of 400 Wh/kg, valid designs could only be generated for aircraft below 700 NM design range, while for cells with 800 Wh/kg and higher, design solutions for all considered aircraft up to 98 passengers at 1200 NM could be found. Except for aircraft that are close to the sizing limits, an ESAR advantage compared to conventional kerosene-based solutions could be shown.

6.2. Outlook

The focus of this thesis was to develop a methodical framework for electric propulsion in preliminary aircraft design, including an application of these methods for an evaluation of potential applications. It is in the nature of things that the spectrum that has to be considered for this task covers a wide range of technologies and aspects all across the aeronautic disciplines. At some points it was therefore necessary to make simplifications and take assumptions which leave room for a further improvement of modeling depth. Specific areas for potential future follow-on work are summarized hereafter.
The high sensitivity of the aircraft characteristics on battery performance has been shown during the electric aircraft sizing exercises that have been performed in this study. Once the specific discharge characteristic of the considered battery technology is known including thermal and ageing effects, a more detailed battery model has to be developed to account for the resulting implications for the power management, as well as for cooling- and safety aspects. The maximum C-rate capabilities will also determine if on-board recharging is an option or if a battery

exchange mechanism has to be foreseen. In addition, detailed solutions for the integration of the battery system will likely reveal structural implications beyond the effects that have been accounted for at this stage.

More detailed operational- and performance characteristics have to be evaluated and mapped also for the superconducting electric motors. Operational aspects like the required cool-down time of the cryogenic system prior to start have to be assessed and a detailed matching of motor, inverter, and transmission bus voltage has to be done. Next to the variable voltage DC distribution considered in this study, also a fixed voltage network with additional DC/DC converters should be investigated.

Since many of the components used for the propulsion system are in an early development stage, there is no quantitative information about reliability and potential failure rates available yet. Once this is known, a detailed safety analysis of the whole propulsion system and the annexed equipment and technologies has to be performed in accordance with certification standards.

In order to assess the environmental footprint of electric aircraft, methods for product lifecycle evaluation have to be developed to account for production, operation and disposal of the equipment and technologies used. This includes also methods to predict the noise characteristics of electrically driven propulsors, as well as an assessment of the emissions for ground based electric power generation.

And last but not least, methods to assess the economic viability have to be developed, since, given that there are no technological show-stoppers, the economics will decide about the future of electric aircraft propulsion in the end. Next to the pure cost of electric energy, this methodology has to account also the capital cost of the new equipment, potential new maintenance and operational procedures, as well as the financial implications of potential emission trading schemes in the future.

Bibliography

[1] European Commission, "Amending Directive 2003/87/EC so as to improve and extend the greenhouse gas emission allowance trading scheme of the Community," Directive 2009/29/EC, 2009.

[2] European Commission, "Flightpath 2050: Europe's Vision for Aviation," Publications Office of the European Union, Luxembourg, DOI: 10.2777/50266, 2011.

[3] Airbus S.A.S, "Global Market Forecast," Airbus S.A.S, Blagnac, France, 2013.

[4] M. Kumhof and D. Muir, "Oil and the World Economy: Some Possible Futures," International Monetary Fund, Working Paper No. 12/256, Washington, D.C., 2012.

[5] Bundesregierung, "Nationaler Entwicklungsplan Elektromobilität der Bundesregierung," Bundesministerium für Bildung und Forschung, Berlin, Germany, 2009.

[6] J. B. Boucher, "History of Solar Flight," in *AIAA/SAE/ASME 20th Joint Propulsion Conference*, Cincinnati, Ohio, 1984. AIAA 84-1429.

[7] P. Masson, "Albert Tissandier," *La Nature,* vol. #1738, p. 256, 1906.

[8] Monash University, "Aeromodellers of the Past 200 Years," June 2015. [Online]. Available: http://www.ctie.monash.edu.au/.

[9] R. Moulton, "An electric aeroplane," *Flight International,* vol. 104, no. 3378, p. 946, 1973.

[10] G. Marzinzik, "Flugbericht Antares: Den Sternen schon sehr nah," *Aerokurier,* no. 10, pp. 50-53, Oktober 2003.

[11] Electric Aircraft Corporation, "ElectraFlyer," March 2014. [Online]. Available: http://www.electraflyer.com.

[12] T. Tomažič, V. Plevnik, G. Veble, T. Jure, F. Popit, S. Kolar, R. Kikelj, J. W. Langelaan and K. Miles, "Pipistrel Taurus G4: on Creation and Evolution of the Winning Aeroplane of NASA Green Flight Challenge 2011," *Journal of Mechanical Engineering,* vol. 57, no. 12, pp. 869-878, 2011. DOI:10.5545/sv-jme.2011.212.

[13] R. Voit-Nitschmann, L. Schumann and S. Geinitz, "e-Genius – Elektroflugzeug in CFK - Bauweise," in *Fachtagung Carbon Composites*, Augsburg, Germany, 2012.

[14] J. L. Felder, H. D. Kim and G. V. Brown, "Turboelectric Distributed Propulsion Engine Cycle Analysis for Hybrid-Wing-Body Aircraft," in *47th AIAA Aerospace Sciences Meeting Including The New Horizons Forum and Aerospace Exposition*, Orlando, Florida, 2009. AIAA 2009-1132.

[15] A. R. Gibson, D. Hall, M. Waters, B. Schiltgen, T. Foster, J. Keith and P. Masson, "The Potential and Challenge of TurboElectric Propulsion for Subsonic Transport Aircraft," in *48th AIAA Aerospace Sciences Meeting Including the New Horizons Forum and Aerospace Exposition*, Orlando, Florida, 2010. AIAA 2010-276.

[16] E. M. Greitzer and H. N. Slater, "N3 Aircraft Concept Designs and Trade Studies, Final Report," NASA Glenn Research Center, NASA CR-2010-216794, Cleveland, Ohio, 2010.

[17] L. Lorenz, H. Kuhn and A. Sizmann, "Hybrid Power Trains for Future Mobility," in *62. Deutscher Luft- und Raumfahrtkongress*, Stuttgart, Germany, 2013.

[18] C. Pornet, C. Gologan, P. C. Vratny, A. Seitz, O. Schmitz, A. T. Isikveren and M. Hornung,

"Methodology for Sizing and Performance Assessment of Hybrid Energy Aircraft," in *Aviation Technology, Integration, and Operations Conference*, Los Angeles, California, 2013. AIAA 2013-4415.

[19] C. Pornet, C. Gologan, P. C. Vratny, A. Seitz, O. Schmitz, A. T. Isikveren and M. Hornung, "Methodology for Sizing and Performance Assessment of Hybrid Energy Aircraft," *Journal of Aircraft,* vol. 52, no. 1, pp. 341-352, 2015. DOI 10.2514/1.C032716.

[20] M. K. Bradley and C. K. Droney, "Subsonic Ultra Green Aircraft Research: Phase I Final Report," NASA Langley Research Center, NASA CR–2011-216847, Hampton, Virginia, 2011.

[21] R. Kluge, "E-Star, E-Fan, E-Thrust, Auf dem Weg zum Elektrischen Luftverkehr," *FliegerRevue - Special Triebwerke,* no. 09, pp. 30-31, September 2013.

[22] S. Stückl, J. van Toor and H. Lobentanzer, ""VoltAir – The All Electric Propulsion Concept Platform – A Vision for Atmospheric Friendly Flight," in *28th International Congress of the Aeronautical Sciences (ICAS)*, Brisbane, Australia, 2012.

[23] P. C. Vratny, A Battery Powered Transport Aircraft: A Concept Study of a Real All Electric Aircraft, Saarbrücken, Germany: AV Akademikerverlag, 2012.

[24] M. Hornung, A. T. Isikveren, M. Cole and A. Sizmann, "Ce-Liner – Case Study for eMobility in Air Transportation," in *Aviation Technology, Integration, and Operations Conference*, Los Angeles, California, 2013. AIAA 2013-4302.

[25] A. T. Isikveren, A. Seitz, P. Vratny, C. Pornet, K. O. Plötner and M. Hornung, "Conceptual Studies of Universally-Electric System Architectures Suitable for Transport Aircraft," in *61. Deutscher Luft- und Raumfahrtkongress*, Berlin, Germany, 2012.

[26] M. Hepperle, "Electric Fight: Potential and Limitations," in *AVT-209 Workshop on Energy Efficient Technologies and Concepts Operation, STO-MP-AVT-209*, Lisbon, Portugal, 2012.

[27] R. A. McDonald, "Fundamental Sizing Implications of Constant or Increasing Weight Aircraft," in *12th AIAA Aviation Technology, Integration, and Operations (ATIO) Conference* , Indianapolis, Indiana, 2012. AIAA 2012-5516.

[28] A. Seitz, A. T. Isikveren and M. Hornung, "Pre-Concept Performance Investigation of Electrically Powered Aero-Propulsion Systems," in *49th AIAA/ASME/SAE/ASEE Joint Propulsion Conference*, San Jose, California, 2013. AIAA-2013-3608.

[29] D. Rakov and J. Thorbeck, "Gestaltung und Modellierung von elektrisch angetriebenen Regionalflugzeugen unter besonderer Berücksichtigung von Start- und Landung," in *62. Deutscher Luft- und Raumfahrtkongress*, Stuttgart, Germany, 2013.

[30] A. Jossen and W. Weydanz, Moderne Akkumulatoren richtig einsetzen, Untermeitingen, Germany: Reichardt Verlag, 2006.

[31] H. J. Bergveld, Battery Management Systems: Design by Modelling, Luxemburg: Springer Science+ Business Media, 2002.

[32] A. Jossen and M. Wohlfahrt-Mehrens, "Overview on current status of lithium-Ion batteries," in *2. International Renewable Energy Storage Conference*, Bonn, Germany, 2007.

[33] K. Tatsumi, "Battery Technologies for Cars," in *International Workshop on Technology*

Learning and Deployment, Paris, France, 2007.

[34] K. A. Friedrich, "Kritische (realistische) Bewertung neuer Batteriesysteme," in *61st Annual Meeting of the International Society of Electrochemistry*, Nice, France, 2010.

[35] Y. Mikhaylik, C. Scordilis-Kelley, M. Safont, M. Laramie, R. Schmidt, H. Schneider and K. Leitner, "High Energy Rechargeable Li-S Battery Development at Sion Power and BASF," in *International Battery Association IBA2013*, Barcelona, Spain, 2013.

[36] K. Kumaresan, Y. Mikhaylik and R. E. White, "A Mathematical Model for a Lithium–Sulfur Cell," *Journal of The Electrochemical Society,* vol. 155 , no. 8, pp. A576-A582, June 2008. DOI: 10.1149/1.2937304.

[37] Y. Mikhaylik, "Fundamental Chemistry of Sion Power Li/S Battery," in *International Battery Association & Hawaii Battery Conference IBA-HBC*, Waikoloa, Hawaii, 2006.

[38] G. Zheng, Y. Yang, J. J. Cha, S. S. Hong and Y. Cui , "Hollow Carbon Nanofiber-Encapsulated Sulfur Cathodes for High Specific Capacity Rechargeable Lithium Batteries," *Nano Leters,* vol. 11, no. 10, pp. 4462-4467, 2011. DOI: 10.1021/nl2027684.

[39] Y. Mikhaylik, I. Kovalev, J. Xu and R. Schock, "Rechargeable Li-S Battery with Specific Energy 350 Wh/kg and Specific Power 3000 W/kg," in *213th Electrochemical Society Meeting*, Phoenix, Arizona, 2008.

[40] J. R. Akridge, "Lithium Sulfur Rechargeable Battery Safety," *Battery Power Products & Technology,* vol. 10, 2001.

[41] G. Girishkumar, B. McCloskey, A. C. Luntz, S. Swanson and W. Wilcke, "Lithium-Air Battery: Promise and Challenges," *The Journal of Physical Chemistry Letters,* vol. 1, no. 14, pp. 2193-2203, 2010. DOI: 10.1021/jz1005384.

[42] A. Dobley, C. Morein, R. Roark and . K. Abraham, "Large Prototype Lithium Air Batteries," in *The proceedings of the 42nd Power Sources Conference*, Philadelphia, Pennsylvania, 2006.

[43] J. Christensen, P. Albertus, R. S. Sanchez-Carrera, T. Lohmann, B. Kozinsky, R. Liedtke, J. Ahmed and A. Kojic, "A Critical Review of Li/Air Batteries," *Journal of The Electrochemical Society,* vol. 159 , no. 2, pp. R1-R30, 2011. DOI: 10.1149/2.086202jes.

[44] A. Kraytsberg and Y. Ein-Eli, "Review on Li–air batteries - Opportunities, limitations and perspective," *Journal of Power Sources,* vol. 196, no. 3, pp. 886-893, 2010. DOI: 10.1016/j.jpowsour.2010.09.031.

[45] C. K. Park, S. B. Park, S. Y. Lee, H. Lee, H. Jang and W. I. Cho, "Electrochemical Performances of Lithium-air Cell with Carbon Materials," *Bulletin of the Korean Chemical Society,* vol. 31, no. 11, pp. 3221-3224, 2010. DOI: 10.5012/bkcs.2010.31.11.3221.

[46] J.-S. Lee, S. T. Kim, C. Ruiguo, N.-S. Choi, M. Liu, K. T. Lee and J. Cho, "Metal–Air Batteries with High Energy Density: Li–Air versus Zn–Air," *Advanced Energy Materials,* vol. 1, no. 1, pp. 34-50, 2011. DOI: 10.1002/aenm.201000010.

[47] J. P. Zheng, R. Y. Liang, M. Hendrickson and E. J. Plichta, "Theoretical Energy Density of Li–Air Batteries," *Journal of The Electrochemical Society,* vol. 155, no. 6, pp. A432-A437, 2008. DOI: 10.1149/1.2901961.

[48] S. Visco, E. Nimon, B. Katz, M. Chu and L. De Jonghe, "High Energy Density Lithium-Air

Batteries with No Self Discharge," in *Proceeedings of the 42nd Power Sources Conference, pp. 201-203*, Philadelphia, Pennsylvania, 2006.

[49] L. Johnson, "The Viability of High Specific Energy Lithium Air Batteries," in *Symposium on Research Opportunities in Electrochemical Energy Storage - Beyond Lithium Ion: Materials Perspectives*, Oak Ridge, Tennessee, 2010.

[50] T. Lösche-ter Horst, "A Vision for Future Mobility – Volkswagen's Fuel and Powertrain Strategy," in *European Sustainable and Responsible Investment (SRI) Conference*, Paris, France, 2009.

[51] A. Thielmann, R. Isenmann and M. Wietschel, "Technologie-Roadmap Lithium-Ionen-Batterien 2030," Fraunhofer-Institut für System- und Innovationsforschung ISI, Karlsruhe, Germany, 2010.

[52] P. C. Vratny, C. Gologan, C. Pornet, A. T. Isikveren and M. Hornung, "Battery Pack Modeling Methods for Universally-Electric Aircraft," in *4th CEAS Air & Space Conference* , Linköping, Sweden, 2013.

[53] W. Hufnagel, Aluminium-Taschenbuch, Düsseldorf, Germany: Aluminium-Verlag GmbH, 1988.

[54] Nexans S.A., "Power Cables 1 - 30 kV," June 2010. [Online]. Available: www.nexans.de.

[55] B. Portwood and M. Sadeghi, "Aircraft Wiring Practices," in *Federal Aviation Administration, Interactive Training and Self-Study Course*, Washington, D.C., 2001.

[56] R. Farrell, "High Temperature Superconducting Underground Power Cable - The "Albany Cable Project"," DOE Cooperative Agreement Number DE-FC36-03GO013301, Schenectady, New York, 2010. DOI: 10.2172/975691.

[57] K. Allweins and E. Marzahn, "Feasibility of HTS DC Cables on Board a Ship," in *10th EPRI Superconductivity Conference*, Tallahassee, Florida, 2011.

[58] T. J. Haugan, J. D. Long, L. A. Hampton and P. N. Barnes, "Design of Compact, Lightweight Power Transmission Devices for Specialized High Power Applications," *SAE International Journal of Aerospace,* vol. 1, no. 1, pp. 1088-1094, 2008. DOI: 10.4271/2008-01-2930.

[59] M. J. Gouge, J. A. Demko, B. W. McConnell and J. M. Pfotenhauer, "Cryogenics Assessment Report," Oak Ridge National Laboratory, Oak Ridge, Tennessee, 2002.

[60] D. Willen, F. Hansen, M. Daumling, C. N. Rasmussen, J. Ostergaard, C. Traholt, E. Veje, O. Tonnesen, K.-J. Jensen, S. K. Olsen, C. Rasmussen, E. Hansen, O. Schuppach, T. Visler, S. Kvorning, J. Schuzster, J. Mortensen, J. Christiansen and S. D. Mikkelsen, "First operation experiences from a 30 kV, 104 MVA HTS power cable installed in a utility substation," *Physica C: Superconductivity and its Applications,* Vols. 372-376, no. 3, pp. 1571-1579, 2002. DOI: 10.1016/S0921-4534(02)01066-3.

[61] H. X. Xi, W. Z. Gong, Y. Zhang, Y. F. Bi, H. K. Ding, H. Wen, B. Hou and Y. Xin, "China's 33.5 m, 35 kV/2 kA HTS ac power cable's operation in power grid," *Physica C: Superconductivity and its Applications,* Vols. 445-448, pp. 1054-1057, 2006. DOI: 10.1016/j.physc.2006.05.075.

[62] G. V. Brown, H. D. Kim and J. Felder, "Materials Aspects of Turboelectric Aircraft Propulsion," in *Annual Meeting Fundamental Aeronautics Program*, Atlanta, Georgia,

2009.

[63] P. Hofmann, Hybridfahrzeuge, Wien, Austria: Springer-Verlag, 2010.

[64] R. Jäger and E. Stein, Leistungs-Elektronik, Berlin, Germany: VDE Verlag, 2000.

[65] K. Iniewski , Radiation Effects in Semiconductors, Boca Ration, Florida: CRC Press, 2010.

[66] D. Izquierdo, A. Barrado, C. Raga, M. Sanz and A. Lazaro, "Protection Devices for Aircraft Electrical Power Distribution Systems: State of the Art," *IEEE Transactions on Aerospace and Electronic Systems,* vol. 47, no. 3, pp. 1538-1550, July 2011. DOI: 10.1109/TAES.2011.5937248.

[67] Hitachi Power Semiconductor Device Ltd., "Hitachi High-power IGBT Modules - Status List," 2012. [Online]. Available: http://www.hitachi-power-semiconductor-device.co.jp.

[68] GIGAVAC LLC, "GIGAVAC Product Catalough - Single Pole Double Throw, SPDT," March 2013. [Online]. Available: http://www.gigavac.com.

[69] Remy International Inc., "Remy HVH250 Series Electric Motors," 2010. [Online]. Available: http://www.remyinc.com/.

[70] M. Dudley, "Promising Electric Aircraft Drive Systems," in *EAA Electric Aircraft World Symposium, ARC-E-DAA-TN2019*, Oshkosh, Wisconsin, 2010.

[71] Wollenberg, Johannes - Siemens AG, "Hybride Antriebssysteme für Luftfahrzeuge," in *Luftfahrt der Zukunft*, Braunschweig, Germany, 2014.

[72] K. Vogt, Elektrische Maschinen. Berechnung rotierender elektrischer Maschinen, Berlin, Germany: VEB Verlag Technik, 1983.

[73] J. Bardeen, L. N. Cooper and J. R. Schrieffer, "Theory of Superconductivity," *Physical Review,* vol. 108, no. 5, pp. 1175-1204, 1957.

[74] P. N. Barnes, M. D. Sumption and G. L. Rhoads, "Review of high power density superconducting generators: Present state and prospects for incorporating YBCO windings," *Cryogenics,* vol. 45, no. 11-12, pp. 670-686, 2005. DOI: 10.1016/j.cryogenics.2005.09.001.

[75] S. Kalsi, "The State of Superconducting Technology," presented at US Naval Graduate School, Monterey, California, 2005.

[76] J. Doernhach, "Assessment of High Temperature Superconducting (HTS) Electric Motors for Rotorcraft Propulsion," NASA Glenn Research Center, NASA-CR-185222, Cleveland, Ohio, 1990.

[77] P. J. Masson, D. S. Soban, E. Upton, J. E. Pienkos and C. A. Luongo, "HTS Motors in Aircraft Propulsion: Design Considerations," *IEEE Transactions on Applied Superconductivity,* vol. 15, no. 2, pp. 2218-2221, 2005. DOI: 10.1109/TASC.2005.849616.

[78] P. J. Masson, T. Nam, T. P. Choi, P. Tixador, M. Waters, D. Hall, C. A. Luongo and D. N. Mavris, "Superconducting Ducted Fan Design for Reduced Emissions Aeropropulsion," *IEEE Transactions on Applied Superconductivity,* vol. 19, no. 3, pp. 1662 - 1668, 2009. DOI: 10.1109/TASC.2009.2018156.

[79] P. J. Masson, G. V. Brown, D. S. Soban and C. A. Luongo, "HTS machines as enabling technology for all-electric airborne vehicles," *Superconductor Science and Technology,* vol. 20, no. 8, pp. 748-756, 2007. DOI:10.1088/0953-2048/20/8/005.

[80] K. Sivasubramaniam, T. Zhang, M. Lokhandwalla, E. T. Laskaris, J. W. Bray, B. Gerstler, M. R. Shah and J. P. Alexander, "Development of a High Speed HTS Generator for Airborne Applications," *IEEE Transactions of Applied Superconductivity,* vol. 19, no. 3, pp. 1656-1661, 2009. DOI: 10.1109/TASC.2009.2017758.

[81] G. V. Brown, "Weights and Efficiencies of Electric Components of a Turboelectric Aircraft Propulsion System," in *49th AIAA Aerospace Sciences Meeting including the New Horizons Forum and Aerospace Exposition*, Orlando, Florida, 2011. AIAA 2011-225.

[82] P. Masson and C. Luongo, "HTS Machines for Applications in All-Electric Aircraft," in *IEEE Power Engineering Society General Meeting*, Tampa, Florida, 2007. DOI: 10.1109/PES.2007.385622.

[83] P. J. Masson, J. E. Pienkos and C. A. Luongo, "Scaling Up of HTS Motor Based on Trapped Flux and Flux Concentration for Large Aircraft Propulsion," *IEEE Transactions on Applied Superconductivity,* vol. 17, no. 2, pp. 1579-1582, 2007. DOI: 10.1109/TASC.2007.898111.

[84] C. Luongo, P. Masson, T. Nam, D. Mavris, H. Kim, G. Brown, M. Waters and D. Hall, "Next Generation More-Electric Aircraft: A Potential Application for HTS Superconductors," *IEEE Transactions on Applied Superconductivity,* vol. 19, no. 3, pp. 1055-1068, 2009. DOI: 10.1109/TASC.2009.2019021.

[85] H. J. M. ter Brake and G. F. M. Wiegerinck, "Low-power cryocooler survey," *Cryogenics,* vol. 42, no. 11, pp. 705-718, 2002. DOI: 10.1016/S0011-2275(02)00143-1.

[86] Creare Inc., "Thermal Management System for Superconducting Aircraft," Creare Inc., NASA Phase 1 SBIR, NNX09CC77P, Hanover, New Hampshire, 2009.

[87] P. Kittel, "Cryocooler Performance Estimator," *Cryocoolers,* vol. 14, pp. 563-572, 2007.

[88] G. V. Brown, A. F. Kascak, B. Ebihara, D. Johnson, B. Choi, M. Siebert and C. Buccieri, "NASA Glenn Research Center Program in High Power Density Motors for Aeropropulsion," NASA Glenn Research Center, NASA TM-2005-213800, Cleveland, Ohio, 2005.

[89] N. E. Anderson, S. H. Loewenthal and J. D. Black, "An Analytical Method To Predict Efficiency of Aircraft Gearboxes," *Journal of Mechanical Design,* vol. 108, no. 3, pp. 424-432, 1986. DOI: 10.1115/1.3258750.

[90] R. H. Zimmermann and W. Robinson, "Equipment Cooling Systems for Aircraft, Part I & II," WADC Technical Report 54-359, Dayton, Ohio, 1954.

[91] M. Drela, "Aerodynamics of Heat Exchangers for High-Altitude Aircraft," *Journal of Aircraft,* vol. 33, no. 1, pp. 176-184, 1996. DOI: 10.2514/3.46919.

[92] G. Hagmann, Leistungselektronik, Wiebelsheim, Germany: AULA-Verlag GmbH, 2009.

[93] P. Haldar, H. Ye, H. Efstathiadis, J. Raynolds, M. J. Hennessy, O. M. Mueller and E. K. Mueller, "Improving Performance of Cryogenic Power Electronics," *IEEE Transactions on Applied Superconductivity,* vol. 15, no. 2, pp. 2370-2375, June 2005. DOI: 10.1109/TASC.2005.849668.

[94] M. Al Sakka, J. Van Mierlo and H. Gualous , "DC/DC Converters for Electric Vehicles," *Electric Vehicles–Modelling and Simulations,* vol. 1, no. 1, pp. 309-332, 2011. DOI: 10.5772/17048.

[95] W. Qian, F. Z. Peng and L. M. Tolbert, "Development of a 55 kW 3X DC-DC Converter for HEV Systems," in *IEEE Vehicle Power and Propulsion Conference*, Dearborn, Michigan, 2009.

[96] E. Torenbeek, Synthesis of Subsonic Airplane Design, Delft, The Netherlands: Delft University Press, 1982.

[97] G. J. D. Zondervan, A Review of Propeller Modelling Techniques Based on Euler Methods, Delft, The Netherlands: Delft University Press , 1998.

[98] K. Ibrahim, "Selecting Principal Parameters of Baseline Design Configuration for Twin Turboprop Transport Aircraft," in *22nd Applied Aerodynamics Conference and Exhibit*, Providence, Rhode Island, 2004. AIAA 2004-5069.

[99] M. Lazareff, "Aerodynamics of Shrouded Propellers," *AGARDograph,* vol. 126, pp. 237-289, 1968.

[100] R. M. Plencner, P. Senty and T. Wickenheiser, "Propeller Performance and Weight Predictions Appended to the Navy/NASA Engine Program," NASA Glenn Research Center, NASA TM 83458, Cleveland, Ohio, 1983.

[101] J. W. Bennett, Fault Tolerant Electromechanical Actuators for Aircraft, Newcastle, United Kingdom: University of Newcastle upon Tyne, 2010.

[102] S. L. Botten, C. R. Whitley and A. D. King, "Flight Control Actuation Technology for Next-Generation All-Electric Aircraft," *Technology Review Journal,* vol. 23, no. 6, p. 55–68, 2000.

[103] P. Laskaridis, "Performance Investigations and Systems Architectures for the More-Electric Aircraft," Ph.D. dissertation, School of Engineering, Cranfield University, Cranfield, United Kingdom, 2004.

[104] M. Garrison and S. Steffan, "Two-Fault Tolerant Electric Actuation Systems for Space Applications," in *42nd AIAA/ASME/SAE/ASEE Joint Propulsion Conference & Exhibit*, Sacramento, California, 2006. AIAA 2006-4939.

[105] S. C. Jensen, G. D. Jenney and D. Dawson, "Flight Test Experience With an Electromechanical Actuator on the F_18 Systems Research Aircraft," in *Digital Avionics Systems Conference*, Philadelphia, Pennsylvania, 2000.

[106] C. P. Lawson and J. M. Pointon, "Thermal management of electromechanical actuation on an all-electric aircraft," in *26th International Congress of the Aeronautical Sciences*, Anchorage, Alaska, 2008.

[107] Rockwell International Corporation, "Airplane Actuation Trade Study," AFWAL-TR-82-3108, Dayton, Ohio, 1983.

[108] R. Slingerland, S. Zandstra, D. Scholz and K. Seeckt, "Green Freighter Systems," in *46th AIAA Aerospace Sciences Meeting and Exhibit*, Reston, Virginia, 2008.

[109] T. R. Ensign, "Performance and Weight Impact of Electric Environmental Control System and More Electric Engine on Citation CJ2," in *45th AIAA Aerospace Sciences Meeting and Exhibit*, Reno, Nevada, 2007.

[110] G. E. Tagge, L. A. Irish and A. R. Bailey, "Systems Study for an Integrated Digital/Electric Aircraft (IDEA)," NASA Langley Research Center, NASA-CR-3840, Hampton, Virginia,

1985.

[111] Avions de Transport Régional (ATR), "ATR 72 Flight Crew Operating Manual," Blagnac, France, 1999.

[112] Z. Goraj, "An Overview of the Deicing and Anti-Icing Technologies with Prospects for the Future," in *24th International Congress of the Aeronautical Sciences*, Yokohama, Japan, 2004.

[113] European Aviation Safety Agency (EASA), "CS-25: Certification specifications and acceptable means of compliance for large aeroplanes," *Amendment 12,* 2012.

[114] A. K. Friedrich, N. Wagner and W. G. Bessler, "Entwicklungsperspektiven von Li-Schwefel und Li-Luft-Batterien," in *Energiespeichersymposium Stuttgart*, Stuttgart, Germany, 2012.

[115] P. Van den Bossche, F. Vergels, J. Van Mierlo, J. Matheys and W. Van Autenboer, "SUBAT: An assessment of sustainable battery technology," *Journal of Power Sources,* vol. 162, no. 2, pp. 913-919, 2005. DOI:10.1016/j.jpowsour.2005.07.039.

[116] H. Smalag and H. Scholze, Keramik, Teil 2: Keramische Werkstoffe, Berlin, Germany: Springer-Verlag, 1983.

[117] C. Bezard, "Risks related to Lithium Batteries," in *18th Flight Safety Conference* , Berlin, Germany, 2012.

[118] T. Nelson, "787 Systems and Performance," Boeing Commercial Airplanes, Renton, Washington, 2005.

[119] R. Flosdorff and G. Hilgarth, Elektrische Energieverteilung, Stuttgart, Germany: Teubner, 1994.

[120] Smartcockpit, "A318/A319/A320/A321 Flight Crew Operating Manual, Electrical," 2013. [Online]. Available: http://www.smartcockpit.com/plane/AIRBUS/A320.html.

[121] I. Cotton and A. Nelms, "Higher Voltage Aircraft Power Systems," *IEEE A&E Systems Magazine,* vol. 23, no. 2, pp. 25-32, Februar 2008. DOI: 10.1109/MAES.2008.4460728 .

[122] ZES Zimmer Electronic Systems GmbH, ""ZES Sensors and Accessories"," 2014. [Online]. Available: www.zes.com.

[123] C. Klumpner and F. Blaabjerg, "Using reverse blocking IGBTs in power converters for adjustable speed drives," *IEEE Transactions on Industry Applications,* vol. 42, no. 3, pp. 807-816, 2006. DOI: 10.1109/TIA.2006.872956.

[124] Avions de Transport Régional (ATR), "ATR: The Optimum Choice for a Friendly Environment," 2001. [Online]. Available: http://www.atraircraft.com.

[125] The MathWorks Inc., "Die Sprache für technische Berechnungen," Copyright 1994-2015, 2015. [Online]. Available: http://de.mathworks.com/products/matlab/.

[126] 328 Support Services GmbH, "Dornier 328-100 (TP)," 2013. [Online]. Available: www.328.eu.

[127] Avions de Transport Régional (ATR), "The Regional Way To Profitability," 2011. [Online]. Available: www.atraircraft.com.

[128] BAE Systems, "Avro RJ - General Data," 2009. [Online]. Available: www.regional-services.com.

[129] Luftfahrttechnisches Handbuch, www.lth-online.de, 2006.

[130] A. Seitz, "Advanced Methods for Propulsion System Integration in Aircraft Conceptual Design," PhD dissertation, Institut für Luft- und Raumfahrt, Technical University of Munich, Munich, Germany, 2012.

[131] S. Stückl, "Conceptual Design of VTOL Tilt Wing Aircraft for Flexible Transport Missions," Diploma thesis, Institut für Luft- und Raumfahrt, Technical University of Munich, Munich, Germany, 2009.

[132] P. D. Raymer, Aircraft Design: A Conceptual Approach, Washington, D.C.: AIAA Education Series, 1992.

[133] A. Seitz, O. Schmitz, A. T. Isikveren and M. Hornung, "Electrically Powered Propulsion: Comparison and Contrast to Gas Turbines," in *61. Deutscher Luft- und Raumfahrtkongress*, Berlin, Germany, 2012.

[134] European Union, "Commission Regulation (EC) No859/2008," *Official Journal of the European Union, OJ L 254,* pp. 1-238, 2008.

[135] J. Anderson, Introduction to Flight, Boston, Massachusetts: McGraw-Hill Higher Education, 2005.

[136] Pratt & Whitney Canada, "PT6 status and information report," Longueuil, Kanada, 1966.

[137] F. Stagliano and H. Lobentanzer, "Impact of Novel Propulsion System Architectures Incorporating Diesel Engines on Mission Fuel Burn for a Tilt-Wing Transport Aircraft," in *12th AIAA Aviation Technology, Integration, and Operations (ATIO) Conference*, Indianapolis, Indiana, 2012. AIAA 2012-5587.

[138] P. Walsh and P. Fletcher, Gas Turbine Performance, Oxford, United Kingdom: Blackwell Science Ltd., 2004.

[139] Bombardier Inc., "Q400 NextGen Brochure," 2014. [Online]. Available: www.q400nextgen.com.

[140] Civil Aviation Authority, "Check Flight Schedule Dornier 328-110 (P&W 119B engines)," CFS 284, Issue 1, Kingsway, United Kingdom, 2013.

[141] National Transportation Safety Board (NTSB), "Aircraft Accident Report: Loss of Control on Approach, Colgan Air, Inc. Operating as Continental Connection Flight 3407, Bombardier DHC-8-400," NTSB/AAR-10/01, Washington, D.C, 2009.

[142] The Research and Innovative Technology Administration (RITA), "Air Carrier Statistics - T100 Domestic Market," United States Department of Transportation, Washington, D.C., 2013.

[143] B. Perrett, "Field of Five," *Aviation Week & Space Technology,* vol. 175, no. 27, p. 38, 2013.

Annex

The methods for aircraft weight modeling and aerodynamic assessment that are used in this thesis are largely based on the standard preliminary design literature. While in section 4.3 only the references to the respective methods are given, the explicit functions and formulas are presented hereafter.

A. Implemented Weight Modeling Methods

Wing weight: Torenbeek [96]**, eq. 8-12**	
$w_{wing}[kg] = k_w {b_s}^{0.75} \left\{1 + \sqrt{\frac{b_{ref}}{b_s}}\right\} {n_{ult}}^{0.55} \left(\frac{b_s/t_r}{W_G/S}\right)^{0.3}$	
$k_w = 6.67 \cdot 10^{-3}$ $W_G = MZFW\ or\ MLW\ [kg]$ $b_s = structural\ wingspan\ [m]$ $b_{ref} = 1.905\ [m]$	$n_{ult} = ultimate\ load\ factor\ [-]$ $t_r = wing\ root\ thickness\ [m]$ $S = wing\ reference\ area\ [m]$

Fuselage: LTH [129]**, MA 508 12-02**	
$w_{fuselage}[kg] = 9.733 \left(\frac{V_D}{100}\right)^{0.359} (1 + \Delta P)^{0.203} \left(\frac{b}{l} \cdot 100\right)^{0.195} (b \cdot l)^{0.814} (1 + k_{FT})^{0.367} {m_N}^{0.197} {m_{ST}}^{0.187}$	
$V_D = design\ dive\ speed\ [km/h]$ $\Delta P = differential\ cabin\ pressure\ [bar]$ $b = fuselage\ width\ [m]$ $l = fuselage\ length\ [m]$	$k_{FT} = 0.4$ $m_N = payload\ mass\ [t]$ $m_{ST} = max. aircraft\ weight\ [t]$

Horizontal tail: Torenbeek [96]**, Eq.8-14**	
$w_{HTP}[kg] = k_h S_h f\left(\frac{{S_h}^2 V_D}{\sqrt{cos\Lambda_h}}\right)$	
$k_h = 1$ (fixed incidence HTP) $S_h = HTP\ reference\ area\ [m^2]$ $V_D = design\ dive\ speed\ [km/h]$	$\Lambda_h = HTP\ sweep\ angle$ $f\left(\frac{{S_h}^2 V_D}{\sqrt{cos\Lambda_h}}\right) = statistical\ correlation, see\ Torenbeek\ fig. 8-5$

Vertical tail: Torenbeek [96]**, Eq.8-15**	
$w_{VTP}[kg] = k_v S_v f\left(\frac{{S_v}^2 V_D}{\sqrt{cos\Lambda_v}}\right)$	
$S_v = HTP\ reference\ area\ [m^2]$ $\Lambda_h = HTP\ sweep\ angle$	$k_v = HTP - size\ dependent\ factor\ for\ fin\ mounted\ HTPs\ [-]$ $f\left(\frac{{S_v}^2 V_D}{\sqrt{cos\Lambda_v}}\right) = statistical\ correlation, see\ Torenbeek\ fig. 8-5$

Nose/ main landing gear: Torenbeek [96]**, Eq.8-17**	
$w_{UC}[kg] = k_{UC}\left\{A + B\,W_{to}{}^{\frac{3}{4}} + C\,W_{to} + D\,W_{to}{}^{\frac{3}{2}}\right\}$	
$k_{UC} = 1.08\ \left(for\ high\ wing\ \frac{A}{C}\right)$ $W_{to} = max\ aircraft\ weight\ [kg]$	$For\ factors\ A, B, C\ and\ D, see\ Torenbeek\ \ tab. 8-6$

Turbo-shaft engine weight: Stückl [131]
$w_{TS}[kg] = 2.5401 \cdot (P_{TO} \cdot 1.341022)^{0.585}$
$P_{TO} = take-off\ rated\ shaft\ power\ [kW]$

Engine/ motor nacelle weight: Torenbeek [96] **Eq.8-24**
$w_N[kg] = 0.0852\ P_{TO}$
$P_{TO} = take-off\ rated\ shaft\ power\ [kW], (per\ engine)$

Surface control group weight: Torenbeek [96] **Eq.8-18**	
$w_{SC}[kg] = 0.45359\ k_{SC}\ k_{ld}\ W_G$	
$k_{SC} = 0.64\ for\ transport\ aircraft$ $k_{ld} = 1.15\ for\ the\ use\ of\ spoilers$	$W_G = MTOW\ [kg]$

Instruments weight: Torenbeek [96] **Eq.8-32**	
$w_I[kg] = k_I\,W_{DE}{}^{5/9}\,R_D{}^{1/4}$	
$k_I = 0.347$ $W_{DE} = design\ empty\ weight\ [kg]$	$R_D = maximum\ range\ [km]$

Electric system weight: Torenbeek [96] **Eq.8-42**	
$w_I[kg] = k_I\,W_{DE}{}^{5/9}\,R_D{}^{1/4}$	
$k_I = 0.347$ $W_{DE} = design\ empty\ weight\ [kg]$	$R_D = maximum\ range\ [km]$

Furnishing and equipment weight: Torenbeek [96] **Tab. 3-2 and Tab. 8-12**
$Pilot\ seats\ [kg] = 43.6$
$Passenger\ seats\ [kg] = \frac{n_{PAX}}{2} * 13.2 + 13.2$
$Galleys\ [kg] = 113.4$
$Lavatories\ [kg] = 75$
$Fuselage\ floor\ covering [kg] = 0.94\ S_{cf}{}^{1.15}$
$Various\ items\ [kg] = 3.69\ V_{pc}{}^{1.14}$
$Cargo\ accomodations\ [kg] = 12.8$
$Oxygen\ system\ [kg] = 13.6 \cdot 0.544\ n_{PAX}$
$Fire\ detection\ [kg] = 0.003\ W_{to}$

$Escape\ provisions\ [kg] = 0.453\ \ (n_{PAX}\ + 4)$	
$n_{PAX}\ = number\ of\ passengers\ [-]$ $W_{to}\ = max. aircraft\ weight\ [kg]$	$S_{cf}\ = cabin\ floor\ area\ [m^2]$ $V_{pc}\ = passenger\ cabin\ volume\ [m^3]$

Operational items weight: Torenbeek [96] **Tab. 8-13**
$Flight\ \&\ cabin\ crew\ with\ luggage\ \ [kg] = \frac{n_{PAX}}{39} \cdot 68 + 2 \cdot 93$ $Passenger\ cabin\ supplies\ \ [kg] = 8.62\ n_{PAX}$ $Potable\ water\ and\ toilet\ chemicals\ [kg] = 0.68\ n_{PAX}$ $Safety\ equipment\ [kg] = 0.907\ n_{PAX}$
$n_{PAX}\ = number\ of\ passengers\ [-]$

B. Implemented Aerodynamic Modeling Methods

Profile drag

Wheel well fairing/ conformal battery compartments drag area: Torenbeek [96] **Section F-5.3**
$(C_{d,WW}S)[m^2] = 0.045\ A_f$
$A_f\ = frontal\ fairing\ area\ [m^2]$

Fuselage drag area: Torenbeek [96] **Section F-5.3**	
$(C_{D,basic}S)[m^2] = C_F\ S_{f,wet}\ (1 + \varphi_f)$	(eq. F-38)
$\Delta_{\alpha\beta}(C_D S) = A_I\left\lvert(\sin\alpha_f)^3\right\rvert +\ A_{II}\frac{\lvert(\sin(\alpha_f-\beta))^3\rvert}{\cos\beta}$	(eq. F-51)
$C_F = flat\ plate\ friction\ coeff.\ [-]$ $S_{f,wet} = fuselage\ whetted\ area\ [m^2]$ $\varphi_f = fuselage\ shape\ factor\ [-]$	$A_I, A_{II} = fuselage\ planform\ areas\ [m^2]$ $\alpha_f = fuselage\ angle\ of attack$ $\beta = fuselage\ tail\ upseeep\ angle$

Wing profile drag coefficient: Torenbeek [96] **Section F-5.3**	
$c_{d,p} = c_{d,p,min} + \Delta l\ c_{d,p}$	(eq. F-28)
$c_{d,p,min} = 2\ C_F\ (1 + \varphi_w)$	(eq. F-29)
$\Delta l\ c_{d,p} = (\Delta l\ c_{d,p})_{ref}\ f\left(\frac{c_l - c_{l,i}}{c_{l,max} - c_{l,i}}\right)^2$	(eq. F-31)
$c_{d,p,min} = min. profile\ drag\ coeff.\ [-]$ $\Delta l\ c_{d,p} = lift\ dependent\ drag\ incr.\ [m^2]$ $\varphi_w = wing\ shape\ factor\ [-]$	$C_F = flat\ plate\ friction\ coeff.\ [-]$ $(\Delta l\ c_{d,p})_{ref}$ $\quad see\ Fig.F-5$ $f\left(\frac{c_l - c_{l,i}}{c_{l,max} - c_{l,i}}\right)$ $\quad see\ Fig.F-7$

Nacelle drag area: Torenbeek [96] **Eq. F-54**	
$(C_D S)[m^2] = C_F \left(1 + \frac{2.2}{\lambda_{n,eff}{}^{1.5}} + \frac{3.8}{\lambda_{n,eff}{}^{3}}\right) S_{n,wet}$	
$C_F = flat\ plate\ friction\ coeff.\ [-]$ $\lambda_{n,eff} = nacelle\ slenderness\ ratio\ [-]$	$S_{n,wet} = nacelle\ whetted\ area\ [m^2]$

Wing fairing drag coefficient: Torenbeek [96] **Section F-4.2 b**	
$\Delta i\ (C_{D,S})_p = 1.5\ C_F\ t_r C_{ci} \left(\cos\frac{\Lambda}{2}\right)^2$	
$C_F = flat\ plate\ friction\ coeff.\ [-]$ $t_r = wing\ root\ thickness\ ratio\ [-]$	$C_{ci} = total\ length\ of\ wing/fuselage\ intersection\ line\ [m]$ $\Lambda =$ wing sweepback angle

Cockpit windshields drag area: Torenbeek [96] **Section F-5.2 b**
$(C_D S)[m^2] = 0.02\ \ (C_{D,fuselage} S)$
$(C_{D,fuselage} S) = fuselage\ drag\ area\ [m^2]$

Landing gear drag area: Torenbeek [96] **Section F-5.2 b**
$\left(C_{D,UC} S\right)_{basic}[m^2] = \frac{1.5 \sum S_{ft}}{S}$
$S_{ft} = Total\ frontal\ area\ of\ thetyres\ [m^2]$

Other drag (excrescences, surface imperfections, etc.): Torenbeek [96] **Section F-5.7**
$Wing$: 6 % $of\ wing\ profile\ drag$
$Fusealge\ \&\ empennage$: 7 % $of\ fuselage\ drag$
$Engine\ installation$: 15 % $of\ nacelles\ drag$
$Systems$: 3 % $of\ zero-lift\ drag$

Vortex drag

Wing vortex drag coefficient: Torenbeek [96] **Section F-5.3**	
$c_{d,v} = (1+\delta)\frac{{C_L}^2}{\pi\ AR}$ (eq. F-9) $\Delta c_{d,v} = 3.7\ x10^{-5} {\varepsilon_t}^2$ (eq. F-20)	
$\delta = lift\ distribution\ impact\ factor\ [-]$ $C_L = aircraft\ lift\ coeff.\ [-]$ $AR = wing\ aspect\ ratio\ [-]$	$\Delta c_{d,v} = increment\ due\ to\ twist\ [-]$ $\varepsilon_t = wing\ twist\ angle\ [deg]$

Fuselage vortex drag area: Torenbeek [96] **Eq. F-24**	
$(C_D S)[m^2] = 0.15\ {\alpha_f}^2 {V_f}^{2/3}$	
$\alpha_f = fuselage\ angle\ of\ attack\ [rad]$	$V_f = fuselage\ volume\ [m^3]$

C. Implemented Trim and Stability Modeling Methods

Empennage size: Raymer [132] **Section 6.4**	
$S_{VTP}[m^2] = c_{VT}\ b_w\ S_w L_{VTP}$ (eq. 6.29) $S_{HTP}[m^2] = c_{HT}\ \bar{C}_w\ S_w L_{HT}$ (eq. 6.28)	
$c_{VT} = vertical\ tail\ vol.coeff.[-]$ $c_{HTP} = horizontal\ tail\ vol.coeff.[-]$ $b_w = wing\ span\ [m]$	$\bar{C}_w = wing\ mean\ cord\ [m]$ $S_w = wing\ reference\ area\ [m^2]$ $L_{VTP}\ \&\ L_{HTP} = distance\ of\ 25\%\ MAC\ points\ [m]$

Aerodynamic center: Torenbeek [96] **Section E-7.1**		
$\left(\frac{x_{ac}}{\bar{C}}\right)_W = 0.25$	AC of the wing	(fig. E-10)
$\frac{\Delta_{f1} x_{ac}}{\bar{C}} = -\frac{1.8}{(C_{L,\alpha})_{wf}} \frac{b_f\, h_f\, l_{fn}}{S\, \bar{C}}$	fuselage correction 1	(eq. E-37)
$\frac{\Delta_{f2} x_{ac}}{\bar{C}} = \frac{0.273}{1+\lambda} \frac{b_f\, c_g\, (b - b_f)}{\bar{C}^2 (b + 2.15\, b_f)}$	fuselage correction 2	(eq. E-38)
$\Delta_n \frac{x_{ac}}{\bar{C}} = \sum k_n \frac{{b_n}^2\, l_n}{S\, \bar{C}\, (C_{L,\alpha})_{wf}}$	nacelles correction	(eq. E-41)
$\frac{x_n}{\bar{C}} = \frac{x_{ac}}{\bar{C}} + \frac{C_{L,h,\alpha}}{C_{L,\alpha}} \left(1 - \frac{d\varepsilon_h}{d\alpha}\right) \frac{S_h l_h}{S\, \bar{C}} \frac{q_h}{q}$	aircraft neutral point	(eq. E-50)
$(C_{L,\alpha})_{wf} = wing - body\ lift\ curve\ slope\ [1/rad]$ $b_f = fuselage\ width\ [m]$ $h_f = fuselage\ height\ [m]$ $l_{fn} = length\ of\ fuselage\ fwd.of\ wing\ [m]$ $S = wing\ reference\ area\ [m^2]$ $\bar{C} = wing\ mean\ chord\ [m]$ $c_g = standard\ mean\ chord\ [m]$ $b = wing\ span\ [m]$ $k_n = -4\ [-]$	$b_n = nacelle\ width\ [m]$ $l_n = nacelle\ length\ [m]$ $C_{L,h,\alpha} = HTP\ lift\ curve\ slope\ [1/rad]$ $C_{L,\alpha} = untrimmed\ lift\ curve\ slope\ [1/rad]$ $\frac{d\varepsilon_h}{d\alpha} = wing\ downwash\ gradient\ [-]$ $S_h = HTP\ reference\ area\ [m^2]$ $l_h = distance\ of\ 25\%\ MAC\ points\ (wing\_HTP)\ [m]$ $\frac{q_h}{q} = dynamic\ pressure\ ratio\ (wing\_HTP)[-]$	